A Thesis Submitted for the Degree of PhD at the University of Warwick

Permanent WRAP URL:

http://wrap.warwick.ac.uk/152078

Experimental and Computational Study of Molecular Communication in Turbulent Fluid Environments

by

Mahmoud Abbaszadeh

Thesis

Submitted to the University of Warwick

for the degree of

Doctor of Philosophy

School of Engineering

November 2020

THE UNIVERSITY OF
WARWICK

Contents

List of Tables v

List of Figures vi

Acknowledgments xii

Declarations xiv

List of Publications xv

Abstract xvii

Abbreviations xix

Chapter 1 Introduction 1
- 1.1 Background 1
- 1.2 Aims & Objectives 3
- 1.3 Thesis Organisation 4

Chapter 2 Literature Review 6
- 2.1 Overview of Molecular Communication 6
  - 2.1.1 Communication Paradigm 8
- 2.2 Channel Capacity 9
- 2.3 Propagation Channel Models 11
  - 2.3.1 Diffusion 11
  - 2.3.2 Advection 13
  - 2.3.3 Turbulent Flows 16
- 2.4 Modulation Schemes 18
  - 2.4.1 Particle Quantity 18
  - 2.4.2 Type and/or Structure of Particles 19

2.4.3 Time of Release 20
2.4.4 Hybrid Modulation Method 21
2.5 Error Correction 21
2.6 Experimental Molecular Communication 22
2.7 Macro-scale Molecular Communication 23
2.7.1 Macro-scale Molecular Communication in Nature 23
2.7.2 Macro-scale Molecular Communication in Engineering 25

Chapter 3 Methodology **30**
3.1 Fluid Flow Equations 30
3.1.1 Navier–Stokes Equations 30
3.1.2 Reynolds Average Navier Stokes Equations 32
3.1.3 k-ϵ Model 32
3.2 Numerical Simulation 37
3.2.1 COMSOL Multiphysics 37
3.2.2 Grid Independence Test 42
3.3 Experimental Systems 43
3.3.1 Armfield Flume (Channel) 43
3.3.2 Particle Image Velocimetry (PIV) 45
3.3.3 Ultrasonic Velocity Profiler (UVP) 51
3.3.4 Planar Laser-Induced Fluorescence (PLIF) 54
3.3.5 CYCLOPS-7 Submersible Fluorometer 58
3.3.6 Data-set 59
3.3.7 Experimental Recommended Practice 60

Chapter 4 Uncertainty Quantification in Turbulent Diffusion Channel **62**
4.1 Motivation 62
4.1.1 Review of Similar Work 63
4.1.2 Uncertainty in Molecular Signal Propagation 64
4.2 Polynomial Chaos Expansion 64
4.2.1 Univariate Polynomial Chaos 64
4.2.2 Example of Usage 66
4.2.3 Parametric Univariate PCE 67
4.2.4 Multivariate PCE 68
4.2.5 Approximation Using PCE 68
4.3 System Model and Method 69
4.3.1 Channel Configuration 69

4.3.2 Non-intrusive PCE 70
4.4 Results & Discussion 72
4.4.1 Convergence Test of PCE 72
4.4.2 Comparing different PDFs in PCE 73
4.4.3 Statistical results 74
4.5 Summary 75

Chapter 5 Towards the High Channel Capacity Using Vortex Rings 77
5.1 Motivation 77
5.2 Review of Similar Works 77
5.2.1 Vortex Rings in Turbulence 78
5.3 Vortex Ring Structure & Generation 78
5.4 Results & Discussion 81
5.4.1 Transmission 82
5.4.2 Effects of Stroke Ratio on CIR 83
5.4.3 Effects of Injection Velocity on CIR 84
5.4.4 Signal-to-Interference Ratio (SIR) 91
5.4.5 Sequential Vortex Rings 92
5.5 Summary 93

Chapter 6 Linearity of Turbulent Diffusion Channel 94
6.1 Motivation 94
6.1.1 Review of Similar Works 95
6.2 System Model 95
6.3 Non-linearity Analysis 97
6.3.1 Single Emission Scenario 97
6.3.2 Scenario with Consecutive Emissions 98
6.3.3 Signaling Envelop Analysis 101
6.4 Interference Modeling 102
6.5 Summary 105

Chapter 7 Noise Distribution and Mutual Information in Turbulent Diffusion Channel 106
7.1 Motivation 106
7.1.1 Review of Noise Models 106
7.2 Modelling of the Channel 107
7.2.1 Steady Flow Regime 109
7.2.2 Turbulent Flow Regime 112

7.3 Mutual Information 112
  7.3.1 Steady Flow 113
  7.3.2 Different Receiver Size & Detection Threshold 115
7.4 Summary 116

Chapter 8 Kolmogorov Turbulence and Information Dissipation in Molecular Communication 117
8.1 Motivation 117
  8.1.1 Review of Similar Works 118
8.2 Channel Configuration 119
8.3 On-off Key Dye Injection 120
  8.3.1 Injection Mechanism 120
  8.3.2 Concentration Data 121
8.4 Turbulent Velocity Signal 122
  8.4.1 Velocity Correlation and Integral Length Scale 123
  8.4.2 Energy Cascade 124
8.5 Results and Discussion 128
  8.5.1 Information Length Scale 128
  8.5.2 Information Dissipation Rate 129
  8.5.3 Mutual Information 132
8.6 Summary 133

Chapter 9 Experimental Design of Single Molecule Sensing 135
9.1 Motivation 135
  9.1.1 Review of Nanopore Sensing 135
9.2 Experimental Set-up 138
  9.2.1 Device Fabrication 138
  9.2.2 Electrical Measurements 139
9.3 Results 140

Chapter 10 Conclusions and Future Work 145
10.1 Conclusion 145
10.2 Future Work 147
  10.2.1 Suggestions for Macro-scale MC 147
  10.2.2 Suggestions for Micro-scale MC 147

List of Tables

3.1 Empirical coefficients for the transport equations models. 36
3.2 Summary of features of PIV and PLIF methods. Equipment required for running experiment and websites for purchasing those equipment. 56

4.1 Simulation parameters for PCE simulation. 71

6.1 Simulation parameters for linearity analysis 97

7.1 Experimental parameters for quantifying noise distribution and mutual information. 107

List of Figures

1.1 Illustration of nanotechnology communication between micro-robots. Image is taken from: www.news.itmo.ru/en/news/6393. 3

2.1 Block-diagram shows the basic elements of the a) conventional, and b) molecular communication channelS. 8
2.2 Modulation techniques for conventional and molecular communication systems. 19

3.1 COMSOL desktop, including quick access toolbar, ribbon, model builder, setting window, and graphic window. 39
3.2 Geometry section in model builder. 39
3.3 Material section in model builder. Predefined materials in gas, liquid, and solid phases are available in this section. 40
3.4 CFD module section. Different turbulent models are available in the setting window. Initial and boundary conditions can be changed in the model builder window. 41
3.5 Transport of concentrated species section. Three different transport mechanisms can be selected in the setting window. 42
3.6 Grid independence test for the vortex ring numerical modelling. . . . 43
3.7 a) Armfield-flume (channel) configuration. It is 15 m long, 0.3 m wide, and 0.6 m deep, b) Rod obstacle used for generating the turbulence in the channel, c) Transmitter pipe, d) Receiver station. 45
3.8 Injection system. It comprises of power, stepper motor, syringe, solenoid valve, and a box that contains all electronic boards. 46
3.9 Schematic of PIV set-up. Laser sheet excites the flow seeded by tracer particles, and the camera captures the motion of the particles in successive frames. Cross-correlation of successive images yields the velocity field. 47

3.10 a) An original PIV image in the vertical plane, b) PIV image with sub divided interrogation areas. 48
3.11 Two PIV images taken at times t and t+Δt where Δt = 0.01 s. . . . 49
3.12 Final stage of converting pixel distance to read distance, a) the calibration plate in the vertical plane, b) velocity vector field obtained by analysing a PIV image pair. 49
3.13 Schematic of UVP acquisition set-up. Transducer sends the sound wave and receives the reflected sound from a particle. 52
3.14 Illustration of terms connected with measuring window. 53
3.15 Schematic of PLIF. Laser sheet excites the fluorescence injected by the transmitter and the camera captures the intensity of excited fluorescence. 55
3.16 PLIF images sample taken at time a) 30 s and b) 40 s. 57
3.17 Intensity of the PLIF images in terms of time at the receiver. 57
3.18 Calibration curve obtained from the calibration images. 58
3.19 Final Concentration versus time after calibration. 59

4.1 Schematic of the cross-section cut of the system model illustrating the quiescence environment, transmitter, receiver, and emitted molecules. 70
4.2 Concentration versus time profiles. From left to right shows the increasing of the polynomial order (p). First row is for the PCE and the second row is for the LSPCE. In each column, the p is fixed for better illustration of the increased N. The subsets in the second row shows the Monte Carlo simulation results for comparison. 72
4.3 a) Expectation of LSPCE for different polynomial orders. The inset shows the difference between the expectations by increasing the order of the applied polynomials, b) variances of LSPCE for different polynomial orders. 73
4.4 a) Concentration vs. time using uniform distribution as the PDF of the uncertain input parameters, b) concentration vs. time using Gaussian distribution as the PDF of the uncertain input parameters. Dynamic viscosity of the water (μ) and turbulent Schmidt number(Sc) are uncertain input parameters. 74
4.5 10000 concentration profiles obtained by LSPCE for uncertain input parameters of, a1) c_0, b) u_0, c) v_0, d) w_0. 75

5.1 (a) Illustration of transmitter piston design to generate vortex ring, (b) illustration of vortex ring core properties and its orientation in cylindrical coordinates with a surrounding vortex atmosphere. 78
5.2 Time variant velocity program ,V_0, that shows the motion motion. . 80
5.3 Classical hyperbolic tangent profile, V_{zb}. 81
5.4 Prescribed axial velocity of the piston to generate vortex ring. 82
5.5 Validation of present study with Danaila and Helie's study [Danaila and Hélie, 2008]. 83
5.6 Sequential symbols transmitted, (a) puffs, (b) vortex Rings, and (c) experimentation of Vortex Rings. 84
5.7 Received concentration profile of the vortex ring in τ_1=0.5 and for different piston velocities and stroke ratios. 85
5.8 Received concentration profile of the vortex ring in τ_1=0.7 and for different piston velocities and stroke ratios. 86
5.9 Received concentration profile of the vortex ring for Lp/Dp=1 and in different piston velocities. 87
5.10 Received concentration profile of the vortex ring for Lp/Dp=2 and in different piston velocities. 88
5.11 Received concentration profile of the vortex ring for Lp/Dp=3 and in different piston velocities. 88
5.12 Received concentration profile of the vortex ring for Lp/Dp=4 and in different piston velocities. 89
5.13 Received concentration profile of the vortex ring for Lp/Dp=6 and in different piston velocities. 89
5.14 Received concentration profile of the vortex ring for Lp/Dp=10 and in different piston velocities. 90
5.15 Received concentration profile of the vortex ring for Lp/Dp=14 and in different piston velocities. 90
5.16 SIR of the vortex signal for different piston velocities and τ_1=0.5. . . 91
5.17 Demonstration of sequential vortex ring symbol transmission observed at different times. 92

6.1 Schematic of the system model showing the quiescence environment, the transmitter, the receiver, and the emitted molecules. 96
6.2 CIR for a single emission. 97

6.3 Snapshots of the environment and the emitted molecules at different time instances for consecutive emissions. New emissions sweep the tails of the previous emissions. 98
6.4 Received concentration for six consecutive emissions. Molecule types are changed for distinguishing the effect of each emission. Scenarios (a) without co-flow and (b) with co-flow are considered. Red dashed curve corresponds to emission of single type molecule and the blue dashed curve corresponds to sum of six consecutive emissions with different molecule types. 99
6.5 Envelop analysis with considering two emissions with a time gap. The first emission is released at $t = 0$ and 40, 80, and 120 s after that, the second emission is released. The second emission is shifted to $t = 0$. 100
6.6 Correlation and cosine distance between the two received signals with different time gaps. 101
6.7 Empirical and theoretical received concentration for 10 sequential emissions. Theoretical received signal is obtained by using the fitted base functions and (6.4). 103
6.8 SIR versus the number of previous emissions with different co-flow velocities. 104

7.1 Schematic of the experimental setup 108
7.2 LTI system 109
7.3 a1) The concentration over time for 42 analogous experiments at the Rx (blue dashed line) and the fitted curve. The inset is the zoom-in of the concentration peaks for better illustration of transposition noise. a2) Histogram of n_1(transposition noise) and corresponding Gaussian PDF. a3) Histogram of n_2 (additive noise) and corresponding Gaussian PDF. 111
7.4 Concentration versus time profile in the turbulent case. These are seven sample profiles from the total of 40 sample profiles which is illustrated in the left hand side inset. The right-hand-side inset is the illustration of the C_3 and C_T-C_3 values. 113
7.5 The probability density functions of the received peak concentration for symbol ‘0’ and symbol ‘1’. 114
7.6 a1) Different receiver size and their corresponding histogram for additive noise in steady flow regime. a2) Mutual information versus p_0 with different C_{th}s. 115

8.1 Experimental arrangement in water channel (not to scale). 119
8.2 a1) Concentration profile at d=1.0 m from the transmitter. This profile is fitted by the Gaussian distribution to derive the OOK injector pulse function. The inset shows histogram of the peak values of the concentration profiles at d=1.0 m from the transmitter. Superposition of ten CIRs at a2) d=1.0 m, a3) d=3.0 m a4) d=5.0 m. b1) Seven consecutive signals sent to the channel by the transmitter. Seven consecutive signals received by the receiver at b2) d=1.0 m, b3) d=3.0 m b4) d=5.0 m. 120
8.3 Seven-bit signal sequences for the tracer concentration, for three different values of the Reynolds number Re_0, in steady turbulence. . . . 122
8.4 Seven-bit signal sequences for the tracer concentration for steady turbulence at $Re_0 = 16,000$ in comparison to data for the corresponding flow in the modified turbulence. 123
8.5 Temporal variation of velocity, $u(t)$ at $d = 1$ m from Tx 124
8.6 Spatial variation of velocity, $u(x)$ over a section extending 185 mm upstream of Rx, which itself was located $d = 1$ m downstream of Tx. 125
8.7 Energy spectrum for three different values of the Reynolds number Re_l of the large eddies. 126
8.8 Variation of $\langle C^2 \rangle$ of the molecular signals with distance d from Tx for three different values of the Reynolds number Re_l for modified turbulence 127
8.9 Variation of information dissipation rate ϵ_c of the molecular signals with distance d from Tx for three different values of the Reynolds number Re_l for modified turbulence. 128
8.10 Energy dissipation rate, ϵ_l vs. distance from transmitter. 130
8.11 Superposition of temporal concentration variations for seven individual bit ‘1’ and bit ‘0’ signals in modified turbulence and their associated respective mean curves for three different values of the Reynolds number Re_l ($d = 1.5$ m). 131
8.12 $I(X_1; X_2)$ with various Δt. 133

9.1 Schematic of nannochannel. The nanoparticles are added to the *trans* reservoir and they are driven into the nanopore by electrophoresis force. Grounded Ag/AgCl electrode is placed in *trans* and active Ag/AgCl electrode is placed in *cis*. 137
9.2 TEM image illustrating the size of the nanopore (30 nm). 139

9.3 a) MultiClamp 700B amplifier to generate voltage difference, and Digidata 1550B digitiser to record the acquired current signal, b) Glass capillary that is placed in the PDMS and two electrodes are connected to the the headstage. Headstage is the bridge between the capillary and amplifier. 140
9.4 I-V digram for three different concentrations of KCl electrolyte solutions. 142
9.5 The raw ionic current signal acquired in this experiment. The spikes show that the BSA molecules are passing through the nanopore. Each individual current drop is associated with one BSA molecule translocation. 142
9.6 Threshold-based signal detection used to detect the BSA molecules when they are passing through the nanopore. The detection threshold is -9 pA. 143
9.7 Event charge deficit (ECD) histogram for BSA molecules. It confirms that most of the BSA molecules have the same form. 143
9.8 Peak amplitude histogram for BSA molecules. It shows that the BSA molecules are monodisperesed. 144

10.1 Schematic of data storage on DNA strands. 148

Acknowledgments

I would like to express the deepest appreciation to my supervisor, Professor Peter J. Thomas, who has the substance of a genius: he convincingly guided and encouraged me to be professional and do the right thing even when the road got tough. Without his persistent help, the goal of this project would not have been realized. I want to thank to him not only for his consistent support but also for his incredible patience during my PhD journey. He is the kindest person I have ever met in my entire life. Being his student is the greatest treasure I have ever had.

I wish to express my sincere appreciation to my supervisor, Professor Weisi Guo, who introduced me to the research field and provided me with valuable guidance as well as persistent encouragement. Without his support and funding, this project could not have reached its goal. I would also like to express my gratitude to my co-supervisor, Dr. Jerome Charmet. It is whole-heartedly appreciated that your great advice for my study proved monumental towards the success of this study.

My sincere gratitude also goes to my examiners, Prof. Maged Elkashlan from Queen Mary University of London, and Dr. Soroush Abolfathi from the school of Engineering, University of Warwick.

I would like to express my deepest gratitude to precision engineers, Mr. Ian Bayliss and Mr. Paul Hackett, for the excellent technical supports received during the experimental work. Without their precious supports it would not be possible to conduct this research.

I take this opportunity to say thank you for my friends and mentors, Dr. Petr Denissenko (University of Warwick), Dr. H. Birkan YILMAZ (Bogazici University), Dr. Lin Lin (Tongji University), Dr. Giannis Moutsinas (Coventry University), Dr.

Navid Alemi (University of Warwick), Dr Siavash Esfahani (University of Warwick) for their valuable collaboration and comments on my research, which are indispensable for my research progress. I wish to thank all the people whose assistance was a milestone in the completion of this project. I would like to recognize the invaluable assistance that you all provided during my study.

Finally, with my love and gratitude, I would like to dedicate this thesis to my family who always provide me the unreserved support and selfishless love, especially to my parents, Mrs. Sharifeh Ghasemi, Mr. Amrollah Abbaszadeh, and my fiancée Yifan Liu.

Declarations

I herewith declare that this thesis contains my own research performed under the supervision of Prof. Peter J. Thomas, Prof. Weisi Guo, and Dr. Jerome Charmet, without assistant of third parties, unless stated otherwise. No part of this thesis was previously published or submitted for a degree at any other university.

List of Publications

Journals

[A] **M. Abbaszadeh**, P. J. Thomas, and W. Guo, “Towards high capacity molecular communications using sequential vortex rings”, IEEE Transactions on Molecular, Biological and Multi-Scale Communications, vol. 4, no. 1, pp. 39–42, 2018.

[B] **M. Abbaszadeh**, G. Moutsinas, P. J. Thomas, and W. Guo, “Uncertainty quantification in molecular signals using polynomial chaos expansion”, IEEE Transactions on Molecular, Biological and Multi-Scale Communications, vol. 4, no. 4, pp. 248–256, 2018.

[C] **M. Abbaszadeh**, I. U. Atthanayake, P. J. Thomas, and W. Guo, “Molecular signal tracking and detection methods in fluid dynamic channels”, IEEE Transactions on Molecular, Biological and Multi-Scale Communications, vol. 6, no. 2, pp. 151–159, 2020.

[D] J. Li, W. Zhang, X. Bao, **M. Abbaszadeh**, and W. Guo, “Inference in Turbulent Molecular Information Channels using Support Vector Machine”, IEEE Transactions on Molecular, Biological and Multi-Scale Communications, vol. 6, no. 1, pp. 25–35, 2020.

[E] **M. Abbaszadeh**, Y. Huang, P. J. Thomas, and W. Guo, “Kolmogorov Turbulence and Information Dissipation in Molecular Communication”. IEEE Transactions on Molecular, Biological and Multi-Scale Communications.

[F] W. Guo, **M. Abbaszadeh**, L. Lin, J. Charmet, P. J. Thomas, Z. Wei, B. Li, C. Zhao, "Molecular 6G in Wave-Denied Environments", IEEE Communications Magazine.

Conferences

[G] **M. Abbaszadeh**, P. J. Thomas, and W. Guo, "Empirical turbulent diffusion channel model for molecular communications." in 2018 3rd Workshop on Molecular Communications, Gent, Belgium.

[H] **M. Abbaszadeh**, B. Yilmaz, P. Thomas, and W. Guo, "Linearity of Sequential Molecular Signals in Turbulent Diffusion Channels", in 2019 IEEE International Conference on Communications (ICC), Shanghai, China.

[I] **M. Abbaszadeh**, W. Li, L. Lin, I. White, P. Denissenko, P. J. Thomas,and W. Guo, "Mutual information and noise distributions of molecular signals using laser induced fluorescence", in 2019 IEEE Global Communications Conference (GLOBECOM). Waikoloa, HI, USA, 2019, pp. 1–6.

Abstract

Molecular communication (MC) is a type of communication and networking in the electromagnetic (EM)-denied environments. MC is concerned with information transfer by preserving information in the structure of chemical flow through molecular diffusion, advection or reaction. Hence, the information transmission in MC is closely associated with the physics of fluid dynamics. The mechanism of MC, i.e., using chemical substances for information exchange, is prevalent in nature among organisms at various length scales, from intra-cell signaling and bacterial communication to airborne and waterborne pheromone signals.

At nano-scale the physical conditions are such that the main mechanism of transport is mass diffusion. Therefore fluid turbulence, for which other transport mechanisms are relevant, have hitherto hardly been considered at all in the context of MC. Nevertheless, MC is obviously not restricted to nano-scales, as demonstrated by insect and crustacean pheromone signaling. Here turbulence does become a crucial issue affecting the reliability of the message transfer. The goal of this thesis is to draw on turbulence theory to assess implications of relevance to MC at macro scale.

The results show that in turbulent channels, viscous shear stresses hinder a reliable transfer of the molecular information between the transmitter and the receiver which results in severe inter-symbol-interference (ISI). In order to mitigate the ISI in turbulent channels, vortex ring are proposed as coherent structures representing a means for modulating information symbols onto them. Each vortex ring can propagate approximately 100× the diameter of the transmission nozzle without losing its compact shape. It is shown that by maintaining a coherent signal structure, the signal-to-inference (SIR) ratio is higher over conventional puffs.

Moreover, the results show that the received signals of the same transmitted symbols vary due to the presence of the underlying noise in turbulent channels. To understand the behaviour of the noise in turbulent channels, both of the additive and jitter noises distributions characterised statistically, and a new channel model is proposed. Thereafter, this channel model is used to quantify the mutual information in turbulent channels. Finally, the waterborne chemical plumes are investigated as a paradigm for a means of molecular communication at macro scales. Results from the Richardson's energy cascade theory are applied and interpreted in the context of MC to characterise an information cascade and the information dissipation rate. The results show that the information dissipation rate decreases with increasing the Reynolds number and distance d from transmitter. This may appear counter intuitive because stronger turbulence levels at higher Reynolds numbers increases energy dissipation rates. However, increased turbulence leads to more efficient scalar mixing and, therewith, the power of the molecular signal quickly reduces to low levels. Accordingly the information dissipation rate necessarily reduces due to the remaining low information content available.

Abbreviations

Abbreviations	**Definition**	**Units**	**Chapters**
AC	Acoustic Communication		2
ADE	Advection Diffusion Equation		2,3
AWGN	Additive White Gaussian Noise		2
ASK	Amplitude Shift Keying		2
BER	Bit Error Rate		2,7,8
BSA	Bovine Serum Albumin		9
CFD	Computational Fluid Dynamics		1,3,5,6
CIR	Channel Impulse Response		2,4,6
CMOS	Complementary Metal Oxide Semiconductor		3
CSI	Channel State Information		2
CSK	Concentration Shift Keying		2
CQDs	Carbon Quantum Dots		2
CW	Continuous Wave		3
D-MoSK	Depleted MoSK		2
ECD	Event Charge Deficit		9
EM	Electromagnetic		1,2
FWHM	Full Width at Half Maximum		2
FSK	Frequency Shift Keying		2
FEM	Finite Element Method		3
HWA	Hot-Wire Anemometry		3
IV	Current-Voltage		9

ISI	Inter-Symbol-Interference		All
IPA	Isopropyl Alcohol		2
IG	Inverse-Gaussian		7
I-MoSK	Isomer-based Molecular Shift Keying		2
LOS	Line-of-sight		2
LSPCE	Least Square Polynomial Chaos Expansion		4
LDA	Laser Doppler Anemometry		3
LDV	Laser Doppler Velocimetry		3
MSSK	Molecular Space Shift Keying		2
MCDF	Molecular Coding Distance Function		2
MIMO	Multiple-Input Multiple-Output		2
MMs	Messenger Molecules		3,6
MIMS	Membrane Inlet Mass Spectrometer		2
MC	Molecular communication		All
MCvTD	Molecular communication via turbulent diffusion		1
MI	Mutual Information	bit/symbol	1,2
MPE	Maximum Permissible Exposure		3
MEMS	Micro-Electro-Mechanical System		2
MoSK	Molecular Shift Keying		2
NOHD	Nominal Ocular Hazard Distance		3
NEMS	Nano-Electro-Mechanical System		2
OOK	On-Off-Keying		2,5,8
PCE	Polynomial Chaos Expansion		1,4
PDE	Partial Differential Equation		2,3
PIV	Particle Image Velocimetry		3

PLIF	Planar Laser Induced Florescence	3,7
PDF	Probability Density Function	2,4,7
PPM	Pulse Position Modulation	2
PDMS	Polydimethylsiloxane	9
PCR	Polymerase Chain Reaction	9
RANS	Reynolds-Averaged-Navier-Stokes	3,5
NS	Navier-Stokes	3,5
SIR	Signal to Interference Ratio	5
ssDNA	Single-Stranded DNA	9
TEC	Time-Elapse Communication	2
TEM	Transmission Electron Microscopy	9
QMSSK	Quadrature Molecular Space Shift Keying	2
UVP	Ultrasonic Velocity Profiler	3,8

Symbols	**Definition**	**Units**	**Chapters**
μ	Dynamic Viscosity	$\mathrm{N \cdot s/m^2}$	2
ν	Kinematic Viscosity	$\mathrm{m^2/s}$	2,5,6
ρ	Density of water	$\mathrm{kg/m^3}$	4,6
α	mass diffusivity	$\mathrm{m^2/s}$	6,8
Γ	Circulation	$\mathrm{m^2/s}$	5
Re	Reynolds number	—	2,3,5,6,8
Sc	Schmidt number	—	4,8
Pe	Péclet number	—	2,5,6
σ	Standard Deviation	—	7
δ_{mn}	Kronecker Delta	—	2,4
k_B	Boltzmann's constant	J/K	2
T_T	Temperature	K	2

λ_n	Hankel transform parameter	—	2
ϕ	Porosity of the material	—	2
τ_s	Static threshold value	—	2
φ	Phase of a wave	rad	2
C	Channel capacity	bits/channel	2
D	Coefficient of diffusivity	m^2/s	2
D_ϵ	Eddy diffusivity	m^2/s	3,6,7
D_L	Longitudinal coefficient of diffusivity	cm^2/s	2
D_R	Radial coefficient of diffusivity	cm^2/s	2
D_v	Random forces on a particle	N	2,7
μ_D	Drag forces on a particle	N	2
d	Distance	m	1
c	Concentration	$\mathrm{mol}/\mathrm{m}^3$	All
t	Time	second	All
f	Frequency	Hz	All
A_w	Wave amplitude	—	2
f_d	Doppler-shift frequency	Hz	3
f_0	Transmit frequency	Hz	3
N_{ch}	Number of channels	—	3
P_{max}	Maximum measurable length	m	3
$\mathrm{I}(\cdot;\cdot)$	Mutual information	bit/symbol	2,7
$J(x,t)$	Mass flux	$\mathrm{kg}/\mathrm{m}^2 \cdot \mathrm{s}$	2
$\mathcal{N}(\mu, \sigma^2)$	Gaussian distribution	—	2
M_0	Injected mass to the environment	kg	2
W_n	Wiener Process	—	2
Rx	Receiver	—	All
Tx	Transmitter	—	All
m	Mass a particle	kg	All
$p_v^n(t)$	Particle position	m	2

r	Radius	m	All
L	Characteristic length scale	m	2
W	Channel width	m	2
p	Wetted perimeter of the channel	m	2
A	Area	m^2	2
N_0	Noise power	—	2
S	Signal power	—	2
Ξ	Random variable	—	4
$H(\cdot)$	Polynomial	—	4
ζ	Realization of random variable	—	4
$\mathfrak{F}$	Fourier transform	—	8
R_{xx}	Velocity correlation	—	8
ϵ	Energy dissipation rate	J/s	8
u	Mean flow velocity	m/s	2,
u_x, u_y, u_z	Velocity components	m/s	2
u_{avg}	Average flow velocity	m/s	
x, y, z	Cartesian coordinates	m	2
x_0, y_0, z_0	Injection point	m	2
r, θ, z	Cylindrical coordinates	m	2

Mathematical Notations	**Definition**	**Units**	**Chapters**
$\sum$	Sum		2,4,5
$x \triangleq y$	x equal by definition to y		2
∇	Del operator		2
∇^2	Laplace operator		2
$\mathrm{erf}(\cdot)$	Error function		2
P_{XY}	Joint probability of X given Y		7
$P_{X\|Y}$	Conditional probability of X given Y		2,7

J_0	Bessel function of the 0^{th} kind	—	2
J_1	Bessel function of the 1^{th} kind	—	2
sup	Supremum	—	4
$\mathbb{N}$	Set of natural numbers	—	4
$\mathbb{R}$	Set of real numbers	—	4
$\mathrm{E}[\cdot]$	Expectation	—	4
$\mathrm{Var}[\cdot]$	Variance	—	4

Chapter 1

Introduction

1.1 Background

Human beings have always needed to convey message and information between two separated entities and this information transfer played a vital role in growing of human civilisation. They utilised different methods to encode, transport, and decode the information. Common ways of delivering information were physical packets (mail), speech (acoustic waves), radio waves in phones and optical waves in fibres, and observing visual signals (hand, flag, smoke signal). In 21 century, the communication styles have progressed unprecedentedly in a way that they become faster and smarter. Digital communication allows mankind to transfer tones of information with a handheld device in a minimum amount time over a long distance that was hard to imagine not long ago [Salehi and Proakis, 2007]. This helps people from different walks of life to make informed decision, based on on-demand data availability. In order to establish a reliable communication system, data from area of interest need to communicate to a data distribution network. At micro-scale the data distribution network can be a swarm nano robots which are used in targeted drug delivery and in macro-scale, sensors report the information in industrial environment [Li et al., 2017]. In both scales, many physical principles of digital communication break down. For instance in micro and nano-scale dimensions, the length scale is too small to build an efficient electromagnetic wave antenna [Farsad et al., 2016]. This is because the size of the antenna should be of the same order as the transmitted/received signal. Generating low frequency signal gives longer wavelength with small amount of energy. Also, generating high frequency waves in conventional wireless communications systems such as electromagnetic and acoustic wave-based systems can be unrealistic for communication between nano machines.

In macro-scale MC such as deep water vehicles, they do not communicate well with traditional communication systems such as acoustic waves. These vehicles need to communicate with surface with the purpose of relaying vital information, command and control, or for search and rescue in emergency situations. Their typical carrier wave[1] frequency is 10-37.5 kHz and current technology (180 dB or 1 µPa) at this frequency allows detection of signal at a range of 5 km (normal sea conditions) and 7 km (good sea conditions). If optical communication system (1000 THz) is utilised, its extreme short range and sensitivity to pollutants and objects in water hinders its functionality and makes it undesirable for long range underwater communication. Generally, the attenuation loss (dB) is both a function of distance d and frequency f which makes all wave-based communication systems unreliable in small scales and deep in the oceans. So, the traditional ways of communication need to be revised and more efficient ways are required [Farsad et al., 2016].

However, molecules are used in animal kingdom to send information. The information transfer can be at cellular level where the message is conveyed through the cells or it can be in macro-scale level where a message is conveyed between two separated animals. For instance, in *quorum sensing*, the bacteria can monitor and control the environment for other bacteria and if the number and/or species present in a community changes, they can respond to that in population-wide scale; or moth and dogs release pheromones to convey a message in the environment. This type of communication that is inspired by nature is called **molecular communication** where molecules are the information carrier in both micro and macro scale [Nakano et al., 2013].

Now, the question is that why do we need to devote our time and resources to study molecular communication? One answer is that the scientists are curious to understand how organism and animals communicate with each other. Apart from that, this field of science may help human to move from science fiction and technological speculation into reality by designing a device like nano-machines that can communicate with molecules in electromagnetic-denied environments (i.e. MC in targeted drug delivery with the aid of micro-scale robots). Thousands of cell-size nanorobots are released in the human body while they carry a specific drug. They cooperate and communicate with each other to spot the tumour cell and unload their drug on that specific cell (see Fig. 1.1). Accomplishing this task without communication

---

[1] A carrier wave is wave of constant frequency in which it does not carry much information by itself that we can relate to (such as speech or data). The reason that the carrier wave is used to transfer the the message is that the input signal often has low frequency and this will need appropriate amount of amplification in order to transmit very low frequencies signals. The input signals themselves do not have significant power and need a large antenna to transmit a signal.

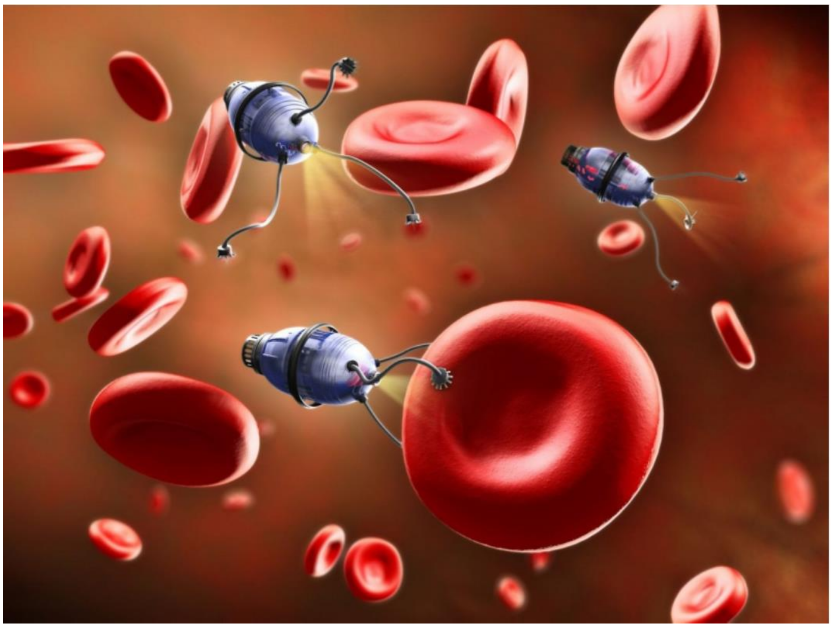

Figure 1.1: Illustration of nanotechnology communication between micro-robots. Image is taken from: www.news.itmo.ru/en/news/6393.

between nanorobots is almost impossible.

1.2 Aims & Objectives

This PhD project is concerned with the molecular communication in the environments where electromagnetic waves is not suitable. Whilst significant research has focused on micro-scale diffusion dominated channels, far less is understood of macro-scale flow dominated channels. The latter introduces complex fluid dynamic processes, one of which is turbulent diffusion. Molecular communication via turbulent diffusion (MCvTD) more accurately reflects realistic molecular channels in both pheromone signaling and chemical engineering. However, a number of open challenges exist in this field. First, we know that the received signal is sensitive to a variety of input and channel parameter variations. Currently we do not understand how uncertainty or noise in a variety of parameters such as injection velocity, initial concentration of molecules, turbulent parameters, etc. affect the received signal concentration, and nor do we have an analytical framework to tackle this challenge. So, we need to show that how uncertainty in parameters propagates to uncertainty in the received signal. Secondly, turbulent flow is severely hindered molecular signal coherence in fluid dynamic channels which causes long molecular tails, which results in severe inter-symbol-interference (ISI) and limits the achievable symbol rate. So, we need to modulate information symbols into stable structures to minimize ISI. Thirdly, current literature assumes linear combining between sequential molecular signals, but this assumption may not hold true when turbulence is introduced. So, we need to investigate the linearity of sequential molecular signals in turbulent diffusion channel. Fourthly, information embedded in the fluid dynamic properties undergo stochastic behaviour due to the high dimensionality and continuous dynamic forces of the environment, which erodes the achievable MI. So, the statistical noise distribution and MI need to be quantified with respect to the key fluid dynamic parameters. Finally and according to the Kelvin's theorem of conservation of the circulation along a fluid contour, it might be possible that the fate of information molecules is tied to that of vorticity field [Sreenivasan, 1991]. We examined this concept and characterised the information cascade and the information dissipation rate.

The main objective of this project is to study macro-scale MC in turbulent flow where the molecular signals undergo stochastic propagation in the channel. This PhD has the following objectives:

(1) Quantifying uncertainty in transmitter parameters.

(2) Increasing the capacity of MCvTD channel by using coherence structure called vortex ring.

(3) Investigating the linearity and characterising the noise distribution and the mutual information in MCvTD channels.

(4) Characterising information cascade and information dissipation rate in MCvTD channels using turbulence theory.

(5) Beginning a short exploratory/preliminary study on nano/micro scale molecular communication and designing an experimental detector at nano-scale.

1.3 Thesis Organisation

This thesis consists of ten chapters. Each of the chapters 3 to 9 has been submitted/published as a journal/conference paper. Chapter 2 covers the literature in MC and reviews the state-of-the-art molecular communication advancements. Chapter 3 explains the methodologies used for experiments and numerical simulation (paper [C]). Uncertainty quantification in turbulent channel is discussed in chapter 4 (paper [B]). In this chapter, we utilise a new method called Polynomial Chaos Expansion (PCE) instead of Monte Carlo to see how the uncertainty and noise in transmitter will propagate through the McvTD channel. In chapter 5, we propose to modulate information symbols into stable vortex ring structures to minimize ISI and increase the channel capacity (paper [A]). Each vortex ring can propagate approximately 100× the diameter of the transmission nozzle without losing its compact shape. In chapter 6, we use computational fluid dynamics (CFD) simulation to show that sequential MCvTD signals do indeed linearly combine (paper [H]). In chapter 7, we quantify the statistical noise distribution and MI with respect to the key fluid dynamic parameters in McvTD channel (paper [I]). In chapter 8, waterborne chemical plume is studied as a paradigm for a means of MC at macro scales (paper [E]). We use the theoretical concept of Richardson energy cascade in turbulent flow to quantify information cascade and information dissipation rate in McvTD channel. In chapter 9, we design an experimental receiver called nanopore for micro/nano-scale molecular communication. This is a short preliminary study to see the feasibility of micro/nano-scale molecular communication experimentally. Chapter 10 is the conclusion and suggestions for the future studies.

Chapter 2

Literature Review

2.1 Overview of Molecular Communication

The ultimate goal of a communication system is to convey a *message* from one point to another point. In order to achieve this goal, the transmitter (Tx) should produce a signal which contains specific information. This message propagates through a channel until it arrives to the receiver (Rx). The Rx then decodes the message to extract the information. Therefore, each communication system has three main components: 1) Transmitter, 2) Receiver, 3) Channel.

In nature, the information at macro-scale can be transmitted by both chemical and electromagnetic (EM) waves whilst in microscale it is mostly done by chemical. As far as the commercial communication is concerned, the EM wave-based communications ranging from radio to optics bands perform very well. However, they have some inherent drawbacks which motivates researchers to seek for other types of communications. As an example, the EM waves are attenuated in aqueous environments or in bounded flows and closed environments (tunnels, pipes, etc.) [Guo et al., 2015; Nakano et al., 2013]. In water, the EM waves are faced a high propagation delay and this problem is exacerbated if the water medium contains minerals such as salt. Salt water has higher conductivity [1] than pure water which results in higher attenuation and it makes it complicated to model the system [Stojanovic, 2003]. Acoustic wave-based communication can be used as an alternative to tackle the problems associated with the EM-based communication systems. In acoustic communication (AC), the information are encoded in the sound waves as opposed to the EM-based communication that information are carried by EM waves.

---

[1] Salt water contains Na^+ and Cl^- ions. Because these ions are free to move in the solution, salt water is electrically conductive. Increased conductivity attenuates the radio waves as the freely-moveable ions absorb and reflect the wave.

Also, AC is more biocompatible than EM-based communication (invertebrates and fish use this method to communicate underwater [Kroodsma and Miller, 1996; Tyack, 1998]). Low diffraction loss makes AC a reliable way of communication underwater, however compared to EM-based communication, AC suffers from low data rates, small available bandwidth, time variations of the channel, multi-path propagation, and high signal attenuation over long distances [Stojanovic and Preisig, 2009]. Another alternative to EM-based communication is optic communication which requires optical fiber for wired communication and a line-of-sight for wireless communication [Tanaka et al., 2000]. There are also several problems when the EM waves are used at nanoscale. Even though it is feasible to have high frequency communication by nanoscale antennas, the engineering problems associated with the integration of the antennas to nanomachines and transceiver design still are significant problems [Akyildiz et al., 2008; Freitas, 1999].

As evidenced by literature, an alternative way of communication is needed to overcome the problems associated with EM-based communication. Molecular communication has proven a reliable communication in EM-denied environments where the path loss [2] is very high [Nakano et al., 2013]. At small scales, Richard Phillips Feynman was the first one who envisaged the fabrication of devices at molecular and atomic level [Feynman, 1960]. On December 29, 1959, he delivered a speech entitled 'There's plenty of room at the bottom' in the American Physical Society meeting at Caltech. In his speech, he invited the researchers to find the solution to the problem of controlling and manipulating the small scales structures. In recent years, the emerging fields of micro- and nano-electro-mechanical system (MEMS and NEMS) have advocated to the miniaturization. Moreover, it has been a long time that the micro-organisms such as bacteria and cells show the ability to send and receive the information from their environment by means of chemical signal molecules. With this action which is called *Quorum Sensing* the bacteria can monitor and control the environment for other bacteria and if the number and/or species present in a community changes, they can respond to that change in population-wide scale [Waters and Bassler, 2005; Miller and Bassler, 2001]. MC is not only restricted to the biological systems, but also the engineering aspects of MC has received remarkable attentions in recent years [Farsad et al., 2016]. Hiyama et al. [2005] were the first group who employed the MC to convey the message between nanomachines in small scales (diffusion-dominated). Since then, the number of researches in MC has increased considerably [Farsad et al., 2016]. At the nano-scale, the physical conditions

---

[2] Path loss, or path attenuation, is the reduction in power density (attenuation) of an electromagnetic wave as it propagates through space. Path loss is a major component in the analysis and design of the link budget of a telecommunication system.

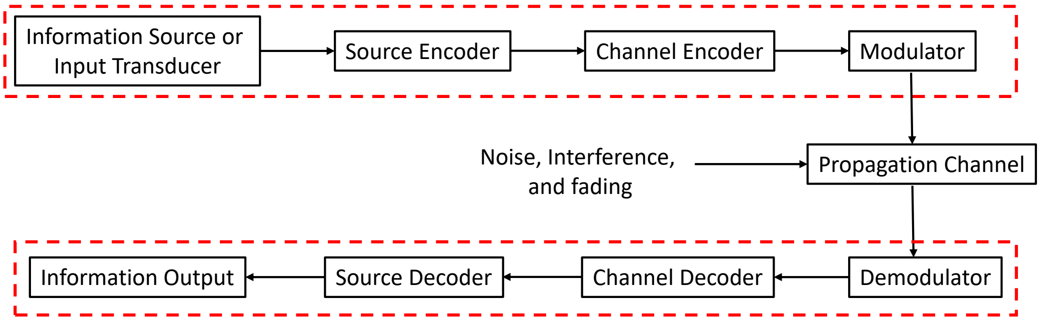

(a) Basic elements of a conventional communication system.

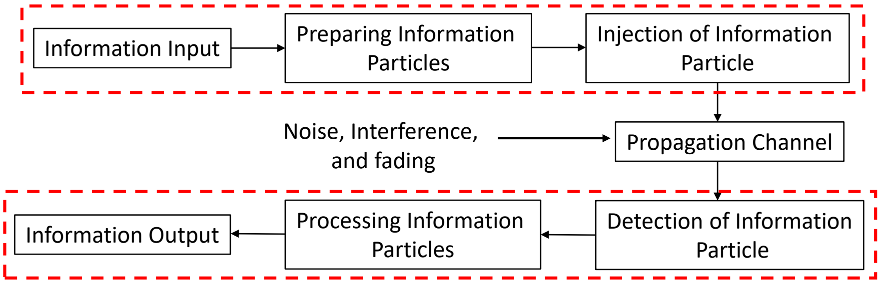

(b) Basic elements of a MC system.

Figure 2.1: Block-diagram shows the basic elements of the a) conventional, and b) molecular communication channelS.

are such that the main mechanism of transport is mass diffusion [Nakano et al., 2013]. Therefore fluid turbulence, for which other transport mechanisms are relevant, have hitherto hardly been considered at all in the context of MC. Nevertheless, MC is obviously not restricted to nano-scales, as demonstrated by insect and crustacean pheromone signaling [Wyatt, 2014]. Here turbulence does become a crucial issue affecting the reliability of the message transfer [Unluturk and Akyildiz, 2017b].

2.1.1 Communication Paradigm

Figure 2.1(a) shows the block diagram of a traditional communication systems where the messages are encoded to the EM waves. *Source encoding* is much about removing the redundant data or the data which is not important for the data to be conveyed to the receiver (something like quantizing and run length coding). *Channel encoding* is more about adding some extra bits in the form of parity bits so that one can protect the data from being corrupted. These data will also serve as the mathematical encryption and can also help in correction of the corrupted data. *Modulation* is more about choosing appropriate signaling scheme and translating the baseband signaling to the high frequency and also involves choosing and using the effective modulation schemes perfect for the channel scenario. After modulating, the signal is transmitting to the channel where it can be wired or wireless. When the signal arrives at the receiver, the signal will be demodulated and the information will be transferred. The noise is inseparable part of any communication channels and it would distort the transmitted signal by degrading the signal power. The source of the noise in traditional communication systems are interference and fading of EM waves.

Figure 2.1(b) illustrates the communication paradigm of the MC systems. The main difference between the traditional and MC communication systems is that in MC the messages are embedded in the molecules which are biological compounds with different sizes. In MC system, the molecules (information particles) should be prepared before modulation. Then, the information are encoded in the concentration of information particles or in the type of the molecules (see Section 2.4). The transmitter may use an external power to inject the molecules into the environment. After transmission, the molecules are propagated into the channel which can be an open environment or it can be an internal flow like pipe flow. Depends on the length scale of the communication, the propagation mechanism can be diffusion, advection or a combination of both. At the receiver, a sensor is required to measure the feature of the molecules, for example, the amplitude of concentration, the type of the molecules, the arrival time of the molecules, etc. After receiving the message, a processing unit is required to decode the information. The unit may need an external power to process the information. Similar to the traditional communication systems, noise is also present in the MC systems. The source of the noise can be imperfect transmission unit, noises associated with the sensor at the receiver, thermal noise, chemical reaction, turbulent mixing at macro-scale, etc.

In this thesis, we only focus on the long-range MC systems. The channel that we will investigate in this thesis is turbulent diffusion channel where the molecules are propagated in the channel by turbulent eddies.

2.2 Channel Capacity

Information theory is a field of science that provides insight into the communication system [Mac Kay, 2003]. In every communication system, the messages are propagated through the channel and if the transmitted message X and the received message Y are the same, the channel is ideal and noiseless. However, this does not happen in reality and channels are noisy. For example, cross-talk happens in telephone lines, or the hardware in the transmission system distorts and adds noise to the transmitted signal. The network in deep space that listened to the Galileo's puny transmitter suffered from background radiation from cosmic and terrestrial sources. Noise also has existed in biological communication systems such as DNA that is subject to the damages and mutation. In disk drives where the data is written by aligning a patch of magnetic material, the noise can be the patch of material that might spontaneously flip magnetization, or it can be caused by the written head that might not induce the magnetization in the first place. In molecular communication, the noise can be introduced by transmitter, the particle interactions, the turbulent flow in the channel, chemical reactions, detector, etc. which hinders a reliable communication [Jamali et al., 2017]. These noises impose an upper bound on the communication channels and the amount of information that can be transmitted reliably. This upper bound is called channel capacity (C). Shannon proposed a model for the maximum channel capacity with additive white Gaussian noise (AWGN) [Shannon, 1948]:

$$C = \log_2 \left(1 + \frac{S}{N_0}\right), \tag{2.1}$$

where N_0 is the noise power and S is the signal power. In MC, channel capacity can be increased by using advection as propagation mechanism or by generating coherent structures in fluid flow such as vortex rings. The latter is discussed in detail in chapter 5.

Capacity of the channel, as defined above, is given by the maximum of the mutual information (MI) between the input and output of the channel, where the maximization is with respect to the input distribution. For a discrete memory-less channel, the achievable MI rate is given by [Gohari et al., 2016; Shannon, 1948]:

$$I(X;Y) = \sum_{x,y} P_{XY}(x,y) log \left[\frac{P_{XY}(x,y)}{P_X(x)P_Y(y)}\right], \tag{2.2}$$

where $I(X;Y)$ is the MI, $P_{XY}(x,y)$ is the joint probability distribution and X and Y are two discrete variables. $P_X(x)$ and $P_Y(y)$ are the marginal probability distributions. The channel capacity for memoryless channel and channel with memory is calculated by [Gohari et al., 2016; Shannon, 1948; Verdú et al., 1994]:

$$C \triangleq \begin{cases} \max\limits_{p(x)} I(X;Y) & \text{for memoryless channel,} \\ \lim\limits_{x \to +\infty} \sup \frac{1}{n} I(X^n;Y^n) & \text{for a channel that has memory,} \end{cases} \tag{2.3}$$

where n is the size of the block in a channel with memory. We will see in chapters 6 and 7 that the MC channels have memory and the ISI should be taken into account in calculating the MI [Gallager, 1968]. In MC, modelling of the channel [Mustam et al., 2017; Turan et al., 2018a; Murin et al., 2018; Ahmadzadeh et al., 2017; Kwak et al., 2020], modelling of noise [Etemadi et al., 2019; Srinivas et al., 2012], and channel capacity [Farsad et al., 2017; Bafghi et al., 2018; Galluccio et al., 2017] have been studied very well in recent years.

2.3 Propagation Channel Models

The propagation of molecules from transmitter to the receiver is categorised as two modes, namely passive and active mode. In passive mode, the molecules randomly diffuse to the receiver (i.e. diffusion) which is suitable for dynamic and unpredictable environments [Pierobon and Akyildiz, 2012, 2010]. On the other hand, in active mode, the molecules are advected directionally towards the receiver by external forces (i.e. motor protein assisted [Hiyama et al., 2010], bacteria assisted [Berg, 2008], fan in turbulent flow [Kennedy et al., 2018], and etc.). In this section, different propagation mechanisms in MC channels are reviewed over the next subsections.

2.3.1 Diffusion

Diffusion is the random movement of molecules from higher concentration region to the lower concentration region. It is known as *Brownian Motion* which is erratic random movements of microscopic particles in a fluid, as a result of continuous bombardment from molecules of the surrounding medium [Karatzas and Shreve, 1998]. In diffusion, the particles do not need any external force for the movement. Diffusion has numerous applications especially in biological processes. For instance, when the O_2 is inhaled into the lung, the O_2 and CO_2 are exchanged by diffusion through a 1-2 µm membrane. Based on the environment where the diffusion is initiated, the definition of diffusion can be different. For example, diffusion in cell membrane is different from that of turbulent diffusion in terms of mathematical concept and model. Generally, we have four types of diffusion; 1)**Anomalous Diffusion** that the behaviour of diffusion is nonlinear with respect to time and it can found in porous media and protein diffusion in cells [Ben-Avraham and Havlin, 2000], 2)**Turbulent Diffusion** where the eddies are responsible for carrying the molecules in the environment [Roberts and Webster, 2002]. This type of diffusion is discussed in detail in this thesis, 3)**Facilitated Diffusion** that diffusion is happened due to spontaneous passive transport like transportation of molecules across a biological membrane [Voet et al., 2013], 4)**Knudsen Diffusion** that is observed in porous media where the pore length is comparable or smaller than the mean free path [3] [Clifford and Hillel, 1986].

Statistical Channel Model

The Brownian motion of the information particles in MC channel can be modelled by **Wiener process** and simulated accurately by **Monte Carlo** simulation [Berthier and Silberzan, 2010]. Gaussian distribution is used to define the Wiener process. Let x_0, y_0, z_0 be the intial position of the molecules at time t_0, and for a discrete values of Δt and for $k \geq 0$, (x_i, y_i, z_i) is the position of the molecules at the time $t = i\Delta t$. Thus, (x_i, y_i, z_i) can be defined as:

$$(x_i, y_i, z_i) = (x_{i-1}, y_{i-1}, z_{i-1}) + (\Delta x_i, \Delta y_i, \Delta z_i), \tag{2.4}$$

where $(\Delta x_i, \Delta y_i, \Delta z_i)$ are random displacement of the particles with normal distribution:

$$\Delta x_i = \mathcal{N}(0,\, \alpha D \Delta t),\ \Delta y_i = \mathcal{N}(0,\, \alpha D \Delta t),\ \Delta z_i = \mathcal{N}(0,\, \alpha D \Delta t), \tag{2.5}$$

where α= 2, 4, and 6 if the channel is 1D, 2D, and 3D, respectively. D is diffusion coefficient and it is estimated by Stokes-Einstein equation [Edward, 1970]:

$$D = \frac{K_B T_T}{6\pi\mu r}, \tag{2.6}$$

where $K_B = 1.38 \times 10^{-23} J/K$ is the Boltzmann constant, T_T is temperature in K, μ is dynamic viscosity of fluid $\left(\mathrm{N} \cdot \mathrm{s/m}^2\right)$, and r is the hydraulic radius of molecules.

Another approach to model the the Brownian motion is to apply Langevin equation [Langevin, 1908]. Based on this equation, the position of particle $(p_v^n(t))$ at time t with the mass of m along any dimension of v is obtained by solving the following equation:

$$m\frac{\partial^2 p_v^n(t)}{\partial t^2} = -6\pi\mu r\frac{\partial p_v^n(t)}{\partial t} + f_N(t), \tag{2.7}$$

where f_N is the noise in the environment. These statistical channel models have been widely used in MC researches such as modelling the noise in ligand-binding [Pierobon and Akyildiz, 2011b], channel capacity in fluid dynamic channel [Pierobon and Akyildiz, 2012], etc.

---

[3] mean free path is the average distance travelled by a moving particle (such as an atom, a molecule, a photon) between successive impacts (collisions) which modifies its direction or energy or other particle properties.

Analytical Channel Model

The analytical channel model interprets the channel as a partial differential equation (PDE). In diffusion-based channel, the channel model is given by Fick's second law [Crank, 1979]:

$$\frac{\partial c}{\partial t} = D \frac{\partial^2 c}{\partial x_i^2}, \tag{2.8}$$

where i =1, 2, and 3 according to the channel dimensions, c is the concentration of molecules based on their spatiotemporal status. Based on the initial and boundary conditions of the problem of interest, (2.8) has different solutions. For example, consider that M_0 molecules are released at t_0, and the initial and boundary conditions are:

$$c(|x|_i > 0,\ t_0) = 0, \tag{2.9a}$$

$$c(x_i = 0,\ t_0) = M_0\ \delta(x_i), \tag{2.9b}$$

$$c(|x|_i \to \infty,\ t) = 0, \tag{2.9c}$$

where $\delta(x_i)$ represents the continuous Dirac delta function in 3D. By applying the initial and boundary conditions in (2.9) to (2.8), the channel model is obtained:

$$c(x_i, t) = \frac{M_0}{(4\pi Dt)^{i/2}} \exp\left(-\frac{x_i^2}{4Dt}\right). \tag{2.10}$$

2.3.2 Advection

Advection is the transportation of the molecules in propagation channel by means of fluid flow [Hundsdorfer and Verwer, 2013]. Similar to the diffusion, advection can be modelled statistically and analytically.

Statistical Channel Model

By adding the velocity terms and modifying (2.5), the flow-assisted propagation channel model will be as:

$$\Delta x_i = u_{x,i-1}(x_{i-1}, y_{i-1}, z_{i-1})\ \mathcal{N}(0,\ \alpha D \Delta t), \tag{2.11a}$$

$$\Delta y_i = u_{y,i-1}(x_{i-1}, y_{i-1}, z_{i-1})\ \mathcal{N}(0,\ \alpha D \Delta t), \tag{2.11b}$$

$$\Delta z_i = u_{z,i-1}(x_{i-1}, y_{i-1}, z_{i-1})\ \mathcal{N}(0,\ \alpha D \Delta t). \tag{2.11c}$$

where $u_{x,i-1}(x_{i-1}, y_{i-1}, z_{i-1})$, $u_{y,i-1}(x_{i-1}, y_{i-1}, z_{i-1})$, and $u_{z,i-1}(x_{i-1}, y_{i-1}, z_{i-1})$ are the flow velocities in x, y, z directions, respectively. Another approach to model the stochastic flow-assisted channel is to use Fokker-Planck equation [Kadanoff, 2000]. In this equation, the time evolution of the PDF of the particle velocity is described under the influence of drag forces ($\mu_D(x,t)$) and random forces ($D_V(x,t)$). Fokker-Planck equation is given by:

$$\frac{\partial p}{\partial t}(x,t) = \mu_D(x,t)\frac{\partial p}{\partial x}(x,t) + D_V(x,t)\frac{\partial^2 p}{\partial x^2}(x,t), \tag{2.12}$$

Based on the boundary conditions that can be infinite source [Leeson and Higgins, 2012b; Ziff et al., 2009], infinite environment [Atakan and Akan, 2010; Meng et al., 2012], and long-term capture [Wang et al., 2014] this equation has different solutions.

Analytical Channel Model

In order to define the channel model analytically, the advection-diffusion equation (ADE) should be solved. This equation in general is defined as:

$$\frac{\partial c(\vec{x},t)}{\partial t} + \nabla \cdot \vec{J}(\vec{x},t) = S(\vec{x},t), \tag{2.13}$$

where $c(\vec{x},t)$ $[kg/m^3]$ is the concentration of a the molecules at the location of $\vec{x} = (x,y,z)$. $S(\vec{x},t)$ $[kg/m^3 s]$ represents the source term and $\vec{J}(\vec{x},t)$ $[kg/m^2 s]$ shows the mass flux of the molecules due to the diffusion and advection and it is equal to:

$$\vec{J}(\vec{x},t) = \vec{J_A} + \vec{J_D} = c\vec{u} - K\nabla c, \tag{2.14}$$

where $\vec{J_A}$ is the advection term and $\vec{J_D}$ is the diffusion term, $\vec{u}$ is the velocity field that assists the molecules to travel faster to the destination. In order to solve (2.13), one approach is to change the stationary reference frame (x,y) to moving frame (λ_x, t), where (λ_x, t) is given by [Jensen and Finlayson, 1980]:

$$\lambda_x = x - u_x t. \tag{2.15}$$

If the moving frame of (2.15) is inserted into (2.13), we have:

$$\frac{\partial c}{\partial t}(\lambda_x,t) = \frac{\partial c}{\partial \lambda_x}\frac{\partial \lambda_x}{\partial t} + \frac{\partial c}{\partial t}\frac{\partial t}{\partial t} = -u_x\frac{\partial c}{\partial \lambda_x} + \frac{\partial c}{\partial t}, \tag{2.16a}$$

$$\frac{\partial c}{\partial x}(\lambda_x,t) = \frac{\partial c}{\partial \lambda_x}\frac{\partial \lambda_x}{\partial x} + \frac{\partial c}{\partial t}\frac{\partial t}{\partial x} = \frac{\partial c}{\partial \lambda_x}, \tag{2.16b}$$

$$\frac{\partial^2 c}{\partial x^2}(\lambda_x,t) = \frac{\partial^2 c}{\partial \lambda_x^2}. \tag{2.16c}$$

Now, by substituting (2.16) into (2.13), we have:

$$\frac{\partial c}{\partial t} = D\frac{\partial^2 c}{\partial \lambda_x^2}. \tag{2.17}$$

As can be seen, (2.17) is the Fick's second law equation and the solution for (2.17) is similar to (2.10) with the only difference that in this case, the reference frame is moving with the particles:

$$c(x,t) = \frac{M_0}{\sqrt{4\pi Dt}}exp\left(-\frac{\lambda_x^2}{4Dt}\right). \tag{2.18}$$

Now, the moving reference frame can be converted into stationary frame by substituting (2.15) into (2.18):

$$c(x,t) = \frac{M_0}{\sqrt{4\pi Dt}}exp\left(-\frac{(x-u_xt)^2}{4Dt}\right), \tag{2.19a}$$

$$c(x,t) = \frac{M_0}{\sqrt{(4\pi Dt)^2}}exp\left(-\frac{(x-u_xt)^2}{4Dt}\right)exp\left(-\frac{\left(y-u_yt\right)^2}{4Dt}\right), \tag{2.19b}$$

$$c(x,t) = \frac{M_0}{\sqrt{(4\pi Dt)^3}}exp\left(-\frac{(x-u_xt)^2}{4Dt}\right)exp\left(-\frac{\left(y-u_yt\right)^2}{4Dt}\right)exp\left(-\frac{(z-u_zt)^2}{4Dt}\right). \tag{2.19c}$$

Equation (2.19) represents the analytical channel model in unbounded flows where at least two boundaries are far from the solution field and they do not interact with the fluid flow [Unluturk and Akyildiz, 2017b; Farsad et al., 2013]. On macro-scale MC, the propagation can be taken place inside a closed system (bounded flows) [Zoofaghari and Arjmandi, 2018; Giannoukos et al., 2017; Khaloopour et al., 2019; Kennedy et al., 2018; Ozmen et al., 2018]. In this case, the boundary layers influence on the flow field as well as propagation of molecules. The advantage of MC in bounded channel compared to unbounded channel is that more chemical would arrive at the receiver and thus, pathloss is lower in bounded flows. Here, the analytical channel model inside a cylinder is discussed. Of course, other cross-sections for bounded flows can be used according to the problem of interest [Arefmanesh et al., 2017; Arani et al., 2018]. If the channel has angular symmetry, the ADE in cylindrical coordinate (r, θ, z) is given by [Chen et al., 2011]:

$$\frac{\partial c}{\partial t} = D_L \frac{\partial^2 c}{\partial z^2} - u \frac{\partial c}{\partial z} + \frac{D_R}{r} \left(r \frac{\partial c}{\partial r} \right), \tag{2.20}$$

where D_L and D_R are longitudinal and radial diffusivity (cm^2/s), respectively.

In order to solve (2.20), different methods can be adopted such as Hankel [Poularikas, 2018] and Laplace Transforms [Chen et al., 2011]. One such solution is given below [Chen et al., 2011]:

$$\begin{aligned} c(r,z,t) = \frac{M_0}{\phi \rho_r^2 \sqrt{D_L \pi^3 t}} \sum_{n=0}^{\infty} \frac{1}{\lambda_n} \Bigg\{ \exp\left[-\frac{(ut-z)^2}{4D_L t} - D_R \lambda_n^2 t \right] - \\ - \frac{u}{2D_L} \exp\left[-\frac{uz}{D_L} - D_L \lambda_n^2 t \right] \operatorname{erfc}\left(\frac{z+ut}{\sqrt{4D_L t}} \right) \Bigg\} \left(\frac{\rho_r^2}{r^2} + \frac{2\rho_r J_1(\lambda_n \rho_r) J_0(\lambda_n r)}{r^2 |(\lambda_n \rho_r)|} \right), \end{aligned} \tag{2.21}$$

where ϕ is the porosity of the material, ρ_r is the radius of the inner injected zone, $J_0(.)$ and $J_1(.)$ are the zero-order and first-order Bessel function of the first kind, respectively. λ_n is the Hankel transform parameter which is calculated by the following transcendental equation:

$$\frac{J_0(\lambda_n r)}{dr} = 0. \tag{2.22}$$

As can be observed from foregoing equations, the closed-form solution for the bounded channels are more complicated than unbounded channels.

2.3.3 Turbulent Flows

In fluid dynamics, laminar flow is characterized by fluid particles following smooth paths in layers, with each layer moving smoothly past the adjacent layers with little or no mixing [White, 1999]. At low velocities, the fluid tends to flow without lateral mixing, and adjacent layers slide past one another like playing cards. There are no cross-currents perpendicular to the direction of flow, nor eddies or swirls of fluids.

In laminar flow, the motion of the particles of the fluid is very orderly with particles close to a solid surface moving in straight lines parallel to that surface. Laminar flow is a flow regime characterized by high momentum diffusion and low momentum convection. In laminar flow, measured concentration or flow attributes can be directly related to laminar flow parameters (e.g. flow speed increases signal-to-noise ratio and throughput [Atthanayake et al., 2018]). However, in turbulent flow, additional processes must be taken into account in terms of the turbulence structure and the size of the eddies. The terms eddy and vortex are used to describe the swirling motion of a fluid. The word eddy is usually associated with small-scale swirling entities whereas a vortex, such as a large-scale tornado, contains eddies on smaller spatial scales. Eddies are created, for instance, when a fluid is injected from a syringe into another larger fluid volume due to the momentum difference and shear stress at the fluid interface. If the injected momentum is high enough mixing leads to a turbulent patch comprising eddies of different diameters. The diameter of an eddy is its characteristic length scale. By analyzing the size distribution of eddies within a turbulent flow one can extract information about the features of turbulence. As the turbulent patch evolves in time there exists a cascade involving larger eddies breaking up in to smaller ones. This evolving process leads to transport of energy from larger to smaller scales, referred to as the **energy cascade**, until the energy is dissipated at a critical length scale by the action of viscosity. This smallest scale is known as the **Taylor microscale**. At this scale fluid viscosity significantly affects the dynamics of the turbulent eddies in the flow (see e.g. [Davidson, 2015]). Small eddies, near the Taylor microscale where viscous effects dominate, do not contribute significantly to the transport of information. This is considered as the lower bound for the molecular communication capacity [Kennedy et al., 2018].

Turbulence is heavily dependent on the bulk flow, and Reynolds number is required to characterize the overall flow conditions within the channel. The physical meaning of the Reynolds number is that it represents the approximate ratio of inertial forces and viscous forces in the flow. For open-channel flow the Reynolds number is defined as [Jeppson, 2010]:

$$Re = \frac{u \times L}{\nu} \ , \tag{2.23}$$

where u is the mean flow velocity and ν is the kinematic viscosity of the liquid. The quantity L represents the characteristic length scale for open channel flow. It is equal to the hydraulic radius of the channel given by A/p, where A is the cross-sectional area of the flow and p is the wetted perimeter of the channel [Jeppson, 2010]. For open channels the flow remains laminar for, approximately, $Re < 500$

and it transitions to turbulent flow above this critical value [Jeppson, 2010].

Turbulence in molecular communications is a new field of study with experimental and/or numerical works and it is discussed in detail in this thesis.

2.4 Modulation Schemes

Modulation is the process of changing the properties of carrier signal according to the symbols that are going to be transmitted. In EM-based communication systems, sinusoids function defines the carrier waves and it is expressed by:

$$s(t) = A_w \sin(2\pi f t + \varphi) \tag{2.24}$$

where A_w is the wave amplitude, f is the wave frequency (Hz), and φ is the wave phase (rad). In EM-based communication systems, the information can be modulated by amplitude (which affects peak-to-peak height of the signal), frequency (which affects the number of cycles per second), and phase (which shifts the signal from origin). However, a combination of these methods can be utilised to modulate information on EM waves. Compared to the traditional communication systems, in MC, information carrier are particles. In the following subsections, different modulating schemes is explained in MC channels.

2.4.1 Particle Quantity

In this method, the information are encoded in the number of molecules used for transmission in microscale, or in concentration (mol/m^3) of the particles in macroscale MC.

Mahfuz et al. [2010] for the first time employed a molecular modulation similar to On-Off-Keying (OOK) of EM-based communication systems where the bit ‘0’ was equal to zero concentration and bit ‘1’ was equal to a certain amount of concentration in diffusion-based propagation channel. Kuran et al. [2011] introduced a new modulation technique for diffusion-based MC channel. In their method, bit ‘1’ is received when the number of the molecules are above a certain threshold (τ_s) and vice versa. This method is called **Concentration Shift Keying (CSK)** [4] and it is similar to Amplitude Shift Keying (ASK) in EM-based communication systems. It is worth noting that the CSK in [Kuran et al., 2011] was designed for a fixed

---

[4] It is called *shift keying* because during the course of transmission of data, the values of the quantity that is used for coding the data (e.g. concentration, time, phase) shift between two (or more) discrete switching (keying) values.

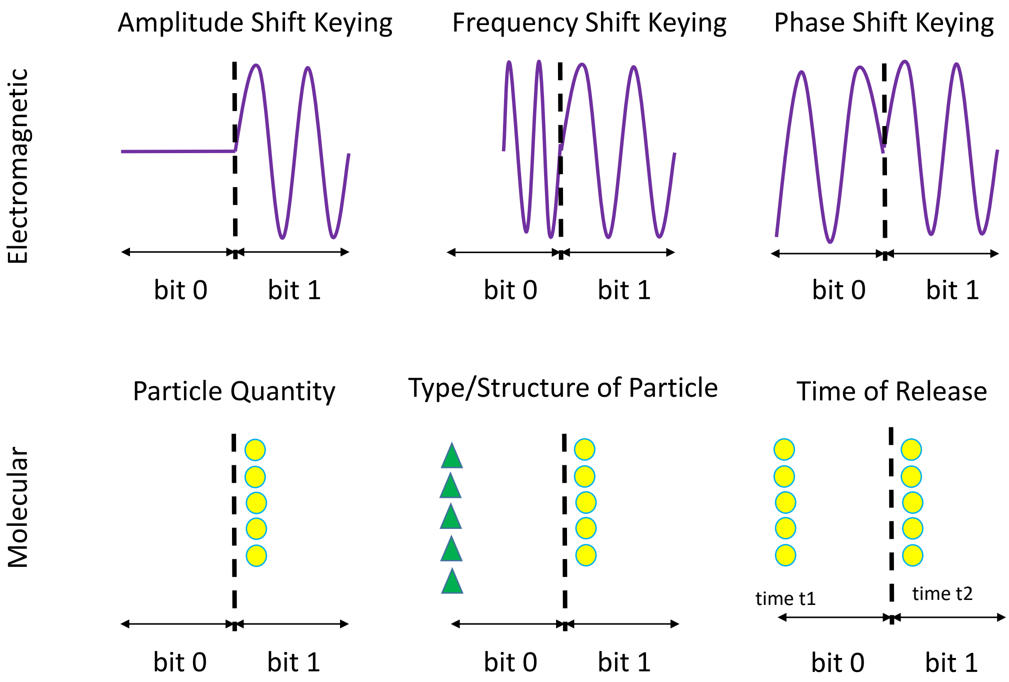

Figure 2.2: Modulation techniques for conventional and molecular communication systems.

transmitter and receiver. However, Lin et al. [2019] used CSK modulation when the transmitter and receiver are mobile.

2.4.2 Type and/or Structure of Particles

Chemical properties of the information particles can be used as individual symbol for transmission. For instance, consider two types of molecules, named A and B, that are transmitted into the channel and the receiver can distinguish them based on their chemical properties such as chemical formula. Symbol '0' is associated with A and symbol '1' is associated with B. Then the receiver can decide which symbol has been transmitted according to the type of the received molecule. Kuran et al. [2011, 2012] modulated the information on the chemical difference of information particles passing a certain threshold (τ_s). They used hydrofluorocarbon based chemicals as information particles and they called this modulation **Molecular Shift Keying (MoSK)**. In another study, Kim and Chae [2013] used aldohexose isomers [5] as

---

[5] In chemistry, isomers are molecules or polyatomic ions with identical molecular formulas that is, same number of atoms of each element, but distinct arrangements of atoms in space.

information molecules instead of hydrofluorocarbon that was used by [Kuran et al., 2012]. They claimed that hydrofluorocarbon is harmful for the body and it is not biocompatible. Also, using isomers synthesis as information carrying molecules in MC systems has less complexity since they have the same number of atoms. They called this modulation as **Isomer-based Molecular Shift Keying (I-MoSK)**. Isotopes which have the same number of protons but different number of neutrons in each atom has been used as information carrying molecules by [Ardelt et al., 2018]. In another modulation technique which is called **Depleted MoSK (D-MoSK)**, the number of the types of molecules was reduced which improves the complexity of nano-machines [Kabir et al., 2015]. In DMoSK, the transmitter sends no molecule (remains off) if all the information bits in a symbol are '0'. Thus, compared to the MoSK, the number of molecules released in D-MoSK is half the number of molecules released in MoSK.

2.4.3 Time of Release

Information can be encoded on the time when the chemical is released by the transmitter [Eckford, 2007]. For example, symbol '0' is sent when molecule A is transmitted at $t = t_1$, and symbol '1' is sent when molecule A is transmitted at $t = t_2$. The receiver can decide which symbol has been sent by measuring the arrival time of the molecules. This modulation is more suitable for flow-assisted MC channels compared to the diffuion-based channels since the propagation of molecules in diffusion-based channels is random. Mahfuz et al. [2010] proposed a new modulation technique similar to Frequency Shift Keying (FSK) in EM-based communication systems. In this modulation, the concentration amplitude of information molecules is changed in accordance to the sinusoidal signal in a given frequency. So, two concentrations could be observed in the environment, one that was there already (c_{avg}) and one that is sent ($c_{amp} \sin(2\pi f)$) into the environment and makes the concentration signal to behave like a wave. Inspired by communication between the bacteria known as quorum sensing [Miller and Bassler, 2001], Krishnaswamy et al. [2013] proposed to modulate the information into the time intervals between pulses which is called **Time-Elapse Communication (TEC)**. This modulation is suitable for biological applications and it was tested on the genetically engineered *Escherichia coli (E.coli)* bacteria. In this method, the bacteria emits certain amount of fluorescence light in accordance with the concentration level of information carrying molecules. TEC improves the data-rate compared to OOK by decreasing the number of communication signals that needs to be transmitted per unit of information. In other words, in this modulation, the stop signal of a particular value is used as the start signal of the next, and thus, the number of communication signals per unit of information is reduced to just one. Another time-dependent modulation technique is **Pulse Position Modulation (PPM)** [Akdeniz et al., 2018]. In this technique, symbol '0' is defined as a short pulse at the middle of a time-frame and symbol '1' is defined as a short pulse and silence for the remainder of the time-frame. In PPM, $\log_2 M$ bits are decoded together by determining the position of the pulse, i.e. released molecules. In particular, each symbol can be visualized as an M-bit length sequence that involves strictly one bit '1' and M-1 bit'0's.

2.4.4 Hybrid Modulation Method

Hybrid modulation method is a modulation technique that employs two or more modulation techniques. Combination of OOK and molecular FSK has been employed by Mahfuz et al. [2010] to improve the throughput of the communication systems. Hsieh et al. [2013] combined the modulation based on the type of molecule and time of release in order to achieve higher information rates compared to the individual modulation technique. Run-length aware hybrid modulation has been proposed by Pudasaini et al. [2014] based on CSK and MoSK modulations. This method improved the ISI in communication systems. In another study, Akdeniz et al. [2017] combined the CSK and MoSK modulation techniques to obtain higher data rates. Very recently, Gursoy et al. [2019] developed a new hybrid modulation to be used in MIMO systems. It is called **Quadrature Molecular Space Shift Keying (QMSSK)** which uses two types of chemical and a molecular spatial modulation which is a combination of MoSK and **Molecular Space Shift Keying (MSSK)** (uses the antennae indices as the information source).

2.5 Error Correction

Any transmitted message in the communication channel is distorted before it arrives to the receiver. So, an algorithm is required to diminish the effects of the noise on the transmitted signal and corrects the error by adding **redundancy** to the transmitted signal [Farsad et al., 2016]. For example, consider the transmitter sends '0000' as bit '0' and '1111' as bit '1'. If the receiver receives '0010' symbol, it would take a majority vote and decoded '0010' as '0' bit [Mac Kay, 2003]. One of the first attempts in MC error correction has done by Leeson and Higgins [2012b]. They applied a Hamming code to the OOK diffusion-based MC system. According to their results, the distance between the transmitter and the receiver affects on the energy efficiency of this error correction code and the code is not energy efficient as the distance reduces. In order to solve the problem of the energy efficiency, Shih et al. [2013] proposed energy efficient codes for use in MC. In another attempt, Leeson and Higgins [2012a] proposed an alternative Hamming distance called **Molecular Coding Distance Function (MCDF)** that performs better than Hamming coding in molecular communication. In this function, the coding distance is defined based on a transition probability not a constant value. Other error correction codes have also been applied to the molecular communication systems: High-order Hamming code [Shih et al., 2013], Minimum energy codes [Bai et al., 2014], Reed-Solomon codes [Dissanayake et al., 2019], Reed-Muller codes [Lu et al., 2015]. Shi and Yang [2017] did a comprehensive error analysis of diffusion-based MC with OOK modulations. Abadi et al. [2018] proposed zero-error codes for MC channels. Error-correction via amplitude width encoding was done by Krishnaswamy and Sivakumar [2018].

Inconsistency across a given distance is a problem of modelling a channel where it is caused by temperature, molecular collision etc. In order to solve this problem, **Channel State Information (CSI)** which describes signal propagation in a channel should be calculated. Based on the known knowledge, the CSI is classified into two categories: the knowledge of the current condition (instantaneous CSI) or the statistical knowledge (statistical CSI). Jamali et al. [2018] employed the constant-composition codes in order to mitigate CSI.

2.6 Experimental Molecular Communication

Experimental molecular communication is critical for a number of research sectors, including: channel characterization [Guo et al., 2016b; Unluturk and Akyildiz, 2017b; Kennedy et al., 2018; Atthanayake et al., 2018; Khaloopour et al., 2019], noise characterization for mutual information analysis [Moore et al., 2009; Pierobon and Akyildiz, 2012; Lin et al., 2018], and system design (e.g. receiver size, mobility [Lin et al., 2018]). Experimental work is lacking at the macro-scale ($\geq$ 1mm), where molecular signals are subject to a variety of flow associated processes, most of which are dynamic and inter-related. Unlike the mass diffusion dominated regime (typically in micro-scale, 1μm-1mm, and nano scale, $\leq 1\mu$m), where the channel and noise model are well understood even for different modulation schemes [Haselmayr et al., 2018; Etemadi et al., 2019; Noel et al., 2014], macro-scale continuum forces make analysis challenging.

Research at macro-scale requires significant undertaking and there is a growing body of work. Theoretical and simulation work on molecular communications with turbulence has shown that the fluid dynamic complexities cannot be ignored

[Unluturk and Akyildiz, 2017b]. Experimentation is essential to capture realistic variational behaviour in fluid dynamics. It can enable us to 1) find stable coherent structures in fluids that point towards better modulation design (e.g., generated self-propagating structures to increase symbol rate and transmission range), and 2) infer channel parameters to aid receiver signal decoding (e.g. maximum likelihood estimation [Meng et al., 2014]).

An overview of experimental molecular communications is given in [Haselmayr et al., 2019]. Early prototyping experimental work started with tabletop prototypes characterizing experimental throughput [Farsad et al., 2013; Koo et al., 2016; Prasanth et al., 2018; Qiu et al., 2014; Lu et al., 2016; Unterweger et al., 2018] and noise processes [Farsad et al., 2014] with crude chemical sensors, which has now advanced to encoding in chemical mixtures [McGuiness et al., 2018; Mcguiness et al., 2019] with mass spectrometer demodulation. This coincides with parallel work in replicating pheromone signals [Cole et al., 2009]. In attempts to understand and improve the achievable MI in macro-scale fluid dynamic channels with complex processes, recent works have characterized the evolving information structure in turbulence [Kennedy et al., 2018] and tracked info-molecules using fluorescence [Tuccitto et al., 2017a; Atthanayake et al., 2018; Kennedy et al., 2018].

2.7 Macro-scale Molecular Communication

Molecular communication underpins biological system coordination across multiple spatial and temporal scales. Whilst significant research has focused on micro-scale diffusion dominated channels, far less is understood of macro-scale flow dominated channels. In the next two sections, we review in detail some outstanding works that have been done in macro-scale MC both in nature and technology.

2.7.1 Macro-scale Molecular Communication in Nature

Pheromones communication is one of the examples of macro-scale MC in nature. For instance, two dogs can gain a wealth of information when they meet and sniff each other. The information includes sex, maturity, and hormonal state of each dog. Also, dogs are able to detect a unique smell sign (signature mixture) of each other and they can remember it when they meet again. Pheromone communication is not restricted to the dogs. Ants sweep antennae over each other (wired) as well as using their olfactory systems (wireless) to send and receive information. They can discover age, sex, caste (worker, soldier, queen), and ovarian stage (reproductive or not) when they communicate with other ants.

The body surface of animals is where they present their chemical profile. This chemical profile is sometimes released as volatile molecules and sometimes it is deposited to form a scent mark (e.g dogs deposit chemical on the lamp-post). Animals leverage from chemical sense which is shared by all organism including bacteria, to detect the chemical profile (information) and act accordingly. This chemosensory information is shared between the organisms. The chemical that is responsible for chemical interaction between organisms is called **Semiochemical**. Pheromone is one of the semiochemical that is widely used among animals. It is noteworthy that the semiochemical should not be confused with the cue signal. For instance, blood-sucking mosquitoes exploit carbon dioxide in exhaled breath as a cue to find the host. Even though it is a signal, it is not considered as a semiochemical signal.

Pheromones

Adolf Butenandt [Butenandt, 1959] and his team [Karlson and Lüscher, 1959] identified the silk moth's sex molecule as the first pheromone. Karlson and Lüscher [1959] envisaged that the pheromone is common by every kind of animal such as fish, crustaceans, mammals, and insects. Since then, we can see that it exists across the animal kingdom, habitat in land or underwater such as lobsters, suckling rabbit pups, termites and etc. Even though pheromone communication in fish, mammals, and insects are well-studied [Wyatt, 2014], less is known about the crabs and other crustaceans [Breithaupt and Thiel, 2010]. Birds also shows the potential to use the olfactory system for pheromones communication but the knowledge is still developing to understand it better [Campagna et al., 2012; Hagelin and Jones, 2007; Caro and Balthazart, 2010].

In most of the animals, pheromone is not a single molecule but rather a species-specific combination of molecules in a precise ratio. The way that the recipient animal responds to the pheromone is innate. Karlson and Lüscher [1959] anticipated that the olfactory and taste are the senses that the pheromone would act but some pheromones are directly digested and act on the brain. These types of pheromones are called **Allohormone** pheromones. Royal jelly in honeybees is the one that has this type of pheromone and it helps him to develop into queens rather than workers [Kamakura, 2011].

Pheromones serve a wide variety of functions in animal kingdom. Some of them are effective on a specific stage of the life. The key feature of the pheromone is that it is anonymous which means that the pheromone is the same in all individuals within a species of the same type (e.g., male or female). However, the quantities of pheromone are not the same among individual or the same individual over the time. For example, pheromones called farnesenes can only be produced by dominant male-mouse territory holders, not subordinates [Hurst and Beynon, 2004], or ant starts to produce a specific pheromone called 9-hentriacontene when she becomes the top (alpha) female [Peeters et al., 1999]. It is noteworthy that both of male-mouse and female ant pheromones are still anonymous and they just indicate the presence of the male-mouse or top ant not individual [Carlin and Hölldobler, 1987; Hölldobler et al., 2009].

2.7.2 Macro-scale Molecular Communication in Engineering

The engineering aspects of the macro-scale molecular communication has received considerable attentions in the past few years. In this thesis, we only focus on this part of MC applications.

Molecular Communication in Unbounded Flows

For the first time in 2013, Farsad et al. [2013] prototyped experimental work on macro-scale MC. The information was encoded in the isopropyl alcohol (chemical signal) and an electronic spray released the molecular signal into the channel. At the receiver (Rx), they employed MQ-3, MQ303A, MR513 alcohol sensors. These receivers are different in terms of sensitivity, power and operation circuit diagrams. They considered two different types of channel including diffusion and flow-assisted channel. In diffusion-based channel, the alcohol diffuses in the air until it arrives to the Rx and in the flow-based channel, a fan pushed and guided the alcohol to the Rx. The distance between the Tx and Rx was 2 m. They used the OOK modulation in order to minimize the amount of chemical used for sending message. To demodulate the signal, they considered a specific concentration threshold where for concentration below the threshold, the signal demodulated as bit ‘0’ and vice versa. They showed that the channel impulse response (CIR) is influenced by three parameters, 1) type of the sensor and its response to the received concentration, 2) type of the fan that generates the flow, 3) the amount of initial molecules that are released by the spray and the amount of the uncertainty arose by that. In order to check the linearity of the propagation channel, they considered a set of periodic sprays, of 100 ms with a period of 2 seconds. They also showed that the overall system response is non-linear. Even though they did not find the source of this non-linearity, they mentioned some possibilities for this non-linearity such as sensor response and resume time, turbulent flow generated by fan, and the environmental factors such as room temperature.

Unluturk and Akyildiz [2017b] studied the characteristics of the molecular communication channel in terms of delay and attenuation for pheromones communication between the plants. The leaves of a plant are the transmitter and receiver. The transmitter emitted molecules in consecutive and stress-driven manner according to the situation that the plants are confronted. They considered the air as propagation channel under the influence of wind and turbulent diffusion. The maximum distance between the transmitter and receiver was 200 m and the slowest wind speed was 1 m/s. In order to define the channel model, they solved (2.13) analytically. They considered three simplification assumptions in order to solve the (2.13): 1) the wind speed is constant and it is aligned with positive x axis, $\vec{u} = (u, 0, 0)$, 2) the diffusion is isotropic, 3) the amount of diffusion in x direction is negligible compared to the turbulent advection. They employed the separation of variable and Laplace transform to solve (2.13) and obtained the channel model as:

$$c(\vec{x}, t) = \frac{Q_T}{8(\pi r)^{3/2}} e^{\left(-(x-ut)^2 - y^2/4r\right)} \left[e^{-(z-H)^2/4r} + e^{-(z+H)^2/4r}\right] \tag{2.25}$$

where Q_T is total amount of pheromones released at $t = 0$, H is the height of the emitting leaf according to the ground, and $r = \frac{1}{u}\int_0^x K(\zeta)d\zeta$. Their results show that as the pheromone puff gets farther from the transmitter under the drift, it diffuses more in y and z directions. They also showed that the increased distance between the transmitter and receiver, increases channel delay and as a result, it takes longer for the pheromones to arrive to the receiver. Finally, they demonstrated that the only source of signal attenuation is the propagation channel, and as the transmitter-receiver distance increases, the attenuation increases too.

Tuccitto et al. [2017b] reported a long-range molecular communication where the molecular signal did not scale linearly with concentration and distance. They encoded the information in the concentration pulse of fluorescent carbon quantum dots (CQDs). CQDs emits fluorescent when it hits the UV light and it has self-quenching properties when they are aggregated. These properties helps CQDs to scale non-linearly with concentration. This means that as the molecular signal travels downstream, not only its concentration does not reduce linearly, but also does the concentration show a non-linear behaviour with distance. This feature allows one to send information for longer distance without concerning any specific decoding algorithms and thus, the shape of the encoded signal will be preserved for longer distance. Furthermore, in conventional MC system, the received signal broadens with distance. Indeed, when the full width at half maximum (FWHM) exceeds half of the width of the 0-bits, the bits ‘0’ and ‘1’ overlaps which causes ISI. The FWHM remains constant for the case of CQDs. In another study, Tuccitto et al. [2018] designed a molecular communication system in which the distance between the transmitter and the receiver was variable. Chemical reaction of the messenger molecules was used to encode and decode the information. In particular, they released non-fluorescent chemical followed by a hydrolysis reaction, induced by changes in pH. This reaction led the chemical to shine and emits fluorescence. They modulated the information in the kinetics of the hydrolysis reaction. Their results show that when the pH is close to neutral, the reaction producing the fluorescence is very slow and it is not feasible to detect the signal at far distance from the transmitter. By increasing the pH, the fluorescence intensity increased. They also showed that when the pH is 12, the intensity of the received signal is independent of the transceiver distance.

Molecular Communication in Bounded Flows

Macro-scale MC in internal flows has received many attentions in recent years. Khaloopour et al. [2019] studied water flow-based macro-scale MC in a semi-cylindrical channel with laminar flow. The transmitter was a plexiglas pipe which released Hydrochloric acid molecules into the pipe. The channel was a hollow cylinder with the length of 2 m and the cross-section radius of 10 cm. The molecules were detected by a chemical sensor and a pH module. The information were encoded in the concentration of the hydrochloric acid molecules and any changes to the concentration resulted in changing the pH at the receiver. They proposed the CIR to an H_3O^+ ion at time t after release:

$$\begin{aligned} p(x,z,t) = {} & \frac{1}{\sqrt{4\pi D t}} exp\left(-\frac{(x - x_{Tx} - v_x t)^2}{4Dt}\right) \\ & \times \left(\frac{1}{w} + \frac{2}{w}\sum_{k=0}^{\infty} exp\left(-D\left(\frac{k\pi}{w}\right)^2 t\right) cos\left(\frac{k\pi z}{w}\right)\right) \end{aligned} \tag{2.26}$$

where v_x is the mean flow velocity, D is the diffusion coefficient, and w is the width of the channel. They found that the channel has the delay in response about 42 seconds. They showed that the channel delay response is due to the distance between the transmitter and the receiver, and the response time of the pH-meter.

In another study, Mcguiness et al. [2019] experimentally investigated MC in a closed boundary channel in order to see the effects of bounded domain on transmission, propagation, and signal delay. They used an in-house built odor generator as a transmitter and a portable membrane inlet mass spectrometer (MIMS) as the detector for the experiments. The channel was a pipe made of clear acrylic with inner diameter of 19.80 mm and outer diameter of 24.25 mm. The length of the channel was variable in the range from 50 cm to 300 cm with 50 cm increments. According to their results, in this type of communication channel, the longitudinal diffusivity coefficient of the propagation (D_L) is the main mechanism for propagation of information particles compared to the transverse diffusion (D_T). Since the $Re \leq 2000$, they considered the flow regime to be laminar and they calculated the (D_L) as follows:

$$D_L = D_m + \left(\frac{\bar{u}^2 R^2}{48 D_m} \right) \tag{2.27}$$

where D_m is the molecular diffusion coefficient (cm^2/s), R is the radius of the pipe, and $\bar{u}$ is the mean velocity of the fluid flow. They also characterised the noise in the channel and they showed that the normal distribution interprets the noise distribution very well. According to their results, the received signal preserved its shape despite changing the distance between the transmitter and receiver and the signal amplitude changed linearly with distance. They also showed that a small change in the receiver radius has significant impact on the received signal energy since the velocity is inversely proportional to the radius of transmission medium.

Kennedy et al. [2018] investigated preservation of modulated information in airborne chemical plume and the limits on information retrieval in turbulent flow. For their experiment, they used a 75 mm pipe as the channel, a fan is provided behind the injector that provided different wind speeds and pushed isopropyl alcohol (IPA) vapor towards the receiver and the receiver was a photoionization detectors (200B miniPID, Aurora Scientific). Modulation of information was done by a computer-controlled solenoid valve which controlled the release of chemical into the pipe. According to their results, the same transmissions did not yield to the same CIRs, and as the velocity increased, the CIR peaks are sharper. In order to improve the detection of signal against the background noise, they introduced duty cycle that is a small fraction of each emission cycle. They showed that shorter emissions yields higher contrast of the received signal against background noise. They also introduced **inter-symbol spacing** which is equal to distant travel per second divided by emission per second ($l = V/S$). They showed that when $l \to \lambda$, BER→0.5 and it is not possible to retrieve the information at this length-scale. It should be noted that λ is Taylor microscale and one of the length-scales of the turbulent flow. At this length-scale, viscous forces causes appreciable dissipation of energy and large eddies are breaking into smaller eddies. In another paper [Ozmen et al., 2018] with the same configuration, they characterised the channel and they investigated the linearity of the channel. They showed that the channel is linear despite of non-linear fluid dynamic forces in the channel.

As evidenced by the aforementioned literature in macro-scale MC, the turbulence flow characteristics such as eddies, mixing length theory, energy cascade, etc. has not been considered in the context of MC. In this thesis, we are trying to leverage from turbulence theory to understand the macro-scale MC systems.

Chapter 3

Methodology

This chapter outlines the numerical and experimental methodologies that were adopted for the research in this thesis. First, we discuss the fluid flow equations and how they have been derived. Then, the importance of numerical modelling in macro-scale molecular communication systems is discussed. Afterwards, the COMSOL Multiphysics is introduced as a powerful software that can simulate the molecular communication channels accurately. In the next step, experimental flume (channel) configuration is illustrated and explained. Finally, the experimental techniques used in this thesis are reviewed. It is noteworthy that the word *channel* in this thesis refers the communication channel and it is different from that of open channel in fluid mechanics. Channel in communication is the conduit between the transmitter and the receiver and it can be open space, air, water, pipe flow, etc.

3.1 Fluid Flow Equations

3.1.1 Navier–Stokes Equations

In physics, the motion of viscous fluid substances can be described by a set of partial differential equations called Navier–Stokes (NS) equations. The NS equations, in general, are the conservation of mass and momentum for Newtonian fluids. They arise from applying Newton's second law to the motion of fluid, accompanied by the assumption that the stress in the fluid is the sum of a diffusing viscous term and a pressure term. The solution of the NS equations is velocity of the flow. It is a vector field whose direction and magnitude are those of the velocity of the fluid at that point in space and at that moment in time.

The NS momentum equation can be defined as:

$$\frac{D\mathbf{u}}{Dt} = \frac{1}{\rho}\nabla \cdot \sigma + f \tag{3.1}$$

where σ is the sum of the viscosity term (τ) and pressure term (p):

$$\rho\frac{D\mathbf{u}}{Dt} = \nabla p + \nabla \cdot \tau + f \tag{3.2}$$

where $\frac{D}{Dt}$ is the material derivative, defined as, $\frac{\partial}{\partial t} + \mathbf{u} \cdot \nabla$. In this equation, ρ is density of the fluid, p is the pressure, τ is the deviatoric stress tensor, which has order 2, f represents body forces acting on the continuum.

Incompressible Flow

An incompressible fluid is a fluid whose density does not change when the pressure changes. There is no real incompressible fluid. However, for many flow situations, the changes of density due to changes in pressure associated with the flow are very small. It greatly simplifies the solution of fluid flow equations to treat the fluid as incompressible.

$$\frac{1}{\rho}\nabla p = \nabla\left(\frac{p}{\rho}\right) \tag{3.3}$$

An incompressible flow is one for which each of the local infinitessimal blobs of fluid has a constant density as it moves through the flow field. The various tiny blobs can each have different densities, but for each one, its density remains constant. In most cases, since the fluid is usually all the same substance, treating the flow as incompressible is accomplished by taking the density to be the same everywhere in the flow field.

The incompressible Navier–Stokes equations are best visualised by dividing for the density:

$$\frac{D\mathbf{u}}{Dt} = -\frac{1}{\rho}\nabla p + \nu\nabla^2\mathbf{u} + f \tag{3.4}$$

where ν is the kinematic viscosity of the fluid and it is equal to $\frac{\mu}{\rho}$. In this thesis, the working fluid is water and it is considered as incompressible. NS equations can be expressed by means of tensor notation. In this case we have:

$$\frac{\partial u_i}{\partial t} + u_j\frac{\partial u_i}{\partial x_j} = f_i - \frac{1}{\rho}\frac{\partial p}{\partial x_i} + \nu\frac{\partial^2 u_i}{\partial x_j \partial x_j} \tag{3.5}$$

3.1.2 Reynolds Average Navier Stokes Equations

The Reynolds Average Navier Stokes (RANS) equations are time-averaged equations of motion for fluid flow. RANS equations are derived by decomposition of instantaneous velocity into the time-averaged and fluctuating velocities.

$$u_i = \bar{u}_i + u_i' \tag{3.6}$$

where $\bar{u}_i$ is the average velocity over time (ensemble average) and u_i' is the fluctuating component of the velocity. By plugging (3.6) into (3.5), the RANS equations will be derived as: [Pope, 2001]:

$$\frac{\partial \langle u_i \rangle}{\partial t} + \langle u_j \rangle \frac{\partial \langle u_i \rangle}{\partial x_j} = g_i + \frac{\partial}{\partial x_j}\left[- \langle p \rangle + \nu \left(\frac{\partial \langle u_i \rangle}{\partial x_j} \right) - \langle u_i' u_j' \rangle \right], \tag{3.7}$$

$$\rho \frac{\partial \overline{u}_i}{\partial t} + \rho \overline{u}_j \frac{\partial \overline{u}_i}{\partial x_j} = \rho \overline{f}_i + \frac{\partial}{\partial x_j}\left[- \overline{p}\delta_{ij} + \mu \left(\frac{\partial \overline{u}_i}{\partial x_j} + \frac{\partial \overline{u}_j}{\partial x_i} \right) - \rho \overline{u_i' u_j'} \right], \tag{3.8}$$

where the dynamic viscosity of the fluid is μ and $\overline{u}_j \frac{\partial \overline{u}_i}{\partial x_j}$ represents the change in mean momentum of the fluid element due to the unsteadiness in the mean flow and the convection by the mean flow. This is balanced by the mean body force $\overline{f}_i$, the isotropic stress from the pressure field $\overline{p}\delta_{ij}$, the viscous stresses, and the apparent stress $-\overline{u_i' u_j'}$ owing to the fluctuating velocity field (Reynolds stress). After determining the velocity field, it needs to be plugged into the (3.21) to obtain the concentration inside the channel.

3.1.3 k-ϵ Model

In (3.8) equation, we can see an additional term (Reynolds stress) which arises from Reynolds averaging process and it is the product of two fluctuating components averaged and then taken the divergence of that term. The Reynolds stress term is unknown in RANS equations. If we want to close the RANS equations and solve it for the mean velocity ($\overline{u_i}$), we need to have a model for Reynolds stress or more correctly, we need to express the Reynolds stress in terms of quantities that we know. In this way, we can solve the RANS equations for the one unknown which is the mean velocity of the flow field. One approach to get rid of the Reynolds stress term is to use the **Boussinesq Hypothesis**. With Boussinesq Hypothesis, we relate the Reynolds stress to the mean velocity gradient in the flow by using *dynamic eddy* *viscosity* which is denoted by μ_t [Davidson, 2015]:

$$\underbrace{-\rho\overline{u_i'u_j'}}_{\text{Reynolds Stress}} = \mu_t \underbrace{\left(\frac{\partial\overline{u}_i}{\partial x_j}+\frac{\partial\overline{u}_j}{\partial x_i}\right)}_{\text{Mean Velocity Gradient}} -\frac{2}{3}\rho k\mathbf{I}-\frac{2}{3}\frac{\partial\overline{u}_i}{\partial x_i} \tag{3.9}$$

$$\frac{\partial\langle u_i\rangle}{\partial t}+\langle u_j\rangle\frac{\partial\langle u_i\rangle}{\partial x_j}=g_i+\frac{\partial}{\partial x_j}\left[-\frac{\langle p\rangle\delta_{ij}}{\rho}+(\nu+\nu_t)\left(\frac{\partial\langle u_i\rangle}{\partial x_j}+\frac{\partial\langle u_j\rangle}{\partial x_i}\right)\right], \tag{3.10}$$

Now, we only need to find a way to calculate the eddy viscosity term in (3.9). If we can find the values of μ_t, we are able to close the RANS equations. For this purpose, we can use the $k-\epsilon$ model. Now the question is that what is $k-\epsilon$ model and how can we derive it? Before $k-\epsilon$ model, the RANS equations used the *mixing length approach* to calculate what the eddy viscosity is. Mixing length physically represents indicative sizes of the turbulent eddies that exist in the flow. As we mentioned in section 2.3.3, we have a full spectrum of sizes and energies of the eddies from the largest possible eddies all the way down to the smaller microscopic eddies in the flow. Mixing length is an indicative size of those eddies. In an area of the flow where we have large eddies, flow is energetic and very turbulent and mixing length is going to be very large. If we consider the mixing length as l_m, the eddy viscosity is defined as [Davidson, 2015]:

$$\mu_t=\rho k^{1/2}l_m, \qquad \mu_t=\rho l_m^2\left|\frac{\partial\overline{u}_i}{\partial x_j}\right| \tag{3.11}$$

where k is turbulent kinetic energy. As can be seen in (3.11), when we have large mixing length, turbulence and eddy viscosity is going to be large and as a result, we can get higher level of mixing. Now, the question is that how can we determine the mixing length? One of the earlier approach was to use **Prandtl Mixing Length** hypothesis [Davidson, 2015]. According to this hypothesis, if we are at some distance y to a wall, then the maximum size of the eddies is limited by the presence of the wall. When we are very close to the wall, the maximum size of the eddies that can exist between our position and the wall is very small and as we move further away from the wall, we are permitted a larger size of eddies in the flow. The Prandtl hypothesis is expressed as [Davidson, 2015]:

$$l_m=\kappa y, \qquad \kappa=0.41 \tag{3.12}$$

This equation shows that the mixing length is proportional to the distance from the wall (y) and the presence of the wall physically blocks the size of the eddies.

Prandtl hypothesis is not the only mechanism that is occurring near the wall. We also have the action of viscosity in viscous sub layer very close the wall. So, an improvement on Prandtl hypothesis is **Van Driest Mixing Model** which expresses that as we approach to the wall, the action of the viscosity is going to dampen those eddies and a way of interpreting this is reducing the effective size of the eddies in the mixing length hypothesis. This model is defined as:

$$l_m = \kappa y \underbrace{\left[1 - exp\left(-\frac{y^+}{A^+}\right)\right]}_{\text{exponential decay}}, \qquad A^+ = 26.0 \tag{3.13}$$

s can be seen in (3.13), as we approach the wall, the mixing length is smaller than what we expect from the Prandtl model. This equation forms the basis of early RANS turbulence models. It is worth mentioning that the mixing length is specified algebraically which means that the mixing length only depends on the distance to the nearest wall. This implies that if we have our given geometry, the distance from the nearest wall is specified throughout the entire domain and this is fixed unless our geometry is moving.

There are also other ways to improve the mixing length models. As we know, the turbulence is convected and diffuses through the flow and it is NOT static and fixed at some distance from the wall. What we would like to do here is to solve the *transport* equation for our turbulence quantities. For this purpose, we solve the transport equation for the turbulent kinetic energy (k) and also to solve the transport equation for the turbulence dissipation rate (ϵ). By solving those equations, the eddy viscosity μ_t is determined by:

$$\mu_t = C_\mu \frac{\rho k^2}{\epsilon} \tag{3.14}$$

By plugging (3.14) back into the RANS equations, we can close the RANS equation system and find the solution for the mean flow velocity. If we take the (3.11) and (3.14), and combine them, what we can see that the l_m is directly related to the dissipation rate ϵ.

$$l_m = \frac{C_\mu k^{3/2}}{\epsilon} \tag{3.15}$$

Thus, when we solve our transport equations in $k - \epsilon$ model. The transport equation for k obviously represents the turbulent kinetic energy in the flow. Equation for ϵ represents as scale determining equation in the $k - \epsilon$ model.

Transport Equation for k

The transport equation for the turbulent kinetic energy k is defined as [Pope, 2001]:

$$\underbrace{\frac{\partial \rho k}{\partial t}}_{\text{Time}} + \underbrace{\nabla \cdot (\rho \mathbf{U} k)}_{\text{Convection}} = \underbrace{\nabla \cdot \left[\left(\mu + \frac{\mu_t}{\sigma_k} \right) \nabla k \right]}_{\text{Diffusion}} + \underbrace{P_k + P_b - \rho\epsilon + S_k}_{\text{Sources+Sinks}} \tag{3.16}$$

where P_k and P_b is the production due to the mean velocity shear and buoyancy, respectively. S_k is the source term. The negative sign of the ϵ shows that the dissipation energy is actually acting to dissipate the turbulent kinetic energy in the flow.

This transport equation for the kinetic energy is the same for RNG, realizable, and standard k_ϵ model. This means that it does not matter which form of equations we are selecting, we are always going to solve the same transport equation for k. The difference in these three models is the dissipation rate equation. Here, we only focus on the standard $k - \epsilon$ model since it is the most popular model. However, the RNG and the realizable followed directly from this with small variations in the equations.

Transport Equation for ϵ

Transport equation for the ϵ is very similar to the transport equation for k.

$$\underbrace{\frac{\partial \rho \epsilon}{\partial t}}_{\text{Time}} + \underbrace{\nabla \cdot (\rho \mathbf{U} \epsilon)}_{\text{Convection}} = \underbrace{\nabla \cdot \left[\left(\mu + \frac{\mu_t}{\sigma_\epsilon} \right) \nabla \epsilon \right]}_{\text{Diffusion}} + \underbrace{C_1 \frac{\epsilon}{k}(P_k + C_3 P_b) - C_2 \rho \frac{\epsilon^2}{k} + S_\epsilon}_{\text{Sources+Sinks}} \tag{3.17}$$

$$\frac{\partial \rho \omega}{\partial t} + \nabla \cdot (\rho \mathbf{U} \omega) = \nabla \cdot \left[\left(\mu + \frac{\mu_t}{\sigma_k} \right) \nabla \omega \right] + \frac{\gamma}{\nu_t} P_k - \beta \rho \omega^2 \tag{3.18}$$

C_1, C_2 and C_3 are empirical model coefficients and they vary depending on the variant of the k_ϵ model that you choose. The model coefficients are in Table 3.1. Once the transport equation for k and ϵ is solved, we can compute μ_t from (3.14). Then we put back the μ_t in the RANS equation and then we can solve the RANS equation.

We saw that the mixing length model, the mixing length is damped close to the wall and the reason for this is to account for the action of viscosity in the viscous sub layer which reduces the effective size of the eddies. In the $k - \epsilon$ model, we do not solve for the mixing length. Instead, we solve for the dissipation rate in place of

Table 3.1: Empirical coefficients for the transport equations models.

Model	σ_k	σ_ϵ	C_1	C_2	C_μ
Jones and Launder [1972]	1.0	1.3	1.55	2.0	0.09
Launder and Spalding [1983]	1.0	1.3	1.44	1.92	0.09
Launder and Sharma [1974]	1.0	1.3	1.44	1.92	0.09

the mixing length. So, we have to have some ways of damping dissipation rate close to the wall since we do not have mixing length. Thus, specific damping functions are required to apply to the *model coefficients*. These functions are f_1, f_2, and f_μ. The subscripts directly corresponds with the coefficients that they are damping. By applying the damping functions, we can use the $k - \epsilon$ model all the way down to the wall. This formulation of the $k - \epsilon$ model is called **low Reynolds number formulation**. So, when we see the low Reynolds number formulation in the CFD codes for the $k - \epsilon$ model, that means some empirical damping functions are being used close to the wall to reduce the effects of dissipation rate in viscous sub layer near the wall. There are several damping functions for the $k - \epsilon$ model. Here we only focus on the original damping functions for the standard $k - \epsilon$ model.

$$f_1 = 1 \tag{3.19a}$$

$$f_2 = 1 - 0.3 \tag{3.19b}$$

$$f_\mu = \exp\left(\frac{-3.4}{\left(1 + (Re_T/50)\right)^2}\right) \tag{3.19c}$$

where Re_T is the turbulent Reynolds number and it is equal to:

$$Re_T = \frac{\text{Turbulence Forces}}{\text{Viscous Forces}} = \frac{\rho k^2}{\mu \epsilon} \tag{3.20}$$

Re_T is the Reynolds number that characterises the strength of the near wall turbulence relative to viscosity. When the Re_T is small, the viscosity is dominated and it shows that we are near the wall.

In summary, in low Reynolds numbers the $k - \epsilon$ model is not suggested [Pope, 2001] and other RANS model such as $k - \omega$ performs better near the wall. The $k - \epsilon$ model performs better for high Reynolds number applications.

3.2 Numerical Simulation

In this thesis, macro-scale molecular communication channel is modelled. In this channel, the molecules are propagated throughout the channel with turbulent eddies. In this case, the information is embedded in the concentration of the emitted molecules and the OOK modulation is used to transmit the information.

In order to obtain the concentration of the emitted molecules at the receiver, the ADE needs to be solved.

$$\frac{\partial c}{\partial t} = \nabla \cdot (D_\varepsilon \nabla c) - \nabla \cdot (\vec{v}c), \tag{3.21}$$

where c is the concentration and D_ε is the eddy diffusivity coefficient of the water molecules. c_0 is the amount of the molecules which are released into the channel at $t = 0$, and v is the velocity field of the environment flow. Generally, there are two restrictions in solving (3.21). First of all, $\vec{v}$ is a function of the space and time which means that in any arbitrarily location and time, the velocity components should be calculated and substituted in (3.21) in order to find concentration distribution. In [Unluturk and Akyildiz, 2017b], this restriction has been neglected and they considered the velocity field constant spatially to find a closed-form solution for the concentration profile. Second, the eddy diffusivity is varied with distance and as the messenger molecules (MMs) go away from the transmitter, the value of eddy diffusivity is changed. In [Farsad et al., 2016], the eddy diffusivity was considered isotropic which means that the information particles in the channel can disperse in all directions equivalently. This assumption is not true since the turbulent flow is not isotropic all the time [Roberts and Webster, 2002].

Based on the foregoing restrictions, finding a closed-form solution for macro-scale molecular communication channel is almost impossible by considering anisotropic velocity field, anisotropic eddy diffusivity, and time-variant velocity. In order to solve this problem, the velocity field needs to be calculated by solving the Navier-Stokes (NS) equations for laminar flow regime and Reynolds-Average-Navier-Stokes (RANS) equations for turbulent flow regime [Davidson, 2015].

3.2.1 COMSOL Multiphysics

Introduction

All events in the world can be described with the aid of a set of physical laws. In the past, to perform physical calculations, these events were simulated in an isolated environment whilst in nature several physical events occur simultaneously and each influences on another. So, real-world events are actually multiphysics. COMSOL Multiphysics is a software that can simulate these events in a single simulation, and engineers can use it to carry out projects and study their designs. COMSOL was produced in 1986 by students at the Royal Swedish Institute of Technology and was formerly known as FEMLAB, and has been renamed the COMSOL Multiphysics since 2005 [Zimmerman, 2006]. COMSOL is a multi-purpose software and it can model and simulate physics-based problems by using developed numerical solution methods. One of the capabilities of COMSOL is that it can analyse processes that involve several coupled physics. Also in COMSOL, it is possible to develop platforms for simulating chemical, physical and electrical applications. COMSOL solves a complete set of differential equations of nonlinear systems by finite element method (FEM) in one, two and three dimensional spaces. Another advantage of doing simulation with COMSOL is that it can solve the problem as a mathematical formula (in the form of equations) and/or physical phenomena (selecting a physical model, e.g. a diffusion process model) and in both cases, a system of equations are solved. Also, there are predefined equations such as heat and electricity transfer, theory of elasticity, molecular diffusion, mass transfer and propagation, wave propagation, etc. that can be used to simulate most phenomena in engineering applications [Pryor, 2009]. Preprocessing, processing and post-processing steps in COMSOL are done independently [Multiphysics, 1998]. Furthermore, COMSOL environment is integrated, which makes it easy to simulate interdisciplinary projects. Comsol software also has the ability to exchange data with CATIA, MATLAB, SolidWorks, AutoCAD.

COMSOL Desktop

Different parts of the COMSOL software is briefly reviewed here. COMSOL starting window is comprised of the Model Builder window, Setting window, Graphic window, Quick access toolbar, and Ribbon (see Fig. 3.1). The first step in simulating with COMSOL is to define the problem. After defining the problem and determining the physics involved in the problem, the geometry needs to be created. Different geometries can be found in the Model Builder on the left-hand side of the COMSOL window. By right-clicking on the **Geometry**, a drop-down list is come out that has different shapes such as sphere, cube, cones, ellipses, line, spiral, etc. (see Fig. 3.2). Also, the user can create any surfaces that is not available in the list. This is done by defining functions in *Parametric Curve* and *Parametric Surface.* By clicking on each shape and defining the centre position and other required parameters (length, radius, etc.) in the settings window, the desired shape will be

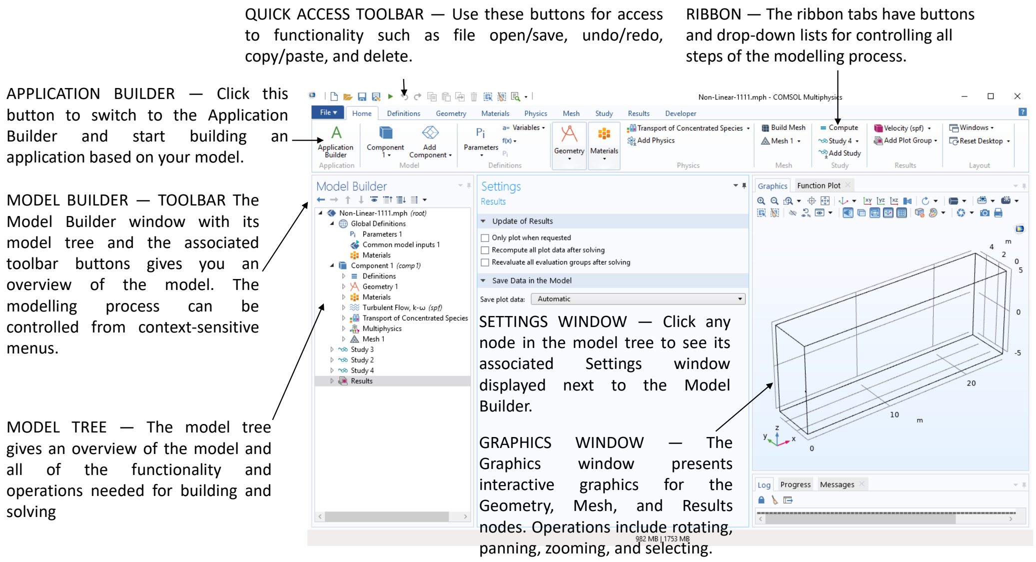

QUICK ACCESS TOOLBAR — Use these buttons for access to functionality such as file open/save, undo/redo, copy/paste, and delete.

RIBBON — The ribbon tabs have buttons and drop-down lists for controlling all steps of the modelling process.

APPLICATION BUILDER — Click this button to switch to the Application Builder and start building an application based on your model.

MODEL BUILDER — TOOLBAR The Model Builder window with its model tree and the associated toolbar buttons gives you an overview of the model. The modelling process can be controlled from context-sensitive menus.

MODEL TREE — The model tree gives an overview of the model and all of the functionality and operations needed for building and solving

SETTINGS WINDOW — Click any node in the model tree to see its associated Settings window displayed next to the Model Builder.

GRAPHICS WINDOW — The Graphics window presents interactive graphics for the Geometry, Mesh, and Results nodes. Operations include rotating, panning, zooming, and selecting.

Figure 3.1: COMSOL desktop, including quick access toolbar, ribbon, model builder, setting window, and graphic window.

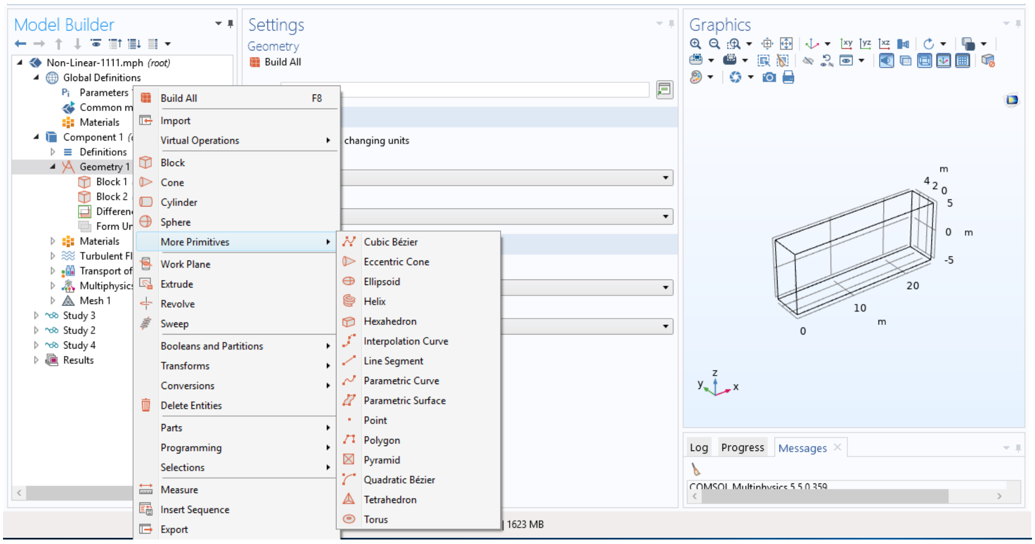

Figure 3.2: Geometry section in model builder.

created on the graphic window. After creating the geometry, materials and their properties should be defined. Materials are defined depends on the physics of the problem. For example, in stress analysis of a solid plate the material can be steel, composite, ceramics, etc., and in fluid mechanics problems the material can be wa-

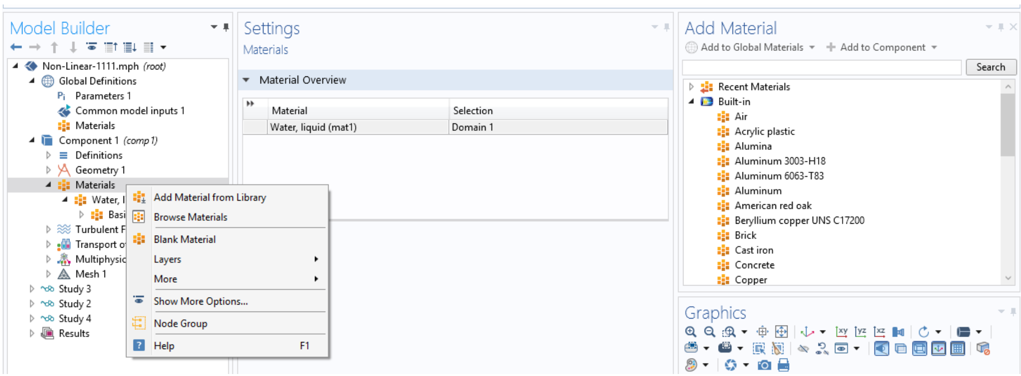

Material	Selection
Water, liquid (mat1)	Domain 1

Figure 3.3: Material section in model builder. Predefined materials in gas, liquid, and solid phases are available in this section.

ter, ethanol, isopropyl alcohol, etc. In **Material** section, various types of materials and their properties such as dynamic viscosity, electrical and thermal conductivity, density, heat capacity, etc. can be found. New materials and their properties can be defined by right-clicking on the Material and choosing *Blank Material* (see Fig. 3.3). Also, the material properties can be varied with other parameters such as time, temperature, etc. The next step is to define the physics of problem. In macro-scale molecular communication systems, the ADE needs to be solved to define the channel model. In ADE, the velocity changes in real time and it is required to solve both RANS equations and ADE simultaneously. So, the **Turbulent Flow** module and velocity fields are coupled by **Transport of Concentrated Species** module in COMSOL. In the setting window for the Turbulent Flow module, different types of flow (compressible or incompressible), numerical turbulence models (k-ϵ, k-ω, shear stress transport (SST), Spalart-Allmaras, etc.), and the discretization methods are shown (see Fig. 3.4). Discretization directly influences on the interpolation degrees of freedom. Though high-order interpolation function improves the accuracy of the results, it requires more time and computational resources. By right-clicking on Turbulent Flow in Model Builder, different boundary conditions can be observed. The *Inlet* boundary condition in fluid dynamics problems usually is velocity, flow rate, and pressure that depends on the problem. The *Symmetry* boundary condition is suitable where the solution field is symmetric and it saves the required simulation time. In the setting window for Transport of Concentrated Species module, one can select different transport mechanisms such as Maxwell-Stefan, Fick's law, Mixture-averaged (see Fig. 3.5). Similar to CFD module, the boundary conditions are in the Model Builder and they come out by right-clicking on the Transport of Concentrated Species module.

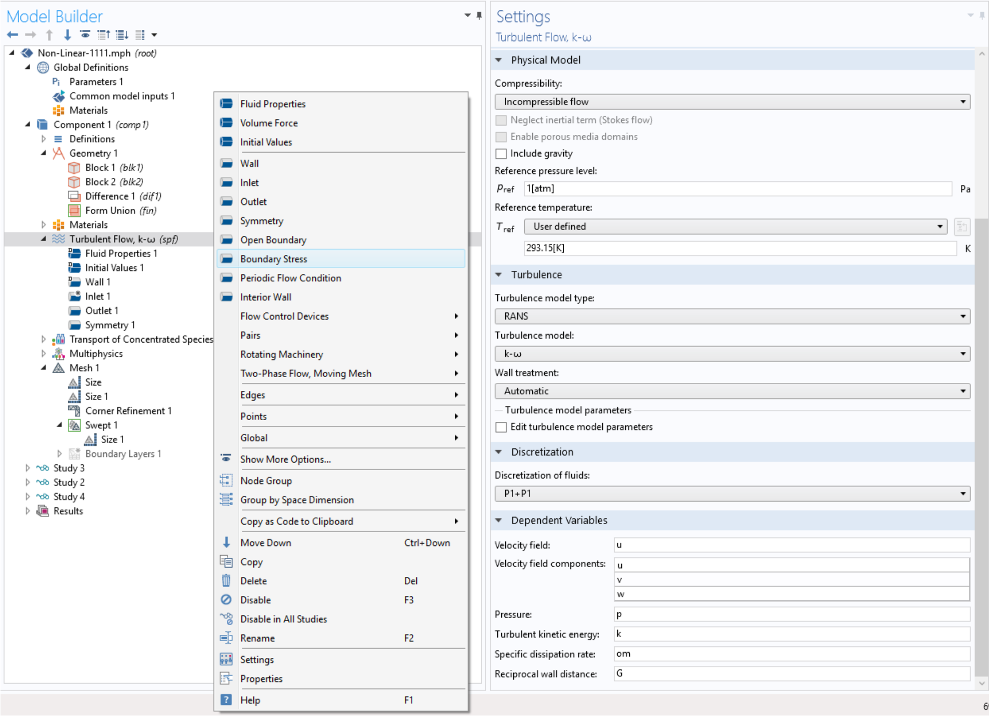

Compressibility: Incompressible flow

☐ Neglect inertial term (Stokes flow)

☐ Enable porous media domains

☐ Include gravity

Reference pressure level: p_{ref} 1[atm] Pa

Reference temperature: T_{ref} User defined 293.15[K] K

Turbulence model type: RANS

Turbulence model: k-ω

Wall treatment: Automatic

Turbulence model parameters

☐ Edit turbulence model parameters

Discretization of fluids: P1+P1

Velocity field: u

Velocity field components: u v w

Pressure: p

Turbulent kinetic energy: k

Specific dissipation rate: om

Reciprocal wall distance: G

Figure 3.4: CFD module section. Different turbulent models are available in the setting window. Initial and boundary conditions can be changed in the model builder window.

The final step before starting to solve the equations is to create a mesh for the solution field. As mentioned before, COSMOL uses FE method to discretize the PDEs. In this method, the solution field is divided into meshes of different shapes (triangular and quadrilateral in 2D; or tetrahedral, pyramid, triangular prism, and hexahedron for 3D geometries). The accuracy of the results is improved by reducing the length of the elements and increasing the number of elements, but it also increases the computation time which is not desirable. Stationary and time dependent solvers are available in COMSOL.

Simulation Parameters

In this thesis, in general we ran numerical modelling in chapters 4, 5, and 6. In each chapter, we considered three different geometry configurations for the numerical modelling. In chapter 4, we considered 3D simulation of the channel where the size of the channel is $400D_p \times 80D_p \times 80D_p$, where D_p is the size of the injector diameter. In chapter 5, we simulated the channel as 2D-axis symmetric where the

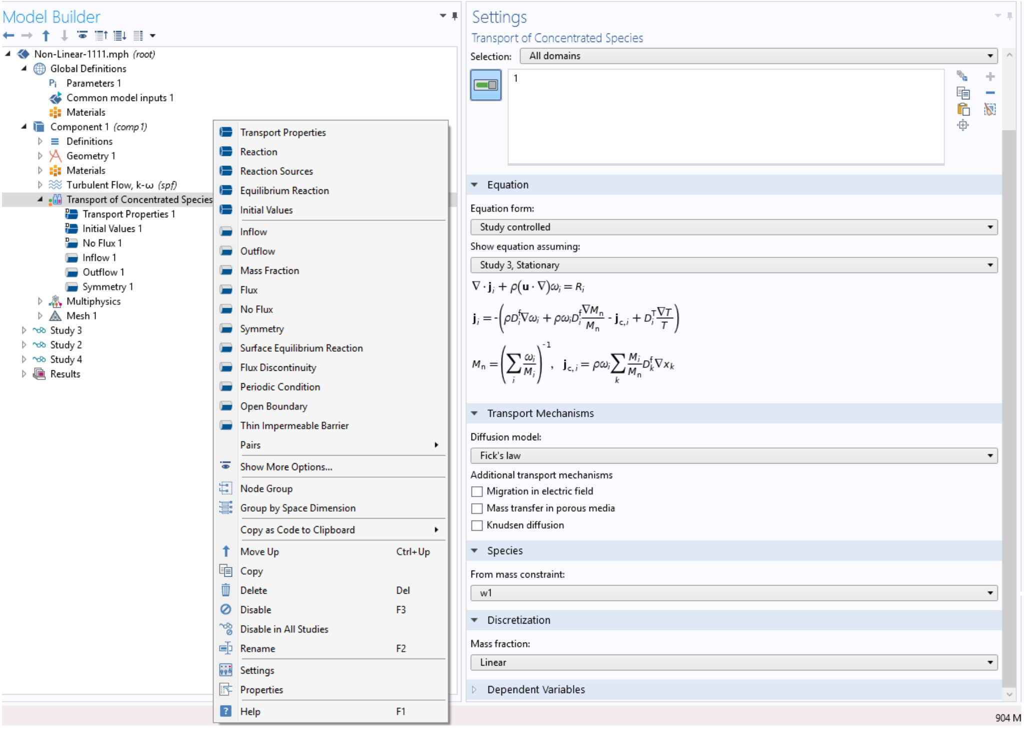

Transport of Concentrated Species

Selection: All domains

1

Equation

Equation form: Study controlled

Show equation assuming: Study 3, Stationary

$$\nabla \cdot \mathbf{j}_i + \rho(\mathbf{u} \cdot \nabla)\omega_i = R_i$$

$$\mathbf{j}_i = -\left(\rho D_i^f \nabla\omega_i + \rho\omega_i D_i^f \frac{\nabla M_n}{M_n} - \mathbf{j}_{c,i} + D_i^T \frac{\nabla T}{T}\right)$$

$$M_n = \left(\sum_i \frac{\omega_i}{M_i}\right)^{-1}, \quad \mathbf{j}_{c,i} = \rho\omega_i \sum_k \frac{M_i}{M_n} D_k^f \nabla x_k$$

Transport Mechanisms

Diffusion model: Fick's law

Additional transport mechanisms

☐ Migration in electric field
☐ Mass transfer in porous media
☐ Knudsen diffusion

Species

From mass constraint: w1

Discretization

Mass fraction: Linear

Dependent Variables

Figure 3.5: Transport of concentrated species section. Three different transport mechanisms can be selected in the setting window.

size of the solution domain is $50D_p \times 20D_p$. In chapter 6, we considered 2D channel $100D_p \times 30D_p$. The reason behind choosing these dimensions is that we wanted to observe the path of the transmitted signal all the way to the downstream of the channel. So, the length of the channel should be large enough to keep the molecular signal inside depends on the transmitted signal velocity. Furthermore, we wanted to prevent the side walls to affect the spanwise motion of the transmitted signal in the channel. So, they were considered far enough from the injector.

The working fluid in this thesis is water and it is considered incompressible. The dynamic viscosity of water is μ =8.9 × 10^{-4} Pa.s and the density of water equals to ρ=1000 kg/m^3.

3.2.2 Grid Independence Test

Grid independence test is a kind of test that is used to describe the improvement of results by using successively smaller grid (mesh) sizes for the numerical modelling. A calculation should approach the correct answer as the mesh becomes finer. Here we explain the grid Independence test for the vortex ring simulation.

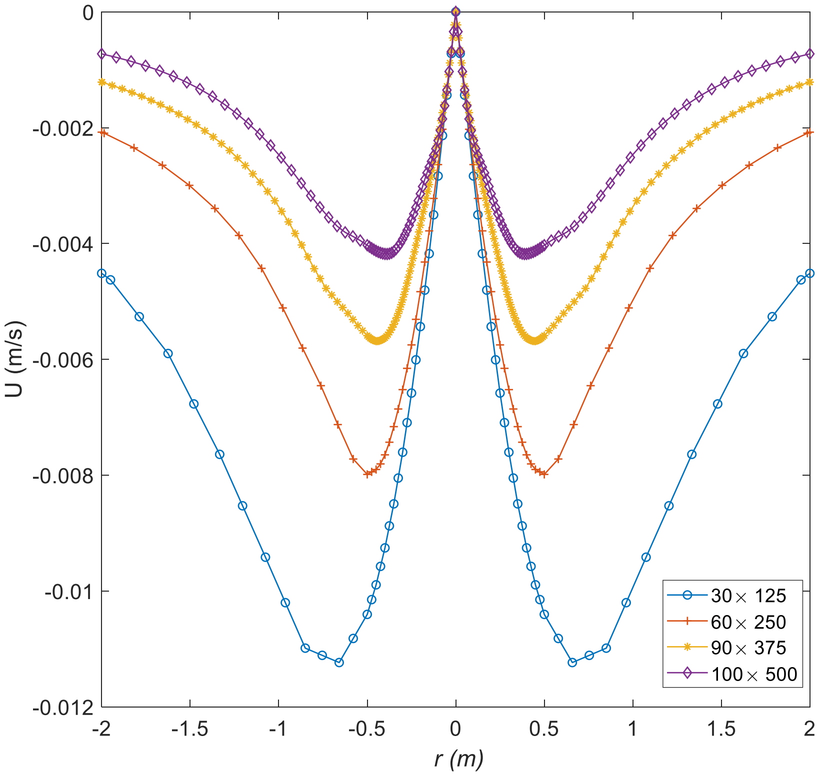

Figure 3.6: Grid independence test for the vortex ring numerical modelling.

For the vortex ring simulation, we considered the structured grid since the geometry of the simulation has rectangular shape. In order to certify the grid independence, we choose 4 different grid and for each case, we calculated the radial velocity of the vortex ring at the receiver. As can be seen in Fig. 3.6, 90 × 375 is the suitable mesh size. In other words, by making the mesh finer, the radial velocity does not change significantly.

3.3 Experimental Systems

3.3.1 Armfield Flume (Channel)

The Armfield flume used for this thesis is displayed in Fig.3.7(a). The open channel is 15 m long, 0.3 m wide, and 0.6 m deep. The channel has glass side walls providing convenient optical access. The flow rate of the channel is controlled by means of a pump. This enables setting the mean flow velocity to a desired constant value. To maintain a constant water level within the flume, an inclined plate is mounted at the channel outlet. The recirculating liquid has to spill across this plate. By adjusting the angle of the plate one can therefore set the water level inside the flume.

Obstacle

An obstacle consisting of an array of smooth steel rods, each of diameter 2.5 cm, is placed between the Tx and Rx downstream of the channel inlet as is illustrated in Fig. 3.7(b). When the water passes the obstacle, turbulence is generated in the wake of the rods. It is assumed that the turbulence in the water channel is statistically steady when the obstacle is absent. The turbulence generated by the obstacle is referred to as unsteady since its statistical properties depend on the downstream distance from the obstacle.

Transmitter

The transmitter for the release of fluorescent tracer liquid is displayed in Fig. 3.7(c). It constitutes a bent pipe with a diameter of 5 mm. The inlet of the pipe is connected to the solenoid valve and the outlet is located submersed under water inside the channel. The transmitter is mounted such that its position within the channel can be varied.

Receiver

Fig. 3.7(d) displays the components forming the receiver of our experimental set-up. The receiver comprises a laser to generate a light sheet for the illumination of a cross section of the flow and a video camera as a means for recording the experiments for the subsequent data analysis using the relevant methods.

Injection System

Injection system is one of the components of the communication channel. This system should be able to release the fluorescence tracer (information particles) sequentially with different timing between the pulses. The injection system that we use is a syringe pump and it is illustrated in Fig. 3.8. The syringe pump is a small, positive-displacement pump used to gradually transfer precise volumes of fluorescence tracer. It is driven via a stepper motor. A lead screw, threaded through a pusher block, precisely turns the pump's stepper motor. This causes the pusher block to move. The fluorescence tracer ejects at an accurate and precise rate during infusion mode, when the pusher block pushes against the plunger of a secured syringe. Brackets on the pusher block hold the plunger of the syringe for withdrawal capabilities. When the stepper motor turns in the opposite direction, the pusher block moves such that

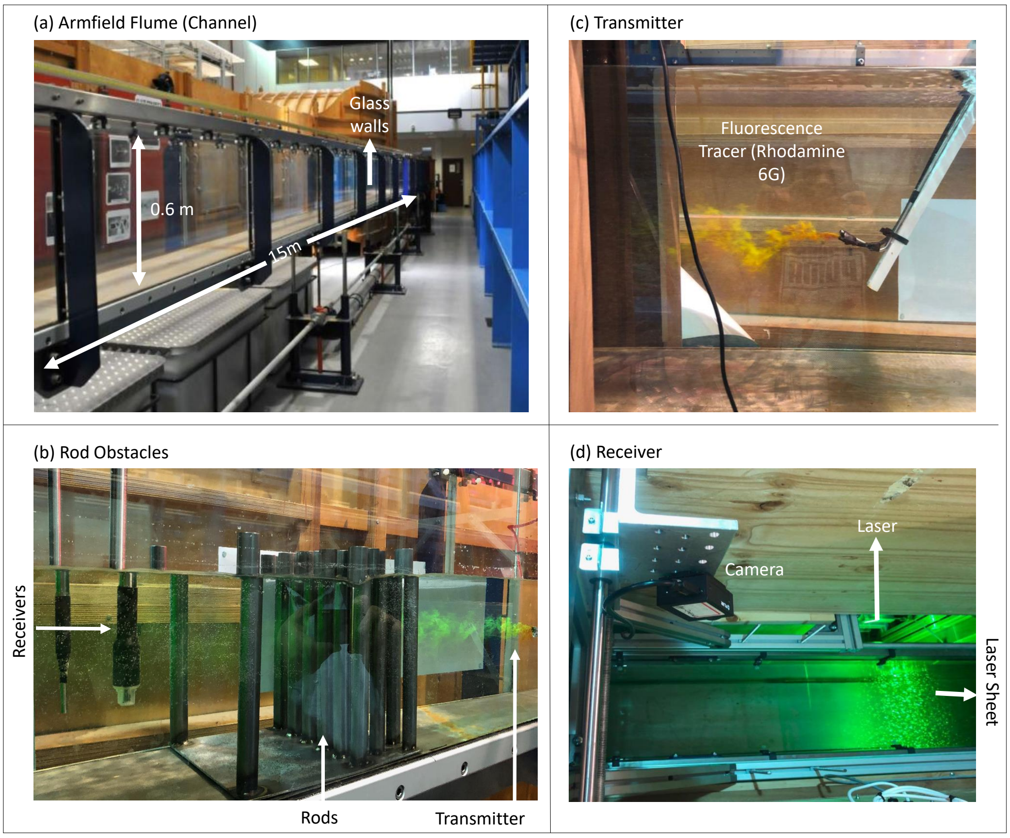

Figure 3.7: a) Armfield-flume (channel) configuration. It is 15 m long, 0.3 m wide, and 0.6 m deep, b) Rod obstacle used for generating the turbulence in the channel, c) Transmitter pipe, d) Receiver station.

the syringe plunger is pulled, thus drawing fluorescence tracer into the syringe. The pusher block moves to the right for infusion and to the left for withdrawal. The electronic components required to drive the stepper motor, which is controlled by an Arduino program, are contained in a small box.

3.3.2 Particle Image Velocimetry (PIV)

The most frequently used modern technique for the analysis of flow fields is PIV. PIV is an optical technique used for the measurement of flow velocities and it thereby provides a tool for flow visualization. The method is referred to as non-intrusive since it is not required to insert flow sensors in the flow field that can potentially alter aspects of the dynamics to be monitored. Technical details of the methodology are summarized in [Raffel et al., 2018]. The following steps are required for a typical

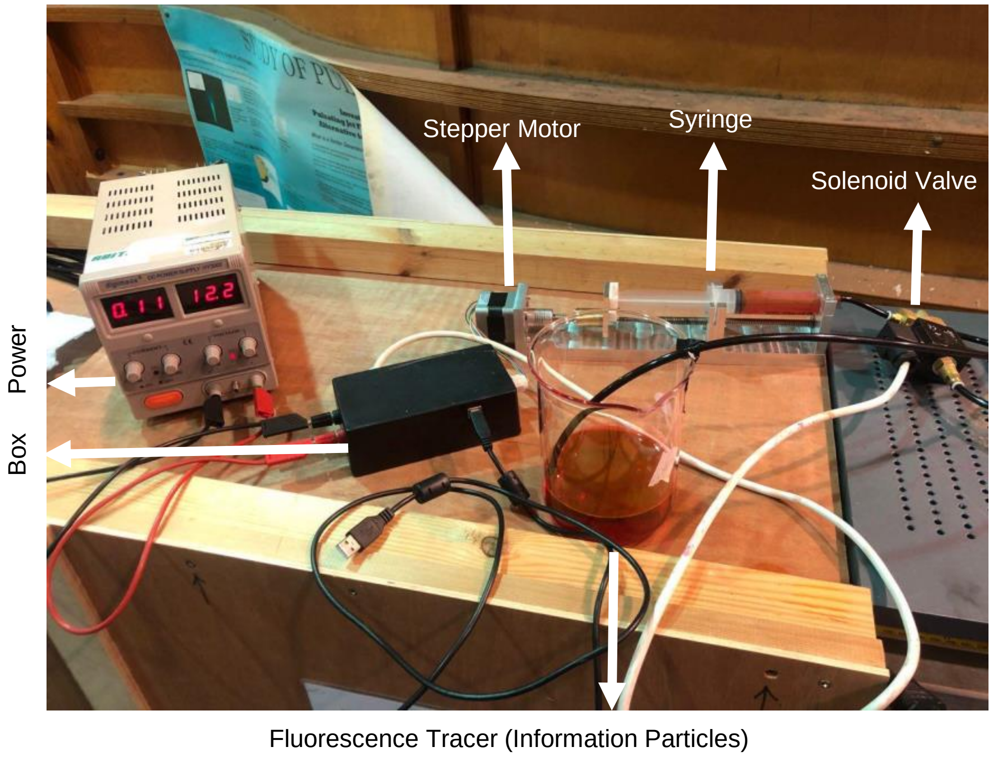

Figure 3.8: Injection system. It comprises of power, stepper motor, syringe, solenoid valve, and a box that contains all electronic boards.

PIV measurement.

- **Tracer:** The flow is seeded with micron-sized tracer particles. Ideally seeding particles are chosen that are neutrally buoyant. This is required such that the particles always faithfully follow the flow and therefore accurately represent the flow velocity at their locations within the flow field [Fond et al., 2015]. In liquids one can use, for instance, hollow-glass spheres as seeding particles, which can be silver-coated to increase their reflectivity as is the case in the experiments of [Atthanayake et al., 2018, 2019]. If the flow is in a gas, then it is not possible to satisfy the requirement for neutral buoyancy and one typically uses, for instance, micron-sized oil droplets as tracer particles.

- **Imaging:** A laser and an optical arrangement, comprising a cylindrical lens, is used to generate a thin light sheet that intersects the flow as illustrated in Fig. 3.9. Tracer particles moving within the light sheet become brightly illuminated. Thus, their motion can be recorded by means of a video camera.

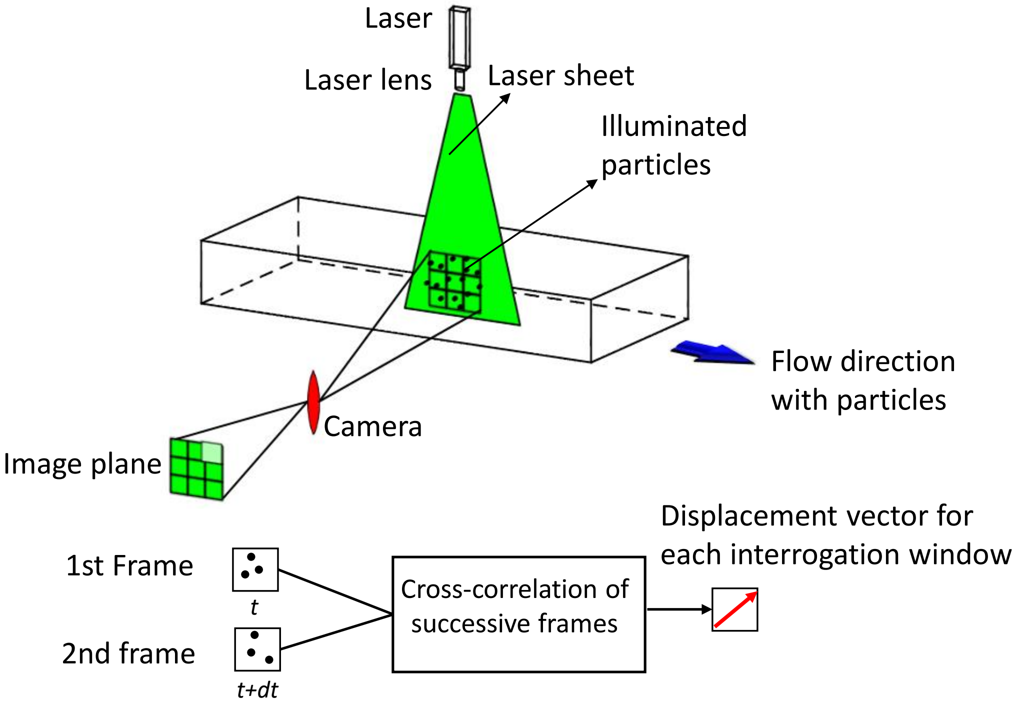

Figure 3.9: Schematic of PIV set-up. Laser sheet excites the flow seeded by tracer particles, and the camera captures the motion of the particles in successive frames. Cross-correlation of successive images yields the velocity field.

- **Analysis:** On any two successive video images taken at a short time interval $\Delta t = t' - t$ apart the tracer particles will appear at slightly shifted locations due to their motion while following the flow field (see Fig. 3.9). By analyzing from where to where particles have moved within the image plane in the known time interval Δt, it is possible to infer the magnitude and the direction of the particle velocity and the flow velocity. Once the basic velocity field is known as a function of time, other quantities such as time averaged velocities, the vorticity or the turbulence characteristics can be obtained from post-processing of the collected data. An in-depth example showing such results from a PIV study is discussed in [Atthanayake et al., 2019].

Processing PIV images

In order to process the PIV data, the raw images taken in successive frames are uploaded to the PIVlab software [Thielicke and Stamhuis, 2014]. The Matlab based PIVlab software is an open-source tool for the analysis and post processing of PIV data. Fig. 3.10(a) shows an image taken from a flow field. The camera is focused

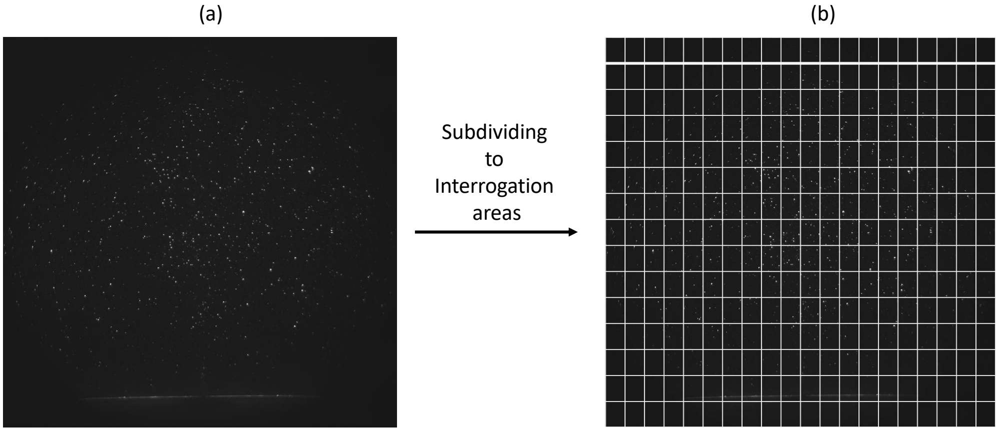

Figure 3.10: a) An original PIV image in the vertical plane, b) PIV image with sub divided interrogation areas.

on the area in the centre of the image, the area of interest. Here the particles are in focus whereas they are somewhat blurred towards the edge of the image frame. Only the area of interest is considered for further analysis of the flow field. To this end, the video images are divided into small **interrogation regions** and corresponding interrogation regions in successive video frames are compared. Figure 3.10(b) displays a PIV image that is divided into interrogation areas of 15×20 pixels. A pair of two consecutive instantaneous video images which are separated by time $\Delta t = 0.01$ s is shown in Fig. 3.11. Each interrogation area of the second image, taken at time $t+\Delta t$, is shifted relative to the first image taken at t. A cross correlation between the two images should be performed. That particular shift for which the correlation function adopts its maximum is then taken as the direction in which the particles within the small interrogation region have collectively travelled. This direction together with the time interval Δt between the two video frames then defines the magnitude and the direction of the flow velocity at the location of the interrogation region [Adrian et al., 2011].

Calibration

The PIV methodology requires calibration to provide a conversion factor relating distances in terms of pixels to their corresponding real-world distance in units of length. For the calibration process a calibration image is used. Figure 3.12(a) displays a typical calibration image which, in this particular case, consists of rows of black circles of constant radius on a white background. The radius of the circles and the distance between their centres represent known reference length. Once the

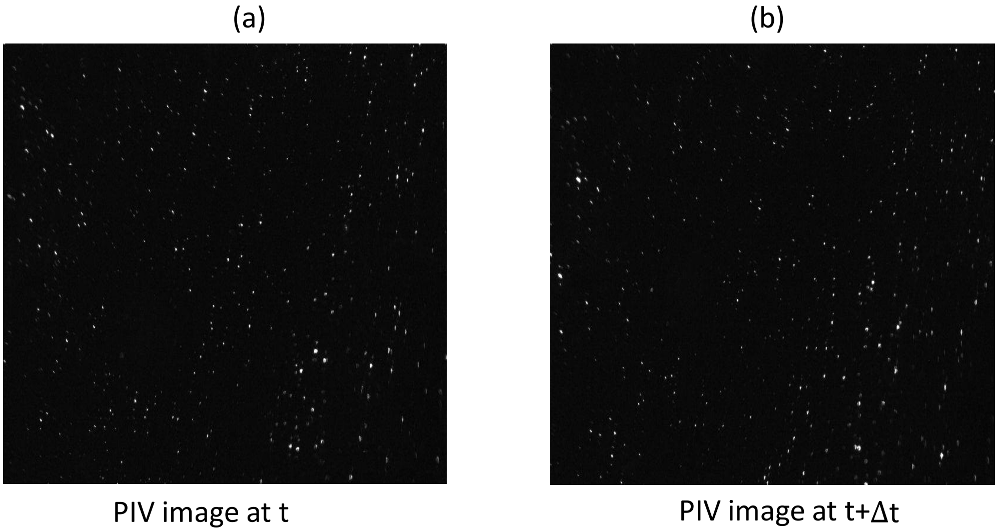

Figure 3.11: Two PIV images taken at times t and t+Δt where Δt = 0.01 s.

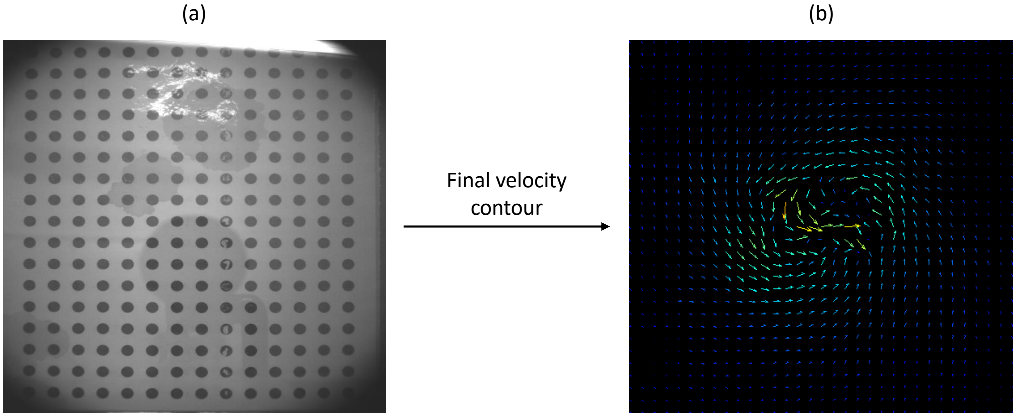

Figure 3.12: Final stage of converting pixel distance to read distance, a) the calibration plate in the vertical plane, b) velocity vector field obtained by analysing a PIV image pair.

real distance of particle displacement is known, a velocity vector for the considered interrogation area is determined. A velocity-vector map over the whole image area is obtained by repeating the procedure outlined in Section 3.3.2 for each interrogation area over the entire image. Figure 3.12(b) shows a typical velocity-vector field calculated from a PIV image pair.

PIV in Comparison to Other Methods

There exist alternative methods for velocity monitoring. One other popular optical technique is Laser Doppler Anemometry (LDA), frequently also referred to as Laser Doppler Velocimetry (LDV) [Zhang, 2010]. Similar to PIV the LDV technique is a non-intrusive methodology that requires optical access to the flow field but no sensors within the flow field. Other common non-optical methods are Hot-Wire Anemometry (HWA) [Brunn, 1971; Lomas, 2011], and Ultrasonic Velocity Profilers (UVP) [Takeda, 2012].

However, for most applications the PIV technique has advantages over all the other methods since it gives the 2D flow field and it is also non-intrusive. Note that with more sophisticated technical arrangements 3D flow field monitoring by means of PIV is nowadays increasingly becoming a viable option.

Similar to PIV, the LDA and UVP techniques also rely on inferring velocity data from the motion of tracer particles carried along with the flowing medium. While PIV relies on monitoring the tracer- particle displacement in the image plane the LDA and the UVP methodology infer the velocity of the tracer particles from the Doppler shift of the scattered and detected laser light (LDA) and the ultrasound waves (UVP). A distinguishing feature of UVP is that, unlike light, ultrasound can propagate through transparent and opaque materials. This means that the probe emitting the ultrasound for the UVP method can be mounted inside the flow field or outside of the material walls enclosing the flow. Thus, UVP can be operated in intrusive or in non-intrusive mode. Most importantly, however, the UVP methodology also enables measuring flow velocities within opaque liquids, such as liquid metals.

While the type of PIV system in Fig. 3.9 yields data for the whole light sheet plane, an LDA system only allows the velocity to be monitored at a single location. In comparison to LDA, the UVP technology is more versatile in that it yields velocity data not only at a single location but for a section near the probe on the straight trajectory along which the transmitted ultrasound beam propagates through the flowing liquid.

Hot-wire anemometry (HWA) is an intrusive technology and requires a small, very fragile and expensive, measurement probe to be inserted into the flow field [Bruun and Anemometry, 1995]. Similar to the LDA method HWA can only measure the velocity at a single location. A HWA probe with a single wire is uni-directional and can only detect one flow component. However, there exist probes with two or three wires to measure more than one velocity component.

3.3.3 Ultrasonic Velocity Profiler (UVP)

UVP technique relies on inferring velocity data from the motion of particles carried along with the flowing medium. When a particle travels through the measurement volume, it reflects a sound. The velocity information is contained in the sound wave that is reflected from the moving particles. The incoming sound wave has a known frequency. The frequency of the sound that is reflected from a particle and detected by means of a receiver, is Doppler shifted. By comparing the frequency of the incoming sound to that of the reflected sound it is possible to infer the velocity of the particle (see Fig. 3.13).

UVP technology is more versatile in that it yields velocity data not only at a single location but along the entire straight trajectory along which the transmitted ultrasound beam propagates through the flowing liquid. The UVP technology has a further advantage that it allows measurements to be conducted in opaque fluids, such as liquid metals [Kotzé et al., 2011]. UVP sensors exist for intrusive and non-intrusive measurement mode.

UVP Velocity

Consider the time delay after which the echo reaches to the transmitter:

$$t = \frac{2x}{c} \tag{3.22}$$

where x is the distance of scattering particle from transducer, and c is the speed of sound in the liquid. If the scattering particle is moving with non-zero velocity component into the acoustic axis of the transducer, Doppler shift of echoed frequency takes place, and received signal frequency becomes Doppler-shifted:

$$\frac{v}{c} = \frac{f_d}{2f_0} \tag{3.23}$$

where v is velocity component into transducer axis. f_d and f_0 are Doppler shift and transmit frequency, respectively. The reason for the '2' in denominator is because of stationary transmitter and receiver. The classical Doppler shift formula considers a moving source of oscillations, and does not include '2'. In our case, both source of oscillations (transducer) and observer (also the transducer) are stationary, and the reflector moves. One Doppler shift is created by relative movement of reflector to source, and additional Doppler shift is created by relative movement of reflector to observer. Hence, twice as high Doppler shift results. The velocity v in (3.23) can be written as:

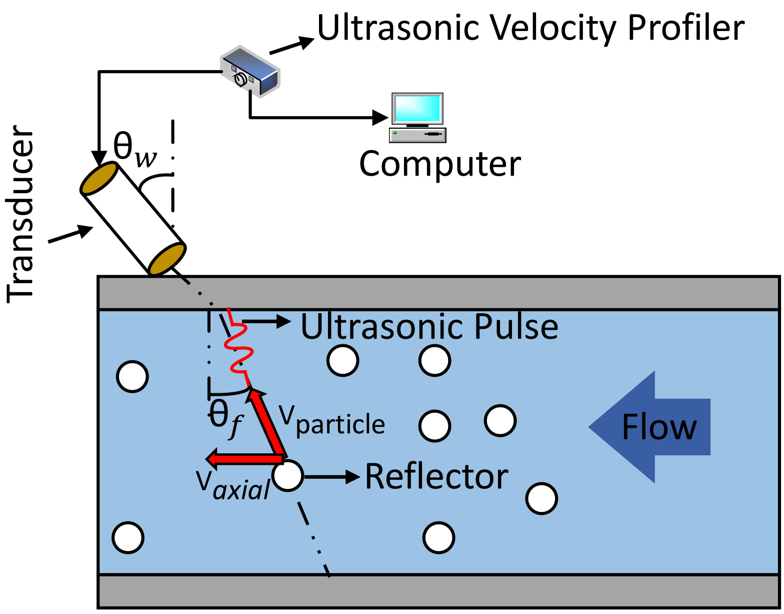

Figure 3.13: Schematic of UVP acquisition set-up. Transducer sends the sound wave and receives the reflected sound from a particle.

$$v = \frac{f_d}{\frac{2f_0}{c}} = f_d.\frac{\lambda}{2} \tag{3.24}$$

where λ is the wavelength of the ultrasound medium.

If UVP succeeds to measure the delay t and Doppler shift f_d it is then possible to calculate both position and velocity of a particle.

Channel Width

The spatial resolution of the velocity is determined by the channel width which is the width of a measurement volume (see Fig. 3.14). The channel width is given by:

$$w = c\frac{n}{2f_0} \tag{3.25}$$

where w is the channel width, n is the number of cycles per pulse, and λ_0 is the wavelength of ultrasound. The most frequently suggested number of cycles per pulse to optimise echo vs. spatial resolution is 4. With transmitting frequency 4 MHz and sound velocity in water $1480\,\mathrm{m\,s^{-1}}$, the minimum theoretical measurable channel width would be 0.74 mm. However, UVP device transducers can generate a minimum of 2 cycles per pulse.

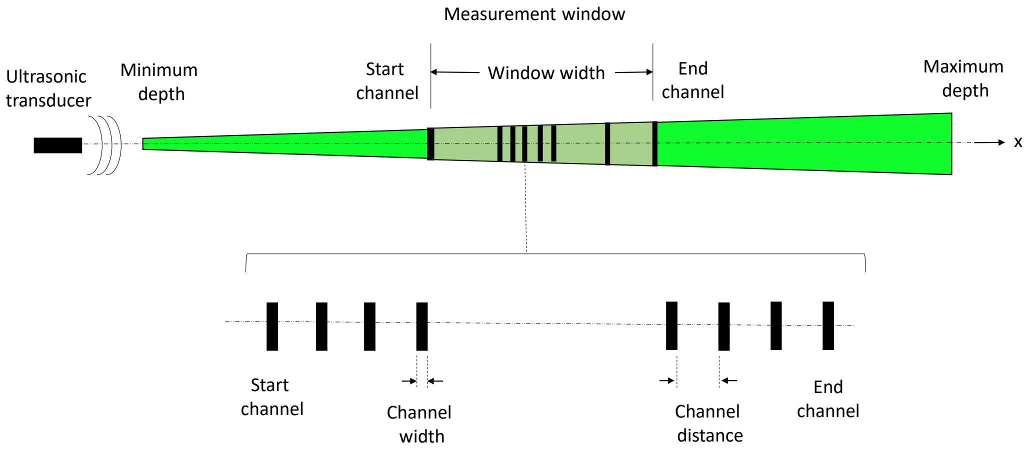

Figure 3.14: Illustration of terms connected with measuring window.

Channel Distance

The distance between the two adjacent channels is called channel width (see Fig. 3.14). Channel distance is fixed throughout the measurement. It has a range from 0 to N_{ch}-1, where N_{ch} is the number of measured channels. For the UVP device, the N_{ch} can change from 10 to 2048 depends on the required spatiotemporal resolution.

Measurement Window

The distance between the centre of the channel 1 (starting channel) and N_{ch} (end channel) is called measurement window. This is given as:

$$W = \mathrm{N}_{ch} - 1 \times \text{channel distance} \tag{3.26}$$

where W is the length of the measurement window. As can be seen in Fig. 3.14, the window end-position has to be smaller than the maximum depth.

Maximum Measurable Depth

The maximum measurable depth is obtained by the pulse repetition frequency (F_{prf}).

$$P_{max} = \frac{c}{2F_{prf}} \tag{3.27}$$

where P_{max} is the maximum measurable length and c is the sound velocity. The physical meaning of the P_{max} is that one cannot ping a new ultrasound pulse into liquid before the echo from previous pulse returns from the maximum measurable depth.

3.3.4 Planar Laser-Induced Fluorescence (PLIF)

Planar laser induced fluorescence is an optical diagnostics technique that can measure the concentration of a fluorescent tracer dye as it gets carried along and diluted in a fluid flow [Torres et al., 2013].

Similar to PIV, PLIF technique requires a cross-section of the flow to be intersected by a laser light sheet as illustrated in Fig. 3.15. After a tracer fluorescence (or information particle) is injected, it is carried along by the fluid flow towards the laser sheet. The laser light excites fluorescence and images are captured to record the intensity of the shining fluorescence (see Fig. 3.16). The fluorescence intensity is primarily dependent on the tracer concentration and is used as a parameter to show the concentration of the tracer. A tracer frequently used is Rhodamine 6G; this has peak adsorption at a wavelength of 532 nm and peak emission at around 560 nm [Sarathi et al., 2012].

In typical signal-transmission experiments a known amount of liquid containing a certain concentration of the fluorescent tracer can be released from, for instance, a small nozzle within the flow field. The fluorescent liquid is then viewed as representing information carrying particles released by a sender. Thus, the fluorescence pattern that becomes visible within the light sheet provides a visual representation of the dynamic behaviour of the information-carrying liquid particles as they get carried along in the flow and, facilitated by the action of eddies and turbulent flow fluctuations, mix with ambient liquid.

PLIF can be combined with PIV to concurrently obtain concentration and velocity data. Table 3.2 summarizes the main features of PIV and PLIF together with the required equipment and websites of commercial product suppliers.

Imaging Apparatus

The radiant power of the laser is 1000 mW. The working voltage of the laser is 110-220 VDC and the working current of the laser is less than 1500 mA. The beam diameter of the laser is 1 mm with the wavelength of 532 nm green color. The laser beam passes through a cylindrical lens to generate a laser sheet. The power intensity of the laser sheet has a Gaussian profile. A notch filter is positioned in front of the camera to remove light not required for the data analysis. In the case of Rhodamine 6G, for instance, light below 550 nm should be filtered out such that only the light from the emission peak at 560 nm is detected by the camera. A high-speed comple-

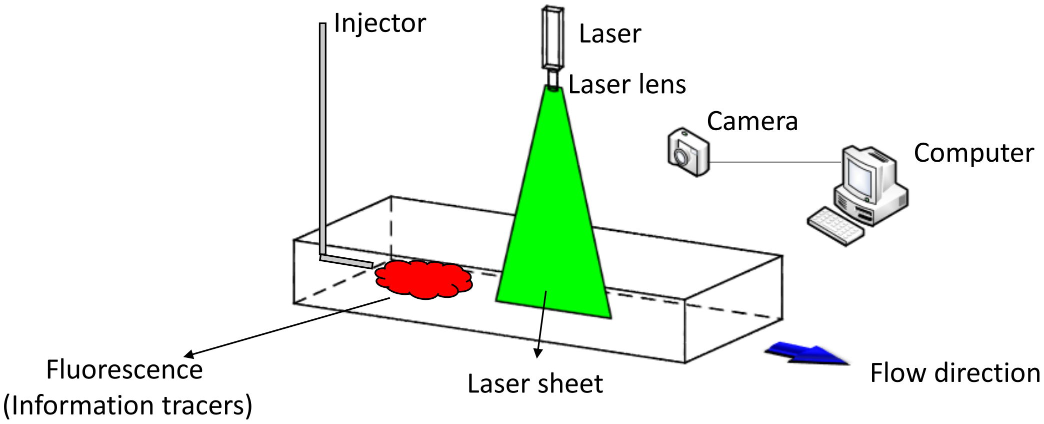

Figure 3.15: Schematic of PLIF. Laser sheet excites the fluorescence injected by the transmitter and the camera captures the intensity of excited fluorescence.

mentary metal–oxide–semiconductor (CMOS) camera captures the light emanating from the Rhodamine 6G tracer illuminated within the laser sheet. The viewing direction of the camera is required to be perpendicular to the light sheet to avoid any parallax data bias. The model and properties of the camera and laser used in the PLIF are included in Table 3.2.

Figure 3.16 shows images captured at different time frames at the receiver. The image 3.16-(a) is captured 30 seconds after the injection and the 3.16-(b) is recorded 40 seconds after the emission. In this figure and as time goes on, more fluorescence dye passes the laser sheet and as a result, the light intensity of the captured images increases. Now, if we consider the whole range of the captured images from the $t = 0s$ to $t = 45s$, we can plot the average image intensity in terms of time (see Fig 3.17). In this figure, for the $t \leq 27s$, the fluorescence dye has not arrived to the laser sheet and the recorded image intensity is zero. When the dye reaches to the laser sheet, they will be excited and as a result, the image intensity increases. What is missing now is that this plot illustrates the image intensity in terms of time whereas the concentration versus time profile is desired to be observed from the MC point of view. Thus, it is now required to associate the average image intensity with a corresponding dye concentration to yield a calibration curve.

Calibration

The relation between the mean image intensity and the dye concentration can be determined by first preparing and then video recording water-dye solutions of known concentration at the location of the receiver. The one-to-one calibration mapping be-

Table 3.2: Summary of features of PIV and PLIF methods. Equipment required for running experiment and websites for purchasing those equipment.

	PIV	PLIF
Features	• Non-intrusive • Currently normally gives velocity in 2D plane but and 3D methods are now becoming available • Low resolution • Hazardous (laser) • Requires transparent liquid	• Non-intrusive • Yields concentration distribution in a 2D plane • Hazardous (laser) • Requires transparent liquids
Equipment	• Laser (Pulsed frequency doubled Nd: YAG at 532 nm wavelength) • Cylindrical lens • Camera (High-speed CMOS camera) • Seeding particles (Hollow glass spheres, Polystyrene, Oxygen bubbles) • External hard drives	• Laser (Pulsed frequency doubled Nd: YAG at 532 nm wavelength) • Camera (High-speed CMOS camera) • Notch filter for the camera (OD 6.0) • Seeding particles (Rhodamine 6G) • External hard drive
Website	Dantecdynamics.com; TSI.com; Lavision.de; Oxfordlasers.com	Dantecdynamics.com; TSI.com; Lavision.de; Oxfordlasers.com

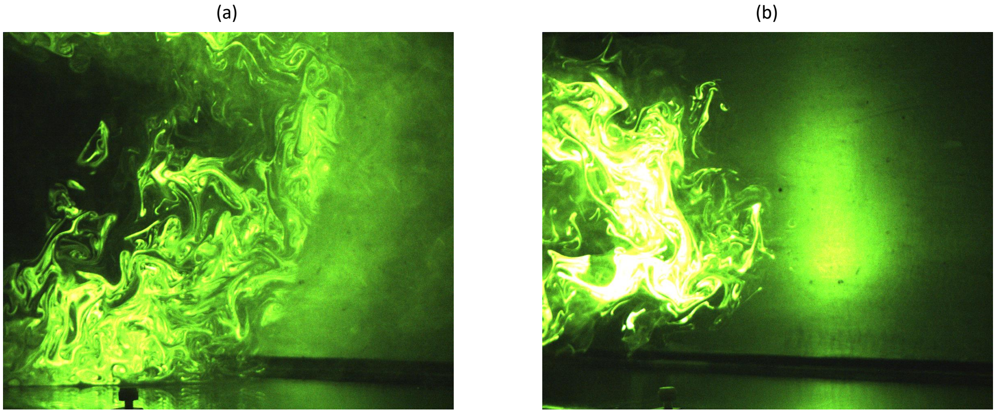

Figure 3.16: PLIF images sample taken at time a) 30 s and b) 40 s.

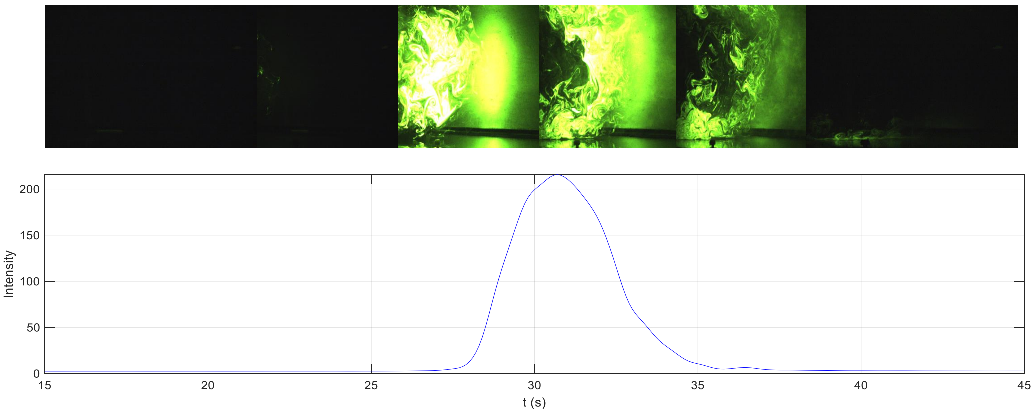

Figure 3.17: Intensity of the PLIF images in terms of time at the receiver.

tween the Rhodamine 6G concentration and the mean intensity for our experiments is shown in Fig. 3.18. Note that the calibration curve increases linearly for the dye concentrations used. However, for very high concentrations the linear behaviour will break down and asymptotically converge to a saturation value. The final graph displaying the concentration as a function of time is displayed in Fig. 3.19.

PLIF in Comparison to the Sensors

An alternative method for measuring the concentration of tracers contained in a liquid is provided by a variety of active electronic (e.g. electronic nose) and passive optical sensors. Using sensors is straightforward and has the advantage of not requiring a laser. However, the disadvantage of sensors in comparison to laser-based methods is that they are intrusive and have to be submersed in the flow field. One

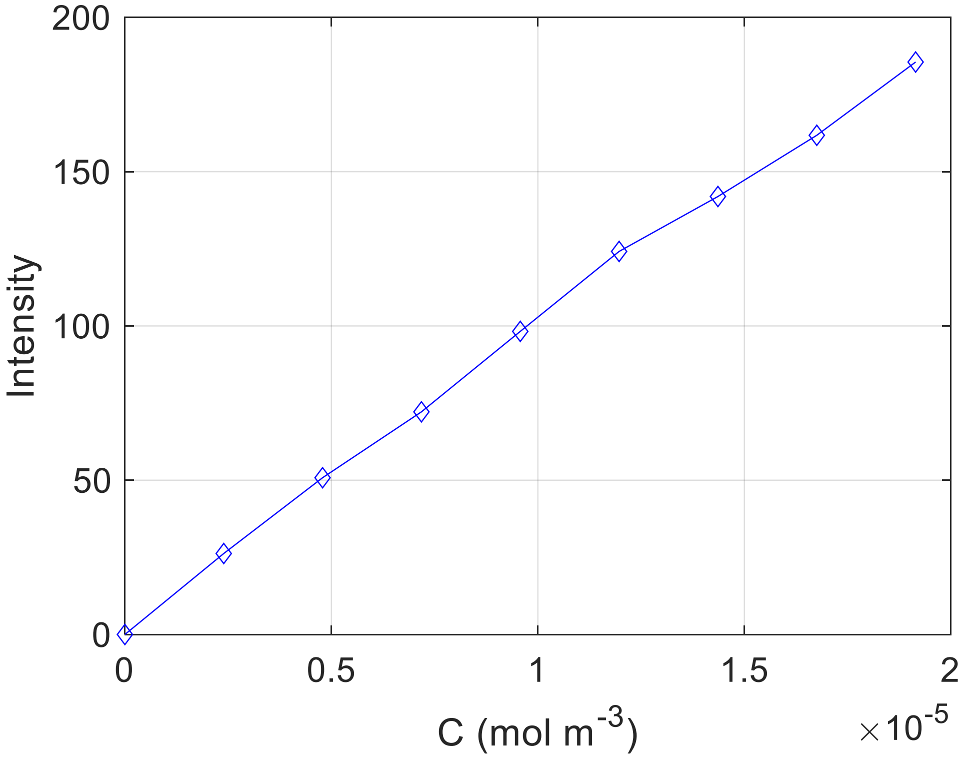

Figure 3.18: Calibration curve obtained from the calibration images.

commonly used sensor is the Turner Designs CYCLOPS-7 Submersible Fluorometer [www.turnerdesigns.com, 2010]. Rhodamine WT, where WT stands for 'water tracing', is often used as the fluorescent tracer but there exist others. The sensor displays and records the level of the tracer concentration in terms of an output voltage. The output voltage increases linearly with the concentration level in the measurable range of the fluorometer.

3.3.5 CYCLOPS-7 Submersible Fluorometer

Turner Designs CYCLOPS-7 Submersible Fluorometer [www.turnerdesigns.com, 2010] is an optical sensor for measuring the concentration. Rhodamine WT, where WT stands for 'water tracing', is often used as the fluorescent tracer but there exist others. The sensor displays and records the level of the tracer concentration in terms of an output voltage. The output voltage increases linearly with the concentration level in the measurable range of the fluorometer. For the calibration procedure the sensor is submersed in water contained in a beaker. Defined amounts of the tracer

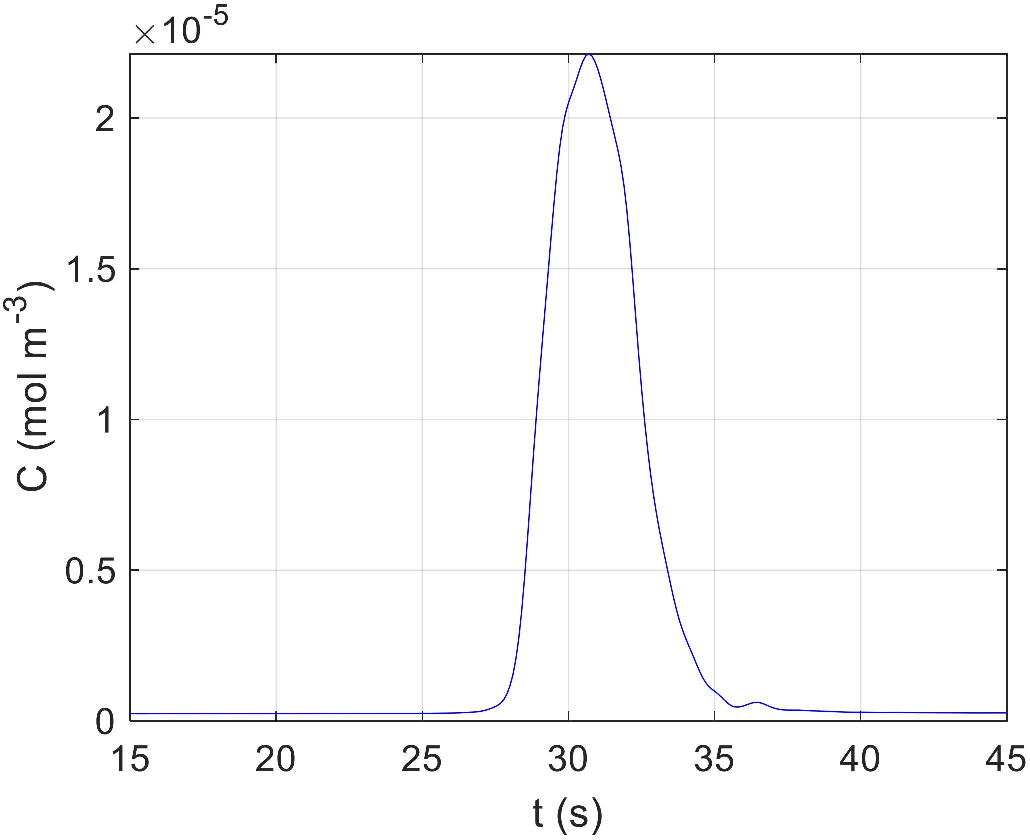

Figure 3.19: Final Concentration versus time after calibration.

are successively added to the liquid and the associated output voltages for the known concentrations are recorded to yield the calibration curve.

3.3.6 Data-set

Sample images of PIV and PLIF experiments have been uploaded to the IEEE Dataport, DOI: 10.21227/eae4-kg81. They are in 22 zip files, the first two files are for the PIV measurement and the others are for the PLIF experiment. PIV test files contain 654 and 1392 images for frame rates of 15 and 90 fps, respectively. The image format is .bmp, and the first image in each set is the calibration image. There are 20 zip files named PLIF-1 to PLIF-20. Each file contains approximately 150 images in .tif format. The first 25 images in each file are calibration images and the rest are images of the laser plane after injection of the tracer fluorescence. All images are recorded with a frame rate of 2 fps so one can calculate the total recording time according to the number of images per file. The MATLAB code has also been provided for each file and assists with the required image processing.

3.3.7 Experimental Recommended Practice

PIV and PLIF methodologies involve lasers and they require compliance with the relevant health and safety regulations. Lasers have potential hazards to the human eye and skin from both direct and scattered beam exposure. The radiant power of lasers used in PIV generally have around 1000 mW with a wavelength of 532 nm and a beam diameter of 1mm (for optimal water transmission). To understand safety, we calculate the maximum permissible exposure (MPE), which is the highest power or energy density of a light source that is considered safe. It is usually about 10% of the dose that has a 50% chance of creating damage under worst-case conditions. The MPE is measured at the cornea of the human eye or at the skin, for a given wavelength and exposure time. Our beam divergence is 3 milli-radians (0.003 radians) and 25 $\mathrm{W/m^2}$ is the eye MPE for a single accidental exposure to a continuous wave (CW) laser beam from 400 to 700 nm. The laser delivery system produces a beam plane which is 0.3m wide, aligned perpendicular to the long axis of the fluid channel. To counter this, the laser area must be fitted into a wooden box structure to cover the Nominal Ocular Hazard Distance (NOHD) [Ritt, 2019]:

$$\mathrm{NOHD} = \frac{\sqrt{\frac{4\times\text{radiant power}}{\pi\times\text{MPE}}} - \text{initial beam diameter}}{\text{beam divergence}}, \tag{3.28}$$

which is the distance from the source at which the intensity or the energy per surface unit becomes lower than the MPE on the cornea and on the skin. In our setup, the NOHD is 3.5 m. For starting the experiments, the laser should be aligned properly. Alignment is dangerous in a sense that the laser sheet should be seen. The safe procedure for alignment is:

- Only those personnel who have been trained in laser safety should align the laser. It is best to perform alignments with another trained person and exclude all unnecessary personnel during the period of alignment.
- Review all procedures before attempting the alignment. Make sure that all of the warning signs, lights, and locks are operating.
- Remove any watches or jewellery, including objects in shirt pockets, and tape over rings so that they will not serve as reflectors. Make sure that any reflective surfaces in the area are blocked or covered.

- Wear protective eye wear at all times during the alignment. Make sure that it is appropriate to the wavelength of the laser.
- Reduce power to lowest possible energy setting of the laser for determining the optical path.
- Make sure that the beam paths are at a safe height (not at eye level when seated or standing).
- Check for stray reflections before continuing the experiment.

Chapter 4

Uncertainty Quantification in Turbulent Diffusion Channel

This chapter focuses on the quantification of the uncertainty in the transmitter (Tx) design. As a first step in this thesis, we focus on the macro-scale MC Tx design and how it can affect the received molecular signal. In other words, Tx is an important part of the communication system and any uncertainty in the Tx design results in getting different channel impulse response (CIR). Here a new method called Polynomial Chaos Expansion (PCE) is introduced that assists in quantifying uncertainty at TX.

4.1 Motivation

Molecular signals undergo stochastic propagation in turbulent channels. The received signal is sensitive to a variety of input and channel parameter variations. Currently we do not understand how uncertainty or noise in a variety of parameters affect the received signal concentration, and nor do we have an analytical framework to tackle this challenge. Yet, simulating all possible permutations and considering all fluid dynamic forces is expensive and there is a need to quantify uncertainty more directly. In this chapter, we utilize PCE to show that uncertainty in parameters propagates to uncertainty in the received signal. In demonstrating its applicability we consider a turbulent diffusion molecular communication (TDMC) channel and highlight which parameters affect the received signals. This can pave the way for future information theoretic insights, as well as guide experimental design.

4.1.1 Review of Similar Work

Monte-Carlo simulation, whilst time consuming, can offer computation convergence guarantees in the face of multiple uncertainties [Mathelin et al., 2005]. Often, as is the case for fluid dynamics, there are divergent solutions to the model. In weather forecasting, extreme weather represents one of the many possible outcomes and uncertainty propagation is essential. In [Farazmand and Sapsis, 2017], the authors use sparse initial weather data to inform the likelihood of divergent solutions forming. In probabilistic programming and numerics [Hennig et al., 2015], uncertainty is cascaded through to yield posterior estimates of the solution, which is computationally expensive for simulations. Nonetheless, the aforementioned scenarios are computationally expensive and data demanding. As such, analytical methods for uncertainty propagation in fluid dynamics are useful.

PCE is a method to determine the propagation of uncertainty in dynamical systems, when there is probabilistic uncertainty in the system parameters. PCE has been used in fluid dynamics since solving the Navier-Stokes equations is computationally expensive. Hosder et al. [2006] employed non-intrusive PCE to add uncertainty in the input of aerodynamic parameters where the uncertainty was associated with the channel geometry and the dynamic viscosity of fluid in the laminar boundary-layer flow. For evaluation, they compared their results with Monte Carlo simulation and a good agreement existed. They show that the advantage of PCE over Monte Carlo methods is that one can achieve the same results with a seven-order computational saving [Hosder et al., 2006].

In molecular signaling, when the propagation channel is described by a stable mass diffusion equation, the uncertainty arises from Brownian motion [Srinivas et al., 2012]. However, when there are fluctuations in the diffusion channel from temperature and diffusivity variations, then uncertainty in the channel propagates to the receiver signal concentration [Qiu et al., 2017]. As evidenced by the literature, there is a lack of uncertainty research in molecular-communication problems that are affected by complex fluid dynamic processes. Uncertainty research will improve our knowledge about noise sources (e.g. transposition noise [Haselmayr et al., 2017]) and the information capacity. In this context PCE represents a good research methodology. It is worth noting that even in the whole area of wireless communication, there is a lack of research in uncertainty propagation [Acikgoz and Mittra, 2017; Boeykens et al., 2014].

4.1.2 Uncertainty in Molecular Signal Propagation

Uncertainty can arise from noise in the input and ambient parameters. This makes deterministic models unreliable in estimating the variational behaviour of complex systems. Many engineering systems are described by complex differential equation models, which give deterministic outputs. In the case of mass diffusion based molecular signaling (and molecular communication), the classic Fick's Law yields a deterministic inverse-Gaussian form [Guo et al., 2016a]. When considering more complex processes (e.g. turbulence, shear stress) [Unluturk and Akyildiz, 2017b; Kennedy et al., 2018], the RANS equations still yield deterministic solutions. This means that externally triggered variations in input parameters (e.g. velocity profile of molecular signal) and the channel parameters (e.g. dynamic viscosity, diffusivity) cannot be accounted for. Monte-Carlo simulations are required to simulate variational behaviour, causing time intensive computation and lacking in direct insight about sensitivity to different parameter combinations.

4.2 Polynomial Chaos Expansion

PCE is a method which facilitates the spectral representation of the uncertainty in physics-based and engineering problems. In this surrogate method, the output can be represented as an expansion of the input random parameters with a specific probability density function (PDF), so the uncertainty in the input parameters is reflected in the outputs [Owen, 2017].

4.2.1 Univariate Polynomial Chaos

Let Ξ be a random variable with known PDF w, and $X = \phi(\Xi)$, where ϕ is a function that is square-integrable on χ ($\chi \subset \mathbb{R}$) with w as a weight function (call this space L^2_w). Our goal is to approximate X by a polynomial series of Ξ. For this purpose, we need a family of polynomials H_n such that H_0 is not 0, and for $n \geq 0$ ($n \in \mathbb{N}$), the polynomial H_n has the order of n and are orthogonal with respect to w. Thus,

$$\langle H_n, H_m \rangle_w = \int_\chi H_m(x) H_n(x) w(x) dx = \gamma_m \delta_{mn}, \tag{4.1}$$

where δ_{mn} is the Kronecker delta and would be 1 if $m = n$ and 0 if $m \neq n$, and γ_m is the normalization constant which is obtained by:

$$\gamma_m \equiv \int_\chi H_m^2(x) w(x) dx. \tag{4.2}$$

We also assume that H_0 is normalized so that $\langle H_0, H_0 \rangle_w = 1$. Depending on the distribution of the Ξ, different set of orthogonal polynomials should be employed to satisfy (4.1).

Legendre Polynomials

If Ξ has a uniform distribution ($\Xi \sim \text{Unif}[-1,1]$), Legendre polynomials should be used [Xiu and Karniadakis, 2003]. By having the first two Legendre polynomials ($H_0(x) = 1$ and $H_1(x) = x$), we can generate the others by following recursive relation [Chihara, 2011]:

$$(m+1)H_{m+1}(x) = (2m+1)xH_m(x) - mH_{m-1}(x), \tag{4.3}$$

where m is the order of the polynomial. The generated polynomials are orthogonal if we consider $w(x) = \frac{1}{2}$ which is the PDF of $\Xi \sim$ Unif[-1,1]. In this case, the normalization constant for $m \in \mathbb{N}$ is $1/(2m+1)$.

Hermite polynomials

When Ξ has a normal distribution ($\Xi \sim \mathcal{N}(0,1)$), then the Hermite polynomials should be employed to build the PCE [Xiu and Karniadakis, 2003]. By considering $H_0(x) = 1$, the recursive relation for Hermite polynomials is [Chihara, 2011]:

$$H_{m+1}(x) = xH_m(x) - \frac{d}{dx}H_m(x). \tag{4.4}$$

The generated polynomials are orthogonal if we consider $w(x) = \frac{\exp(-x^2/2)}{\sqrt{2\pi}}$ which is the PDF of $\Xi \sim \mathcal{N}(0,1)$. In this case, the normalization constant for $m \in \mathbb{N}$ is $m!$.

There are also other PDFs and their corresponding polynomials in the literature that can be considered based on the type of the input variables [Xiu and Karniadakis, 2003]. In this study, we utilize uniform and normal distributions as PDF of the uncertain input parameters in molecular signaling.

Now, the series is constructed by considering the polynomials H_n as a basis for L^2_w.

$$\phi(\Xi) = \sum_{n \geq 0} a_n H_n(\Xi). \tag{4.5}$$

where a_n are deterministic unknown coefficients. Because H_n is an orthogonal basis, the coefficients are calculated by projecting on each basis vector.

$$a_n = \frac{\langle \phi, H_n \rangle_w}{\langle H_n, H_n \rangle_w}. \tag{4.6}$$

After calculating the a_n coefficients, the statistics of the output X are determined spatially. Due to the orthogonality of the applied polynomials, the expectation of the X is estimated by:

$$E[X] \approx \alpha_0, \tag{4.7}$$

which is the coefficient of the zeroth order polynomial. Also, the variance is estimated in the same way.

$$\mathrm{Var}[X] \approx \sum_{n \geq 1} \alpha_n^2 \langle H_n, H_n \rangle_w. \tag{4.8}$$

Since we cannot simplify a product of three or more polynomials, the equations for further moments contain all possible terms of the power of the sum.

4.2.2 Example of Usage

Let $f(x) = xe^{-x} + x$ and let us assume that we need to find the root of the equation $f(x) = \Xi$, which we will denote by $R(\Xi)$. There is no simple close form for the root of equations of this form, but if Ξ is just a number, we can easily find the root using the Newton method. The situation becomes trickier if Ξ is a random variable. In this case $R(\Xi)$ can be considered as a random variable itself. If we wanted to calculate the probability distribution of $R(\Xi)$, we would resort to Monte Carlo simulations, i.e. we would choose a realization of Ξ and we would compute $R(\Xi)$ few tens of thousand times and we would plot the histogram of the values. In more complicated problems this can be computationally expensive. Even calculating the mean and the variance of $R(\Xi)$ requires numerical integration of $R(\Xi)$.

Instead we will use PCE. Let us assume that $\Xi \sim \mathrm{Unif}[-1, 1]$ and that $R(\Xi)$ can be approximated by a third order polynomial expansion using Legendre polynomials

$$R(\Xi) \approx \sum_{n=0}^{3} \alpha_n H_n(\Xi).$$

In order to calculate the coefficients a_n, we choose 10 realizations of Ξ and the corresponding root $R(\Xi)$. The realizations of Ξ will be denoted ξ_i . This means that we have 10 pairs $\big(\xi_i, R(\xi_i)\big)$, so we can use least squares in order to find the optimal values for the coefficients a_n. We will call this Least Square Polynomial Chaos Expansion (LSPCE). We find $\alpha_0 \approx 0.042$, $\alpha_1 \approx 0.52$, $\alpha_2 \approx 0.086$ and $\alpha_3 \approx 0.012$.

Now we have:

$$E[R(\Xi)] = a_0 = 0.042$$

and

$$\mathrm{var}[R(\Xi)] = \sum_{n=1}^{3} \alpha_n^2 \langle H_n, H_n \rangle = 0.091.$$

Furthermore, if we want to approximate the PDF of $R(\Xi)$, instead of using Monte Carlo, we can use the expansion to get values for $R(\Xi)$. In this example, instead of using the Newton method, we evaluate a third order polynomial. In more complicated problems, like turbulent diffusion problem, the gain in computational can be many orders of magnitude.

Finally, we can gauge the error of our method by calculating the fourth order approximation. In this example the first three coefficients were the same up to at four significant digits.

4.2.3 Parametric Univariate PCE

The case where X depends also on an independent parameter, t, can be treated as a straightforward generalization of the previous. In particular if $X = \phi(t, \Xi)$ with $\phi(t, \cdot) \in L^2_w$ for all t, then we can decompose X as

$$\phi(t, \Xi) = \sum_{n \geq 0} a_n(t) H_n(\Xi). \tag{4.9}$$

This becomes particularly useful in the case of differential equations that depend on a stochastic parameter. For example, in the case of a linear differential equation $\dot{X} = L(X) + \psi(\Xi)$, where L is linear and $\psi(\Xi) = \sum_{n \geq 0} b_n H_n(\Xi)$, we can substitute the sum and use the linearity of the equation to get

$$\sum_{n \geq 0} \dot{a}_n(t) H_n(\Xi) = \sum_{n \geq 0} L(a_n(t)) H_n(\Xi) + \sum_{n \geq 0} b_n H_n(\Xi). \tag{4.10}$$

and by projecting on each H_n we get the equations $\dot{a}_n = L(a_n) + b_n$, whose solutions are the coefficients of the expansion. Notice that all the equations now are deterministic.

In the case of non-linear differential equation, one has products of polynomial chaos expansions. This means that one gets an infinite system of deterministic differentiable equations. This method of computing the coefficients is called intrusive method because it requires to change drastically the solver [Xiu and Karniadakis, 2003].

4.2.4 Multivariate PCE

Let $X = \phi(\Xi_1, \Xi_2)$ where Ξ_1 and Ξ_2 are random variables with PDFs w_1 and w_2, respectively and $\phi(\cdot, \Xi_2) \in L^2_{w_1}$, $\phi(\Xi_1, \cdot) \in L^2_{w_2}$ for all Ξ_1 and Ξ_2. Let $H_{1,m}$ and $H_{2,m}$ be polynomial families that form an orthogonal basis in $L^2_{w_1}$ and $L^2_{w_2}$, respectively and $\langle H_{1,0}, H_{1,0}\rangle_{w_1} = \langle H_{2,0}, H_{2,0}\rangle_{w_2} = 1$. Then we can decompose X as the deterministic part (coefficients) and stochastic terms.

$$\phi(\Xi_1, \Xi_2) = \sum_{m\geq 0}\sum_{n\geq 0} a_{m,n}\, H_{1,m}(\Xi_1) H_{2,n}(\Xi_2). \tag{4.11}$$

One can project on the basis to get the coefficients, i.e.

$$a_{m,n} = \frac{\langle\langle \phi, H_{1,m}\rangle_{w_1}, H_{2,n}\rangle_{w_2}}{\langle H_{1,m}, H_{1,m}\rangle_{w_1} \langle H_{2,n}, H_{2,n}\rangle_{w_2}}. \tag{4.12}$$

Similarly to the univariate case the relations for the first two moments are relatively simple. For the expectation one has $E[X] \approx a_{0,0}$ and for the variance we have:

$$Var[X] \approx \sum_{m\geq 1}\sum_{n\geq 1} a^2_{m,n}\, \langle H_{1,m}, H_{1,m}\rangle_{w_1} \langle H_{2,n}, H_{2,n}\rangle_{w_2}. \tag{4.13}$$

This expansion can be generalized to more than two random variables in a straightforward way. The PDF of each random variable defines as inner product in the space $L^2_{w_i}$ and we have to choose an orthogonal basis in this space. Then one just expands X with respect to every family of basis functions. Similarly we can generalize this scheme to treat parametric multivariate cases. One just needs to notice that the coefficients of the expansion depend only on deterministic parameters.

4.2.5 Approximation Using PCE

In order to do any computation with a PCE series, we have to truncate it since it is not feasible to expand the PCE series to infinity. For this purpose, we notice that if the series converges, then the size of the coefficients go to 0 if we take the limit of any index to infinity. This means that for every convergent series, we can ignore terms of order higher than some N. However, for a given problem it is not trivial to find which exactly this N is. Usually this is done by trial and error, where we calculate more terms until the size of the new terms is smaller than the precision required.

We start by truncating the series to an arbitrary order N,

$$\phi_n(\Xi) = \sum_{n=0}^{N} a_n H_n(\Xi) \tag{4.14}$$

and assume that this is enough for the considered precision. By using a truncated series, the intrusive method produces a finite system of differential equations which should be solved to get the coefficients.

There is also a non-intrusive method which was first introduced by Walters [2003]. In this case, we observe that (4.14) is linear with respect to a_n's, so we treat the simulator as a black box. We generate $M \geq N$ instances of the random variable Ξ, $\{\xi_1, \ldots, \xi_M\}$ and we calculate the deterministic outputs by simulator, $\{\phi(\xi_1), \ldots, \phi(\xi_M)\}$. Then for every ξ_i we have the equation:

$$\phi(\xi_i) = \sum_{n=0}^{N} a_n H_n(\xi_i). \tag{4.15}$$

Notice that $\phi(\xi_i)$ and $H_n(\xi_i)$ are just numbers and now we can compute the coefficients a_n by solving a linear regression. After that, we compute $\sup_\Xi |a_N H_N(\Xi)|$ and if it is smaller than the precision, we stop, otherwise we increase N and repeat the process.

4.3 System Model and Method

PCE is a surrogate approximation method for Monte Carlo simulation which has been widely used in communication area especially in molecular communication. In this study, to mimic the reality, we employed PCE in a TDMC channel to add uncertainty in a set of parameters such as inlet velocity, initial concentration, dynamic viscosity of the ejected fluid, and the turbulent Schmidt number (or Sc which describes the ratio between the rates of turbulent transport of momentum and the turbulent transport of mass).

4.3.1 Channel Configuration

The system model in this chapter is a 3D $50 \times 10 \times 10$ m^3 water channel (see Fig. 4.1). The water molecules are ejected into a quiescence aqueous environment with $\mathbf{V} = u_0 i + v_0 j + w_0 k$ velocity where u_0 is taken as $4\,\mathrm{m/s}$ and the other two

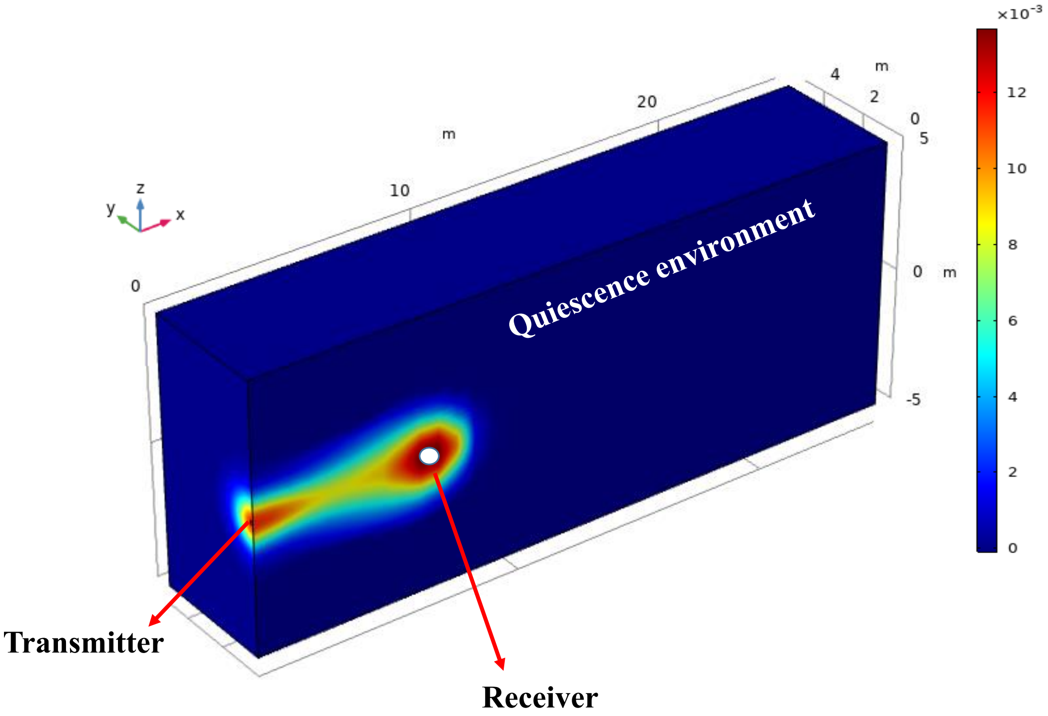

Figure 4.1: Schematic of the cross-section cut of the system model illustrating the quiescence environment, transmitter, receiver, and emitted molecules.

components assumed to be zero if we have ideal injection system. The concentration of the ejected water is measured at the receiver site which is located at $40 \times r_{in}$ where r_{in} is the radius of the injector and the initial concentration of the water molecules is $4\,\mathrm{mol/m^3}$. The sidewalls and the outlet has been considered far enough from the transmitter so that we can neglect their effects on the fluid flow. The properties of the water and the other system parameters are given in Table 4.1.

4.3.2 Non-intrusive PCE

In practice, it is impossible to be certain about the exact values of the initial conditions in any applied problem since the input parameters are subject to uncertainties that originate from various sources (e.g. injection delay, concentration of information molecules, etc). For example, in our problem, when we say that the inlet velocity and initial concentration are $\mathbf{V} = \alpha_1 i + \alpha_2 j + \alpha_3 k$ m/s and β mol/m^3, respectively, they are not precisely these values and they can be $\mathbf{V} = (\alpha_1 \pm \Delta\alpha_1)i + (\alpha_2 \pm \Delta\alpha_2)j + (\alpha_3 \pm \Delta\alpha_3)k$ m/s and $\beta \pm \Delta\beta$ mol/m^3 where $\Delta\alpha_1, \Delta\alpha_2, \Delta\alpha_3$, and $\Delta\beta$ are the amount of uncertainty in each input parameters. For adding such uncertainties

Table 4.1: Simulation parameters for PCE simulation.

Variable	Value
Maximum injection velocity, u_0	$4\,\mathrm{m/s}$ at $t = 0$
Dynamic viscosity of water, μ	$8.9 \times 10^{-4}\,\mathrm{Pa.s}$
Density of water, ρ	$1000\,\mathrm{kg/m^3}$
Transmit concentration, c_0	$4\,\mathrm{mol/m^3}$
Pulse width, T_0	$0.7\,\mathrm{s}$
Radius of the injector (r_{in})	$12.5\,\mathrm{cm}$
Distance between TX and RX, $d_{Tx,Rx}$	$40 \times r_{in}$
Simulation dimensions	$50 \times 10 \times 10\ \mathrm{m}^3$

in our simulation, we employ the non-intrusive PCE method meaning that we do not have to make any changes in the built-in solver code. For constructing the PCE, the expansion in (4.11) should be truncated (see Section 4.2.5). Generally, there are methods for truncating the PCE, 1) truncating the series up to an order of interest. For example, if the order of interest is z, then for the series of (4.11), we have:

$$\phi(\Xi_1, \Xi_2) = \sum_{0 \leq (n+m) \leq z} a_{m,n}\, H_{1,m}(\Xi_1) H_{2,n}(\Xi_2). \tag{4.16}$$

2) we can consider all possible combinations of the order for each univariate polynomial. This method is called *tensor product truncation* and it is given by:

$$\phi(\Xi_1, \Xi_2) = \sum_{0 \leq n \leq z} \sum_{0 \leq m \leq z} a_{m,n}\, H_{1,m}(\Xi_1) H_{2,n}(\Xi_2). \tag{4.17}$$

We utilize the first method since it is time-efficient and does not substantially change the accuracy [Owen, 2017]. If the number of the uncertain input parameters is n and the maximum order of the applied polynomial is p, then the number of the terms in the truncated PCE (or size of experimental design) will be $N = \binom{n+p}{p}$ for the first truncation method, and for the tensor product truncation it will be $N = (p+1)^n$ [Owen, 2017]. After generating N random numbers for each uncertain input parameter, the COMSOL code should be evaluated for these random numbers to obtain the left hand side of (4.15). Thereafter, the polynomials on the right hand side of (4.15) are also calculated at these points and finally, by solving a linear regression problem, the a_n coefficients will be obtained. It should be noted that all of the terms in (4.15) are matrices. Now, we can construct the expansion and use it as an approximation formula without running the solver for a new set of random numbers for each uncertain input parameter.

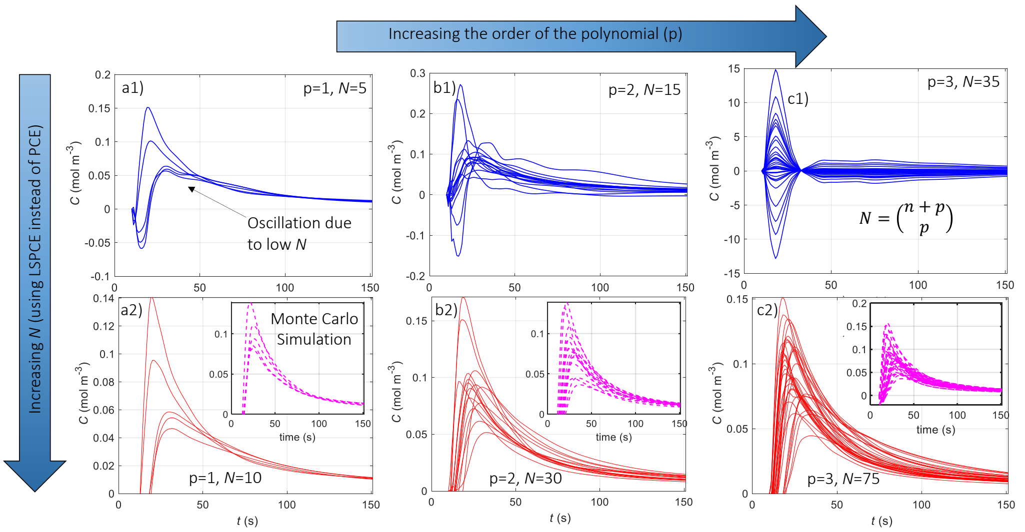

Figure 4.2: Concentration versus time profiles. From left to right shows the increasing of the polynomial order (p). First row is for the PCE and the second row is for the LSPCE. In each column, the p is fixed for better illustration of the increased N. The subsets in the second row shows the Monte Carlo simulation results for comparison.

What is crucial in the context of the regression is the size of the experimental design or N. If we evaluate the PCE exactly at N random numbers, it will produce oscillations in the established PCE (see Fig. 4.2(a1), (b1), (c1)). To resolve this problem, we can choose the size of the experimental design $2\times N$ as suggested by Hosder et al. [2007] and Owen [2017]. After evaluating the series in $2\times N$ random numbers, it is required to interpolate the results by means of the least-squares regression. This formalism removes the oscillations and yields a stabilized series (see Fig. 4.2(a2), (b2), (c2)).

4.4 Results & Discussion

4.4.1 Convergence Test of PCE

The number of the uncertain input parameters (n) of any particular problems is fixed. Increasing the order (p) of the polynomial improves the convergence of the values of the coefficients ($a_{m,n}$). However, increasing the order of the polynomial means that a substantially higher number of simulations is required. Therefore a compromise between accuracy and required computational time is necessary.

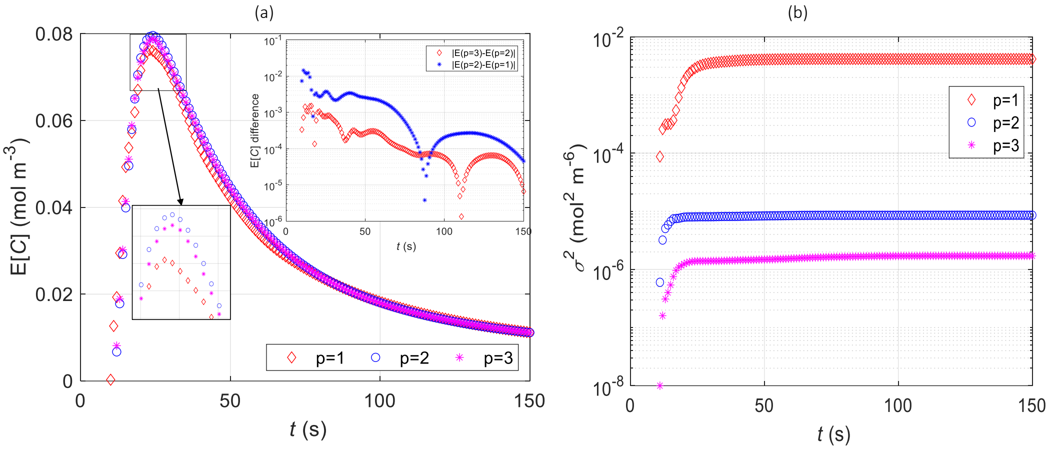

Figure 4.3: a) Expectation of LSPCE for different polynomial orders. The inset shows the difference between the expectations by increasing the order of the applied polynomials, b) variances of LSPCE for different polynomial orders.

Reference to the graphs in Fig. 4.2(a2), (b2), (c2) reveals that it is not possible to infer which order of the p yields sufficient convergence of the PCE process. Therefore, the statistics of the random outputs have to be considered. To this end, the expectation and the variance of the concentration in Fig. 4.2(a2), (b2), (c2) are calculated from (4.7) and (4.8), respectively. These two quantities are shown in Fig. 4.3. It can be seen that the expectation for $p = 2$ and $p = 3$ almost overlap while there is a significant difference for $p = 1$ compared to $p = 2$. The inset in Fig. 4.3(a1) displays the absolute difference of the expectations for $p = 2$, $p = 3$ and $p = 2$, $p = 1$. It can be seen that the difference is one order magnitude. Thus, using a polynomial of order $p = 1$ is certainly not sufficient.

The change of the variance by increasing the polynomial order is displayed in Fig. 4.3(a2). It can be seen that the variance between cases $p = 2$ and $p = 3$ changes by one order of magnitude whereas for $p = 1$ and $p = 2$ the change is two orders. Thus, $p = 2$ can be considered as the appropriate choice for the polynomial order. Choosing higher order polynomials substantially increases the required simulation time with minor effects on improving the accuracy of the results.

4.4.2 Comparing different PDFs in PCE

Depending on the input variables different types of PDFs should be employed to obtain the most reliable results in PCE. For instance, consider the dynamic viscosity of water (μ) and the turbulent Schmidt number (Sc) are the uncertain input parameters. The dynamic viscosity varies with temperature (it is 8.9×10^{-4} Pa.s at

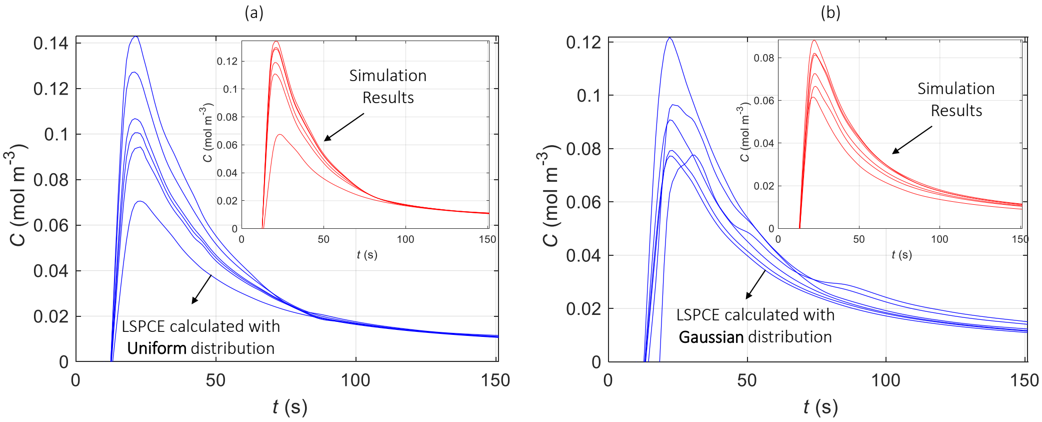

Figure 4.4: a) Concentration vs. time using uniform distribution as the PDF of the uncertain input parameters, b) concentration vs. time using Gaussian distribution as the PDF of the uncertain input parameters. Dynamic viscosity of the water (μ) and turbulent Schmidt number(Sc) are uncertain input parameters.

25°C). The uncertainty of the turbulent Schmidt number arises since it is determined experimentally. Figure 4.4 displays predictions for the concentration as a function of time using normal and uniform PDF distributions for both the viscosity and the Schmidt number. The figure reveals that the curves for the concentration profiles when using a uniform PDF are smoother than those based on a normal distribution (cf. Fig.4.4(a) and (b)). This is a result of the uniform distribution being bounded, between -1 and 1, whilst the normal distribution is not. That is, for input parameters like dynamic viscosity of the water that is small and only subject to small variations considering an unbounded PDF would not yield reliable results.

4.4.3 Statistical results

In Fig. 4.5 we employed the LSPCE approach to investigate the statistical properties of the TDMC channel with one of the input parameters being subject to uncertainty only. In Fig. 4.5(a1) the uncertain parameter is c_0, in Fig. 4.5(a2) to (a4) the uncertain parameters are different components of the inlet velocity ($\mathbf{V} = u_0 i + v_0 j + w_0 k$). Six simulations per parameter ($\frac{(n+p)!}{n!p!} = \frac{(1+2)!}{2!} = 3 \times 2 = 6$ LSPCE) were conducted to construct the PCE. The expansion is then used to calculate the concentration for 10000 different cases, and the random number being generated from a uniform distribution in each case. The ratio between the computational times required to arrive at the same result by means of 10000 3D COMSOL Monte Carlo simulations and the LSPCE simulations is of the order of 10^5.

The varying color density displayed by the plots in Fig. 4.5(a1)-(a4) moreover

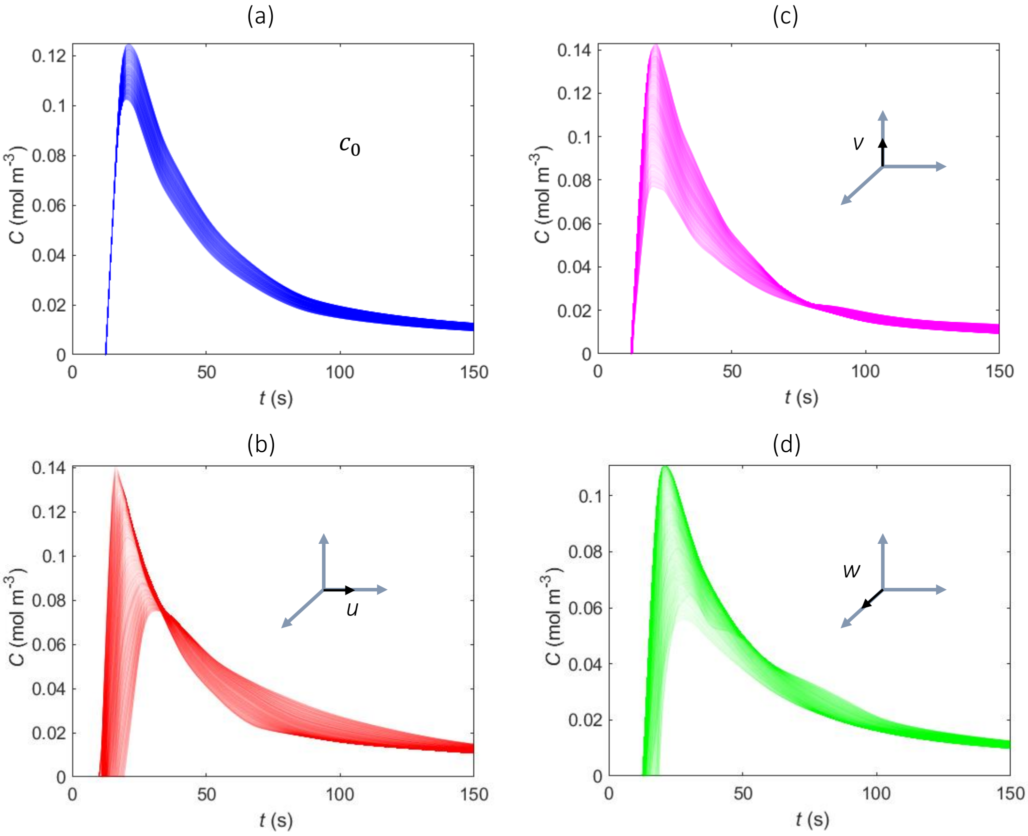

Figure 4.5: 10000 concentration profiles obtained by LSPCE for uncertain input parameters of, a1) c_0, b) u_0, c) v_0, d) w_0.

illustrates that the uncertainty in the input is mostly reflected in the peak of the CIR while the tail is not affected. This means that only the signal strength is subject to the uncertainty whilst the ISI is not. It can moreover be seen that the channel response is more sensitive to the uncertainty of the inlet velocity than to the initial concentration. This represents a crucial result in the context of experiments. It implies that geometric details of piston and cylinder of the transmitter, which govern the inlet velocity, have a stronger effect on simulated data than the amount of the released molecules.

4.5 Summary

In this chapter, we utilize polynomial chaos expansion to show how the uncertainty in parameters propagates to uncertainty in the received signal. The PCE method has a significant time saving compared to Monte-Carlo simulations and offers theoretical insight. Our uncertain parameters are initial concentration, injection velocity, dynamic viscosity of the water, and turbulent Schmidt number. We demonstrated that how the uncertainty in the aforementioned parameters propagates through the channel and can affect the received signal response. The research conducted here in PCE and uncertainty propagation can pave the way for future information theoretic insights, as well as guide experimental design.

After quantifying the uncertainty in the Tx, in the following chapters we will focus on the channel part of the macro-scale MC system. In the next chapter, we will show that by generating certain structures called vortex rings and encoding information on them, we can significantly reduce the ISI compared to the normal TDMC channels. Of course generating such structures requires professional protocols that we will mention it. Thus, in chapter 6 and afterwards, we will get back to the TDMC channels that information are encoded on the puffs and we try to characterise the noise and mutual information on this kind of channels.

Chapter 5

Towards the High Channel Capacity Using Vortex Rings

5.1 Motivation

Molecular signal coherence in fluid dynamic channels is severely hindered by mass, momentum, and turbulent diffusive processes. The combination of such forces causes long molecular tails, which results in severe ISI and limits the achievable symbol rate. Before proposing a channel model for the TDMC channels and characterising the noise in this kind of channels, we propose to modulate information symbols into stable vortex ring structures to minimize ISI. Each vortex ring can propagate approximately 100× the diameter of the transmission nozzle without losing its compact shape. First, we show the conditions required for the generation of the vortex rings, and the effective parameters that control the formation of the vortex ring. Afterwards, we show that how the parameters such as stroke ratio and injection velocity will affect the CIR and SIR. In the next step, we show that the ISI from sequential transmissions is minimal and increases rapidly with increasing of stroke ratio. Finally, we show that by maintaining a coherent signal structure, the signal-to-inference (SIR) ratio is higher over conventional puffs. Also, we demonstrate the vortex ring using a proof-of-concept prototype.

5.2 Review of Similar Works

Conventional molecular signals are represented by discontinuous molecular puffs that are ejected into a fluid or gas channel. After ejection, at the macro-scale, the signal is subject to various pressure, velocity, shear stress gradients, as well as reaction

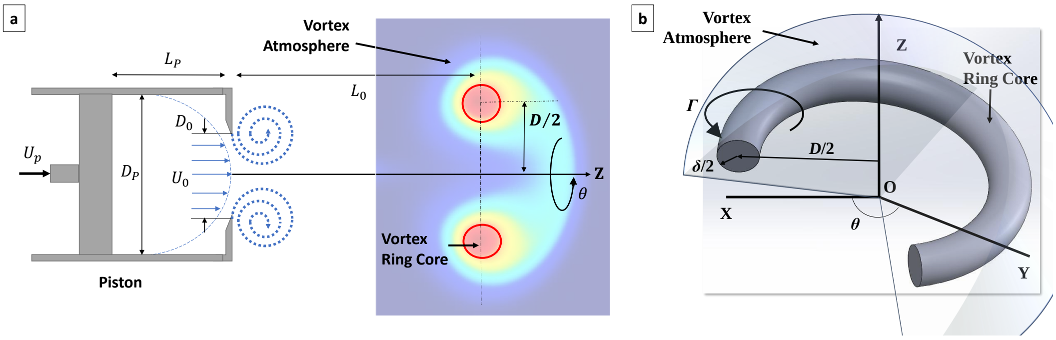

Figure 5.1: (a) Illustration of transmitter piston design to generate vortex ring, (b) illustration of vortex ring core properties and its orientation in cylindrical coordinates with a surrounding vortex atmosphere.

forces. The coupling relationships between these forces and the flow rate are well described by the Navier-Stokes equations [Unluturk and Akyildiz, 2017a]. Existing literature in molecular communications has predominantly used isotropic diffusion channel models due to their tractable expressions [Guo et al., 2016a], assuming a Péclet number below 1 (e.g. mass diffusion dominates). Whilst this is reasonable for cell membranes and capillary blood flow, advection and external forces will dominate at larger-scales.

5.2.1 Vortex Rings in Turbulence

Turbulence is not only inherently very difficult to model, but it also doesn't directly help us understand the communication capacity of the channel. Yet, we can take advantage of a certain structure called *vortex ring* that propagates well in turbulent fluid channels. The vortex ring retains spatial structure through its rotational momentum and has a sharper concentration time profile than a standard puff. This has the potential to significantly reduce ISI from sequential transmissions and as such allows us to transmit at a higher symbol rate. The vortex ring core is a torus shaped fluid or gas structure, that retains shape (e.g. mitigates dispersion) for long propagation distances (typically 100×nozzle diameter) [Brend and Thomas, 2009] - see Fig.5.1. Each vortex ring is a region, where the molecules mostly spin around an axis in a closed loop.

5.3 Vortex Ring Structure & Generation

A vortex ring is a bounded region of vorticity in which the vortex lines form closed loops [Lim and Nickels, 1995]. Vortex rings which are circular and stable and have the ability to retain molecular information in a self-sustained structure. It is worth noting that the vortex core can become wavy (Widnall instability) at some point during its existence depending on conditions. The general properties of every vortex ring can be observed in Fig.5.1, where the vortex ring core has diameter of D (approximately 1.3× the nozzle diameter D_0) and the bulk of vorticity in the region has diameter of δ. There is also a small atmosphere surrounding the core - see Fig.5.1(b).

In order to design the transmitter that can generate a vortex ring, careful consideration is needed - see Fig. 5.1(a). First, the molecules inside the piston must be subjected to a sufficient shear stress profile such that vortices are generated. This occurs when the molecules are pushed out at a sufficiently high Reynolds number, generating a vortex ring head. In the case of vortex rings, the Reynolds number is given by $Re_\Gamma = \frac{\Gamma}{\nu}$ where ν is the kinematic viscosity of the ejected fluid and Γ is the circulation given in (5.1). To find Re_Γ, we first need to define the inertial forces inside a region of vorticity, with molecules spinning around an imaginary axis in a closed loop.

$$\Gamma = \int_S \nabla \times \mathbf{u}\, \mathrm{d}\mathbf{S} = \oint_l \mathbf{u}\, \mathrm{d}\mathbf{l}, \tag{5.1}$$

where $\mathbf{S}$ is a closed surface which is bounded by line $\mathbf{l}$ and $\mathbf{u}$ is the velocity field in the flow domain. Equation (5.1) is derived based on the Kelvin–Stokes theorem [Zill et al., 2011]. Given a vector field, the theorem relates the integral of the curl of the vector field over some surface, to the line integral of the vector field around the boundary of the surface. The classical Kelvin-Stokes theorem can be stated in one sentence: The line integral of a vector field over a loop is equal to the flux of its curl through the enclosed surface.

To generate the vortex ring, a prescribed axial velocity can be defined at the transmitter to simulate the motion of the piston and also to define the vorticities at the edge of the piston [Danaila and Hélie, 2008]:

$$V_z(t,r) = V_0(t) V_{zb}(r), \tag{5.2}$$

where $V_0(t)$ is the time-variant velocity program that expresses the piston motion and given by [Danaila and Hélie, 2008]:

$$V_0(t) = \begin{cases} \frac{U_p}{2}\left\{1 + \tanh\left[\frac{5}{\tau_1}(t - \tau_1)\right]\right\}, & t < \tau_1 + \frac{\tau_2}{2} \\ \frac{U_p}{2}\left\{1 + \tanh\left[\frac{5}{\tau_1}(\tau_1 + \tau_2 - t)\right]\right\}, & t \geq \tau_1 + \frac{\tau_2}{2} \end{cases} \tag{5.3}$$

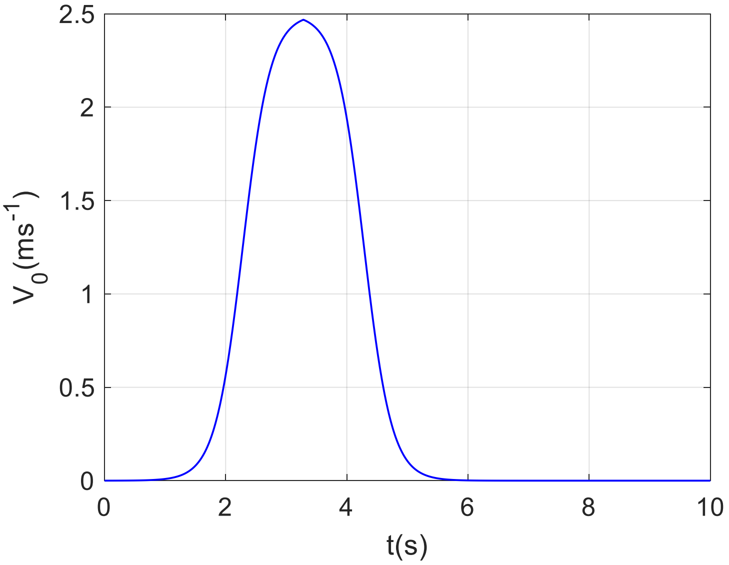

Figure 5.2: Time variant velocity program ,V_0, that shows the motion motion.

where U_p is the maximum piston velocity. Parameter τ_1 is a short-time acceleration/deceleration of the impulsive piston, and the value of the τ_2 is equal to stroke ratio ($\tau_2 \approx L_p/D_P$). In the stroke ratio formula, L_p is the stroke length, and if the piston reaches to the end of the cylinder, we have maximum stroke ratio as shown in Fig. 5.1(a). Figure 5.2 illustrates V_0 profile considered in this thesis.

Also, V_{zb} is the classical hyperbolic tangent profile which has been derived from experiment and represents the thickness of vorticity layer at the edge of the cylinder [Danaila et al., 2009]:

$$V_{zb}(r) = \frac{1}{2}\left\{1 + \tanh\left[\frac{1}{2\delta_w}\left(\frac{D_p}{2r} - \frac{2r}{D_p}\right)\right]\right\}, \tag{5.4}$$

where δ_w is the dimensionless thickness of vorticity layer at the transmitter and it is considered 0.05 in this chapter (shows a thin vorticity layer). The diameter of piston is D_p and r is the radial distance from the center of inlet. Figure 5.3 displays the V_{zb} that is considered in this thesis. Also, Fig. 5.4 shows the final velocity profile of the piston in order to generate the vortex ring. For $L_p/D_p \geq 4$, the leading vortex ring is followed by an active trailing jet-like region [Gharib et al., 1998], and as the stroke ratio increases, more ejected fluid stay behind the leading vortex ring. Actually, the maximum circulation that a vortex ring can attain, occurs at $L_p/D_p \approx 4$ which is

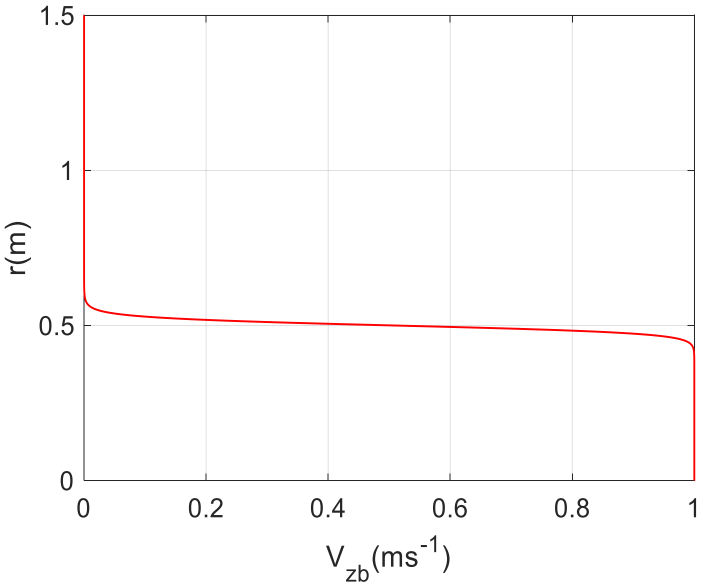

Figure 5.3: Classical hyperbolic tangent profile, V_{zb}.

referred as **formation number** [Gharib et al., 1998] and after that, as the stroke ratio increases, the leading vortex ring sheds excessive ejected fluid behind. Also, all the quantities in the present study are normalized by D_p and U_p as the characteristic length and velocity, respectively. Also, D_p/U_p is used to normalize the time.

In order to ensure the accuracy of our numerical program, we simulate the Danaila and Helie's [Danaila and Hélie, 2008] injector and present the results in Fig. 5.5 where a good agreement can be observed between our results and Danaila and Helie's [Danaila and Hélie, 2008] study. In this figure, r is the normalized radial distance from the center of piston outlet and V_z is the normalized axial velocity.

5.4 Results & Discussion

In this section, the effects of the vortex ring parameters on the received signal is discussed. We considered 3 different injection velocities 1, 2.5, and 5 m/s; seven stroke ratios 1, 2, 3, 4, 6, 10, and 14, and two τ_1 0.5 and 0.7. At first and as an illustration, we demonstrate the vortex ring and puff contours to better visualise the the ISI difference for two different stroke ratios. Then, we will discuss how the vortex parameters will affect the SIR. Finally, we show the sequential vortex rings and their potential for consecutive molecular transmission.

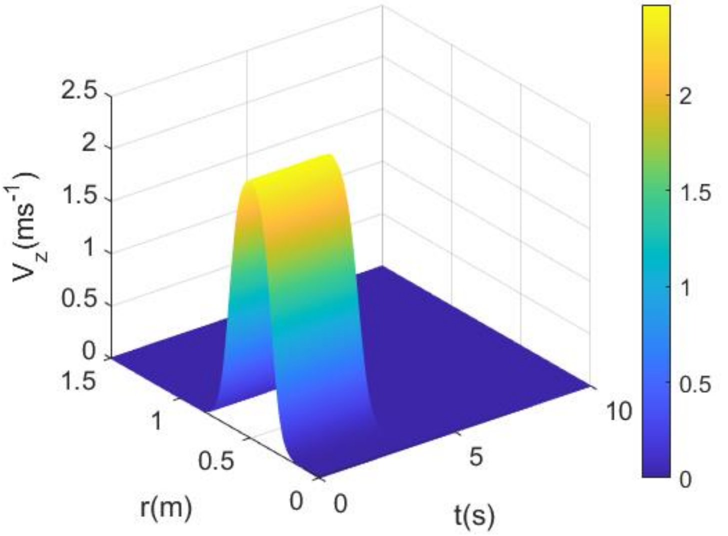

Figure 5.4: Prescribed axial velocity of the piston to generate vortex ring.

5.4.1 Transmission

The simulations are conducted using industrial standard COMSOL software (see Section 3.2). A sequence of puffs and vortex rings are shot. The forward concentration (space domain) profiles is shown in Fig. 5.6. Each received signal is given by: $c(t) = \sum_k^K a_k h(t - kT)$, where a is 1 or 0 (OOK), T is the symbol period, and the channel $h(\cdot)$ is a complex fluid dynamic channel described by the RANS equations to solve for the turbulence effects.

It is worth noting that under RANS, these are the averaged profiles over a small simulation element. We assume that the vortex rings are sufficiently separated such that each behaves independently.

Puff Sequence - Fig. 5.6(a-i) shows the concentration profile, where there is a rapid deterioration in concentration structure and intensity over distance. As such, the tail from prior symbols leads to strong ISI. Fig. 5.6(a-ii) is the 3D concentration profile and reveals that there is not a specific circular ring in the environment and the tail of the puff remains in the environment for the whole period of transmission.

Vortex Ring Sequence - The results in Fig. 5.6(b-i) show that the vortex ring core has a high concentration compared to the quiescence environment and maintains this into distance. This means that the vortex ring is carrying the momentum of the transmitter and is dominant in the way it propagates through the environment. Fig. 5.6(b-ii) shows the concentration profile in three dimensional,

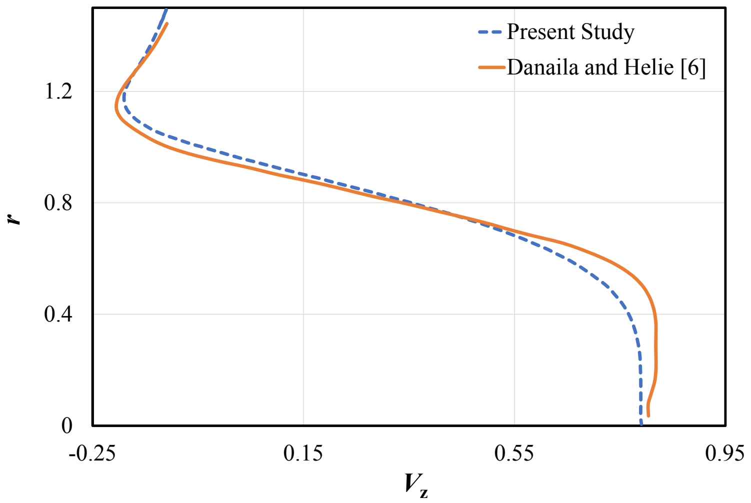

Figure 5.5: Validation of present study with Danaila and Helie's study [Danaila and Hélie, 2008].

where high concentration is maintained and the ISI effects are small. Overall, we observe that the ISI tail is significantly lower for the vortex ring.

We also present a proof-of-concept demonstration of the vortex ring, being shot 20 m into an uncontrolled environment in Fig.5.6(c). We have a 0.5 m diameter vortex canon that is shooting a vortex ring captured on a slow motion camera. The red rings label the location of the vortex ring as it propagates away from the canon. The vortex ring becomes clearer as it moves into the distance.

5.4.2 Effects of Stroke Ratio on CIR

In this section, the effects of the stroke ratio (L_p/D_p) at the time of vortex ring generation on the CIR is discussed. The receiver is observing receiver and it located $3 \times D_p$ downstream of the transmitter. As can be seen, by increasing the stroke ratio, the CIR changes severely. The reason is that when we increase the stroke ratio, more molecules will be ejected into the channel with a constant velocity. This will push high concentration molecules further downstream of the channel. It is more clear in figures 5.7(c) and 5.8(c) where the injection velocity of 5 m/s and stroke ratio of 14 do not let the fluid to be separated from the central ring area. Under this circumstance, the central ring area acts like a carrier and it translates the lump of molecules to the downstream of the channel. Furthermore, we can observe from figures 5.7 and 5.8 that by increasing the stroke ratio, the ISI increases. Thus, it appears that increasing stroke ratio hinders the detection of the received signal. On the other hand, when

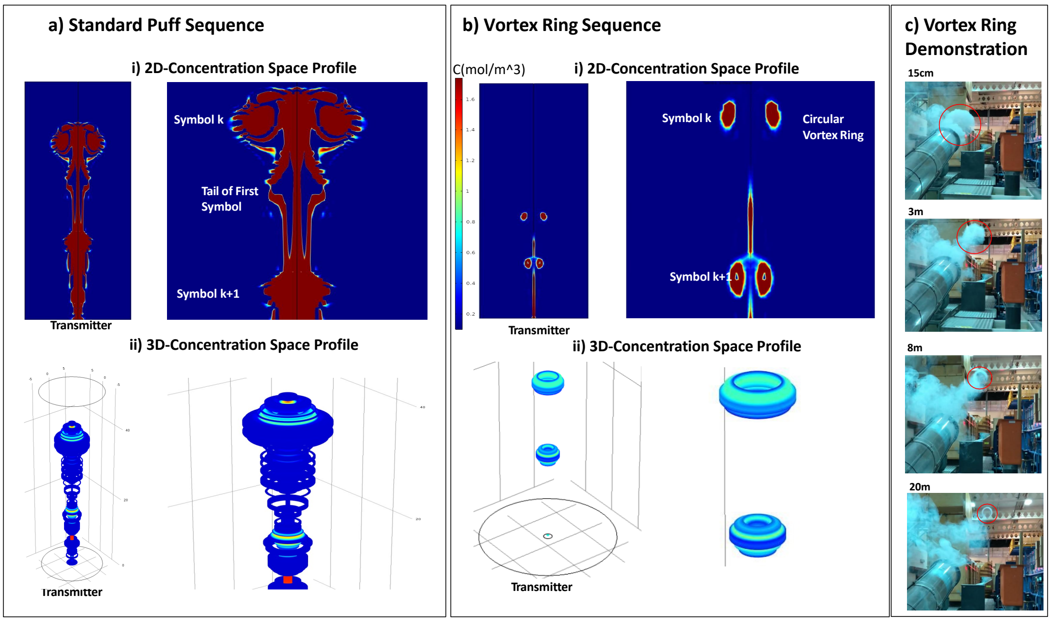

Figure 5.6: Sequential symbols transmitted, (a) puffs, (b) vortex Rings, and (c) experimentation of Vortex Rings.

we have a high stroke ratio, we can see that the peak of the received signal increases which is favorable. Thus, we cannot isolate the signal strength or ISI and discuss about the effects of the stroke ratio on the received signal quality. For this purpose we need to consider that SIR. In the section 5.4.4, this quantity will be measured for different stroke ratios.

5.4.3 Effects of Injection Velocity on CIR

The effects of the injection velocity on the CIR is illustrated in figures 5.9 to 5.15. As can be seen in these figures, by increasing the U_p, the amplitude of the CIR increases for all stroke ratios. The reason behind this is that when we have high injection velocity, the amount of the circulation that a vortex ring can attain is high. Thus, the vortex ring retains its shape for longer distance downstream of the transmitter. Furthermore, by increasing U_p, the ISI decreases which is desirable in terms of signal detection. Another important observation is the effects of τ_1 on the CIR. As can be seen, CIR does not change by changing the τ_1. This means that the physical acceleration/deceleration of the piston does not affect the CIR. Also, for the stroke ratios greater than 4, the ISI increases significantly. This can be observed in fig. 5.12. This stroke ratio is called formation number and it is proved that for the

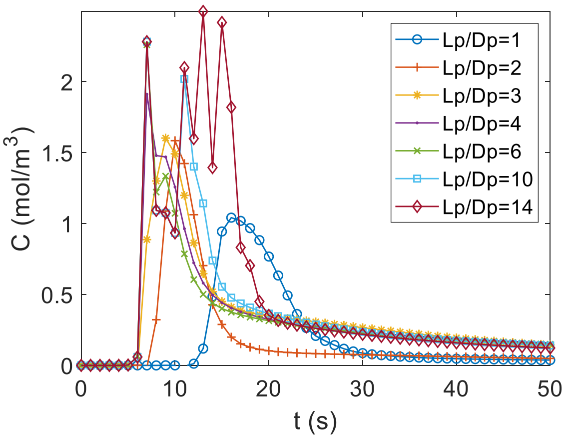

(a) $U_p = 1\,\mathrm{ms}^{-1}$

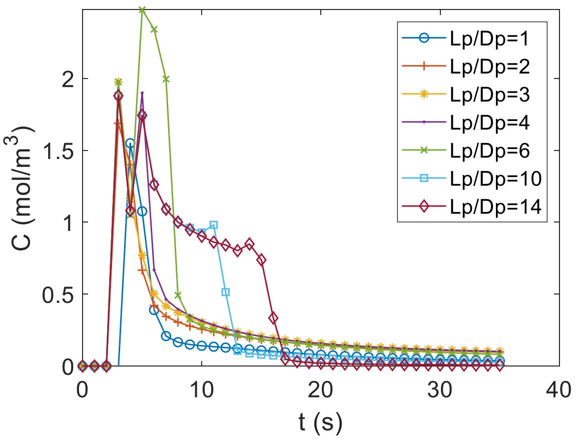

(b) $U_p = 2.5\,\mathrm{ms}^{-1}$

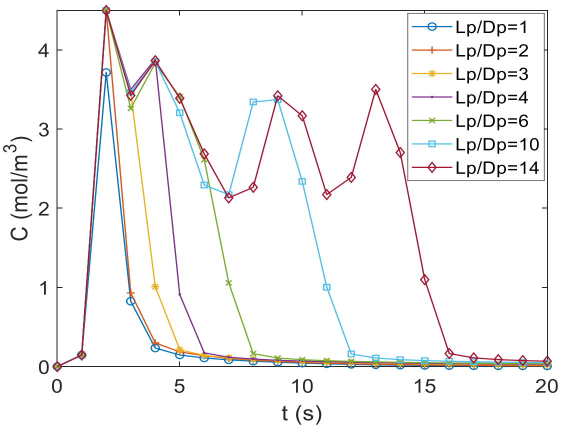

(c) $U_p = 5\,\mathrm{ms}^{-1}$

Figure 5.7: Received concentration profile of the vortex ring in τ_1=0.5 and for different piston velocities and stroke ratios.

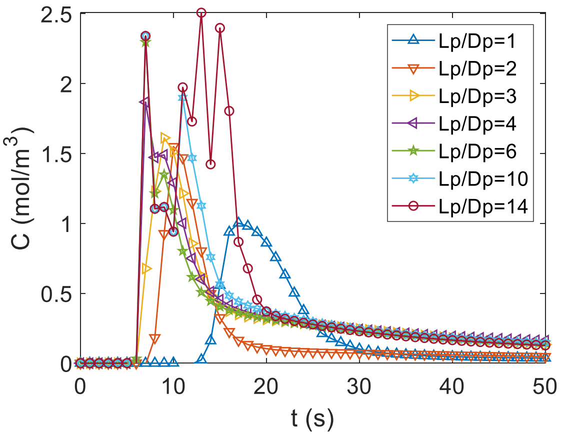

(a) $U_p = 1\,\mathrm{ms}^{-1}$

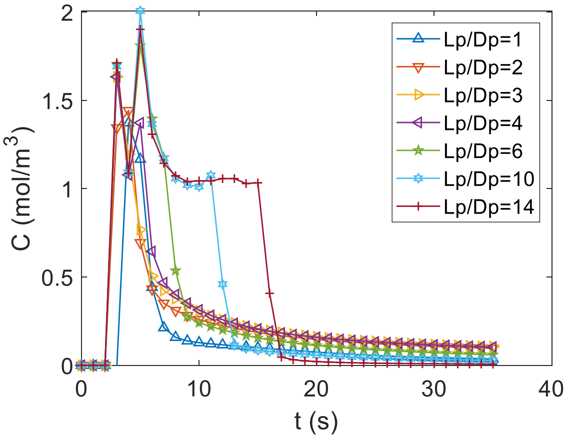

(b) $U_p = 2.5\,\mathrm{ms}^{-1}$

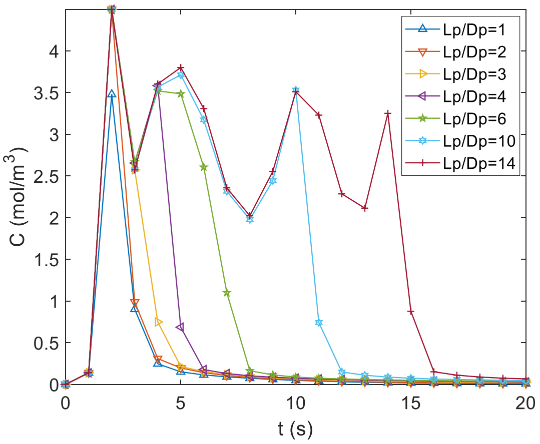

(c) $U_p = 5\,\mathrm{ms}^{-1}$

Figure 5.8: Received concentration profile of the vortex ring in τ_1=0.7 and for different piston velocities and stroke ratios.

stroke ratios greater than the formation number, the vortex ring is not able to attain more circulation [Gharib et al., 1998]. This means that this formation number can be considered as boundary between formation of the vortex ring and puff.

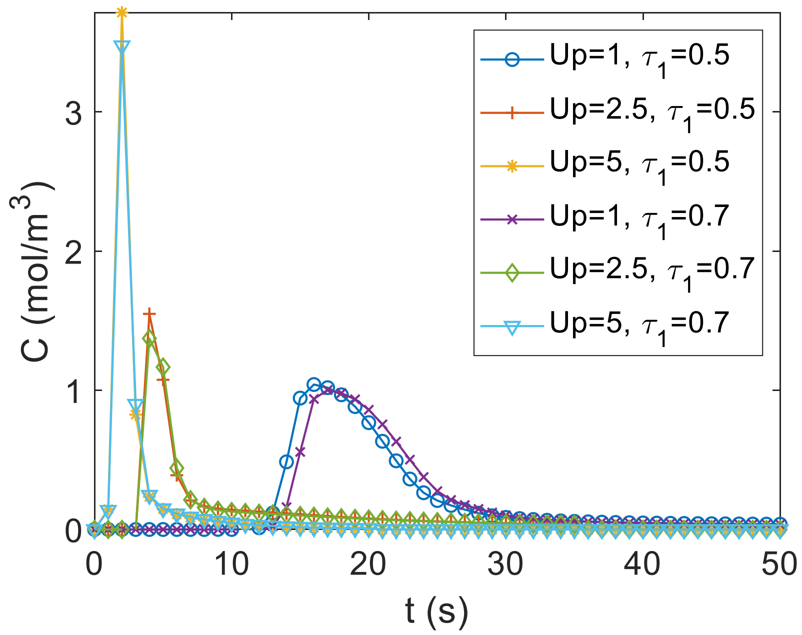

Figure 5.9: Received concentration profile of the vortex ring for Lp/Dp=1 and in different piston velocities.

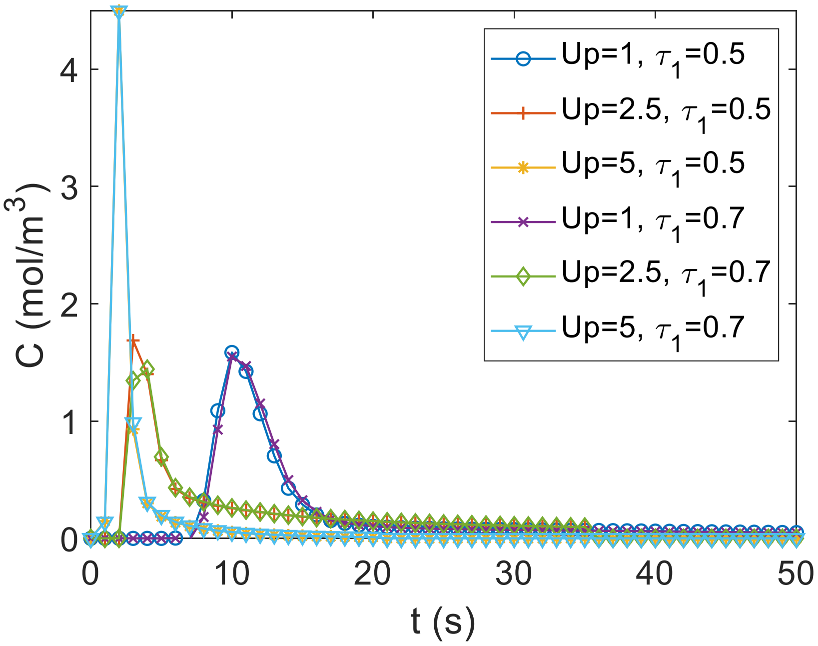

Figure 5.10: Received concentration profile of the vortex ring for Lp/Dp=2 and in different piston velocities.

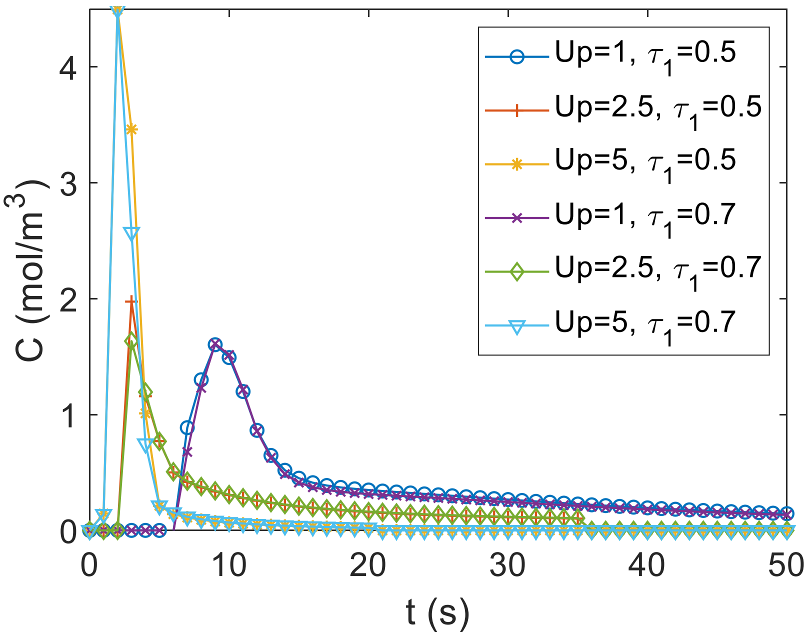

Figure 5.11: Received concentration profile of the vortex ring for Lp/Dp=3 and in different piston velocities.

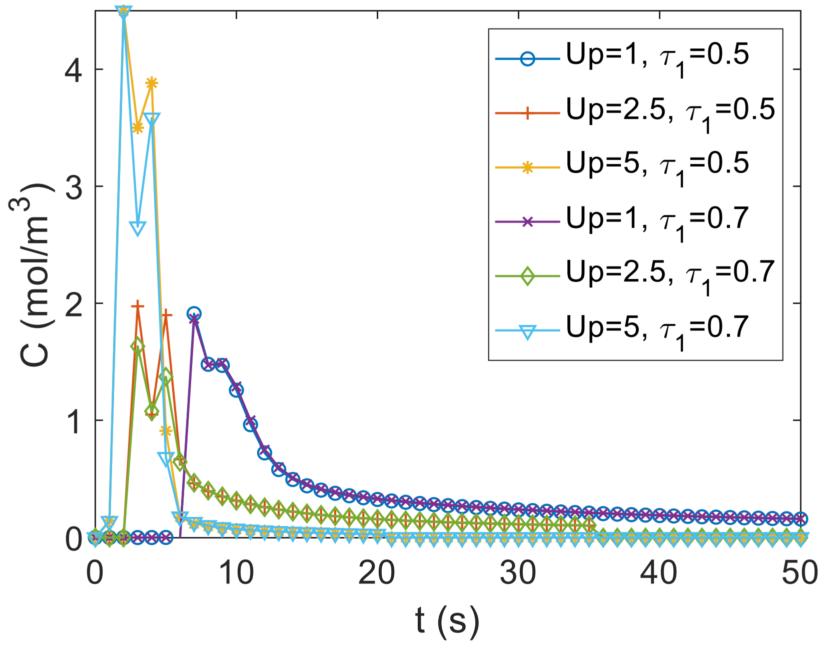

Figure 5.12: Received concentration profile of the vortex ring for Lp/Dp=4 and in different piston velocities.

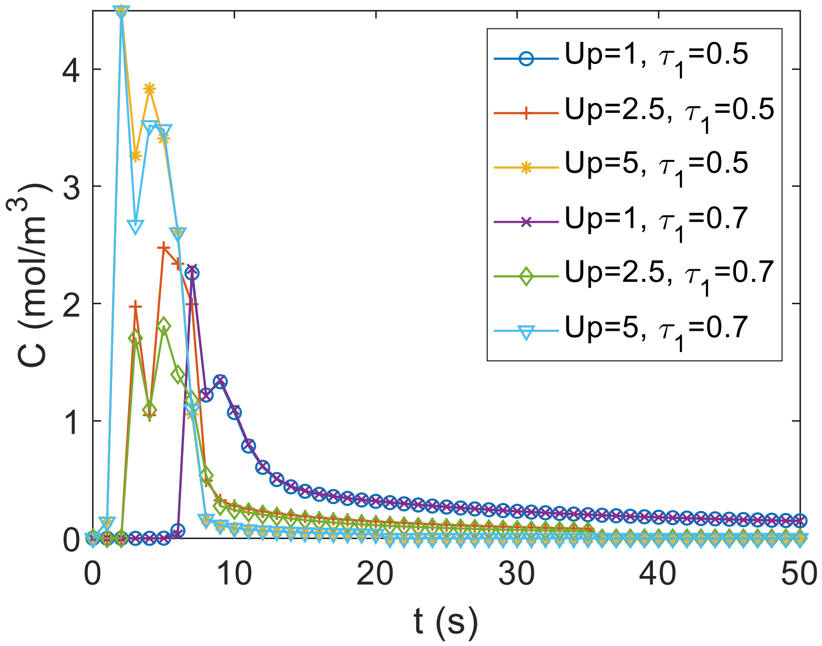

Figure 5.13: Received concentration profile of the vortex ring for Lp/Dp=6 and in different piston velocities.

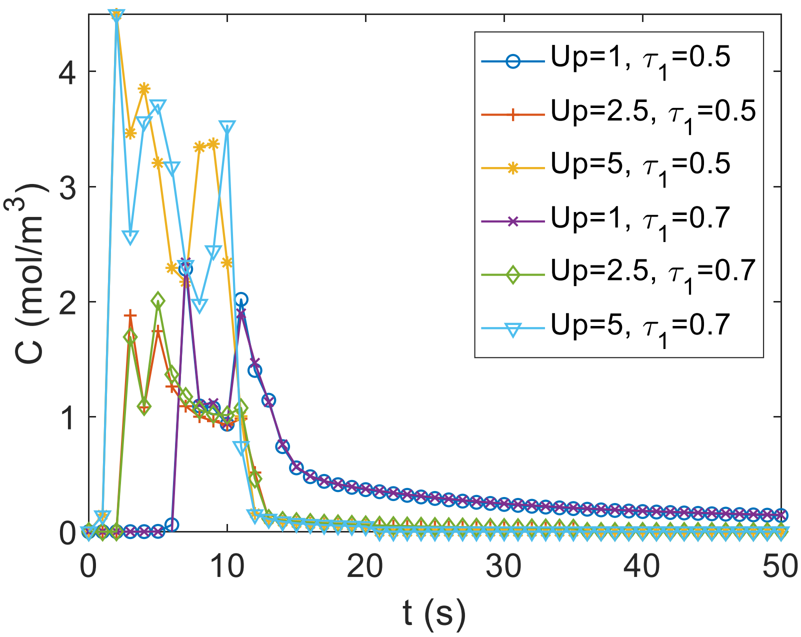

Figure 5.14: Received concentration profile of the vortex ring for Lp/Dp=10 and in different piston velocities.

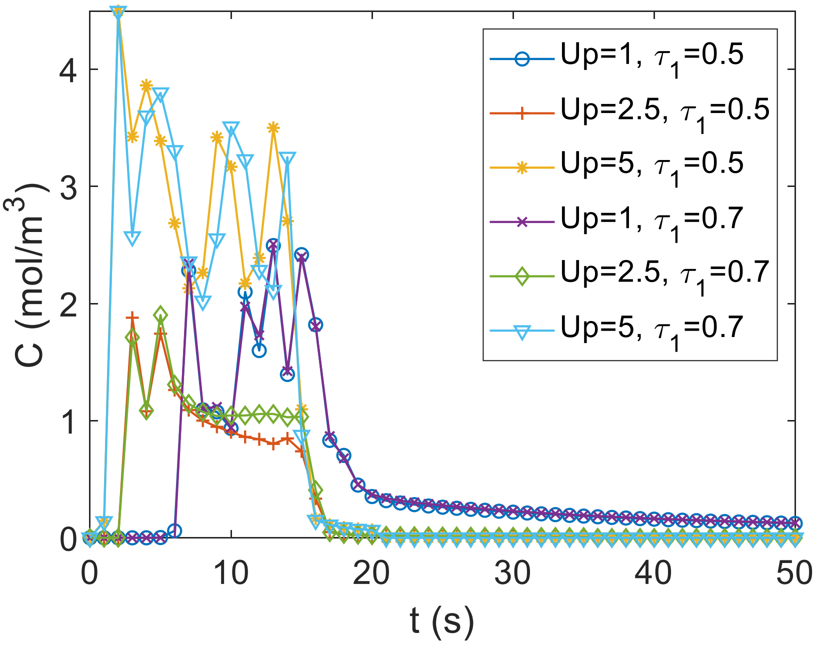

Figure 5.15: Received concentration profile of the vortex ring for Lp/Dp=14 and in different piston velocities.

5.4.4 Signal-to-Interference Ratio (SIR)

As mentioned in previous section, in order to see the effects of the stroke ratio and injection velocity on the received signal, both of the signal strength and ISI should be considered simultaneously. Thus, in this section we illustrate the variation of the metric SIR with stroke ratio and injection velocity. For the received signal with empirical response $h(t)$, we define the signal $S = \int_0^T h(t)\,\mathrm{d}t$ as the aggregate peak concentration values detected over symbol period T. We define the ISI as $I = \sum_k \int_0^T h(t+kT)\,\mathrm{d}t = \int_T^{+\infty} h(t)\,\mathrm{d}t$ as the remaining tail concentration $t > T$. As can be seen in fig. 5.16, by increasing the stroke ratio, the SIR degrades continuously. Furthermore, increasing the velocity leads to the higher signal amplitude and as a result, the SIR increases.

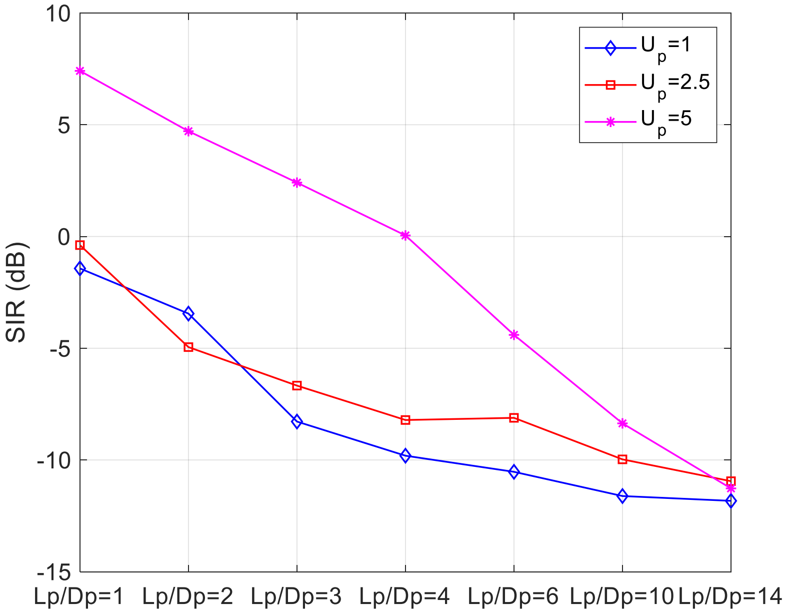

Figure 5.16: SIR of the vortex signal for different piston velocities and τ_1=0.5.

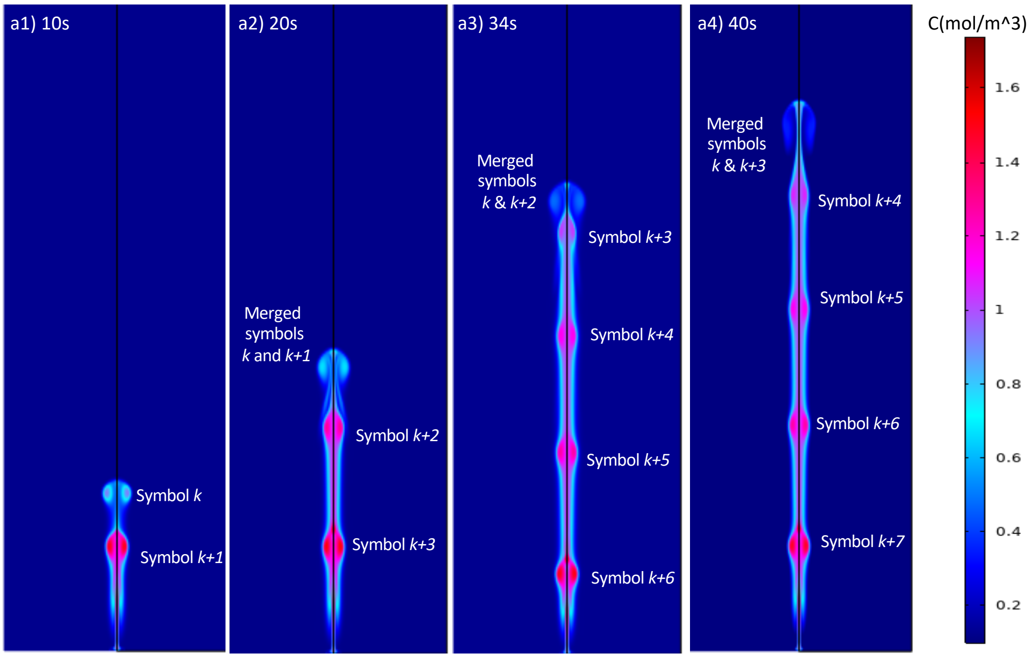

Figure 5.17: Demonstration of sequential vortex ring symbol transmission observed at different times.

5.4.5 Sequential Vortex Rings

In this section, eight vortex rings is transmitted in order to observe the effects of the each vortex ring on the others and to see how a sequence of information can be carried by vortex rings with minimum interference and maximum symbol rate. Parameters: $U_p = 5\,\mathrm{m/s}$ and the $L_p/D_p = 1$. The vortex rings concentration profiles are displayed in Fig. 5.17 at four different time snapshots after transmission. After 10 s (Fig. 5.17(a)), we can see that the second vortex ring $k+1$ catches up to the first k, due to the lower drag forced faced by the second, and merge at 20 s. This also repeats for symbols $k+2$ and $k+3$. As a consequence, when the symbol period is small, the first four vortex rings will merge together (Fig. 5.17(c-d)). However, subsequent vortex rings remain separated and can be detected coherently. This seems to indicate that an initial sacrifice of 4 symbols is needed to clear the channel up to the $50D_p$ critical distance, allowing subsequent symbols to propagate coherently. Any longer distances and the vortex rings become unstable. As such, we may regard the first 4 symbols as pilot symbols to sense the channel or communicate non-data bearing information. In contrast, if we consider the receiver at a critical distance (for example in this simulation setup, the critical distance is $10D_p$), the merging would not be happened and the receiver can detect each symbol separately.

5.5 Summary

In this chapter, we demonstrate how packing information in vortex rings can effectively mitigate ISI using CFD numerical simulation and proof-of-concept experimentation. We show that the vortex ring generation parameters such as stroke ratio of the cylinder and piston and the injection velocity will affect the CIR and SIR. We showed that by increasing the stroke ratio and the injection velocity, the SIR decreases and increases, respectively. We defined a threshold of $L_p/D_p = 4$ in which for the $L_p/D_p < 4$ the effects of the ISI is minimum but for the stroke ratios greater than this value, the ISI affects the received signal severely.

Furthermore, in this chapter we saw that even though the vortex rings performs better than puffs, a sophisticated method is required to generate the vortex rings. Thus, in the following chapters we focus on the puffs that are easy to generate and helps us to model the macro-scale MC channels for more realistic cases. In the next chapter, we will first prove that the TDMC channel is linear and in the following chapters, we will characterise the noise and mutual information in TDMC channels.

Chapter 6

Linearity of Turbulent Diffusion Channel

In the previous chapter we observed that how the vortex rings can improve the SIR in the macro-scale MC channels. This happens at the expense of generating such structures which requires sophisticated methodology. Thus, considering normal puffs for transmitting information is more practical compared to the vortex rings. Any injectors (Tx) with an arbitrary amount of shear stress can generate puffs. Therefore, in this chapter and the following chapters, we will only focus on the TDMC channels where the information are encoded on the puffs rather than vortex rings. Before characterising the noise and mutual information in TDMC channels, we need to make sure whether these kinds of channels are linear or not. Since the turbulence forces are highly non-linear, we expect to see the non-linear channels. There is a nuance difference between the definition of linearity in fluid mechanics and communication theory that has to be taken into account. In fluid mechanics, the non-linearity comes form the Navier-Stokes equations that we explained in chapter 3. This means that the Navier-Stokes equations are mathematically non-linear. In communication theory, the linearity means that for the the transmitted signal x, if we have $x_1 + x_2 = y_1 + y_2$, then $a_1x_1 + a_2x_2 = a_1y_1 + a_2y_2$. In this chapter, we will focus on the linearity concept from the communication point of view.

6.1 Motivation

In this chapter, we use CFD simulation to show that sequential TDMC signals linearly combine. This is a non-trivial and non-intuitive result and our conclusion allows the research field to leverage on existing linear combining signal analysis. To ensure robustness of our results, we test for the received signal strength and ISI under different concentrations, co-flow rate, and the information sequence. Also, we introduce a basis for the channel model in a way that for any k sequential signals in which $k \geq 4$, by understanding the $1 \leq k \leq 3$ signals and the last signal, the other signals can be represented.

6.1.1 Review of Similar Works

In general, the MC application environment can be classified into two broad regimes. In the micro- to nano-scale regime, mass diffusion dominates propagation and the vast majority of current literature [Guo et al., 2016b]. For a mass diffusion-dominated MC channel, we assume that the molecular trajectories are independent and identically distributed, which gives rise to linear combining at any given point. As such, this makes signal and ISI analysis linear [ShahMohammadian et al., 2012; Garralda et al., 2011].

In this chapter, we consider the turbulent diffusion regime whereby the Pe is large. In this case, when the flow (co-flow) dominates the propagation mechanism, turbulence can become a dominate factor (high Reynolds number) and the analysis becomes non-trivial. This is typical in pheromone communications between animals and plants [Unluturk and Akyildiz, 2017a], underwater signaling [Lanzagorta, 2012], and in heavy industry applications (e.g. chemical plants). In past laboratory experiments [Farsad et al., 2013; Atthanayake et al., 2018], preliminary findings indicate potential non-linearity, but the causal mechanisms are not well understood [Farsad et al., 2014]. Later work have attempted to both characterize non-linear turbulent effects in a stationary environment [Unluturk and Akyildiz, 2017a] and embed information optimally in turbulent structures [Kennedy et al., 2018].

To continue this line of research, we employed the CFD module in COMSOL (see Section 3.2) to simulate and analyse the degree of non-linearity in the turbulent diffusion propagation for sequential signal pulses.

6.2 System Model

Molecular communication via turbulent diffusion system is at least composed of a Tx node, environment, the MMs, and the Rx node (see Fig. 6.1). We consider turbulent diffusion as the carrier mechanism since it is the most realistic model for real life applications [Davidson, 2015]. In turbulent diffusion, the effects of the molecular diffusion are negligible and the eddy diffusivity effects are responsible for transporting the MMs.

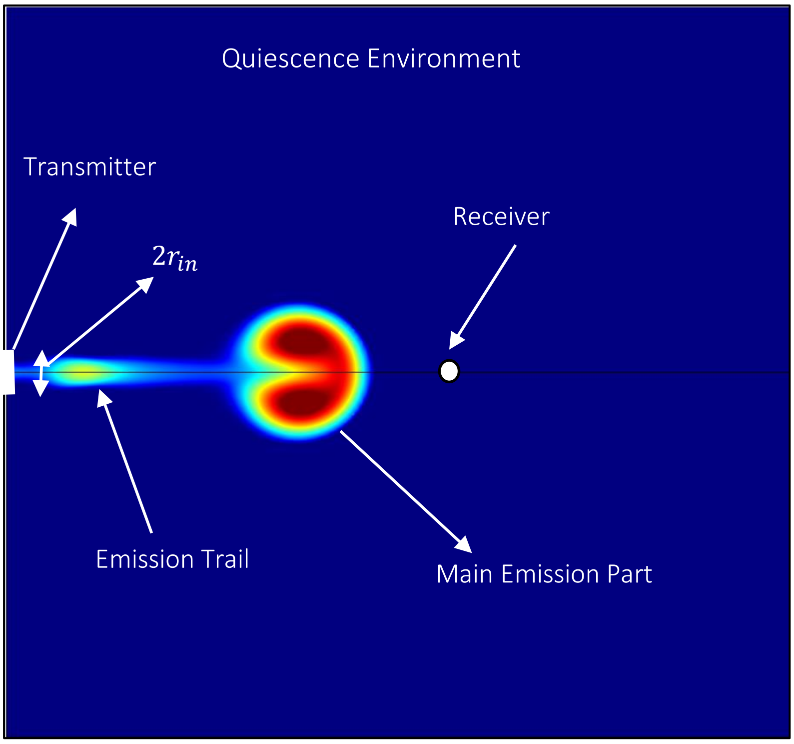

Figure 6.1: Schematic of the system model showing the quiescence environment, the transmitter, the receiver, and the emitted molecules.

The system model is comprise of an injector which releases the water molecules into the quiescence aqueous environment with the velocity of u_{in} (see Fig. 6.1). The radius of the injector is r_{in}, and in order to simulate the motion of the injector piston, a hyperbolic function is defined at the inlet boundary. The flow domain is $10 \times 6\,\mathrm{m}^2$, and the lateral boundaries are $60 \times r_{in}$ far from the transmitter and the outlet is located $200 \times r_{in}$ away from the transmitter, so their effects on the flow field and emitted molecules are negligible. The distance between the transmitter and the receiver is considered as $60 \times r_{in}$, and the concentration of the molecules are measured at the observing receiver. It is noteworthy that during the propagation of the molecules the main deriving process is governed by the turbulent diffusion. The properties of the water and the other system parameters are given in Table 6.1.

Table 6.1: Simulation parameters for linearity analysis

Variable	Value
Maximum injection velocity, u_{in}	$2\,\mathrm{m/s}$ at $t = 0$
Kinematic viscosity of water, ν	$1 \times 10^{-6}\,\mathrm{m^2/s}$
Density of water, ρ	$1000\,\mathrm{kg/m^3}$
Transmit concentration, c_0	$1\,\mathrm{mol/m^3}$
Pulse width, T_0	$0.7\,\mathrm{s}$
Radius of the injector (r_{in})	$10\,\mathrm{cm}$
Distance between Tx and Rx, $d_{Tx,Rx}$	$60 \times r_{in}$
Simulation space length	$200\,r_{in}$
Simulation space width	$60\,r_{in}$

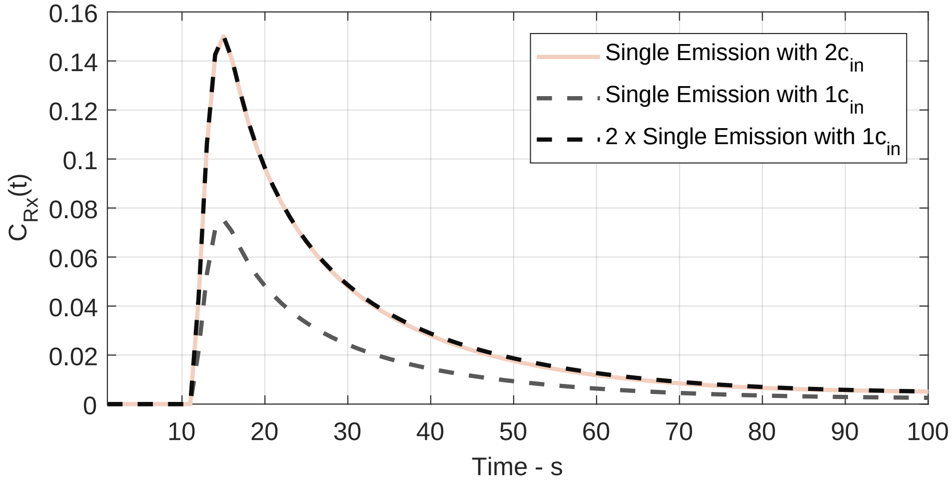

Figure 6.2: CIR for a single emission.

6.3 Non-linearity Analysis

The non-linearity of the TDMC channel is investigated in two scenarios: single emission and consecutive emissions:

6.3.1 Single Emission Scenario

In this scenario, at first we release water molecules with the concentration of c_{in} and in the second case, we emit $2 \times c_{in}$ concentration. Then, we double the observed concentration for the c_{in} emission and finally compare them with the $2 \times c_{in}$ concentration. In Fig. 6.2, concentration versus time is illustrated. Output of the CFD simulator shows that the CIR has the multiplicative property, which holds for infinitely many different cases with the same Reynolds number due to the non-dimensional solution.

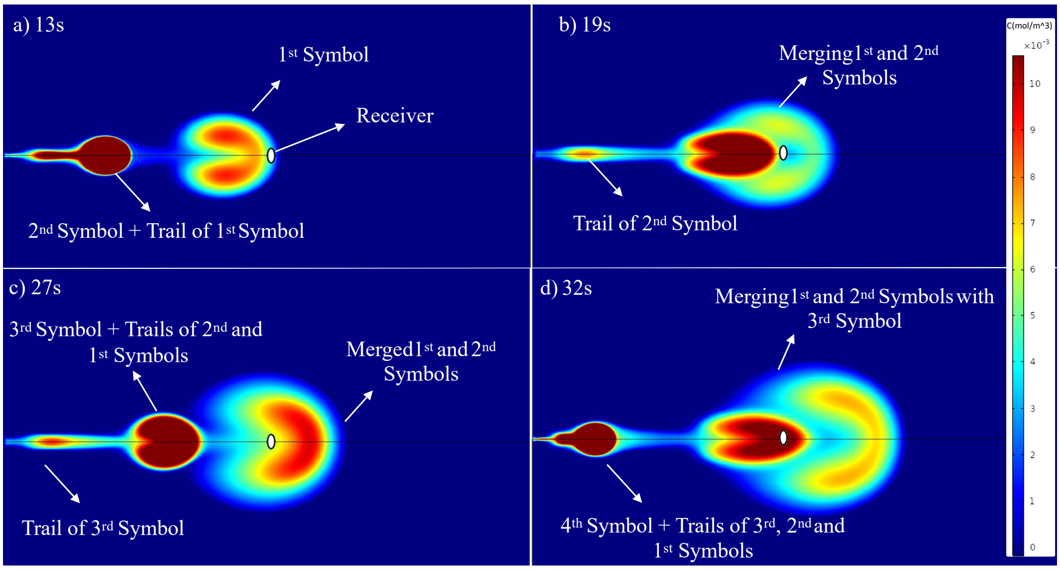

Figure 6.3: Snapshots of the environment and the emitted molecules at different time instances for consecutive emissions. New emissions sweep the tails of the previous emissions.

6.3.2 Scenario with Consecutive Emissions

Sequential emissions of marked water molecule types are released to see the channel response of the n-th emission. In Fig. 6.3, we can see that the second emission sweeps the tail of the first emission and this behaviour is also seen in the other subplots of the Fig. 6.3. The outcome of this behaviour is that some of the emitted molecules reach to the receiver lately and we have two or more peaks in the concentration profile at the receiver for the same molecule type (see Fig. 6.4). It should be mentioned that when we have only one emission like Fig. 6.2, we cannot observe the second and smaller peak as far as there is no other emission afterward that sweeps the tail of the previous emission. If there is no successive emissions that pushes the tail, the tail of the emission does not arrive to the receiver and remains in the environment (see Fig. 6.1).

In Fig. 6.4, time versus the received concentration is shown for the scenarios without and with co-flow. First critical observation is that there are four different classes of emissions in terms of CIR. First emission is different than the other emissions since the environment is quiescence and the first emission should overcome a higher drag force compared to the other emissions. The concentration at the receiver due to the first emission has two significant modes: the main and the tail parts (see Fig. 6.3 for contour plots for sequential emissions). The effect due to tail

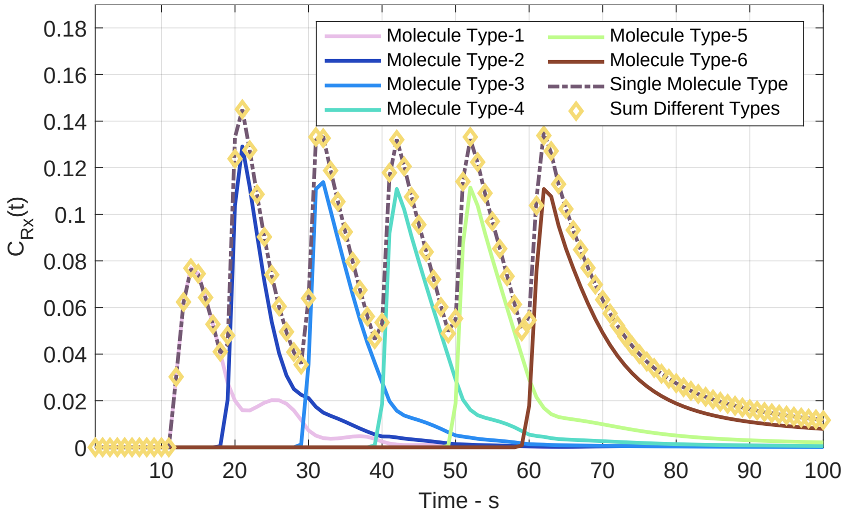

(a) $u_{co} = 0\,\mathrm{ms}^{-1}$

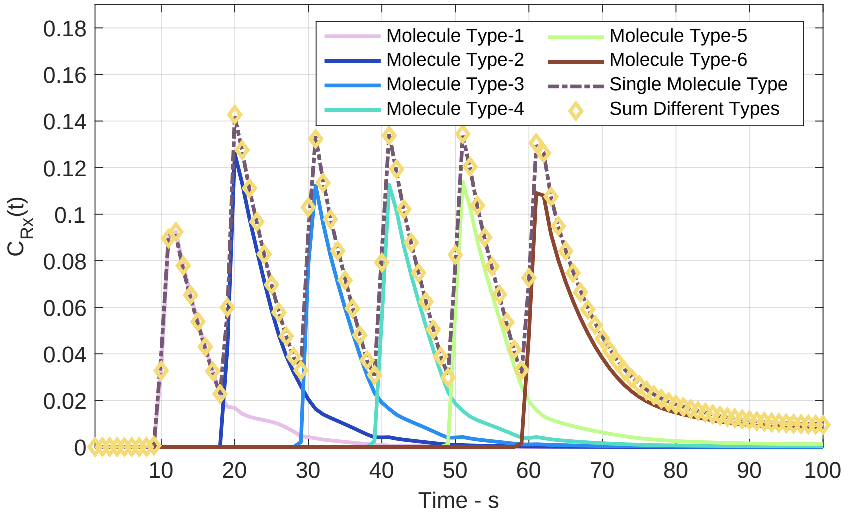

(b) $u_{co} = 0.02\,\mathrm{ms}^{-1}$

Figure 6.4: Received concentration for six consecutive emissions. Molecule types are changed for distinguishing the effect of each emission. Scenarios (a) without co-flow and (b) with co-flow are considered. Red dashed curve corresponds to emission of single type molecule and the blue dashed curve corresponds to sum of six consecutive emissions with different molecule types.

decreases when there is a co-flow in the environment. Second emission is unique (i.e., it has a higher peak value compared to other emissions) since it experiences less drag force compared to the first emission and most of the molecules can easily penetrate through the environment. Also, the second emission is more compact when it meets the receiver compared to the other emissions. By comparing the Fig.

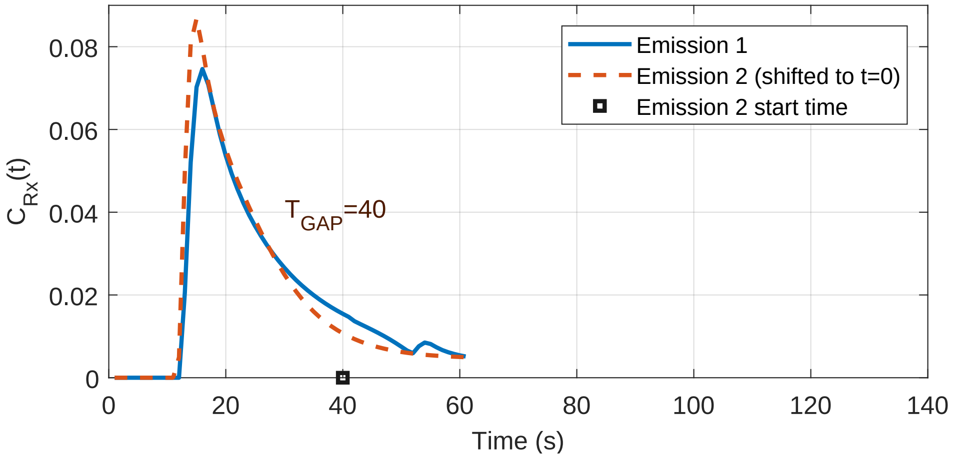

(a) $T_{\mathrm{GAP}} = 40\,\mathrm{s}$

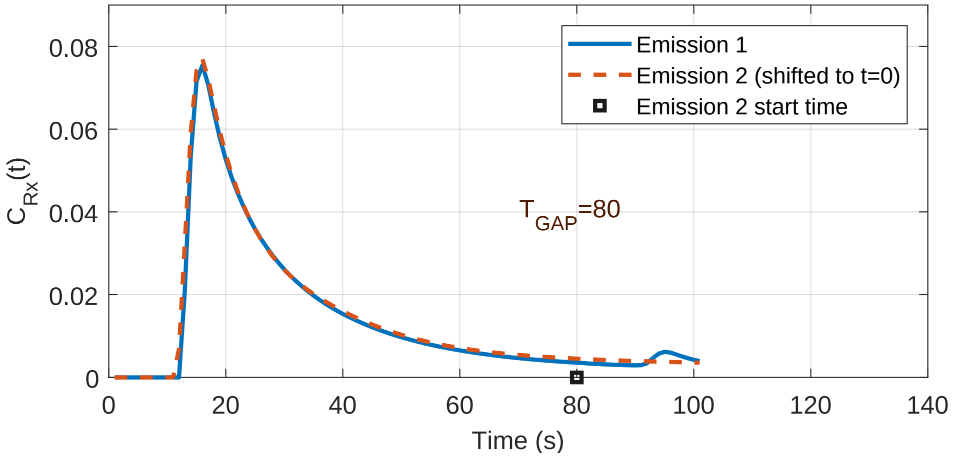

(b) $T_{\mathrm{GAP}} = 80\,\mathrm{s}$

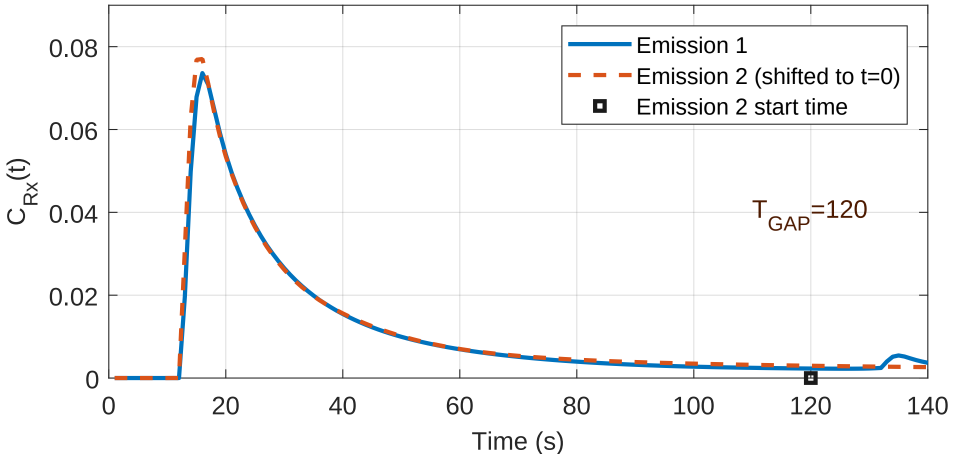

(c) $T_{\mathrm{GAP}} = 120\,\mathrm{s}$

Figure 6.5: Envelop analysis with considering two emissions with a time gap. The first emission is released at $t = 0$ and 40, 80, and 120 s after that, the second emission is released. The second emission is shifted to $t = 0$.

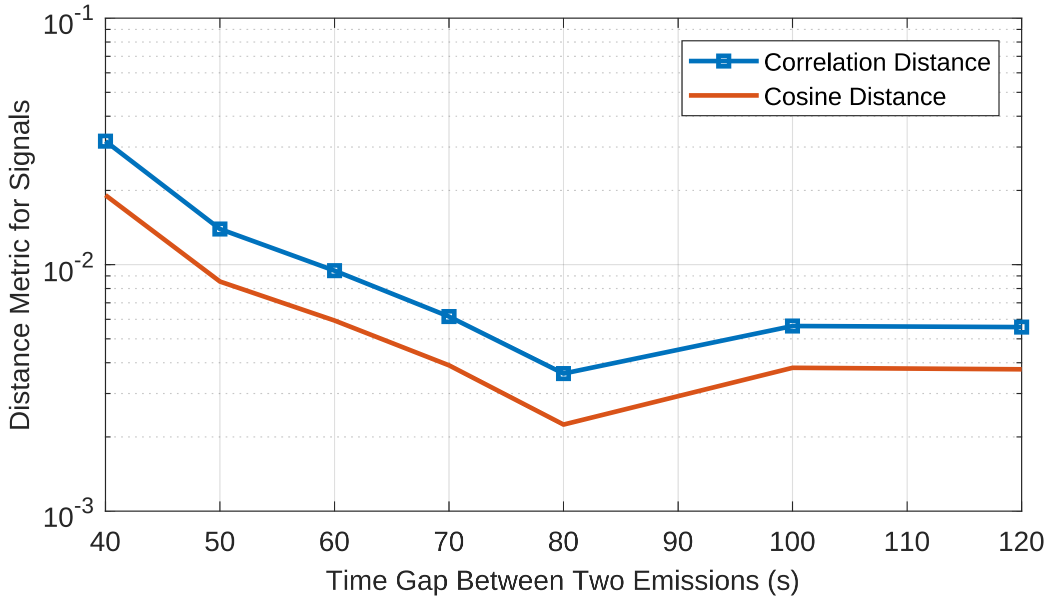

Figure 6.6: Correlation and cosine distance between the two received signals with different time gaps.

6.3(b) and Figs. 6.3(c) and (d), it can be observed that the second emission is more compact than the third and fourth emissions and as a result, the concentration of the molecules in second emission is more than the others. The last emission has different characteristics since there is no other following emission that pushes off the molecules. The rest of the emissions (i.e., the third, fourth, and the fifth for the six emission scenario in Fig. 6.4) have similar structure.

In Fig. 6.4, we also observe that the sum of the six CIRs due to the sequential emissions gives nearly the same when a single molecule is utilized. This additive property enables us to model the received signal (including interference).

6.3.3 Signaling Envelop Analysis

Signaling envelop shows the time required for having similar channel with the first emission. In other words, it represents the required time to have a clear channel that does not contain any molecules from previous emissions. To do so, we released one emission and waited for 40, 80, and 120 s before releasing the second emission. After receiving both signals at the receiver, the second signal which is associated to the second emission is shifted to $t = 0$. Figure 6.5 illustrates the received signals of the first emission and time shifted of the second emission. According to this figure, both received signals are overlapped when the time difference between the emissions is 80 s and more. In order to quantify the similarity level of the two received signals, correlation distance and cosine distance are calculated. Correlation distance is parameter that shows the distance between two random variables with finite variances. If the correlation between two random variables is x, then their correlation distance is defined as $d_1 = 1 - x$. Similar to correlation distance, the cosine similarity is a measure of similarity between two non-zero vectors of an inner product space. If cosine similarity is y, cosine distance is equal to $d_2 = 1 - y$. As the correlation between two random variables increases, the d_1 is reduced and when the cosine similarity increases, two vectors get closer. Figure 6.6 shows the correlation distance and cosine distance between the two received signals with three different time gaps. As can be observed from this figure, after $T_{GAP} = 100\ s$ both of the distance metrics (correlation distance and cosine distance) do not change with time. This means that if two successive symbols are released with less than 100 s time difference, the second symbol would interfere with the former one and the ISI needs to be taken into account.

6.4 Interference Modeling

Due to the additive property, we can introduce the channel model by considering the summation of the effect of sequential emissions. For this purpose, we use a model function for the received signal at a given point (x, y) with some control coefficients as follows:

$$c^{\mathrm{mdl}}(t|x,y) = \begin{cases} b_1 \frac{\sqrt{x^2+y^2}}{t^{b_2}} e^{-b_3 \frac{x^2+y^2}{t}} & \text{for } t > 0 \\ 0 & \text{otherwise} \end{cases} \tag{6.3}$$

where b_1, b_2, and b_3 are fitting parameters. The model function in (6.3) has the similar structure with the diffusion equation in 2D environment [Jackson, 2006]. After we run simulations with COMSOL, we fit the received signal classes/types with (6.3) and obtain the fitting parameters for each class.

We observe four different classes of received signal patterns in Fig. 6.4. We leave the first emission as is (i.e., we used the empirical result c_1^{emp}) and fit the other three classes: $c_2^{\mathrm{mdl}}(t)$, $c_{\mathrm{last}}^{\mathrm{mdl}}(t)$, and $c_{\mathrm{mid}}^{\mathrm{mdl}}(t)$. Hence, the set forms a basis for our modeling which is equal to $\mathscr{B}_c = \{c_1^{\mathrm{emp}}(t),\, c_2^{\mathrm{mdl}}(t),\, c_{\mathrm{mid}}^{\mathrm{mdl}}(t),\, c_{\mathrm{last}}^{\mathrm{mdl}}(t)\}$. After obtaining the basis $\mathscr{B}_c$, for a case with K emissions in T_s-long symbol durations ($K \geq 4$), the

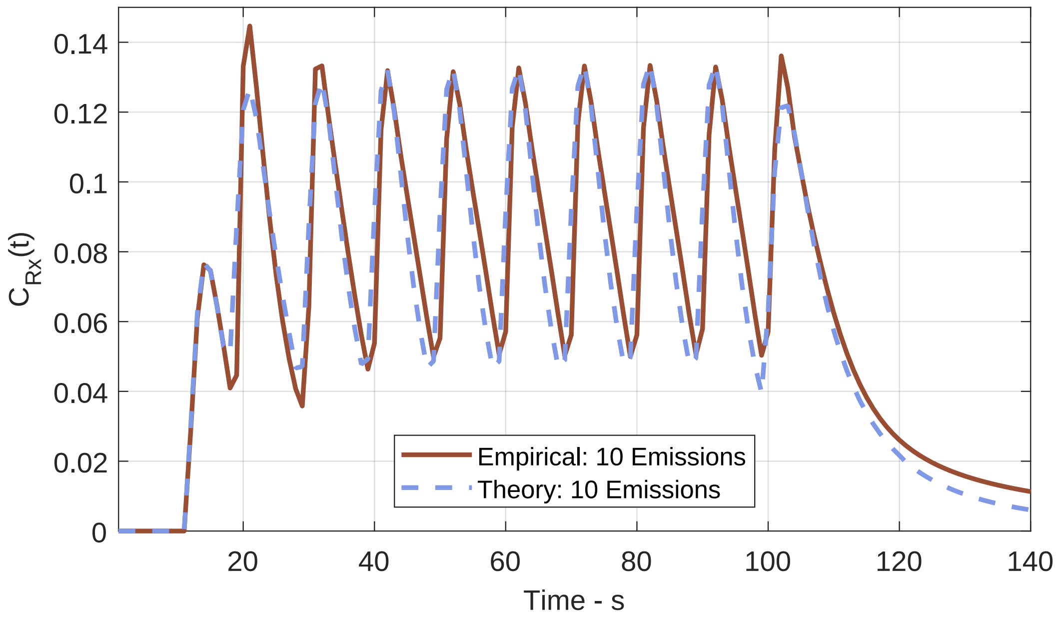

Figure 6.7: Empirical and theoretical received concentration for 10 sequential emissions. Theoretical received signal is obtained by using the fitted base functions and (6.4).

received signal is given in (6.4).

$$C_{\mathrm{Rx}}(t) = \begin{cases} c_1^{\mathrm{emp}}(t) & \text{If } t \in [0, T_s) \\ c_1^{\mathrm{emp}}(t) + c_2^{\mathrm{mdl}}(t - T_s) & \text{if } t \in [T_s, 2\,T_s) \\ c_1^{\mathrm{emp}}(t) + c_2^{\mathrm{mdl}}(t - T_s) + \sum\limits_{i=0}^{j-2} c_{\mathrm{mid}}^{\mathrm{mdl}}(t - (j-i)T_s) & \text{if } t \in [j\,T_s, (j+1)\,T_s) \text{ for } 2 \le j \le K-2 \\ c_1^{\mathrm{emp}}(t) + c_2^{\mathrm{mdl}}(t - T_s) + \sum\limits_{i=1}^{j-2} c_{\mathrm{mid}}^{\mathrm{mdl}}(t - (j-i)T_s) + & \\ c_{\mathrm{last}}^{\mathrm{mdl}}(t - (K-1)T_s) & \text{If } t \in [(K-1)\,T_s, K\,T_s) \end{cases} \tag{6.4}$$

The model for the received signal is defined as a piece-wise function in which the cases are determined according to the symbol duration. In (6.4), most complicated case with at least four emissions is given, similarly lower number of emissions can be modeled with omitting the middle terms. For example, if we have only two emissions we should consider $c_1^{\mathrm{emp}}(t)$ and $c_{\mathrm{last}}^{\mathrm{mdl}}(t)$.

In Fig. 6.7, empirical and theoretical received signals are shown for a case with

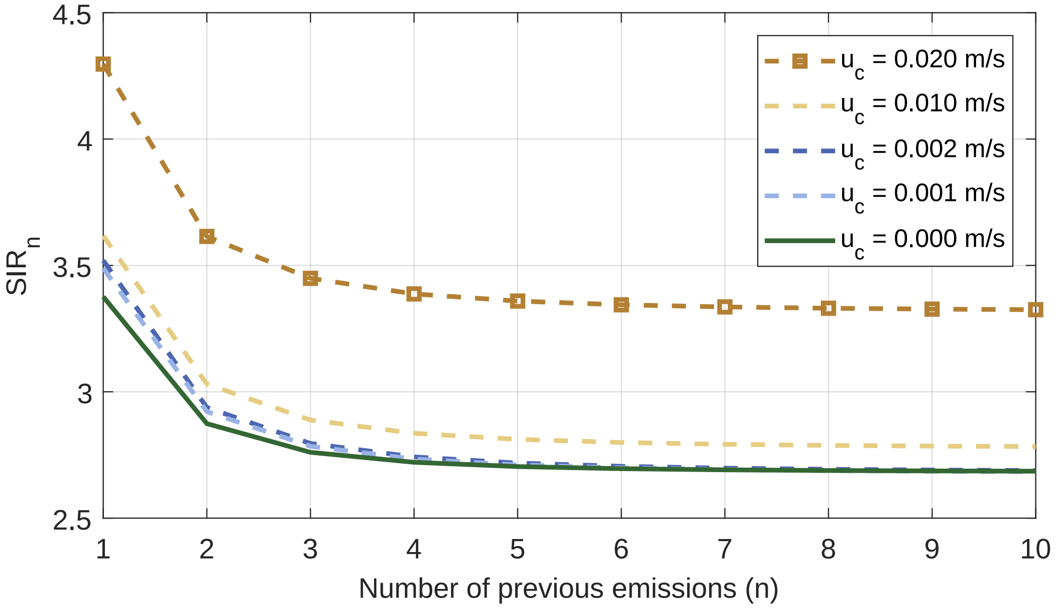

Figure 6.8: SIR versus the number of previous emissions with different co-flow velocities.

10 sequential emissions. Considering $\mathscr{B}_c$ enables us to model the received signal that includes interference. It can be clearly seen that the theoretical $C_{\text{Rx}}(t)$ in (6.4) that is utilizing $c_1^{\text{emp}}(t)$, $c_1^{\text{emp}}(t)$, $c_{\text{mid}}^{\text{emp}}(t)$, and $c_{\text{last}}^{\text{mdl}}(t)$ is capable of modeling the received signal for the analyzed system. Thus, we can consider the interference effect of any number of sequential emissions.

To analyze the effect of interference, we first define signal-to-interference ratio (SIR$_n$) for a given ISI window length (i.e., the number of previous emissions that is considered for the interference) as follows:

$$\text{SIR}_n = \frac{\int\limits_0^{T_s} C_{\text{Rx}}(t)\,dt}{\int\limits_{T_s}^{(n+1)\,T_s} C_{\text{Rx}}(t)\,dt}. \tag{6.5}$$

We also introduced different co-flows into the environment and analyzed the effect of interference under different system conditions. For different system conditions we obtained basis $\mathscr{B}_c$ and evaluated SIR$_n$ via theoretical model for different ISI window lengths to see the significant ISI window length.

In Fig. 6.8, ISI window length versus SIR$_n$ values are plotted for different co-flow cases. Case without co-flow has the lowest SIR_n and adding co-flow increases SIR_n and the signal quality. We observe that the increment in SIR_n is not linear with the increment in co-flow. After $u_c = 0.01\,\mathrm{m/s}$, doubling the co-flow increases SIR_n more compared to $u_c = 0.001\,\mathrm{m/s}$ case. Another critical observation is about the ISI window length. We observe that the effect of ISI (by considering the change in SIR_n) becomes negligible after considering five previous emissions for the given system parameters. This observation depends on T_s and if T_s is reduced to half, then significant ISI would cover twice the number of symbol duration.

6.5 Summary

In this chapter, the non-linearity aspect of the turbulent diffusion channels is investigated for a sequential signal emissions. It is demonstrated that the sequential molecular signals will be added together at the receiver linearly in a turbulent diffusion channel. Different information sequence is used to distinguish each emission and also the same information is considered in all emissions to see their linearity effects in the receiver site. The received molecular signal that includes ISI is also modeled. Theoretical model utilizes a base of four signal types that includes the adequate information to model the received signal for sequential emission case. The analytical model enabled us to formulate the effect of ISI via SIR_n. Results and the empirical channel model showed that the current emission is affected by a specific number of previous emissions (e.g., five for the considered parameters) and the interference effects of the earlier emissions are negligible.

After proving that the channel is linear, in the next chapter we focus on characterising the noise and MI in TDMC channels.

Chapter 7

Noise Distribution and Mutual Information in Turbulent Diffusion Channel

7.1 Motivation

Quantifying the statistical noise distribution and mutual information with respect to the key fluid dynamic parameters is important to molecular communication. Here, we empirically study macro-scale molecular signal propagation using a planar laser induced fluorescence (PLIF) method. We first statistically characterize both the additive and jitter noise distribution. We show that mutual information is maximized under certain transmission strategies and varies with the receiver size.

7.1.1 Review of Noise Models

Noise characterization is important for understanding the achievable mutual information [Moore et al., 2009; Pierobon and Akyildiz, 2012; Lin et al., 2018]. In mass diffusion regime, the additive noise is well modeled [Pierobon and Akyildiz, 2011a; Singhal et al., 2014], and the transposition/jitter [1]/timing noises have also studied in recent works [Farsad et al., 2015; Haselmayr et al., 2018; Etemadi et al., 2019]. Indeed, the combined knowledge allows us to unify noise models [Noel et al., 2014] and understand reliability via eye diagrams [Turan et al., 2018b]. Additional research has also examined thermally induced diffusivity changes [Qiu et al., 2017], mobility [Lin et al., 2018], and their impact on received signal uncertainty. Whilst

---

[1] Jitter is the variation in a signal's timing from its nominal value. Jitter will manifest itself as variations in phase, period, width, or duty cycle.

Table 7.1: Experimental parameters for quantifying noise distribution and mutual information.

Variable	**Value**
Steady flow velocity	0.086 m/s
Turbulent velocity	0.26 m/s
Dynamic viscosity of water, μ	8.9×10^{-4} Pa.s
Transmit volume, Q	5 ml
Eddy diffusivity, D	3.4×10^{-4} m^2/s
Tx-Rx distance, d	2.7 m

micro-/nano-scale mass diffusion dominated molecular communications is well understood, additional fluid dynamic forces at the macro-scale mean that for this case analytical expressions for noise have not yet been obtained.

Research at macro-scale requires significant undertaking and there is a growing body of work. Theoretical and simulation work on molecular communications with turbulence has shown that the fluid dynamic complexities cannot be ignored [Unluturk and Akyildiz, 2017a]. Experimentation is essential to capture realistic variational behaviour in fluid dynamics. Early experimental work started with tabletop prototypes characterizing experimental throughput [Farsad et al., 2013; Koo et al., 2016] and noise process [Farsad et al., 2014] with crude chemical sensors, which has now advanced to encoding in chemical mixtures [McGuiness et al., 2018] with mass spectrometer demodulation. This coincides with parallel work in replicating pheromone signals [Cole et al., 2009]. In our attempts to understand and improve the achievable mutual information in macro-scale fluid dynamic channels with complex forces, Kennedy et al. [2018] has characterized the evolving information structure in turbulence, tracked info-molecules using fluorescence [Tuccitto et al., 2017a; Atthanayake et al., 2018], characterized the linearity of sequential pulse combining (chapter 6), and generated self-propagating structures to increase symbol rate and transmission range (chapter 5).

In this chapter, we contribute to this growing area of experimental research by experimentally quantifying additive and transposition noise in macro-scale MC, under the heterogeneous forces of shear stress, eddies, and diffusion-advection; and finding the corresponding mutual information and optimal transmission strategy.

7.2 Modelling of the Channel

Schematic of the channel is illustrated in Fig. 7.1. We employed the PLIF experimental technique to measure the concentration in the channel. Channel configuration is explained in Section 3.3.1 and the PLIF experimental technique is discussed in

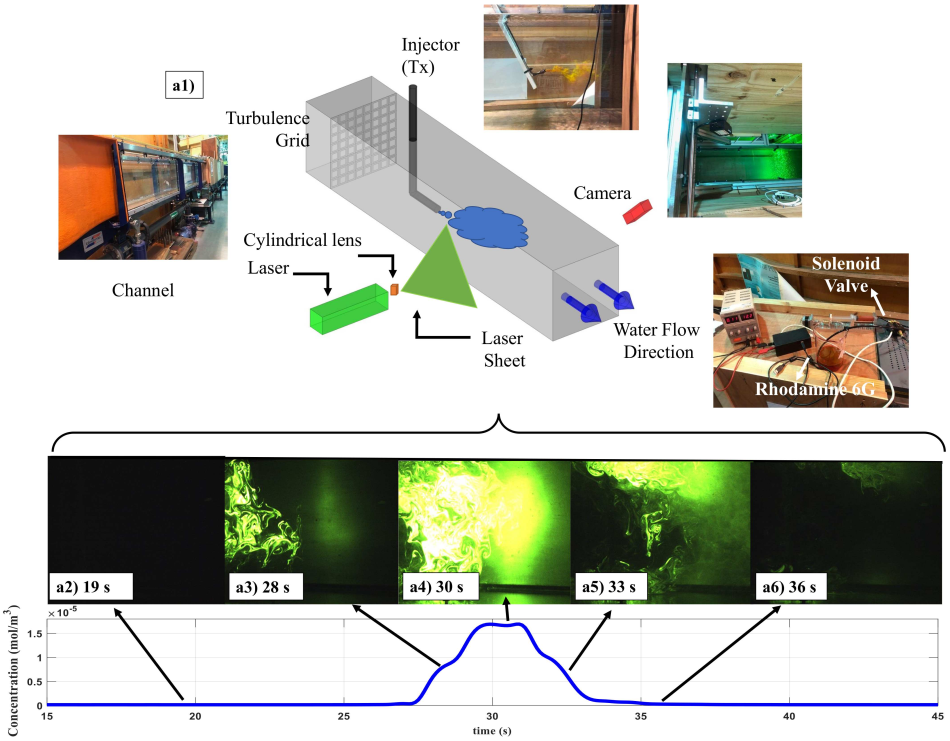

Figure 7.1: Schematic of the experimental setup

Section 3.3.4. Experimental parameters are given in Table 7.1.

The channel model in this chapter is referred to as steady flow when there is no obstacle in the channel, otherwise it is turbulent due to the disturbances in the flow field. For generating turbulence, we use an obstacle to artificially introduce disturbance to the channel [Kistler and Vrebalovich, 1966]. We adopt a generalized inverse-Gaussian (IG) kernel for modelling the channel and inferring the noise in the steady flow regime. The model can be expressed as [Guo et al., 2016b]:

$$C_1(t) = \frac{Q}{(4\pi Dt)^{3/2}} \exp\left[-\frac{(d - vt)^2}{4Dt}\right], \tag{7.1}$$

where d represents the distance between the Tx and Rx (centre of laser sheet), v represents the flow velocity, D is the eddy diffusivity and Q is the released volume of the information-carrying tracer. Note that D is no longer the mass diffusion coefficient since in the macro-scale regime, the contribution of the eddies in carrying the information particles is substantially more pronounced than pure diffusion [Davidson, 2015]. As such, we interpret the model in (7.1) as an empirical proxy, and eddy diffusivity D is a heterogeneous diffusivity that includes viscous diffusion.

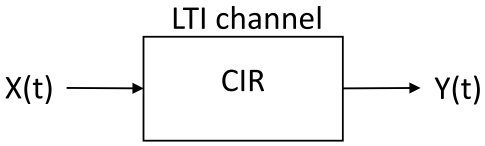

Figure 7.2: LTI system

The injector is a syringe consists of cylinder and piston so the the motion of the piston is considered as a rectangular function since the piston has a constant speed. Therefore, the model in (7.1) is modified as:

$$C_2(t) = \text{rect}(\frac{t - \frac{T_p}{2}}{T_p}) * \frac{Q}{(4\pi Dt)^{3/2}} \exp{[-\frac{(d - vt)^2}{4Dt}]}, \tag{7.2}$$

where T_p is the injection time, $\text{rect}(\cdot)$ is the rectangular function. Rectangular function is defined as the summation of Heaviside step functions. In our case, $\text{rect}(\frac{t-\frac{T_p}{2}}{T_p}) = u(t) - u(t - T_p)$ where $u(\cdot)$ is the Heaviside step function. Moreover in (7.2), the rectangular function is convoluted to $C_1(t)$ to obtain the received signal in the communication channel. This is done by considering the channel as LTI system (see Fig. 7.2).In previous chapter, we showed that the turbulent channel is linear.

7.2.1 Steady Flow Regime

Fig. 7.3(a1) displays the detected concentration values as a function of time for 40 CIRs (blue dashed lines). The initial and boundary conditions of the experiments are the same (see Table 7.1). The concentration profiles have jitters over time as can be observed in the inset of Fig. 7.3(a1). These jitters can be interpreted as either a narrowing of the eye diagram [Turan et al., 2018b] in continuous signaling systems or transposition noise in discrete signaling systems. Separately, there is also additive noise. Based on these two observations, the channel model in (7.2) is further modified as:

$$C_3(t) = \text{rect}(\frac{t - \frac{T_p}{2}}{T_p}) * \frac{Q}{(4\pi Dt)^{3/2}} \exp{[-\frac{(d - vt + n_1)^2}{4Dt}]} + n_2, \tag{7.3}$$

The random variable n_1 accounts for unstable flow velocity, uncertainty in injection time, and other factors which finally influences the peak time of the received concentration profile and generate the jitter. Similarly, n_2 reflects the uncertainty of the amplitude of the received concentration, akin to widely used counting noise in molecular communication [Pierobon and Akyildiz, 2011a].

In order to analyze statistical properties of n_1 and n_2, the eddy diffusivity D needs to be calculated using the concentration values. So, an average eddy diffusivity is assumed over the entire experimental environment. Generally, D is calculated by $D = u'l_m$ where u' is the large eddy velocity and l_m is the Prandtl mixing length which is equal to the size of the largest eddy. Here, we do not have the velocity data to obtain these two quantities. Thus, curve fitting is used to obtain D as shown in Fig. 7.3(a1). D is equal to 3.4× 10^{-4} m^2/s. The peak time t_{peak} can be obtained from experimental raw data. In order to plot the histogram of n_1, we derive the relationship between n_1 and t_{peak}. We simplify (7.3) as:

$$C_4(t) = \frac{Q}{(4\pi Dt)^{3/2}} \exp\,[-\frac{(d - vt + n_1)^2}{4Dt}] + n_2, \tag{7.4}$$

take the derivative of (7.4) with respective to t, and set it to zero. Then we get the relationship between n_1 and t_{peak} as

$$n_1 = \sqrt{v^2 t_{peak}^2 + 6Dt_{peak}} - d. \tag{7.5}$$

Fig. 7.3(a2) shows the histogram of n_1. It can be seen that the histogram can be fitted by a Gaussian curve, with the mean -0.02027 and the variance 0.0016398.

The next step is to find the statistical properties of n_2. To plot the histogram of the received concentration samples so that to analyze the distribution of n_2, each concentration profile in Fig. 7.3(a1) is shifted horizontally to align the peak time of each profile. At the same time, the concentration value is adjusted with the following formula:

$$C(t') = \frac{C_2(t')}{C_2(t)} \times C(t), \tag{7.6}$$

where t' is the time instant we want to align to, $C(t)$ is the sampled concentration at time t. n other words, $C(t)$ is the values of maximum concentration in each CIR data. $C_2(t')$ is the maximum concentration calculated from the (7.2) or the fitted curve. $C_2(t)$ is the values of maximum concentration taken from C_4 where the n_1 is added to the closed-form channel model. If we rearrange (7.6), we have $\frac{C(t')}{C(t)} = \frac{C_2(t')}{C_2(t)}$. It shows that the proportion of the peak concentration after shifting to the peak concentration values obtained from the data is equal to peak concentration taken from the closed-form included the n_1 term over the closed-form without the n_1 term. Figure 7.3(a3) shows the histogram of n_2. We can see that it is approximated as a

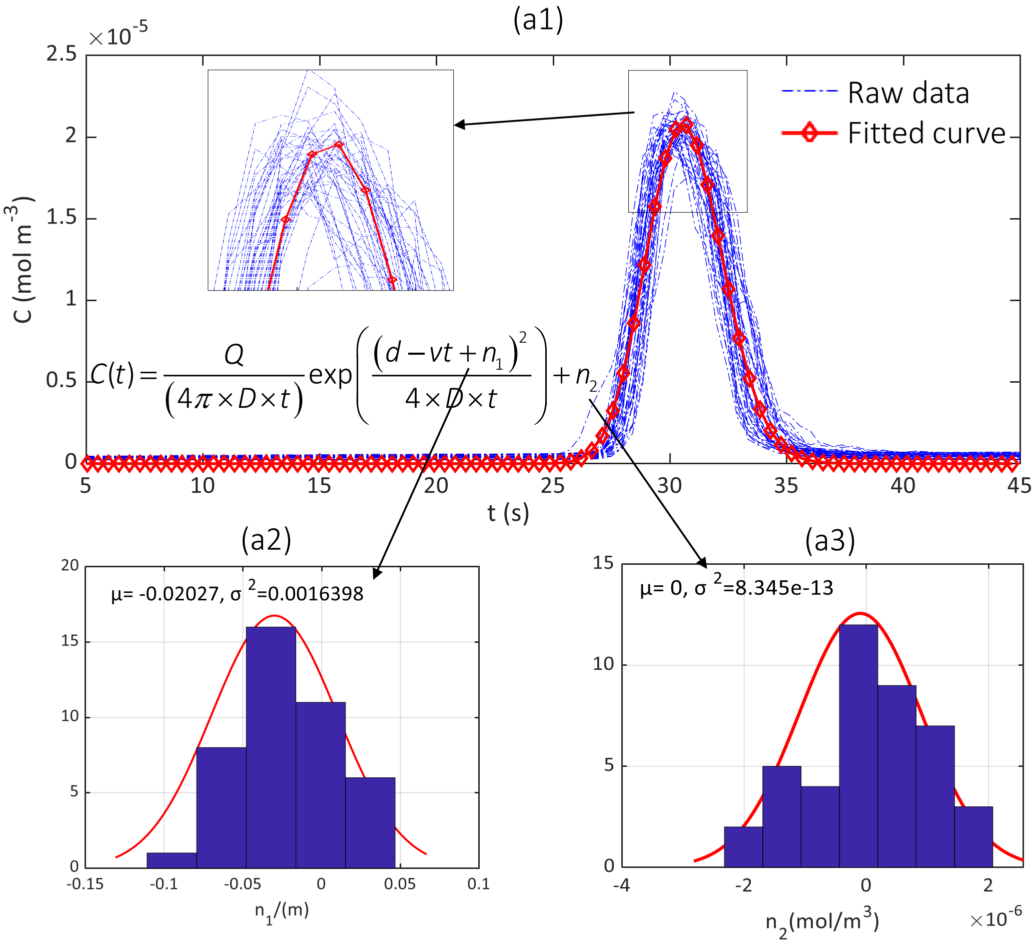

Figure 7.3: a1) The concentration over time for 42 analogous experiments at the Rx (blue dashed line) and the fitted curve. The inset is the zoom-in of the concentration peaks for better illustration of transposition noise. a2) Histogram of n_1(transposition noise) and corresponding Gaussian PDF. a3) Histogram of n_2 (additive noise) and corresponding Gaussian PDF.

Gaussian distribution. Based on the above analysis it is concluded that (7.3) can be used as the channel model for modelling the steady flow diffusion channel.

7.2.2 Turbulent Flow Regime

Figure 7.4 shows the received concentration versus time for the turbulent case with seven CIRs. The entire 40 experiments are shown in the left subset of Fig. 7.4. It can be seen that compared to the received concentration in the steady flow regime (Fig. 7.3), the profiles in Fig. 7.4 fluctuates severely which is the essence of the turbulent flow regime. Substantial efforts in the past have gone into modeling of the turbulent regime analytically [Barkley, 2011; Speziale, 1991], but the high dimensionality and dynamic change of the flow hinders attaining a robust model for that regime. Inspired by the literature [Barkley, 2011; Speziale, 1991] in this field and based on the features of the curve in Fig. 7.4, we use the following exponential function with sinusoidal oscillation to model the turbulence channel:

$$C_T(t) = C_3(t) + a[C_3(t) - C_3(t-m)]\sin(\omega t), \tag{7.7}$$

where m represents time delay, a and ω are the amplitude and the frequency of the sinusoidal component. In this thesis, $m = 1$, $a = 0.2$, and $\omega = 4\pi$. From Fig. 7.4, it is seen that the concentration goes up in the beginning without considerable fluctuations, especially when it reaches to the peak, the fluctuation becomes strong. When the concentration starts to decay, the turbulence shows a sinusoidal pattern which decays gradually. This behaviour could be due to the turbulence fluctuating inside the channel causing an oscillatory concentration phenomenon. The fitted curve in Fig. 7.4 matches the trend very well. This can also be reflected in Fig. 7.4, where the first term and the second term in (7.7) are separately shown in the right inset (we temporarily let n_1 and n_2 equal zero in the right inset). In (7.7) a feedback term $C_3(t-m)$ with delay m is used. The reason of the delay and feedback is likely due to the delay caused by the turbulence of the injected liquid.

7.3 Mutual Information

In this section the mutual information for steady flow case is derived [Lin et al., 2018]. It is assumed that no molecular information is transmitted if bit ‘0’ is sent with the probability p_0. Bit ‘1’ is sent with the probability of p_1. The threshold for signal detection is C_{th}.

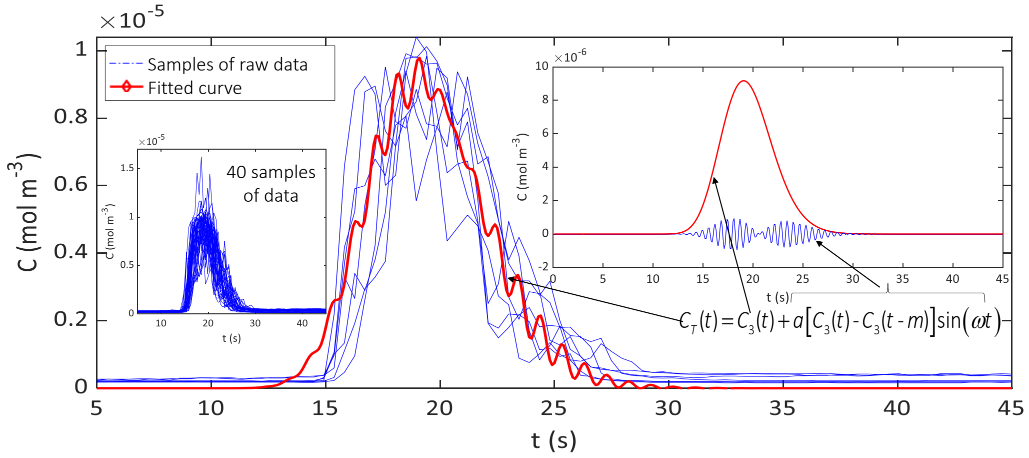

Figure 7.4: Concentration versus time profile in the turbulent case. These are seven sample profiles from the total of 40 sample profiles which is illustrated in the left hand side inset. The right-hand-side inset is the illustration of the C_3 and C_T-C_3 values.

7.3.1 Steady Flow

We assume that the total concentration of the ISI follows a Gaussian distribution with mean μ_l and standard deviation σ_l. This is reasonable because n_2 follows a Gaussian distribution, and the total concentration of the ISI is a linear combination of each ISI component (chapter 6). We have

$$\begin{aligned} P(1|0) &= \int_{C_{th}}^{\infty} \frac{1}{\sqrt{2\pi}\sigma_l} \exp[\frac{-(r-\mu_l)^2}{2\sigma_l^2}]dr \\ &= 1 - Q(\frac{C_{th}-\mu_l}{\sigma_l}), \\ P(0|1) &= \int_{-\infty}^{C_{th}} \frac{1}{\sqrt{2\pi}\sigma_2} \exp[\frac{-(r-c_{peak})^2}{2\sigma_2^2}]dr \\ &= Q(\frac{c_{peak}-C_{th}}{\sigma_2}), \end{aligned} \tag{7.8}$$

where $Q(\cdot)$ is the Q function and it is equal to

$$Q(C_{th}) = \int_{C_{th}}^{\infty} \frac{1}{\sqrt{2\pi}} \exp[-\frac{1}{2}r^2]dr \tag{7.9}$$

This is called the right-tail probability and is the probability of exceeding a given value [Kay, 1993]. $Q(x)$ is also referred to as the complementary cumulative distribution function. If we define $\phi(C_{th}) = \int_{-\infty}^{C_{th}} \frac{1}{\sqrt{2\pi}} \exp[-\frac{1}{2}r^2]dr$, then we have $Q = 1 - \phi$. Both of the Q and ϕ hypothesis are illustrated in Fig. 7.5.

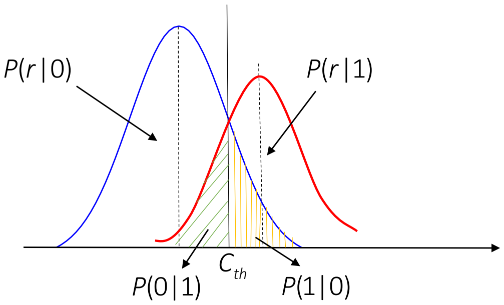

Figure 7.5: The probability density functions of the received peak concentration for symbol '0' and symbol '1'.

The standard deviation of n_2 for the peak concentration is σ_2. We calculated c_{peak} based on (7.5). To calculate the μ_l and σ_l, several CIRs were generated from closed-form form of the channel model and the noise parameters were calculated based on these CIRs. The joint probability $p(x, y)$ ($x \in \{0, 1\}$, $y \in \{0, 1\}$) represents the probability that the symbol x is transmitted and the symbol y is detected, and is derived as

$$\begin{aligned} p(0,0) &= p_0(1 - P(1|0)), \\ p(0,1) &= p_0 P(1|0), \\ p(1,0) &= p_1 P(0|1), \\ p(1,1) &= p_1(1 - P(0|1)). \end{aligned} \tag{7.10}$$

The mutual information can be expressed as

$$I(X;Y)|_{n_1} = \sum_{y \in Y} \sum_{x \in X} p(x,y) \log \frac{p(x,y)}{p(x)p(y)}, \tag{7.11}$$

X is the transmitted symbol which can be '0' or '1'. We considered different probability values from 0.1 to 0.9 for each bit with the knowledge that $p_0 + p_1 = 1$. Also, equations (7.4) and (7.5) are used to calculate Y.

As it is proven that n_1 can be approximated as a Gaussian distributed random variable with mean μ_1 and standard deviation σ_1 whose PDF is

$$f(n_1) = \frac{1}{\sqrt{2\pi}\sigma_1} \exp[\frac{-(-n_1 - \mu_1)^2}{2\sigma_1^2}] dn_1, \tag{7.12}$$

then the expected mutual information by concurrently considering both n_1 and n_2

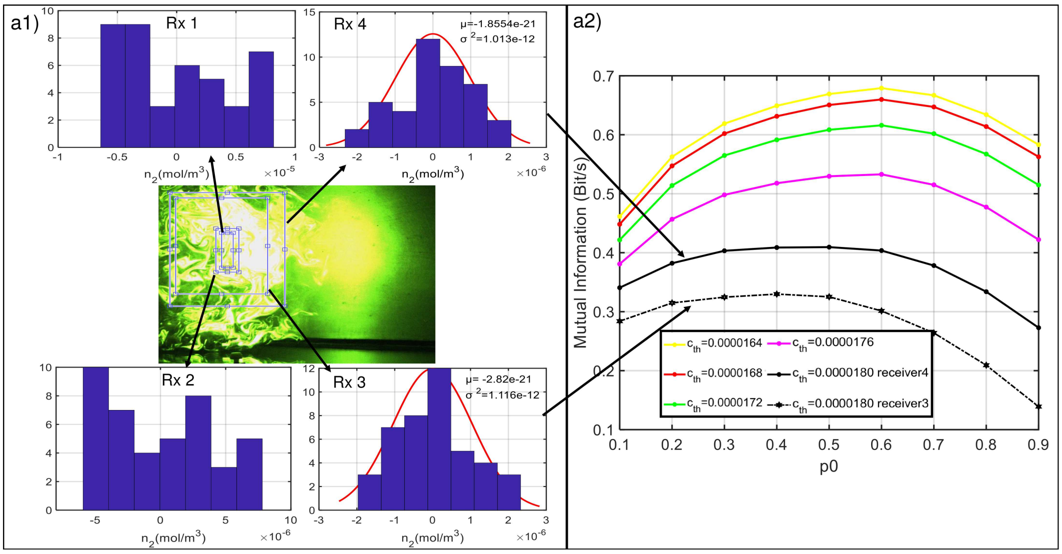

Figure 7.6: a1) Different receiver size and their corresponding histogram for additive noise in steady flow regime. a2) Mutual information versus p_0 with different C_{th}s.

can be expressed as

$$I(X;Y) = \int f(n_1) I(X;Y)|_{n_1} dn_1. \tag{7.13}$$

In order to calculate MI, we have two terms that represent noise: n_1 and n_2. We kept the additive noise and we got rid of the effects of he jitter noise by using the conditional MI in (7.11). Actually, for different values of n_1, we calculated the MI. Then in (7.13), the expected value of MI is calculated. It is worth saying that the transmitter and the receiver are synchronized [Lin et al., 2017].

7.3.2 Different Receiver Size & Detection Threshold

We now consider different receiver size and detection thresholds C_{th}. The receiver is a window on the captured image, within which the concentration is calculated. Receiver window size varies from largest to smallest (see Fig. 7.6(a1)): Rx-4>Rx-3>Rx-2>Rx-1. Fig. 7.6(a2) shows the mutual information vs. p_0 with different C_{th}s. As the receiver window size decreases (Rx-4 to Rx-3), the mutual information decreases.

The solid curves are for Rx-4 which has the largest window size. It is seen that for Rx 4, with the increase of C_{th}, the mutual information decreases. The reason is that the increase of C_{th} leads to larger $P(0|1)$ based on (7.8), which further decreases the mutual information. It can also be seen that the largest mutual information is achieved when $p_0 > 0.5$. This is because $P(1|0)$ is smaller than $P(0|1)$, so if $p_0 > 0.5$, then the error probability decreases and the mutual information increases. Whilst this is an intuitive and general result in molecular communications (e.g. transmit more zeroes than ones to minimize ISI), our findings in modeling the underlying real world noise models and achievable mutual information is still useful for future research.

From Fig. 7.6, it can be seen that as the window size decreases the mutual information decreases. We can conclude that using a larger window size of the captured image results in more information being obtained by the receiver. This represents an advantage of laser induced fluorescence receivers in comparison to sensor type receivers which are only capable of sensing concentrations around a single physical point in space.

7.4 Summary

Quantifying the statistical noise distribution and mutual information with respect to the key fluid dynamic parameters is important to molecular communication. Here, we have empirically studied macro-scale molecular signal propagation using a planar laser induced fluorescence (PLIF) method. We have first statistically characterized both the additive and jitter noise distribution in steady flow conditions and also proposed a new channel model for the turbulent case. We found that the mutual information is maximized under certain transmission strategies and that it varies with the receiver size.

After showing the linearity of the TDMC channels in chapter 6 and characterising the noise and MI information in these types of channels in the previous chapter, we are going to investigate the dissipation of the molecular information in TDMC channels. This concept is inspired by the concept of the energy dissipation rate of the turbulent flow. Since the underlying turbulent flow is responsible for carrying the information particles in TDMC channel, we expect to see a type of correlation between these two concepts. In the next chapter, we will discuss this correlation in detail.

Chapter 8

Kolmogorov Turbulence and Information Dissipation in Molecular Communication

8.1 Motivation

According to the Kelvin's theorem of conservation of the circulation along a fluid contour, or integrated vorticity within the contour, it might be possible that the fate of information molecules is tied to that of vorticity field [Sreenivasan, 1991]. In this sense, we consider the concentration of molecules as a passive scalar that do not have any dynamical influence on the vorticity field. This is an huge assumption especially when the molecules are injected into another fluid which causes shear stress between the mean flow and the ejected molecules. In this chapter, we are going to observe the correlation of information cascade and energy cascade of the turbulence.

For this purpose, waterborne chemical plumes are studied as a paradigm for representing a means for molecular communication in a macro-scale system. Results from the theory of fluid turbulence are applied and interpreted in the context of molecular communication to characterize an information cascade, the information dissipation rate and the critical length scale below which information modulated onto the plume can no longer be decoded. The results show that the information dissipation decreases with increasing Reynolds number and that there exists a theoretical potential for encoding smaller information structures at higher Reynolds numbers.

8.1.1 Review of Similar Works

The information transmission in MC is closely associated with the physics of fluid dynamics. At nano-scale the physical conditions are such that the main mechanism of transport is mass diffusion [Nakano et al., 2013]. Therefore fluid turbulence, for which other transport mechanisms are relevant, have hitherto hardly been considered at all in the context of MC. Nevertheless, MC is obviously not restricted to nano-scales, as demonstrated by insect and crustacean pheromone signaling [Wyatt, 2014]. Here turbulence does become a crucial issue affecting the reliability of the message transfer [Unluturk and Akyildiz, 2017b].

The conceptual framework for the theoretical description of fluid turbulence was defined by Kolmogorov [Kolmogorov, 1941a,b]. In the idealized scenario of homogeneous, isotropic turbulence - that is turbulence which is statistically invariant under translations and rotations, Kolmogorov's approach was based on Richardson's notion that larger eddies in a turbulent flow field are unstable and break up into successively smaller eddies. Thereby a cascade is created by which energy is transferred from the largest to the smallest length scales. The energy is eventually dissipated by the viscosity at a critical smallest length scale (cf. [Pope, 2001; Davidson, 2015]).

The paradigm for MC at the macro-scale with turbulence is both abundant in nature and useful technologically (e.g. sensing contamination in underground water networks). In many such cases, these plumes carry a biological signal (e.g. communication mediated by pheromones [Wyatt, 2014; Weissburg, 2010; Breithaupt and Thiel, 2010; Weissburg et al., 2002]) and in others the chemical plume patterns are a proxy signal for a hazardous process (e.g. oil leakage [Lu et al., 2012] and source localisation [Naeem et al., 2007; Pang and Farrell, 2006]).

If the information is embedded in the physical pattern of the plumes, controlling chemical plumes then becomes an essential aspect beneficial to health and safety of marine life. Quantities such as the concentration amplitude level [Kuran et al., 2011] and spatiotemporal characteristics [Huang et al., 2019; Huang et al., 2019; Kennedy et al., 2018; Ozmen et al., 2018] can be used for information encoding. The information modulated onto the chemical plume then propagates through the transmission channel and eventually arrives at the receiver side, where the proper signal detection schemes recover the transmitted information [Llatser et al., 2013; Khaloopour et al., 2019].

In terms of fluid dynamics the chemical used to encode the information represents a passive scalar. That is a quantity which has no dynamic influence on the ambient turbulence itself. The concentration of the chemical varies in space and time as it becomes mixed and distributed by the turbulent flow. From an information-

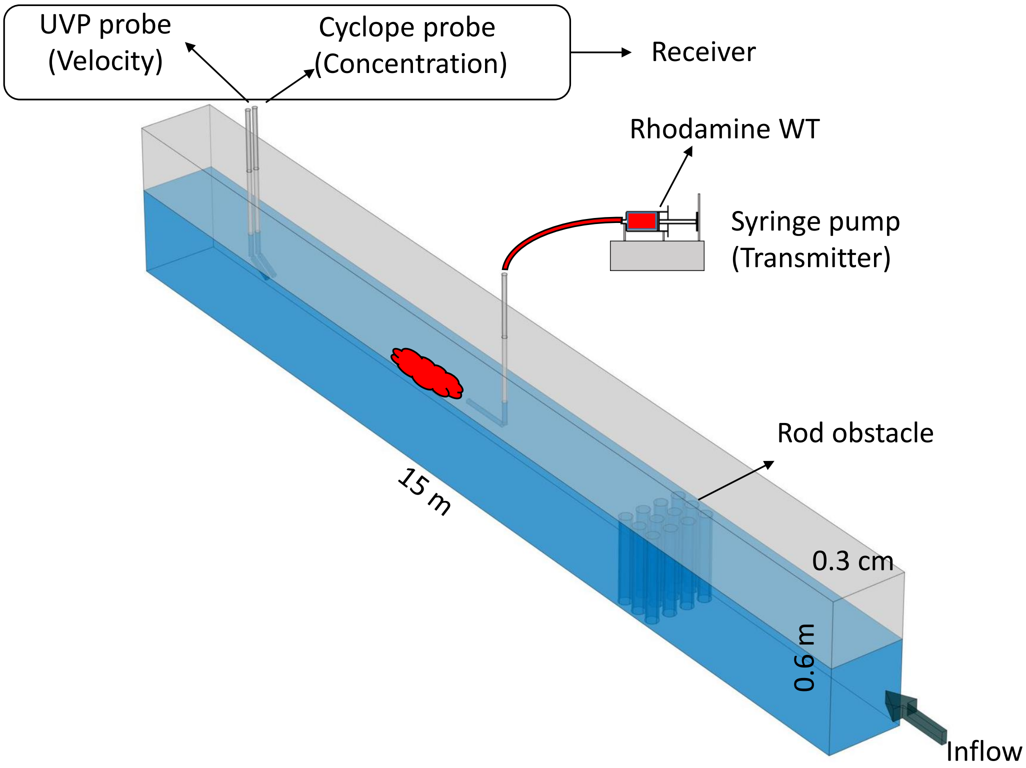

Figure 8.1: Experimental arrangement in water channel (not to scale).

theoretical point of view, the velocity field of the chemical plume contains a certain amount of information. This is so because the velocity field near the emitter of the plume is correlated to the velocity field some distance away [Cerbus and Goldburg, 2013; Granero-Belinchon et al., 2016; Davidson, 2015; Atthanayake et al., 2018].

The goal here is to introduce established theoretical concepts for the energy cascade of turbulence and for the mixing of passive scalars, and apply these to chemical plumes as an example for a macro-scale MC system, interpreting the results from the viewpoint of information theory. The aim is to find the critical smallest length scale below which information modulated onto chemical plumes by means of a passive tracer can no longer be decoded and the rate at which information is dissipated.

8.2 Channel Configuration

Experiments were conducted inside a water channel which is explained in Section 3.3.1. The experimental arrangement is schematically illustrated in Fig. 8.1. The

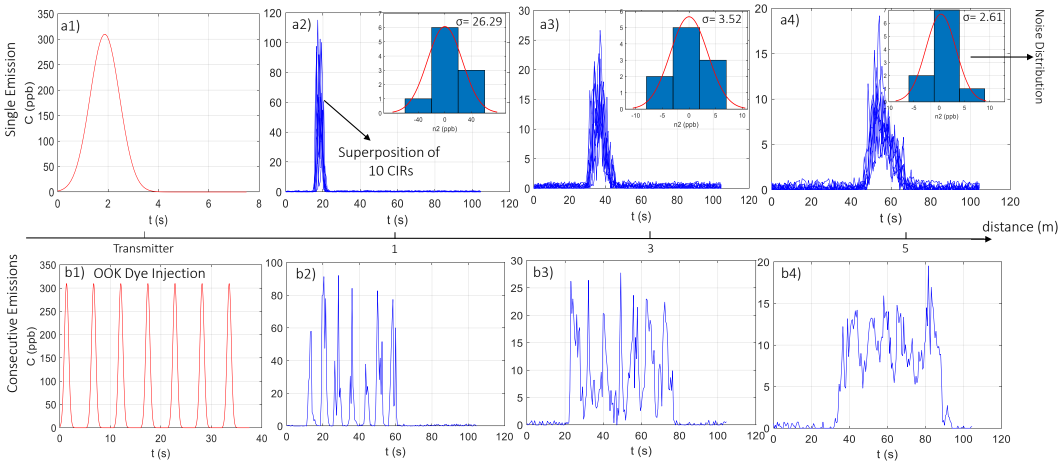

Figure 8.2: a1) Concentration profile at d=1.0 m from the transmitter. This profile is fitted by the Gaussian distribution to derive the OOK injector pulse function. The inset shows histogram of the peak values of the concentration profiles at d=1.0 m from the transmitter. Superposition of ten CIRs at a2) d=1.0 m, a3) d=3.0 m a4) d=5.0 m. b1) Seven consecutive signals sent to the channel by the transmitter. Seven consecutive signals received by the receiver at b2) d=1.0 m, b3) d=3.0 m b4) d=5.0 m.

receiver comprises an Ultrasonic Velocity Profiler (see Section 3.3.3) combined with a CYCLOPS-7 Submersible Fluorometer (see Section 3.3.5) such that it can concurrently measure the flow velocity and the tracer concentration.

The velocity component in the main flow direction inside the channel is measured as a function of time t and distance x from Rx and referred to by $u(t, x)$. The time-averaged mean flow velocity at any particular location in the flow field is denoted by u_0 and its associated fluctuating component is u'. Similarly the tracer concentration is $C(t, x)$ with random fluctuation (variance) $\langle C^2 \rangle$. On-off keying (OOK) modulation [Shi and Yang, 2017], a special case of the binary concentration shift keying, is used for the tracer release at Tx. Note that in OOK, the transmission of bit '1' is represented by the emission of a chemical plume for a time period of t_p, while the bit '0' message corresponds to a period of no tracer release.

8.3 On-off Key Dye Injection

8.3.1 Injection Mechanism

Single emission and consecutive emissions are considered for OOK dye injection. In single emission, 10 mL of fluorescent tracer liquid (the information carrier) is released into the channel for a period of t=2.5 s. A perfect step-pulse release is unrealistic. Therefore the concentration profile in steady turbulence at a location 1 m downstream of the injector (transmitter) is considered as the release function (see Fig. 8.2(a1)) representing bit '1'. The superposition of 10 single emissions in 3 different locations downstream of the injector is displayed in Fig. 8.2(a2-a4). The distribution of the peak amplitudes at each location is displayed in the inset of each of Fig. 8.2(a2-a4). The figures reveal that the variance of the peak amplitudes decreases with distance from the transmitter. The consecutive-emission scenario is illustrated in Fig. 8.2(b1-b4). The symbol duration for each bit '1' is $t_p = 7.5$ s with time delay $\Delta t_p = 5.0$ s between each pair of successive puffs. At $d = 1.0$ m downstream of the transmitter, the individual bit '1' is distinguishable but as the distance from the transmitter increases, the effects of ISI on the received signal is intensified in a way that at $d = 5.0$ m a sophisticated detection algorithm is required to detect the received signal.

8.3.2 Concentration Data

Figure 8.3 displays raw data for the concentration $C(t)$ recorded by the Fluorometer for the release of seven consecutive bit '1' symbols in steady turbulence. The Fluorometer was located $d = 1.0$ m downstream of Tx, the symbol duration for each bit '1' is $t_p = 7.5$ s with time delay $\Delta t_p = 5.0$ s between each pair of successive puffs. Data for the three different release Reynolds numbers Re_0 are included.

Figure 8.3 shows that the information at higher Re_0 arrives at Rx earlier than those with lower Re_0 resulting from higher mean velocity U_0 at higher Re_0. The result to note from Fig. 8.3 is that the tracer concentration detected by the Fluorometer decreases substantially with increasing Reynolds number. This reflects increased turbulence levels and, associated, more effective mixing at higher Re_0. The significant reduction in the signal amplitude can degrade the so-called bit error rate (BER) performance. This is an important index characterizing the reliability of a communication system. It is defined as the ratio of incorrectly decoded bit number to the total transmitted bit number; such that lower BER values represent better performance.

Figure 8.4 compares measured concentration levels for the seven-bit sequence of Figure 8.3 at $Re_0 = 16,000$ for steady turbulence to a corresponding bit sequence for modified turbulence existing when the obstacle is in place. The figure reveals that the concentration levels for the modified turbulence are substantially lower than those for the steady turbulence. This signal attenuation implies that the turbulence generated by the obstacle has significantly increased the mixing efficiency.

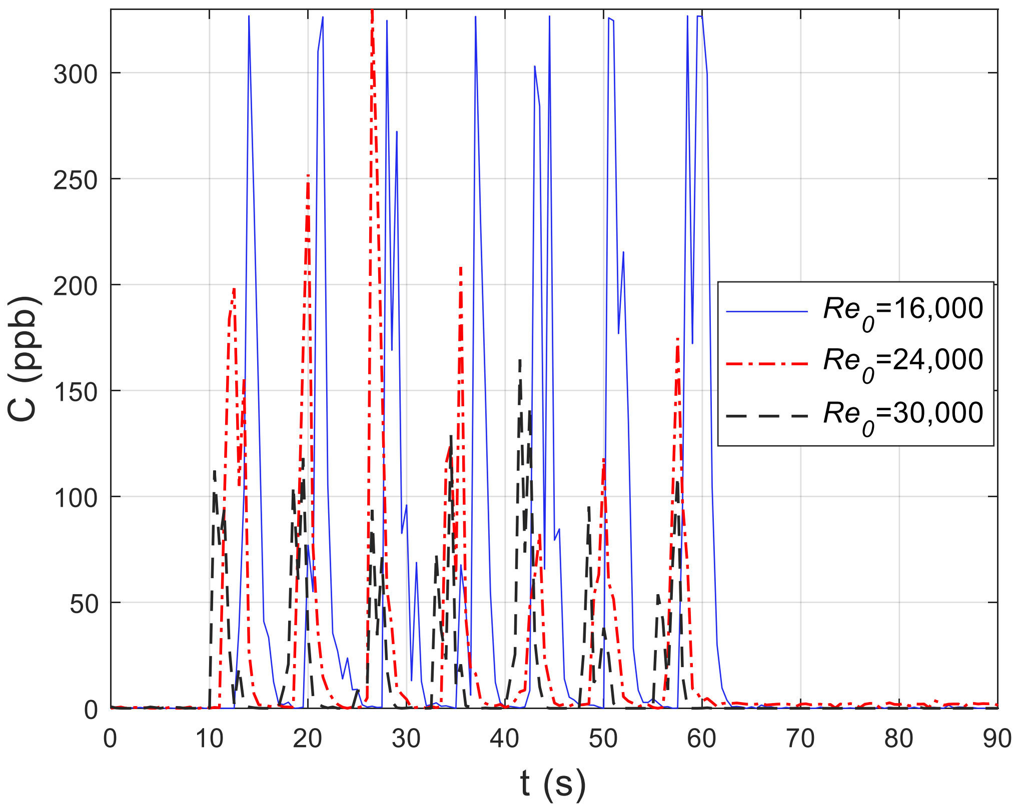

Figure 8.3: Seven-bit signal sequences for the tracer concentration, for three different values of the Reynolds number Re_0, in steady turbulence.

The measurements revealed that the obstacle leads to an almost tenfold increase of the turbulence level $\langle u'^2 \rangle$ in comparison to steady turbulence in the absence of the obstacle.

8.4 Turbulent Velocity Signal

To quantify the different length scales of a turbulent flow the spatiotemporal variation of the velocity field is required. Figure 8.5 and Fig. 8.6 illustrate examples of such variations obtained from our experiments. Figure 8.5 displays the temporal variation of the flow velocity $u(t)$ at a point $d = 1.0$ m downstream of Tx. The random nature of the signal reflects that a wide range of frequencies associated with the hierarchy of tangled eddies of varying sizes are embedded in the turbulent flow. Lower frequency components are associated with large eddies and higher frequency components correspond to smaller eddies.

Whilst Fig. 8.5 illustrated temporal velocity fluctuation Fig. 8.6 shows a

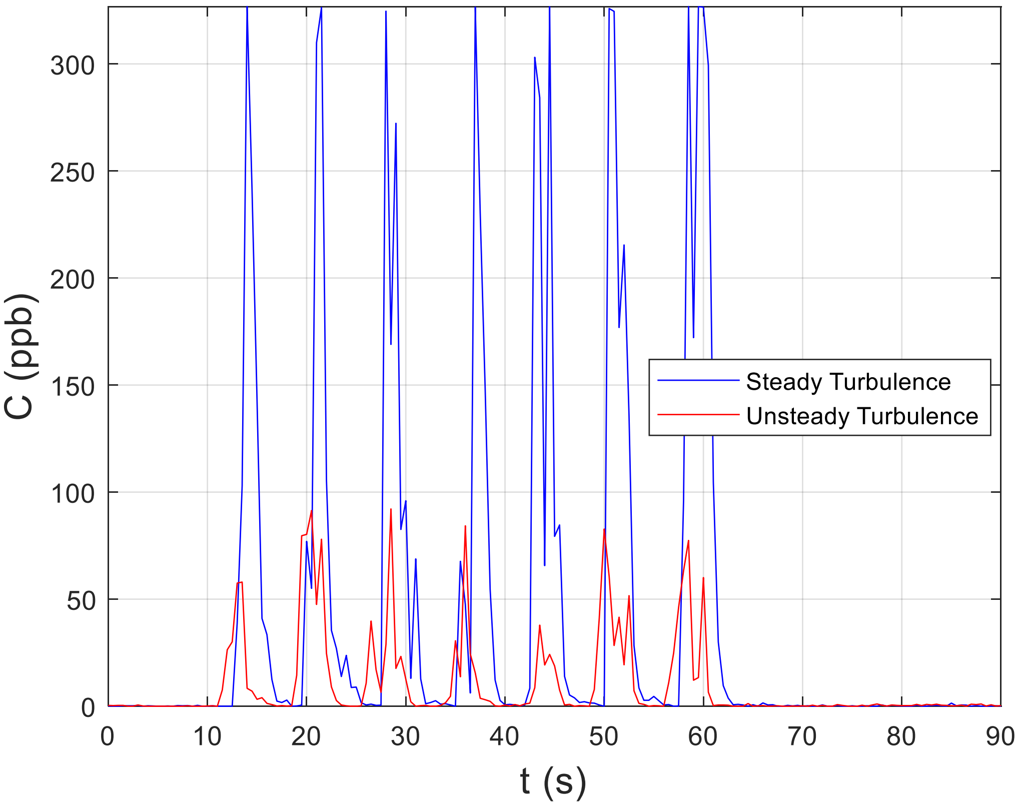

Figure 8.4: Seven-bit signal sequences for the tracer concentration for steady turbulence at $Re_0 = 16,000$ in comparison to data for the corresponding flow in the modified turbulence.

spatial velocity variation $u(x)$ of a flow section at a particular instance in time. The large-scale fluctuations in the lower plot of Fig. 8.6 qualitatively reflect the approximate scale of the largest eddies. A quantitative measure of this scale follows below.

8.4.1 Velocity Correlation and Integral Length Scale

The correlation function is one main tool for analyzing velocity data in fluid turbulence. It can be used to assess the distance required between sample points in the flow field for the velocity values to become effectively uncorrelated. The velocity correlation is given by the ensemble average [Davidson, 2015]

$$R_{xx} = \int_{-\infty}^{\infty} u'(x)u'(x+r)dr = \langle u'(x)u'(x+r)\rangle \ . \tag{8.1}$$

The associated longitudinal velocity correlation function is a dimensionless

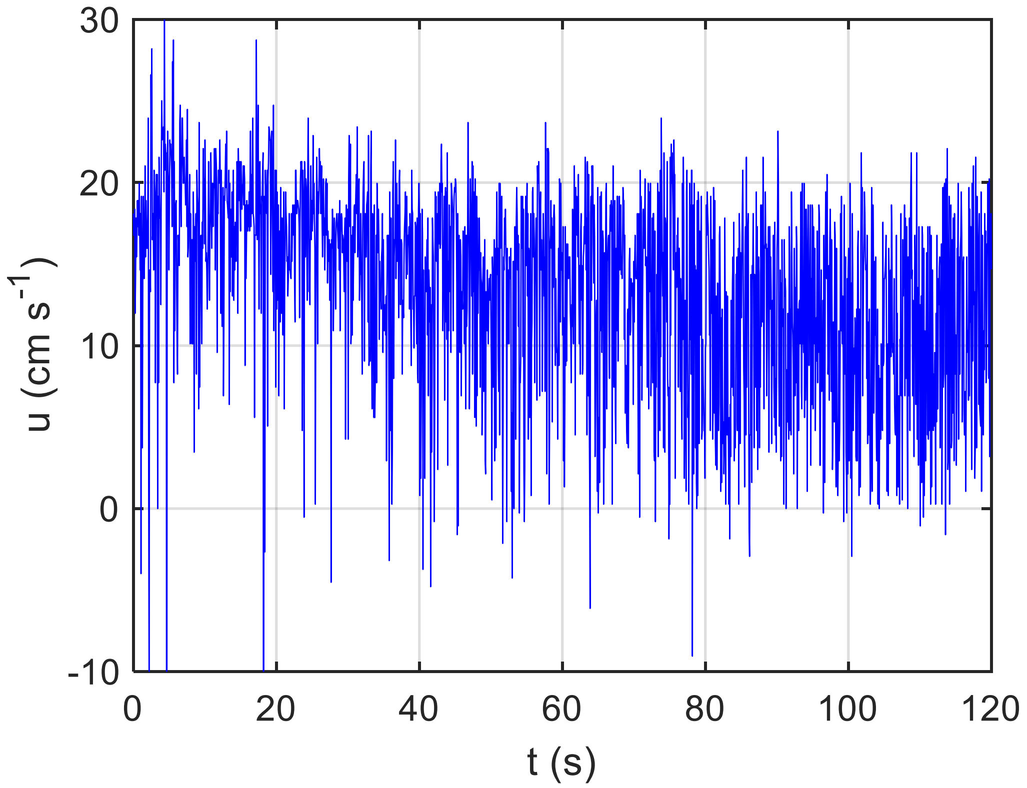

Figure 8.5: Temporal variation of velocity, $u(t)$ at $d = 1$ m from Tx

component of R_{xx} given by [Davidson, 2015]

$$f(r) = \frac{R_{xx}(r)}{R_{xx}(r=0)} \tag{8.2}$$

and satisfying $f(r=0) = 1$.

The integral scale l characterizes the extent of the region where velocities are appreciably correlated. It represents the length scale of the largest eddies containing most of the energy (cf. Fig. 8.6) and it is given by [Davidson, 2015]

$$l = \int_0^{\infty} f(r)dx \ . \tag{8.3}$$

8.4.2 Energy Cascade

According to the Wiener–Khinchin theorem [Chatfield, 2004] the Fourier transform $\mathfrak{F}$ of the autocorrelation function R_{xx} of (8.1) yields the one-dimensional energy spectrum $E(k)$ of u'

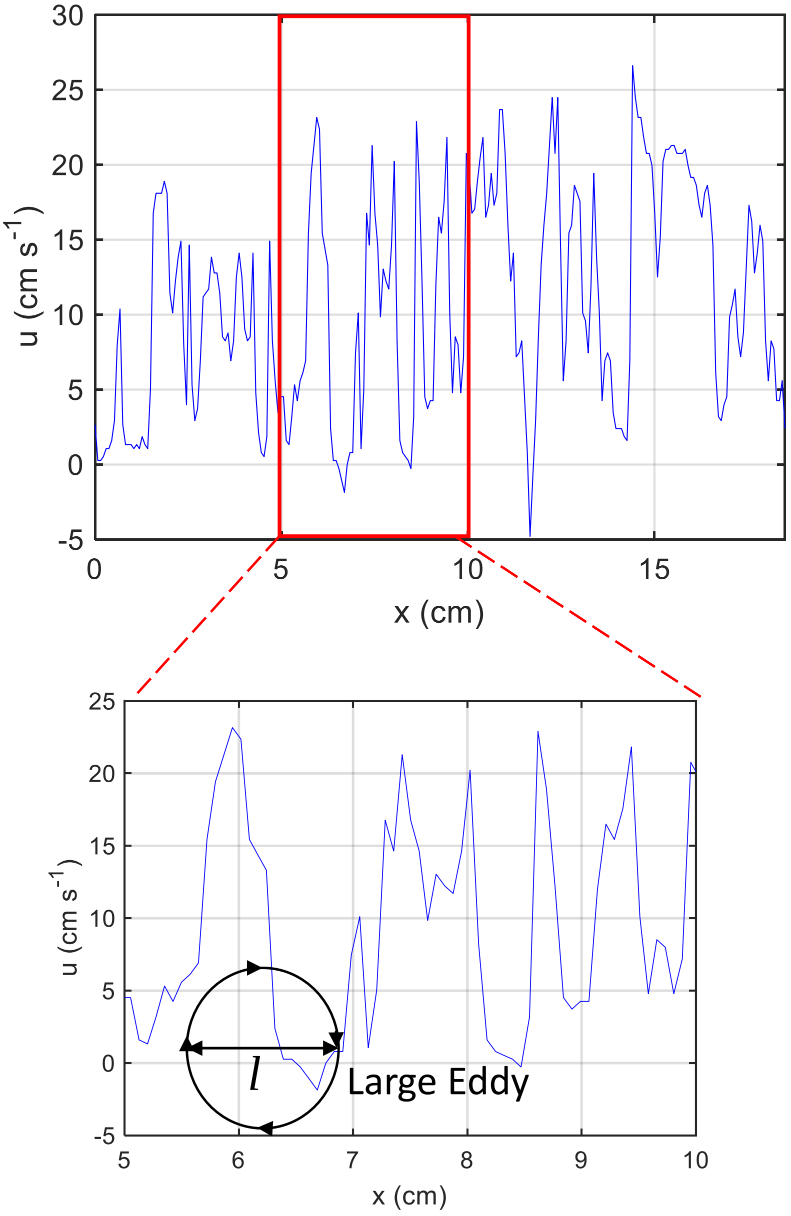

Figure 8.6: Spatial variation of velocity, $u(x)$ over a section extending 185 mm upstream of Rx, which itself was located $d = 1$ m downstream of Tx.

$$\mathfrak{F}[R_{xx}] = 2\pi|U(k)|^2 = E(k) \tag{8.4}$$

where $U(k) = \mathfrak{F}(u')$ is the Fourier transform of u' and k is the wavenumber.

Figure 8.7 displays the energy spectrum of the velocity field as a function

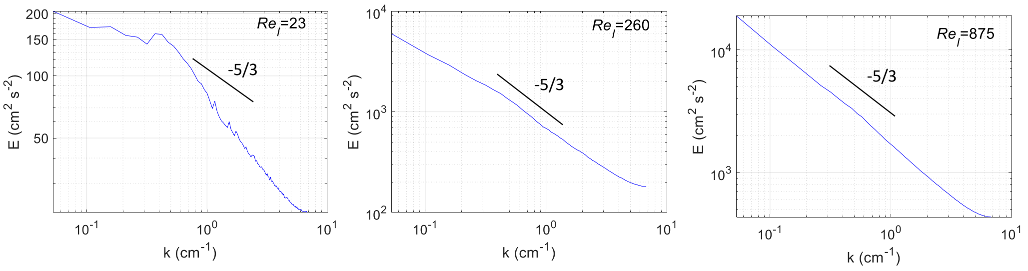

Figure 8.7: Energy spectrum for three different values of the Reynolds number Re_l of the large eddies.

of the wavenumber k. Data are shown for three different values of a large-scale Reynolds number defined as $Re_l = lu_l/\nu$. Here u_l is velocity of the largest eddies for which estimates can be inferred from the measured UVP data. The figure reveals that the data approach $E \propto k^{-5/3}$ for increasing Re_l. To readers unfamiliar with fluid dynamics we highlight that this relation between E and k, at high Reynolds number, represents one of the most celebrated results in turbulence and is referred to as the Kolmogorov five-thirds law. The fact that the $-5/3$ dependence is obtained for the present measurements gives us confidence in our UVP velocity data.

While the integral scale of (8.3) represents the measurable scale of the largest eddies the size of the smallest eddies, η, and their associated velocity u_η cannot be resolved experimentally; they have to be obtained from theoretical consideration. A Reynolds number associated with these two quantities is defined as $Re_\eta = \eta u_\eta/\nu$.

It is known (cf. [Davidson, 2015]) that most eddies break up on a time scale of their turn-over time. For the largest eddies this time scale is l/u_l. Therefore the rate at which energy (per unit mass) is transferred down the energy cascade from the largest eddies is [Davidson, 2015]

$$\epsilon_l = \frac{u_l^2}{l/u_l} \; . \tag{8.5}$$

The energy cascade comes to a halt at small scales where the viscous forces are dominant and Re_η will be of order unity. The rate of dissipation of energy at the smallest scales is given by (cf. [Davidson, 2015]),

$$\epsilon_\eta = \nu \frac{u_\eta^2}{\eta^2} \tag{8.6}$$

When the turbulent flow is statistically steady, the rate of the generation and dissipation of energy at large and small scales are the same. If this were not the

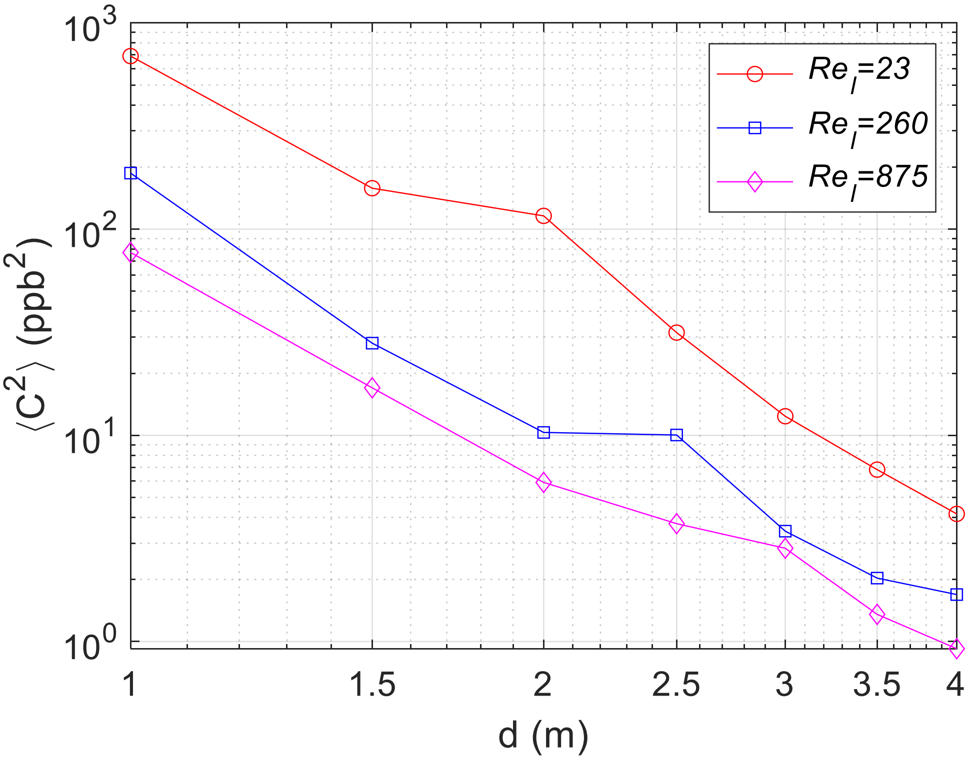

Figure 8.8: Variation of $\langle C^2 \rangle$ of the molecular signals with distance d from Tx for three different values of the Reynolds number Re_l for modified turbulence

case, then energy would accumulate at an intermediate scale. From (8.5) and (8.6) it therefore follows that

$$\frac{u_l^3}{l} \sim \nu \frac{u_\eta^2}{\eta^2} \ . \tag{8.7}$$

The Reynolds number $Re_\eta = \eta u_\eta / \nu$ at smallest scales, where viscous forces dominate, must be of order unity. Rearranging (8.7) by considering $Re_\eta \sim 1$ yields

$$\eta \sim l Re_l^{-3/4} \ . \tag{8.8}$$

The expression in (8.8) provides a means to quantify the smallest scale η of the turbulent energy cascade based on the known size l of the largest eddies and their associated Reynolds number Re_l. The length scale η and the velocity scale u_η are referred to as the Kolmogorov microscales [Davidson, 2015].

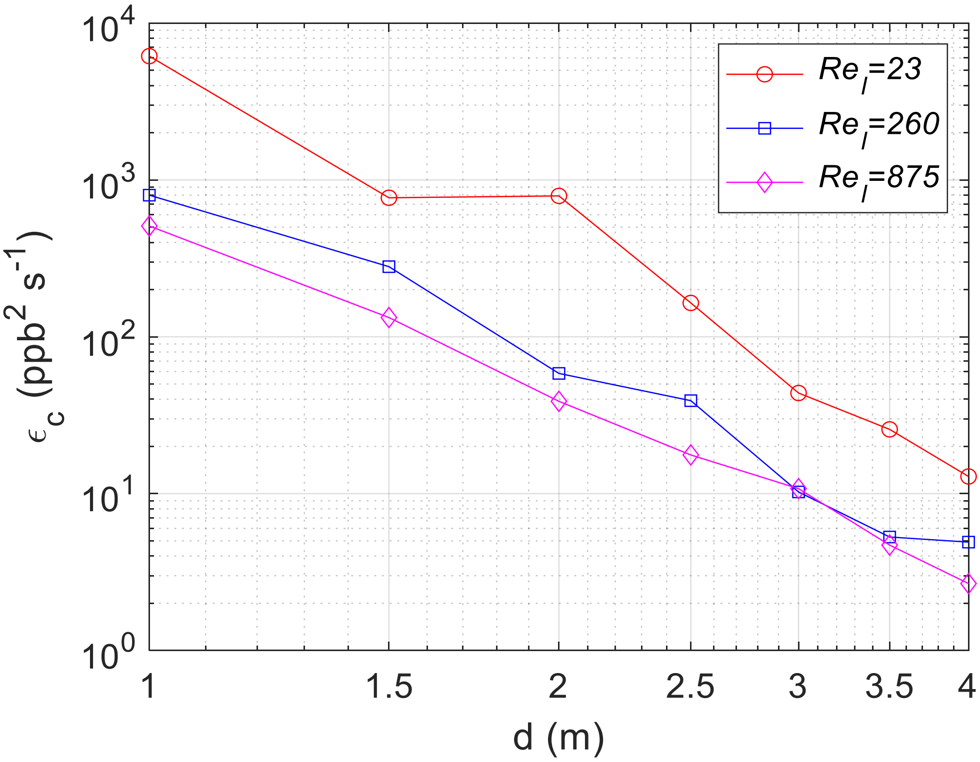

Figure 8.9: Variation of information dissipation rate ϵ_c of the molecular signals with distance d from Tx for three different values of the Reynolds number Re_l for modified turbulence.

8.5 Results and Discussion

8.5.1 Information Length Scale

Analogous to the Kolmogorov microscale η for turbulence, one can define a characteristic length scale, η_c, for the molecular information. When the length scale of the eddies is smaller than η_c, the propagation of the information molecules is dominated by diffusion. The kinetic energy of the molecules is small and the Reynolds number Re_η is of order unity. Therefore inertial effects are negligible and viscous forces cause dissipation of energy.

The length scales η and η_c are related by the Schmidt number (cf. [Davidson, 2015]). This non-dimensional number is defined as $Sc = \nu/\alpha$ and characterizes the ratio of momentum diffusivity, ν, and mass diffusivity, α. When $\nu > \alpha$ then vorticity diffusion is more effective than the diffusion of C and vice versa.

For the current experiments with Rhodamine in water the data of [Culbertson et al., 2002] provide $Sc \sim 2100$. This value implies that the diffusion of vorticity is substantially more effective than mass diffusivity. Therefore it is expected that a fine-scale structure of the concentration will develop such that $\eta_c < \eta$.

For high Schmidt number, η and η_c are related by [Davidson, 2015]

$$\eta_c \sim \eta(\frac{\alpha}{\nu})^{1/2} \ . \tag{8.9}$$

Thus, for $Sc = 2100$ one has $\eta_c/\eta \approx 0.02$. The range between η_c and η is referred to as the viscous-convective subrange in the literature [Davidson, 2015]. From (8.8) and (8.9) one finds for the current study where $Re_l = 23, 260, 875$ that $\eta_c = 0.011, 0.0084, 0.0049$ mm, respectively. Thus, η_c decreases with increasing Re_l. This implies that, theoretically, smaller information structures can be embedded in flows at higher Reynolds numbers.

In the context of MC the main implication of these considerations is that η_c is the theoretical smallest scale for which messages from a molecular signal concentration can be decoded. For values that lie below the diffusion-dominated scale η_c, it will no longer be possible to recover the original signal.

8.5.2 Information Dissipation Rate

In the preceding section η_c is the transition length scale between the energy containing and diffusion-dominated length scales. As is discussed in [Davidson, 2015] the quantity arises from considerations that suggest that the energy cascade resulting in the energy dissipation rate of (8.5) should be accompanied by a corresponding cascade of $\langle C^2 \rangle$. The discussions conclude that when the same mechanism is used to create the turbulence and the scalar fluctuations, as is the case in our experiments, then the flux of scalar $\langle C^2 \rangle$, can be estimated by [Davidson, 2015]

$$\epsilon_c \sim \frac{\langle C^2 \rangle}{l/u} \ . \tag{8.10}$$

The expression in (8.10) warrants a comment. In conventional diffusion-based MC, at nano scales, the of the concentration $\langle C^2 \rangle$ is ordinarily regarded as resulting from random noise with constant probability distribution [Nakano et al., 2013; Abbaszadeh et al., 2019]. Similarly, in steady homogeneous isotropic turbulence the statistics of the noise of the channel would not change with location such that $\langle C^2 \rangle$ would also remain constant. However, in the presence of a disturbance-generating device, such as the turbulence-generating obstacle in Fig. 8.1, the variance $\langle C^2 \rangle$ is modified according to the particular characteristics of the device in place and, therefore, $\langle C^2 \rangle$ changes with the spatial separation from the device. Thus, the device-specific modifications of $\langle C^2 \rangle$ become an inherent part of the MC channel.

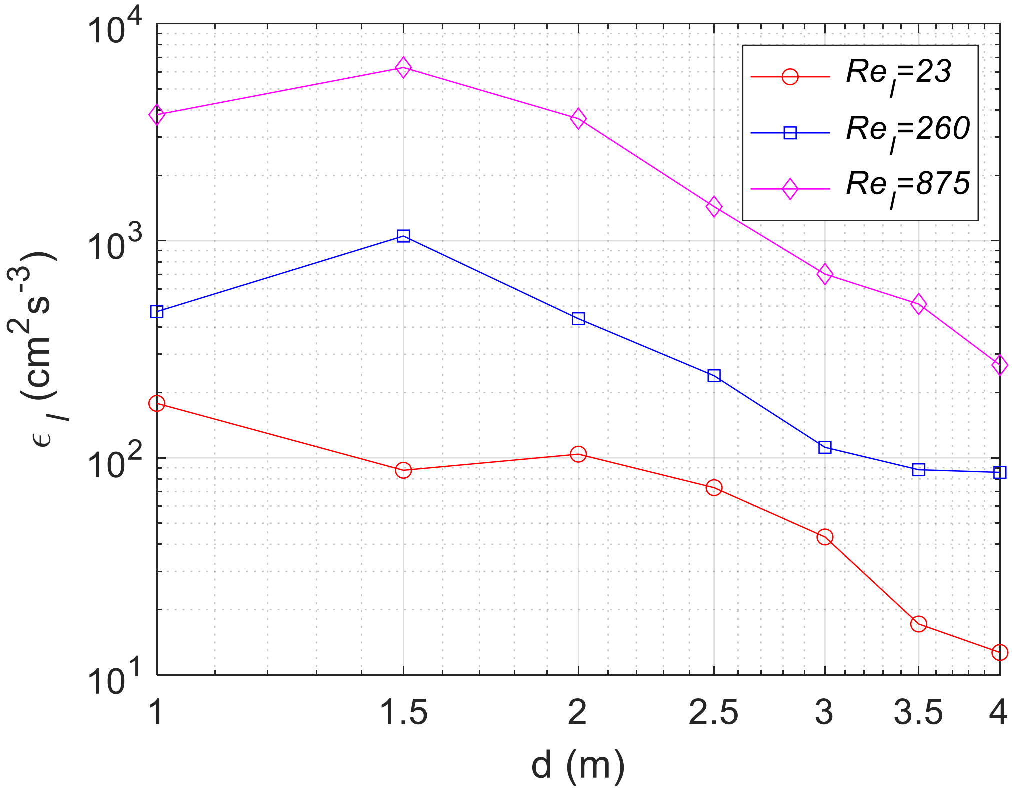

Figure 8.10: Energy dissipation rate, ϵ_l vs. distance from transmitter.

Figure 8.8 displays the decrease of $\langle C^2 \rangle$ as a function of the distance d from Tx in the downstream flow field of the obstacle for three different values of Re_l. The figure also reveals that, in the present case one has, approximately, $\langle C^2 \rangle \propto d^{-3.3}$.

Similar to (8.5), the information dissipation rate ϵ_c of (8.10) is calculated using the length scale l and the velocity scale u for the largest eddies which can be inferred from signals measured by the UVP probe (cf. Fig. 8.6). Figure 8.9 displays ϵ_c as a function of the distance d for three different values of the Reynolds number Re_l.

The figure reveals two results. Firstly, the information dissipation rate decreases with increasing distance d from Tx. This means that, as the information carrying tracer gets diluted to successively lower concentrations the rate at which it dilutes further must decrease. Secondly, at any particular distance d the information dissipation rate also decreases with increasing Re_l.

For comparison to ϵ_c of Figure 8.9 the energy dissipation rate ϵ_l from (8.5) is displayed in a corresponding plot in Fig. 8.10. Figure 8.10 shows that ϵ_l also decreases with increasing distance d. Most importantly, however, the figure reveals

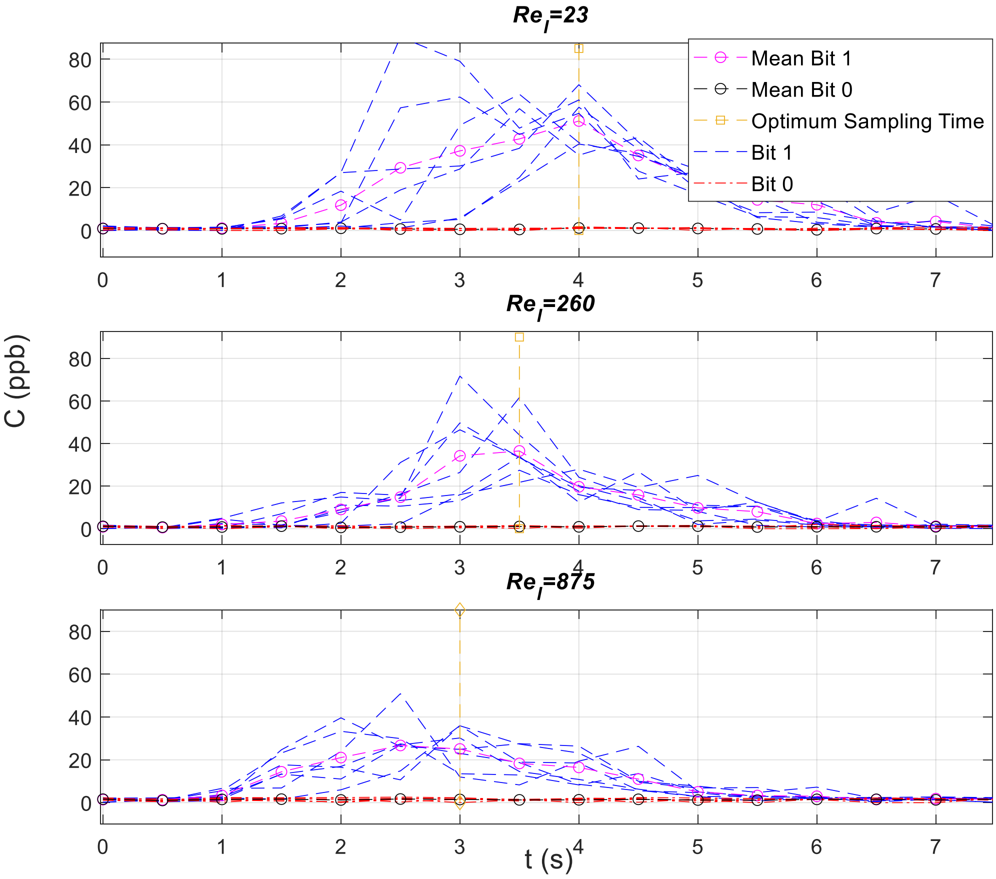

Figure 8.11: Superposition of temporal concentration variations for seven individual bit '1' and bit '0' signals in modified turbulence and their associated respective mean curves for three different values of the Reynolds number Re_l ($d = 1.5$ m).

that, contrary to ϵ_c, for any particular distance d the value of ϵ_l increases with Re_l.

The result that the information dissipation rate ϵ_c decreases with increasing Re_l may appear counter intuitive because stronger turbulence levels at higher Reynolds numbers have increased energy dissipation rates. However, increased turbulence leads to more efficient scalar mixing and, therewith, the power of the molecular signal quickly reduces to low levels. Accordingly the information dissipation rate necessarily reduces due to the remaining low information content available. This issue is illustrated in Fig. 8.11. The figure shows the superposition of seven individual bit '1' and bit '0' signals together with their associated respective mean curves in the modified turbulence. The figure illustrates that the information amplitude has reduced to low levels for the highest value of Re_l.

In summary, the issues of turbulence and mixing of passive scalars are of fundamental relevance to macroscale MC systems. From the viewpoint of information theory, it is important to understand that the energy cascade and the associated information cascade are interrelated and they cannot be examined separately.

8.5.3 Mutual Information

In the current context, the transmitted signal is represented by the concentration of ejected fluorescent liquid, and the corresponding received signal is the concentration at the receiver with the unsteady turbulence background. We saw in the previous chapter that the mutual information between the scalar input and output random variables X and Y quantifies the uncertainty reduction of the random variable X or Y, given the observation of another one.

$$\begin{aligned} I(X;Y) &= H(X) - H(X|Y) = H(Y) - H(Y|X) \\ &= \sum_x \sum_y P(X=x, Y=y) \log \frac{P(X=x, Y=y)}{P(X=x)P(Y=y)}, \end{aligned} \tag{8.11}$$

where $H(\cdot)$ is the entropy function, and $P(\cdot)$ represents the probability. Note that the probability distribution functions are required to obtain the analytical mutual information.

To avoid the strong turbulence effect in the near field, the concentration value with steady turbulence at $d = 1\,\mathrm{m}$ can be sampled as the transmitted signal. In each realization, the transmitted concentration signal has a sharply rising trend to reach its peak at the first stage, and it then undergoes a rapid decline.

Since there are multiple samples of the transmitted signal, we may further consider the mutual information between the n-dimensional random vector $(X_1, X_2, \ldots, X_n)$ and random variable Y. To find the dependency between the samples of the transmitted signal at different times, mutual information can be used as the metric [Noel et al., 2014]. Without loss of generality, we consider $I(X_1, X_2)$, where X_1 and X_2 are the observation random variable sampled at t_1 and t_2, and their time difference is defined by

$$\Delta t = |t_2 - t_1| = nT_s, \tag{8.12}$$

where n is an integer, and T_s represents the sampling period. Due to the absence of probability density functions, we resort to Kraskov's method, which provides a way for mutual information estimation that only requires the data set of random variables [Kraskov et al., 2004]. In light of this, the roughly estimated mutual information between the samples that has various time difference is shown in Fig. 8.12.

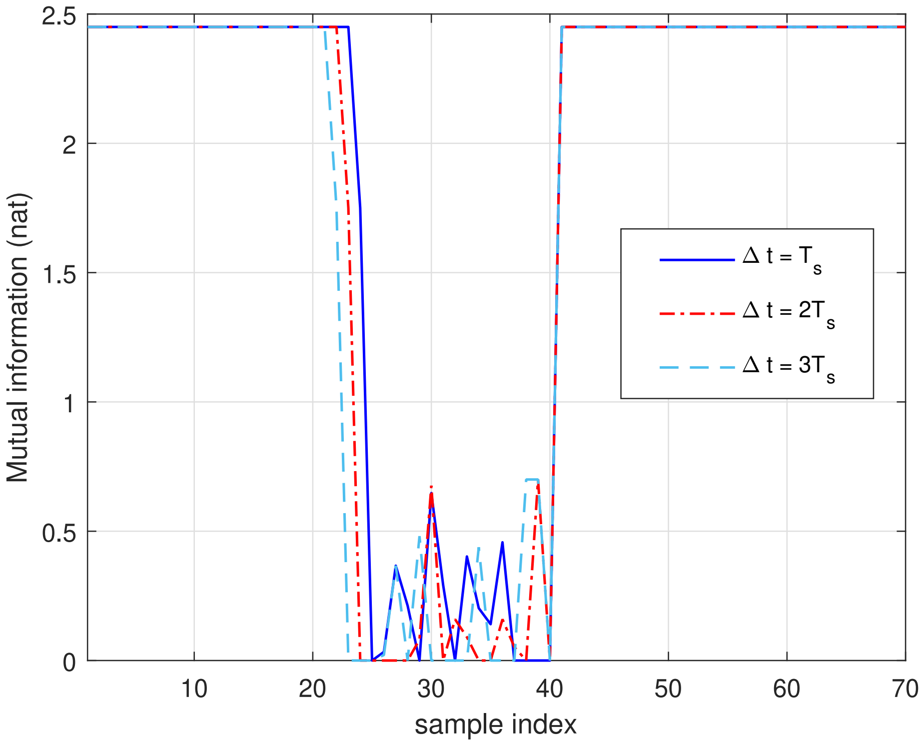

Figure 8.12: $I(X_1; X_2)$ with various Δt.

Intuitively, the neighbour samples have strong dependency.

By using the chain rule [Cover and Thomas, 2006], we have

$$I(X_1, X_2, \ldots, X_n; Y) = \sum_{i=1}^{n-1} I(X_i; Y | X_1, X_2, \ldots, X_{i-1}). \tag{8.13}$$

Hence, compared with (8.11), one may obtain higher mutual information by using the random vector as input instead of the scalar random variable. Yet, its computation requires more probability distribution functions, making the analytical results hard to obtain.

8.6 Summary

Waterborne chemical plumes were studied as a paradigm for a means of MC at macro scales. In experiments information was modulated onto chemical plumes represented by means of pulse sequences of a fluorescent tracer. As fluid turbulence mixes the tracer with the ambient carrier fluid and spatiotemporal concentration fluctuations are established in the flow field whose development is governed by the background turbulence field.

Results from the theory of fluid turbulence describing the turbulent energy cascade were applied and interpreted in terms of a corresponding information cascade associated with the mixing of the tracer. This enabled characterizing the theoretical critical information micro-scale below which information modulated onto the plume can no longer be decoded. This scale decreases with increasing turbulence which implies a theoretical potential for encoding smaller information structures at higher Reynolds number. Moreover, the information dissipation rate was found to decrease for the increased turbulence levels at higher Reynolds number. The latter result arising due to more efficient mixing at higher Reynolds numbers which decreases the remaining power of the molecular signal.

In summary, we started by quantifying the uncertainty in the transmitter. After that, we focused on the channel part of the communication system. We proposed channel model and quantified the information cascade in TDMC channels. Until now, we have not discussed about the receiver of the communication system. In order to investigate the receiver, we will take a detour to the micro-scale MC and we will design a receiver experimentally that can detect molecules of sizes nano and micron. The reason behind this is to get a rough idea that how small scale detection works. This would pave the way for the future studies to encode tons of information on the DNA and other proteins.

Chapter 9

Experimental Design of Single Molecule Sensing

9.1 Motivation

The goal of the final part of the project, which focused on macroscopic molecular communication, is to begin a short exploratory/preliminary study to investigate the feasibility of micro/nano communication. To this end, we have developed an experimental set up and designed a detector (biosensor) in order to sense Bovine Serum Albumin (BSA) protein molecules by means of a nanopore [Wanunu, 2012]. In principle, nanopore works based on the simple resistive pulses and the molecules can be detected by the exclusion of ions when they go through a nanoscale channel. Our results show that the sensor works efficiently in detection of BSA molecules. In future, this system can be employed to decode the information from DNA molecules.

It is emphasized that it was not the intention to proceed all the way to conducting experiments employing DNA. This is currently substantially beyond Warwick's capabilities and beyond the scope of the project. The goal here is to begin exploring the challenges lying ahead and involved in progressing to micro/nano research in a follow-on PhD project to be conducted by another student.

9.1.1 Review of Nanopore Sensing

Nanopore is a single-molecule sensor that allows biomolecules such as DNA, RNA, protein, non-biological polymers, etc. to be detected in a label-free manner. Due to the fact that biological analytes are often hard to detect purely on basis of their intrinsic physical properties, biosensors often require labels such as enzymes and fluorescent or radioactive molecules attached to the targeted analyte. As a result, the final sensor signal corresponds to the amount of labels, representing the number of bound target molecules. As a drawback, label-based technologies are often labor- and cost-intensive as well as time-consuming. In addition, labeling of biomolecules can block active binding sites and alter the binding properties. Altogether, this may adversely affect the affinity-based interaction between the recognition elements and the target molecules. In contrast, label-free biosensing technologies, by definition, do not require the use of labels to facilitate measurements. Instead, they utilize intrinsic physical properties of the analytes, such as molecular weight, size, charge, electrical impedance, dielectric permittivity, or refractive index, to detect their presence in a sample. Label-free biosensing methods have made enormous progress in recent years due to their ability for rapid and inexpensive bio-detection in small reaction volumes. Moreover, they lend themselves for integration into lab-on-chip platforms and allow monitoring the concentration of target analytes in real time.

Physically, nanopore refers to thin and highly insulating membrane that has a nanometer sized channel [Wanunu, 2012]. Nanopore is a bridge between two reservoirs (see Fig. 9.1), so analytes and electrolyte solution can only pass through this nanochannel to go to another reservoir. The main driving force is an electric field which induces an ionic current that is proportional to the cross-sectional area and length of the nanochannel. When an individual analyte passes through the nanopore, the pore conductance changes according to the size and surface charge of the analyte [Hoogerheide et al., 2009]. This *translocation event* is sensed by nanopore and an ionic current drop is observed in the received signal (see Fig. 9.1).

David Deamer visualised the concept of nanopore sensing in his notebook for the first time in 1989 [Deamer et al., 2016] and six years later, it was filed as a patent [Church et al., 1998]. In 1996, the first nanopore that made from α-hemolysin[1] has been used for sensing nucleic acid [Kasianowicz et al., 1996]. They showed that single stranded DNA (ssDNA) can successfully passes through the α-hemolysin by the electrophoresis forces and they observed ionic current drop during ssDNA translocation. In order to confirm that ssDNA passed the nanopore, they employed polymerase chain reaction [2] (PCR) followed by gel electrophoresis [3] of the solution in the opposite reservoir. They envisaged nanopore as a tool for the next

---

[1] α-hemolysin is a natural protein secreted by *Staphylococcus aureus.*

[2] Polymerase chain reaction (PCR) is a method widely used to rapidly make millions to billions of copies of a specific DNA sample, allowing scientists to take a very small sample of DNA and amplify it to a large enough amount to study in detail.

[3] Gel electrophoresis is a method for separation and analysis of macromolecules (DNA, RNA and proteins) and their fragments, based on their size and charge. It is used in clinical chemistry to separate proteins by charge or size (IEF agarose, essentially size independent) and in biochemistry and molecular biology to separate a mixed population of DNA and RNA fragments by length, to estimate the size of DNA and RNA fragments or to separate proteins by charge.

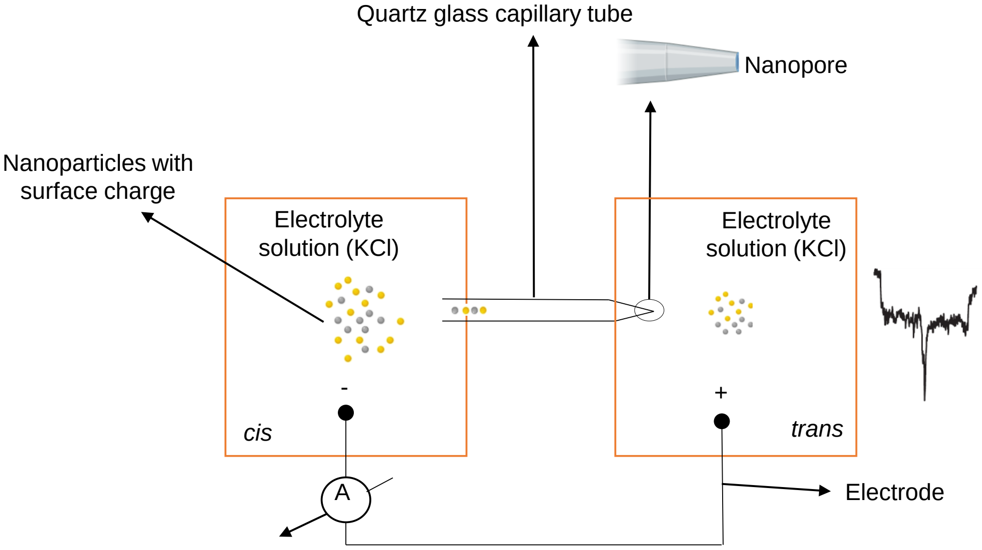

Figure 9.1: Schematic of nannochannel. The nanoparticles are added to the *trans* reservoir and they are driven into the nanopore by electrophoresis force. Grounded Ag/AgCl electrode is placed in *trans* and active Ag/AgCl electrode is placed in *cis*.

generation DNA sequencing and they claimed that the saptiotemporal resolution and mechanical robustness of nanopore needs improvements for practical use. In 1999, Akeson et al. [1999] showed that nanopore is able to discriminate between different nucleotides such as polyadenine, polycytosine, and polyuracil. They showed that each nucleotide generates a unique ionic current drop in terms of magnitude and duration during translocation through α-hemolysin nanopore. The main problem that they faced was the translocation speed and they claimed that slower translocation is required in order to resolve each single molecule. Therefore, several strategies have been proposed to slow down the translocation of nucleotide [Howorka et al., 2001; Venkatesan and Bashir, 2011; Derrington et al., 2010]. One of the state-of-the-art idea was to employ phi29 DNA polymerase enzyme in order to reduce the translocation speed. This enzyme was bound to DNA and slowed down the translocation. [Cherf et al., 2012; Schneider and Dekker, 2012].

In early 21 century, the solid-state nanopores have been emerged for the first time. Solid-state nanopores do not have the limitations associated with the biological nanopores (e.g. α-hemolysin) such as physical and chemical instability and unmodifiable pore size [Li et al., 2001; Dekker, 2007; Storm et al., 2003]. Inspired by biological nanopores, conventional solid-state nanopores are made by perforating a nanopore in 10-20 nm freestanding membrane silicon nitride (SiN) that is supported by a silicon (Si) substrate. Solid-state nanopore has adjustable pore size and it is robust in contact with various biomolecules. The problem of translocation speed in solid-state nanopore is more important than biological nanopore since the the speed is few orders of magnitude faster in solid-state nanopore [Venkatesan and Bashir, 2011]. Several solutions have been reported to solve the translocation speed problem: changing experimental conditions such as changing the electrolyte solution [Fologea et al., 2005; Kowalczyk et al., 2012], employing optical or magnetic tweezers to drag the analyte molecules to the nanopore [Hyun et al., 2013; Keyser et al., 2006a,b], decorating the nanopore surface chemically to drag molecule by surface interaction [Banerjee et al., 2015; Larkin et al., 2013; Krishnakumar et al., 2013; Squires et al., 2013].

Another major problem associated with the solid-state nanopores is low spatiotemporal resolution. In 2010, graphene membrane was proposed to improve the resolution of the solid-state nanopores [Garaj et al., 2010; Merchant et al., 2010; Schneider et al., 2010]. After that, other materials such as hexagonal boron nitride (h-BN) [Park et al., 2016] and molybdenum disulfide (MoS2) [Feng et al., 2015] were reported. After that, the glass nanopipettes has been proposed as a cost-effective and high-sensitive nanopores [Kong et al., 2016]. The fabrication of glass nanopipettes is easier than previous solid-state nanopores and it allows the user to precisely control the dimensions of the nanopore. Recently, several companies such as Oxford Nanopore Technology and Ionera have succeeded in producing commercial nanopores [Jain et al., 2016].

9.2 Experimental Set-up

9.2.1 Device Fabrication

The capillary tubes that are used in this experiment are made of quartz with inner diameter 0.2 mm and outer diameter 0.5 mm and containing a fused filament. In order to clean the capillaries, they are sonicated in acetone for 30 min followed by drying. A laser assisted capillary puller (Sutter P-2000) is used to draw down the capillary to nanometer scale. The capillary puller applies forces to the two end of the capillary while a CO_2 laser is concentrating on the centre of the capillary and melting the quartz. Finally, the capillary tapers down and breaks up into two pieces at the centre of the capillary. In order to measure the size of the nanopore, Transmission Electron Microscopy (TEM) is employed and it shows that the size of the nanopore is 30 nm (see Fig. 9.2). The next step is to place the capillary in a polydimethylsiloxane (PDMS) in order to reduce the electrical noise. For this purpose, a mold is 3D printed

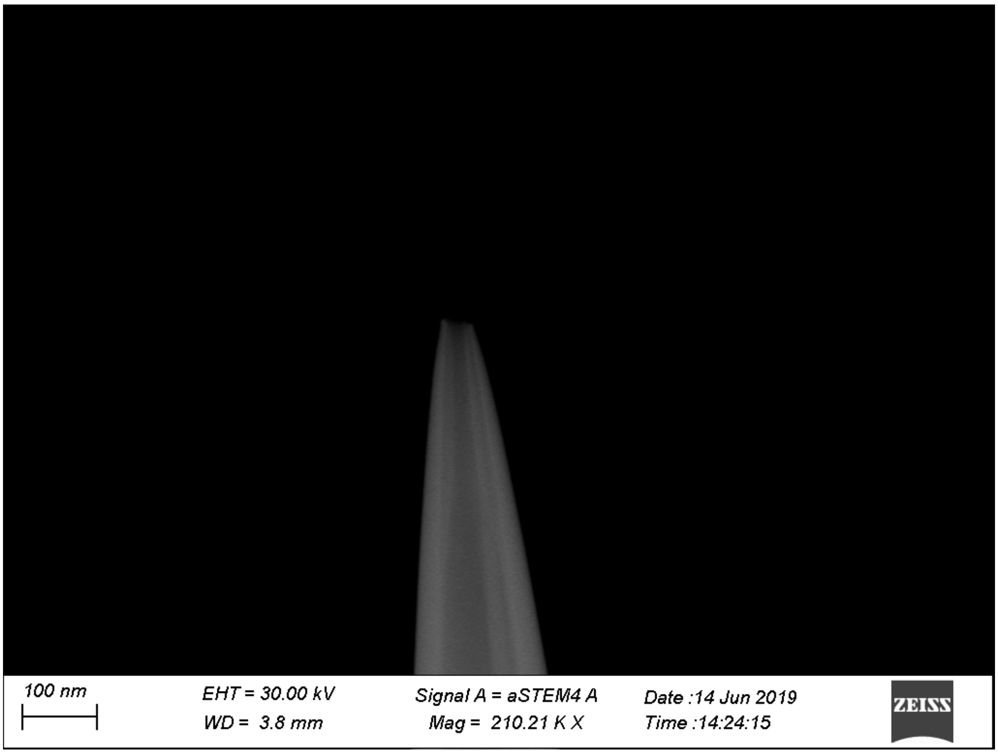

Figure 9.2: TEM image illustrating the size of the nanopore (30 nm).

with ABS filament which is durable in high temperature. Then, PDMS is prepared by mixing elastomer and curing agent in a ratio of 10:1 and it is cured in the mold at 60°C for 24 h. The glass capillary are placed in a groove located in the cured PDMS and then, it is bonded to a glass slide by plasma. For the sealing of the area between the capillary and PDMS, we poured uncured PDMS on the capillary and baked it at 120°C for to cure PDMS. The electrolyte solution that we used for the experiment was 10 mM Tris–EDTA (pH = 8.0) buffer and 1 M KCl. Also, we added 16 nm BSA protein to the solution and we tried to detect it. A grounded Ag/AgCl electrode is placed in the reservoir faced the nanopore (*trans*) and the active Ag/AgCl electrode is placed in the other reservoir (*cis*).

9.2.2 Electrical Measurements

As illustrated in Fig. 9.3(a), the main electrical components are 1) amplifier (MultiClamp 700B), 2) oscilloscope (Digidata 1550B). Amplifier is a computer-controlled microelectrode device that is used for electrophysiology and electrochemistry. The amplifier can support up to two headstages. Headstages convert the voltage to the

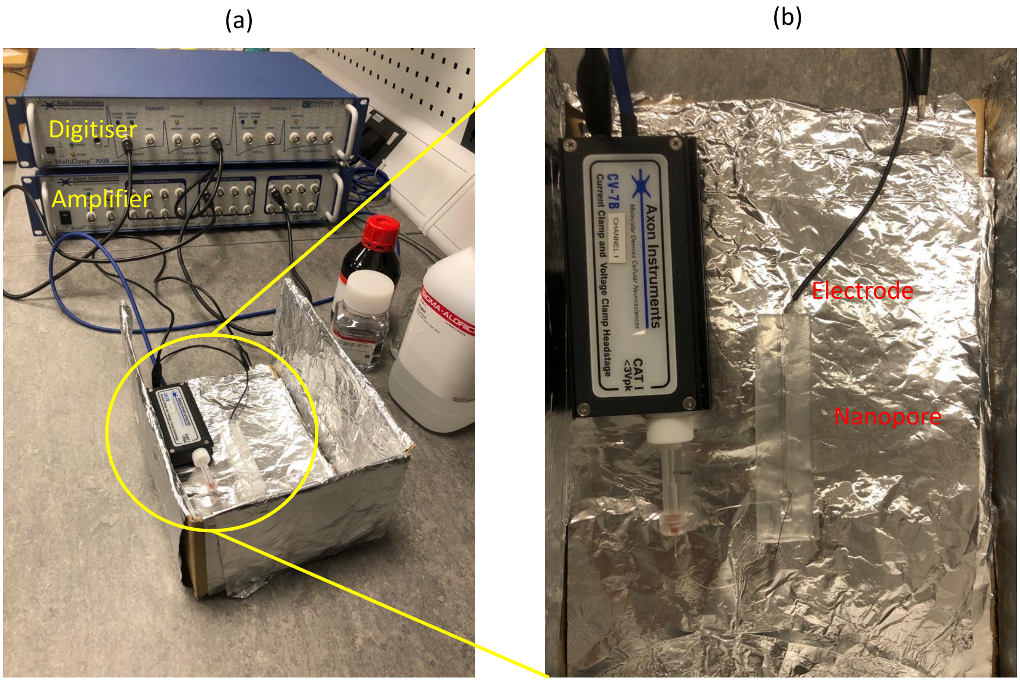

Figure 9.3: a) MultiClamp 700B amplifier to generate voltage difference, and Digidata 1550B digitiser to record the acquired current signal, b) Glass capillary that is placed in the PDMS and two electrodes are connected to the the headstage. Headstage is the bridge between the capillary and amplifier.

current. The current signal is filtered at 20 KHz with a 6 pole Bessel filter. The oscilloscope is a high-resolution, low-noise digitiser that is particularly designed for electrophysiology experiments. The oscilloscope sends and receives signals from microelectrode amplifiers. In this experiment, the current is recorded at 100 KHz sampling rate with 16 bit resolution using pClamp software. Current traces are analysed in Clampfit software which has been designed for Digidata 1550B.

9.3 Results

Current-Voltage (IV) diagram for the KCl electrolyte solution with the concentration of 1 mM [4], 10 mM, and 100 mM is illustrated in Fig. 9.4. Based on the Ohm's law, a linear relationship should exist between the voltage and current. According to Fig. 9.4, by increasing the voltage from -200 mV to +200 mV, the ionic current increases linearly for different KCl concentrations. This verifies the system perfor-

---

[4] “mM” is the molar mass of KCl solution. Molar mass is the mass of the KCl sample divided by the amount of substance in that sample, measured in moles.

mance based on the Ohm's law. Also, by increasing the concentration of electrolyte solution, the slope of IV diagram increases. This is because of increasing the number of ions travelling through the nanopore.

In the next step, BSA nanoparticles are added into *cis* reservoir and 100 mV is applied across the channel. The isoelectric point (pI) of the BSA protein is ranging from 5.1 to 5.5 pH [Peters Jr, 1985]. Therefore, the BSA protein has negative surface charge at pH$\sim$8. It is noteworthy that the isoelectric point, is the pH at which a molecule carries no net electrical charge or is electrically neutral in the statistical mean. Since BSA protein has negative surface charges, they move towards the oppositely charged electrode and there will be a balance between the force trying to move it towards the electrode, the electrostatic force and the friction force due to the viscosity of the liquid. The resulting terminal velocity will be proportional to the electric field and the proportionality constant is called the electrophoretic mobility, μ_e and it is given by:

$$v_e = E\mu_e \tag{9.1}$$

where v_e is electrophoretic velocity (measureable), E is electric field strength (defined), and μ_e is the electrophoretic mobility (calculated). The raw ionic current signal is illustrated in Fig. 9.5. Each spike in the signal is called *event*. The events show that the BSA molecules have arrived to the nanopore and they have obstructed the passage of KCl ions. The detection threshold is considered -9 pA which means that if the spike amplitude (current-drop) is less than -9 pA, the BSA molecule has passed the nanopore, and if it is more than -9 pA, the spike may occur due to the noise (See Fig. 9.6). From the shape of an individual event, useful information about the physical and chemical properties of the BSA molecules can be inferred. Other than that, the statistics of the events give useful information about the analytes.

One of the interesting statistic is event charge deficit (ECD) histogram. The definition of ECD is the integral of obstructed ionic current over the duration of an event, $\int \Delta I(\text{event})dt$. The unit of ECD is kilo electron charge. The ECD is used to distinguish between different forms of proteins. For instance in DNA proteins, if the number of the base pairs is the same, the ECD would be the same regardless of the form of the DNA (linear, circular relaxed, or supercoiled form) and vice versa. According to Fig. 9.7, the fitted Gaussian function to the histogram is narrow and has small standard deviation which confirms that the form of the BSA molecules are the same. Another useful statistic is the peak amplitude histogram. At nanoscale, it is difficult to make sure that all the particles have the same size. To understand whether the particles are monodisperesed or not, peak amplitude histogram can be

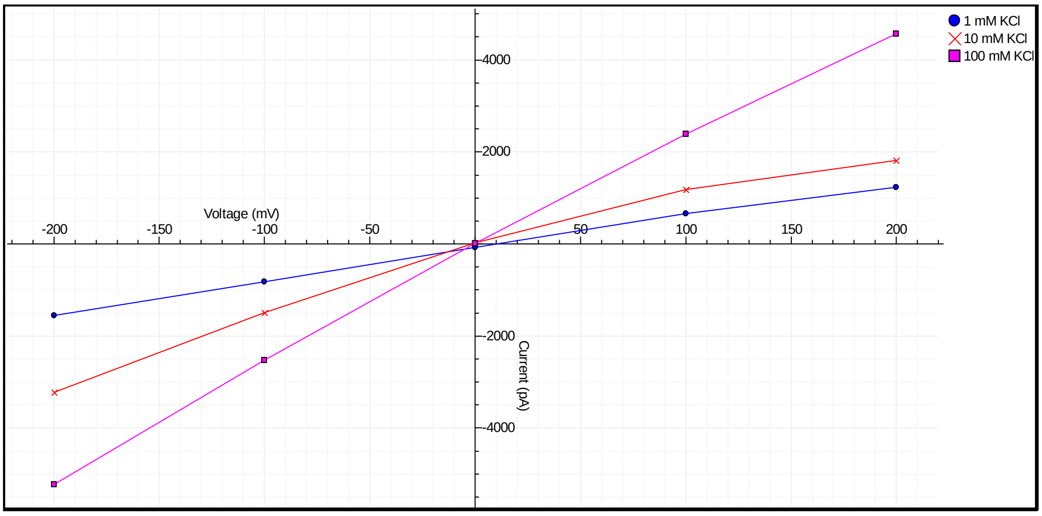

Figure 9.4: I-V digram for three different concentrations of KCl electrolyte solutions.

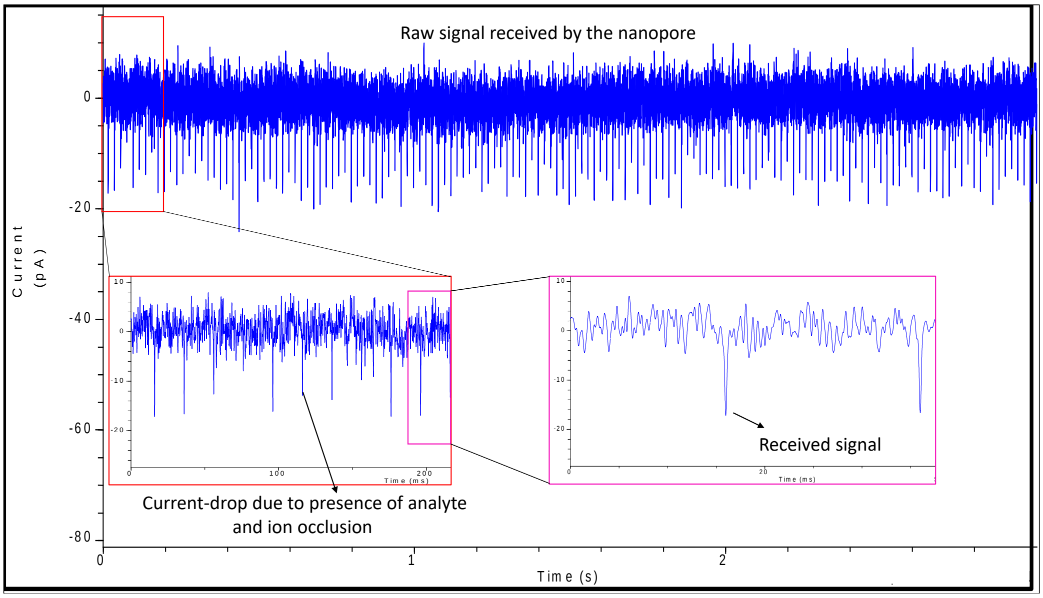

Figure 9.5: The raw ionic current signal acquired in this experiment. The spikes show that the BSA molecules are passing through the nanopore. Each individual current drop is associated with one BSA molecule translocation.

used. In other words, same size particles leads to the same peak amplitude. As can be seen in Fig. 9.8, the histogram has Gaussian distribution and thus, we can consider the the particles as monodispersed.

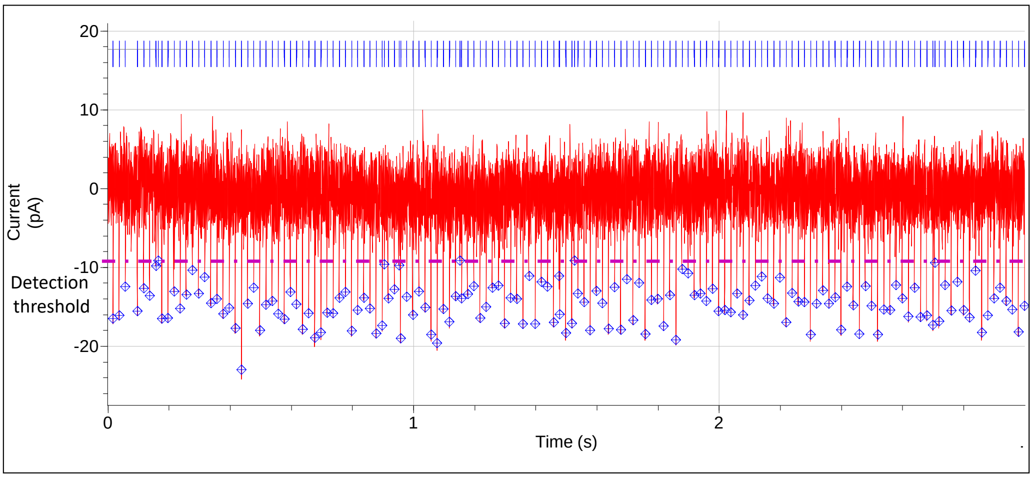

Figure 9.6: Threshold-based signal detection used to detect the BSA molecules when they are passing through the nanopore. The detection threshold is -9 pA.

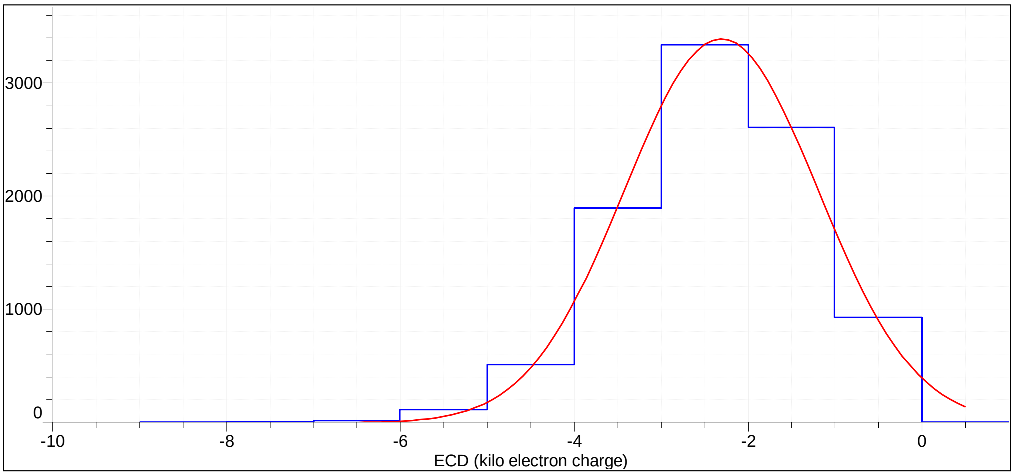

Figure 9.7: Event charge deficit (ECD) histogram for BSA molecules. It confirms that most of the BSA molecules have the same form.

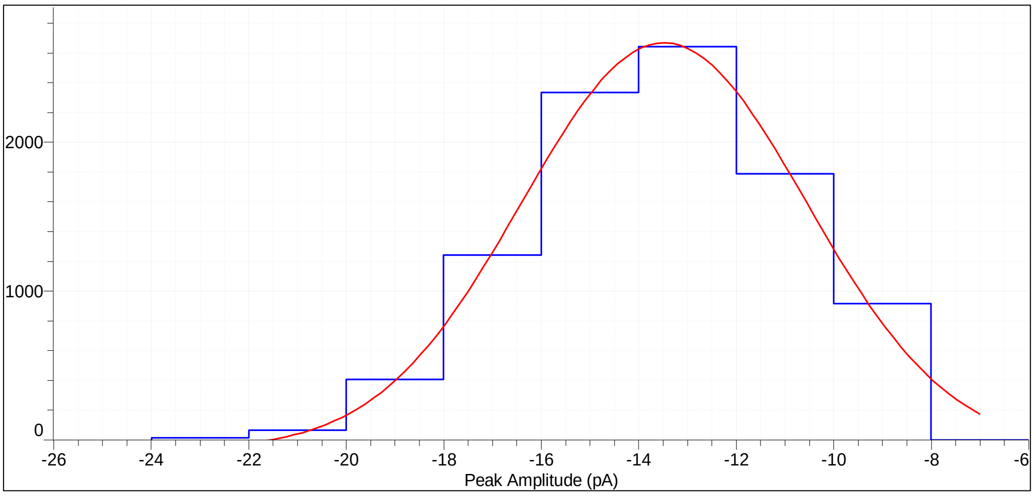

Figure 9.8: Peak amplitude histogram for BSA molecules. It shows that the BSA molecules are monodisperesed.

Chapter 10

Conclusions and Future Work

10.1 Conclusion

The research summarized in this thesis is involved with the investigation of molecular communication in turbulent flow. Information embedded in turbulent flow properties undergo stochastic behaviour when propagating from a transmitter to a receiver. This is due to the high dimensionality and continuous dynamic forces of the environment. Computational fluid dynamics codes and experimental techniques were employed to study molecular communication in complex environments dominated by turbulent flow.

In the first step, we quantified the uncertainty in the transmitter part of the TDMC channels. Polynomial chaos expansion was utilized to show how the uncertainty in input parameters propagates to uncertainty in the received signal. The application of the PCE method results in significant time saving compared to Monte-Carlo simulations. It was shown that the uncertainty in the input parameters is mostly reflected in the peak of the channel response while the tail is not affected. This means that only the signal strength is subject to effects by the uncertainty while the ISI is not. Moreover, the channel response is more sensitive to the uncertainty of the inlet velocity than to the initial concentration.

Afterwards, we concentrated on the channel part of the macro-scale MC systems.In the channel, coherent fluid flow structures was used to transmit the information in turbulent diffusion channels. It was then demonstrated how vortex rings can effectively mitigate ISI. It was shown that the ISI is reduced by one order of magnitude compared to noncoherent puff emissions.

As far as generating the vortex rings requires an accurate methodology, then, we focused on the channel where the transmitter only encode the information on normal puffs rather than the vortex rings. Before modeling the channel, we investigated the linearity of the turbulent diffusion channel for sequential signal emissions. It was demonstrated that turbulent diffusion channel is linear. Furthermore, the received molecular signal that includes ISI is modelled. The adopted theoretical model utilizes a base of four signal types that includes the adequate information to model the received signal for a sequential emission case. The analytical model enabled formulating the effect of ISI via SIR_n.

Thereafter the statistical noise distribution and mutual information with respect to the key fluid dynamic parameters was quantified. At first, both the additive- and jitter-noise distributions in steady flow conditions are characterised statistically and a new channel model for the turbulent case is proposed. It was found that the mutual information is maximized under certain transmission strategies and that it varies with the receiver size.

Inspired by the energy cascade of the turbulent flow, then, we showed that we can define information cascade concept. Waterborne chemical plumes were studied as a paradigm for a means of MC at macro scales. In experiments information was modulated onto chemical plumes represented by means of pulse sequences of a fluorescent tracer. As fluid turbulence mixes the tracer with the ambient carrier fluid and spatiotemporal concentration fluctuations are established in the flow field whose development is governed by the background turbulence field. Results from the theory of fluid turbulence describing the turbulent energy cascade were applied and interpreted in terms of a corresponding information cascade associated with the mixing of the tracer. This enabled characterizing the theoretical critical information micro-scale below which information modulated onto the plume can no longer be decoded. This scale decreases with increasing turbulence which implies a theoretical potential for encoding smaller information structures at higher Reynolds number. Moreover, the information dissipation rate was found to decrease for the increased turbulence levels at higher Reynolds number. The latter result arising due to more efficient mixing at higher Reynolds numbers which decreases the remaining power of the molecular signal.

The thesis concludes with a preliminary study on experimental micro/nano-scale communication. A biosensor commonly referred to as nanopore was used as a detector for nano-communication systems. It was shown that the nanopore could detect 16 nm BSA protein molecules. This paves the way for future experimental studies in micro/nano-scale communication to detect information embedded in DNA strands.

10.2 Future Work

10.2.1 Suggestions for Macro-scale MC

Future studies on macro-scale MC can focus on

- Analysing the mutual information of the turbulent case, where noise is non-Gaussian, and use these statistical noise models to analyse the impact on communication reliability, and design superior modulation coding schemes,
- Investigating the molecular MIMO and see how different molecular signals will affect each other in lateral direction and explore the notions of spatial diversity,
- Focusing on understanding the channel capacity as a function of uncertainty,
- Encoding information on the velocity components of coherent structures such as vortex ring,

10.2.2 Suggestions for Micro-scale MC

As discussed in the last chapter, it is possible to encode information on DNA strands and decode the information by means of nanopore (see Fig. 10.1). Indeed, compared to traditional communication and information systems, DNA communication systems promise to reduce encoding and storage cost by 100x for the same capacity and endurance performance. Furthermore, biological information systems offer a new dimension of secrecy and resilience against standard electronic attacks and countermeasures. Ultimately, DNA could be stored in living organisms. In this case, it would be relied on their capacity to self-replicate for storage (and transmission). However, the amount of continuous information that can be stored in DNA in a living organism is limited as it should not disrupt vital cellular processes.

For future work, it is suggested to develop a simple, yet highly secure, DNA barcode sorting method to enable the retrieval of information from a number of DNA strands. Current strategies rely on the decoding of a long single strand in a laboratory setting [De Silva and Ganegoda, 2016]. For DNA storage and communication to function outside a lab, it will require bacteria hosts. In such a case the long strand must be fragmented in order to fit inside bacteria without disrupting the host's functionalities. In this case, it is critical to be able to cut a long DNA strand into appropriate fragments and re-assemble them later on. It is also necessary to add a level of security as this is likely to be used in adversarial defence and security environments. So, it is suggested to use low resolution nanopore sensing to read the barcode formed by the combination of 1) the information bearing single carrier strand and 2) a number of

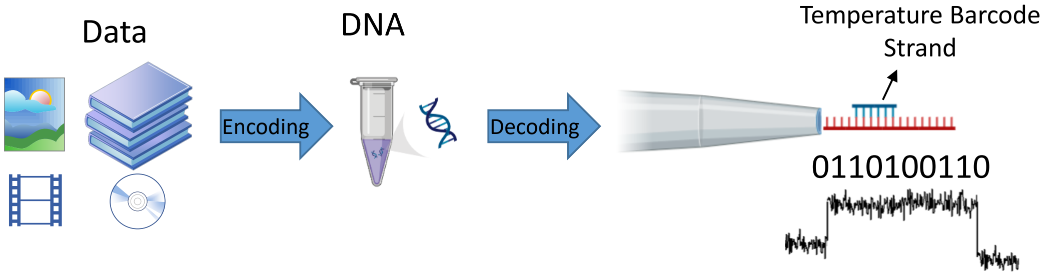

Figure 10.1: Schematic of data storage on DNA strands.

temperature-encrypted complementary short-strands. Every temperature-encrypted strand will be designed so as to have different lengths and therefore hybridise (in specific location) with the information bearing strand at a specific temperature. The system will be optimised so that the barcode coding for the "ID" of the information bearing strand is read at a specific temperature (known by the decoder).

After the barcode is read (at the right temperature), the strand will be passed on to a high temperature stage (above the melting temperature of the barcode forming complementary strands) before reaching a sequencer where the information bearing single strand will be read. This system will therefore enable the researchers to read the information stored on the DNA and assign it a unique ID. This approach is critical when trying to piece together information from various sources, but it can also be useful for additional security encoding such as considering the temperature as a layer of security to avoid eavesdropping in communication channels.

Bibliography

Nastaran Abadi, Amin Aminzadeh Gohari, Mahtab Mirmohseni, and Masoumeh Nasiri-Kenari. Zero-error codes for multi-type molecular communication in random delay channel. In *2018 Iran Workshop on Communication and Information Theory (IWCIT)*, pages 1–6. IEEE, 2018.

M. Abbaszadeh et al. Mutual information and noise distributions of molecular signals using laser induced fluorescence. In *Proc. IEEE Global Communications Conf. (GLOBECOM)*, pages 1–6, Waikoloa, USA, Dec. 2019.

Hulusi Acikgoz and Raj Mittra. Statistical analysis of electromagnetic structures and antennas using the polynomial chaos expansion method. In *Antennas and Propagation (EUCAP), 2017 11th European Conference on*, pages 798–800. IEEE, 2017.

Lara Adrian, Ronald J Adrian, and Jerry Westerweel. *Particle image velocimetry*. Number 30. Cambridge University Press, 2011.

Arman Ahmadzadeh, Vahid Jamali, and Robert Schober. Statistical analysis of time-variant channels in diffusive mobile molecular communications. In *GLOBECOM 2017-2017 IEEE Global Communications Conference*, pages 1–7. IEEE, 2017.

Bayram Cevdet Akdeniz, Ali Emre Pusane, and Tuna Tuğcu. A novel concentration-type based modulation in molecular communication. In *2017 25th Signal Processing and Communications Applications Conference (SIU)*, pages 1–4. IEEE, 2017.

Bayram Cevdet Akdeniz, Ali Emre Pusane, and Tuna Tugcu. Position-based modulation in molecular communications. *Nano communication networks*, 16:60–68, 2018.

Mark Akeson, Daniel Branton, John J Kasianowicz, Eric Brandin, and David W Deamer. Microsecond time-scale discrimination among polycytidylic acid, polyadenylic acid, and polyuridylic acid as homopolymers or as segments within single rna molecules. *Biophysical journal*, 77(6):3227–3233, 1999.

Ian F Akyildiz, Fernando Brunetti, and Cristina Blázquez. Nanonetworks: A new communication paradigm. *Computer Networks*, 52(12):2260–2279, 2008.

Ali Akbar Abbasian Arani, Ali Arefmanesh, and Amirhossein Niroumand. Investigation of fully developed flow and heat transfer through n-sided polygonal ducts with round corners using the galerkin weighted residual method. *Int. J. Nonlinear Anal. Appl*, 9(1):175–193, 2018.

Gunther Ardelt, Christoph Külls, and Horst Hellbrück. Towards intrinsic molecular communication using isotopic isomerism. *Open Journal of Internet Of Things (OJIOT)*, 4(1):135–143, 2018.

A Arefmanesh, AA Abbasian Arani, and A Niroumand. Thermally developing flow of al2o3-water nanofluid through regular n-sided polygonal ducts: A semi-analytic weighted residuals approach. *international journal of refrigeration*, 78:136–156, 2017.

Baris Atakan and Ozgur B Akan. Deterministic capacity of information flow in molecular nanonetworks. *Nano Communication Networks*, 1(1):31–42, 2010.

I. Atthanayake, S. Esfahani, P. Denissenko, I. Guymer, P. Thomas, and W. Guo. Experimental molecular communications in obstacle rich fluids. *Proc. ACM Int. Conf. on Nanoscale Comput. Commun. (NANOCOM)*, 2018.

IU Atthanayake, P Denissenko, YM Chung, and PJ Thomas. Formation–breakdown cycle of turbulent jets in a rotating fluid. *Journal of Fluid Mechanics*, 868:666–697, 2019.

Hamid G Bafghi, Amin Gohari, Mahtab Mirmohseni, Gholamali Aminian, and Masoumeh Nasiri-Kenari. Diffusion-based molecular communication with limited molecule production rate. *IEEE Transactions on Molecular, Biological and Multi-Scale Communications*, 4(2):61–72, 2018.

Chenyao Bai, Mark S Leeson, and Matthew David Higgins. Minimum energy channel codes for molecular communications. *Electronics Letters*, 50(23):1669–1671, 2014.

Shouvik Banerjee, James Wilson, Jiwook Shim, Manish Shankla, Elise A Corbin, Aleksei Aksimentiev, and Rashid Bashir. Slowing dna transport using graphene–dna interactions. *Advanced functional materials*, 25(6):936–946, 2015.

Dwight Barkley. Modeling the transition to turbulence in shear flows. In *Journal of Physics: Conference Series*, volume 318, page 032001. IOP Publishing, 2011.

Daniel Ben-Avraham and Shlomo Havlin. *Diffusion and reactions in fractals and disordered systems*. Cambridge university press, 2000.

Howard C Berg. *E. coli in Motion*. Springer Science & Business Media, 2008.

Jean Berthier and Pascal Silberzan. *Microfluidics for biotechnology*. Artech House, 2010.

Freek Boeykens, Hendrik Rogier, and Luigi Vallozzi. An efficient technique based on polynomial chaos to model the uncertainty in the resonance frequency of textile antennas due to bending. *IEEE Transactions on Antennas and Propagation*, 62 (3):1253–1260, 2014.

Thomas Breithaupt and Martin Thiel. *Chemical communication in crustaceans*. Springer Science & Business Media, 2010.

MA. Brend and PJ. Thomas. Decay of vortex rings in a rotating fluid. *Physics of Fluids*, 2009.

HH Brunn. Linearization and hot wire anemometry. *Journal of Physics E: Scientific Instruments*, 4(11):815, 1971.

HH Bruun and Hot-Wire Anemometry. Oxford science publications. *New York*, 1995.

VA Butenandt. About the sex-attractant of the silkworm bombyx mori. *presentation and constitution. Z. Naturforschg, b*, 14:283, 1959.

Sylvie Campagna, Jérôme Mardon, Aurélie Celerier, and Francesco Bonadonna. Potential semiochemical molecules from birds: a practical and comprehensive compilation of the last 20 years studies. *Chemical Senses*, 37(1):3–25, 2012.

Norman F Carlin and Bert Hölldobler. The kin recognition system of carpenter ants (camponotus spp.): Ii. larger colonies. *Behavioral Ecology and Sociobiology*, pages 209–217, 1987.

Samuel P Caro and Jacques Balthazart. Pheromones in birds: myth or reality? *Journal of Comparative Physiology A*, 196(10):751–766, 2010.

RT Cerbus and WI Goldburg. Information content of turbulence. *Phys. Rev. E*, 88 (5):053012, Nov. 2013.

Chris Chatfield. *The analysis of time series: an introduction.* CRC Press, Florida, US, 6th edition, 2004.

Jui-Sheng Chen, Yiu-Hsuan Liu, Ching-Ping Liang, Chen-Wuing Liu, and Chien-Wen Lin. Exact analytical solutions for two-dimensional advection–dispersion equation in cylindrical coordinates subject to third-type inlet boundary condition. *Advances in water resources*, 34(3):365–374, 2011.

Gerald M Cherf, Kate R Lieberman, Hytham Rashid, Christopher E Lam, Kevin Karplus, and Mark Akeson. Automated forward and reverse ratcheting of dna in a nanopore at 5-å precision. *Nature biotechnology*, 30(4):344–348, 2012.

Theodore S Chihara. *An introduction to orthogonal polynomials.* Courier Corporation, 2011.

G Church, DW Deamer, D Branton, R Baldarelli, and J Kasianowicz. Measuring physical properties. *US5795782*, 1998.

Stephen M Clifford and Daniel Hillel. Knudsen diffusion: The effect of small pore size and low gas pressure on gaseous transport in soil. *Soil science*, 141(4):289–297, 1986.

Marina Cole, JW Gardner, Z Ráczu, S Pathak, TC Pearce, J Challiss, D Markovic, A Guerrero, L Muñoz, G Carot, et al. Biomimetic insect infochemical communication system. In *SENSORS, 2009 IEEE*, pages 1358–1361. IEEE, 2009.

T. M. Cover and J. A. Thomas. *Elements of Information Theory.* Wiley, New Yourk, NY, USA, 2006.

John Crank. *The mathematics of diffusion.* Oxford university press, 1979.

Christopher T Culbertson, Stephen C Jacobson, and J Michael Ramsey. Diffusion coefficient measurements in microfluidic devices. *Talanta*, 56(2):365–373, 2002.

Ionut Danaila and Jérôme Hélie. Numerical simulation of the postformation evolution of a laminar vortex ring. *Physics of Fluids*, 2008.

Ionut Danaila, Claudiu Vadean, and Sterian Danaila. Specified discharge velocity models for numerical simulations of laminar vortex rings. *Theoretical and Computational Fluid Dynamics*, 2009.

Peter Alan Davidson. *Turbulence: an introduction for scientists and engineers.* Oxford University Press, 2015.

Pavani Yashodha De Silva and Gamage Upeksha Ganegoda. New trends of digital data storage in dna. *BioMed research international*, 2016, 2016.

David Deamer, Mark Akeson, and Daniel Branton. Three decades of nanopore sequencing. *Nature biotechnology*, 34(5):518–524, 2016.

Cees Dekker. Solid-state nanopores. *Nature nanotechnology*, 2(4):209–215, 2007.

Ian M Derrington, Tom Z Butler, Marcus D Collins, Elizabeth Manrao, Mikhail Pavlenok, Michael Niederweis, and Jens H Gundlach. Nanopore dna sequencing with mspa. *Proceedings of the National Academy of Sciences*, 107(37):16060–16065, 2010.

Maheshi Buddhinee Dissanayake, Yansha Deng, Arumugam Nallanathan, Maged Elkashlan, and Urbashi Mitra. Interference mitigation in large-scale multiuser molecular communication. *IEEE Transactions on Communications*, 67(6):4088–4103, 2019.

Andrew W Eckford. Nanoscale communication with brownian motion. In *2007 41st Annual Conference on Information Sciences and Systems*, pages 160–165. IEEE, 2007.

John T Edward. Molecular volumes and the stokes-einstein equation. *Journal of Chemical Education*, 47(4):261, 1970.

Ali Etemadi, Paeiz Azmi, Hamidreza Arjmandi, and Nader Mokari. Compound poisson noise sources in diffusion-based molecular communication. *IEEE Transactions on Communications*, 67(6):4104–4116, 2019.

Mohammad Farazmand and Themistoklis P Sapsis. A variational approach to probing extreme events in turbulent dynamical systems. *Science Advances*, 3(9):e1701533, 2017.

N. Farsad, N. Kim, A. Eckford, and C. Chae. Channel and Noise Models for Nonlinear Molecular Communication Systems. *IEEE Journal on Selected Areas in Communications*, 32, 2014.

Nariman Farsad, Weisi Guo, and Andrew W Eckford. Tabletop molecular communication: Text messages through chemical signals. *PloS one*, 8(12):e82935, 2013.

Nariman Farsad, Weisi Guo, Chan-Byoung Chae, and Andrew Eckford. Stable distributions as noise models for molecular communication. In *2015 IEEE Global Communications Conference (GLOBECOM)*, pages 1–6. IEEE, 2015.

Nariman Farsad, H Birkan Yilmaz, Andrew Eckford, Chan-Byoung Chae, and Weisi Guo. A comprehensive survey of recent advancements in molecular communication. *IEEE Communications Surveys & Tutorials*, 18(3):1887–1919, 2016.

Nariman Farsad, Christopher Rose, Muriel Médard, and Andrea Goldsmith. Capacity of molecular channels with imperfect particle-intensity modulation and detection. In *2017 IEEE International Symposium on Information Theory (ISIT)*, pages 2468–2472. IEEE, 2017.

J Feng, Ke Liu, Michael Graf, Martina Lihter, Roman D Bulushev, Dumitru Dumcenco, Duncan TL Alexander, Daria Krasnozhon, Tomislav Vuletic, Andras Kis, et al. Electrochemical reaction in single layer mos2: nanopores opened atom by atom. *Nano letters*, 15(5):3431–3438, 2015.

Richard P Feynman. There's plenty of room at the bottom. *California Institute of Technology, Engineering and Science magazine*, 1960.

Daniel Fologea, James Uplinger, Brian Thomas, David S McNabb, and Jiali Li. Slowing dna translocation in a solid-state nanopore. *Nano letters*, 5(9):1734–1737, 2005.

Benoit Fond, Christopher Abram, and Frank Beyrau. On the characterisation of tracer particles for thermographic particle image velocimetry. *Applied Physics B*, 118(3):393–399, 2015.

Robert A Freitas. *Nanomedicine, volume I: basic capabilities*, volume 1. Landes Bioscience Georgetown, TX, 1999.

Robert G Gallager. *Information theory and reliable communication*, volume 2. Springer, 1968.

Laura Galluccio, Alfio Lombardo, Giacomo Morabito, Sergio Palazzo, Carla Panarello, and Giovanni Schembra. Capacity of a binary droplet-based microfluidic channel with memory and anticipation for flow-induced molecular communications. *IEEE Transactions on Communications*, 66(1):194–208, 2017.

Slaven Garaj, W Hubbard, A Reina, J Kong, D Branton, and JA Golovchenko. Graphene as a subnanometre trans-electrode membrane. *Nature*, 467(7312):190–193, 2010.

Nora Garralda, Ignacio Llatser, Albert Cabellos-Aparicio, and Massimiliano Pierobon. Simulation-based evaluation of the diffusion-based physical channel in molecular nanonetworks. In *IEEE Conference on Computer Communications Workshops*, pages 443–448, 2011.

M. Gharib, E. Rambod, and K. Shariff. A universal time scale for vortex ring formation. *Journal of Fluid Mechanics*, 1998.

Stamatios Giannoukos, Alan Marshall, Stephen Taylor, and Jeremy Smith. Molecular communication over gas stream channels using portable mass spectrometry. *Journal of The American Society for Mass Spectrometry*, 28(11):2371–2383, 2017.

Amin Gohari, Mahtab Mirmohseni, and Masoumeh Nasiri-Kenari. Information theory of molecular communication: Directions and challenges. *IEEE Transactions on Molecular, Biological and Multi-Scale Communications*, 2(2):120–142, 2016.

Carlos Granero-Belinchon, Stephane G Roux, and Nicolas B Garnier. Scaling of information in turbulence. *Europhys. Lett.*, 115(5):58003, Sept. 2016.

W. Guo, T. Asyhari, N. Farsad, H. Yilmaz, A. Eckford, and C.B. Chae. Molecular Communications: Channel Model and Physical Layer Techniques. *IEEE Wireless Communications*, Oct. 2016a.

Weisi Guo, Christos Mias, Nariman Farsad, and Jiang-Lun Wu. Molecular versus electromagnetic wave propagation loss in macro-scale environments. *IEEE Transactions on Molecular, Biological and Multi-Scale Communications*, 1(1):18–25, 2015.

Weisi Guo, Taufiq Asyhari, Nariman Farsad, H. Birkan Yilmaz, Bin Li, Andrew Eckford, and Chan-Byoung Chae. Molecular communications: channel model and physical layer techniques. *IEEE Wireless Communications*, 23(4):120–127, August 2016b.

Mustafa Can Gursoy, Ertugrul Basar, Ali Emre Pusane, and Tuna Tugcu. Index modulation for molecular communication via diffusion systems. *IEEE Transactions on Communications*, 67(5):3337–3350, 2019.

Julie C Hagelin and Ian L Jones. Bird odors and other chemical substances: a defense mechanism or overlooked mode of intraspecific communication? *The Auk*, 124(3):741–761, 2007.

W. Haselmayr, S. Aejaz, A. Asyhari, A. Springer, and W. Guo. Transposition errors in diffusion-based mobile molecular communication. *IEEE Communications Letters*, 21(9):1973–1976, 2017.

Werner Haselmayr, Neeraj Varshney, A Taufiq Asyhari, Andreas Springer, and Weisi Guo. On the impact of transposition errors in diffusion-based channels. *IEEE Transactions on Communications*, 67(1):364–374, 2018.

Werner Haselmayr, Andreas Springer, Georg Fischer, Christoph Alexiou, Holger Boche, Peter A Hoeher, Falko Dressler, and Robert Schober. Integration of molecular communications into future generation wireless networks. *1st 6G Wireless Summit. IEEE, Levi, Finland*, 2019.

P. Hennig, M. Osborne, and M. Girolami. Probabilistic numerics and uncertainty in computations. *Proc. Royal Society A*, 471, Jun. 2015.

S Hiyama, Y Moritani, T Suda, R Egashira, A Enomoto, M Moore, and T Nakano. Molecular communication. *in 2005 NSIT Nanotechnology Conference*, pages 33–40, 2005.

Satoshi Hiyama, Yuki Moritani, Riho Gojo, Shoji Takeuchi, and Kazuo Sutoh. Biomolecular-motor-based autonomous delivery of lipid vesicles as nano-or microscale reactors on a chip. *Lab on a Chip*, 10(20):2741–2748, 2010.

Bert Hölldobler, Edward O Wilson, et al. *The superorganism: the beauty, elegance, and strangeness of insect societies.* WW Norton & Company, 2009.

David P Hoogerheide, Slaven Garaj, and Jene A Golovchenko. Probing surface charge fluctuations with solid-state nanopores. *Physical review letters*, 102(25): 256804, 2009.

Serhat Hosder, Robert Walters, and Rafael Perez. A non-intrusive polynomial chaos method for uncertainty propagation in cfd simulations. In *44th AIAA Aerospace Sciences Meeting and Exhibit*, page 891, 2006.

Serhat Hosder, Robert Walters, and Michael Balch. Efficient sampling for non-intrusive polynomial chaos applications with multiple uncertain input variables. In *48th AIAA/ASME/ASCE/AHS/ASC Structures, Structural Dynamics, and Materials Conference*, page 1939, 2007.

Stefan Howorka, Stephen Cheley, and Hagan Bayley. Sequence-specific detection of individual dna strands using engineered nanopores. *Nature biotechnology*, 19(7): 636–639, 2001.

Ya-Ping Hsieh, Yen-Chi Lee, Po-Jen Shih, Ping-Cheng Yeh, and Kwang-Cheng Chen. On the asynchronous information embedding for event-driven systems in molecular communications. *Nano Communication Networks*, 4(1):2–13, 2013.

Y. Huang, M. Wen, L. L. Yang, C. Chae, and F. Ji. Spatial modulation for molecular communication. *IEEE Trans. Nanobiosci.*, 18(3):381–395, Mar. 2019.

Y. Huang et al. Space shift keying for molecular communication: Theory and experiment. In *Proc. IEEE Global Commun. Conf. (GLOBECOM)*, pages 1–6, Waikoloa, USA, Dec. 2019.

Willem Hundsdorfer and Jan G Verwer. *Numerical solution of time-dependent advection-diffusion-reaction equations*, volume 33. Springer Science & Business Media, 2013.

Jane L Hurst and Robert J Beynon. Scent wars: the chemobiology of competitive signalling in mice. *Bioessays*, 26(12):1288–1298, 2004.

Changbae Hyun, Harpreet Kaur, Ryan Rollings, Min Xiao, and Jiali Li. Threading immobilized dna molecules through a solid-state nanopore at$>$ 100 μs per base rate. *Acs Nano*, 7(7):5892–5900, 2013.

Meyer B Jackson. *Molecular and cellular biophysics.* Cambridge University Press, 2006.

Miten Jain, Hugh E Olsen, Benedict Paten, and Mark Akeson. The oxford nanopore minion: delivery of nanopore sequencing to the genomics community. *Genome biology*, 17(1):239, 2016.

Vahid Jamali, Arman Ahmadzadeh, Nariman Farsad, and Robert Schober. Scw codes for optimal csi-free detection in diffusive molecular communications. In *2017 IEEE International Symposium on Information Theory (ISIT)*, pages 3190–3194. IEEE, 2017.

Vahid Jamali, Arman Ahmadzadeh, Nariman Farsad, and Robert Schober. Constant-composition codes for maximum likelihood detection without csi in diffusive molecular communications. *IEEE Transactions on Communications*, 66(5): 1981–1995, 2018.

Ole Krogh Jensen and Bruce A Finlayson. Solution of the transport equations using a moving coordinate system. *Advances in Water Resources*, 3(1):9–18, 1980.

Roland Jeppson. *Open channel flow: numerical methods and computer applications.* CRC Press, 2010.

WP Jones and Brian Edward Launder. The prediction of laminarization with a two-equation model of turbulence. *International journal of heat and mass transfer*, 15 (2):301–314, 1972.

Md Humaun Kabir, SM Riazul Islam, and Kyung Sup Kwak. D-mosk modulation in molecular communications. *IEEE transactions on nanobioscience*, 14(6):680–683, 2015.

Leo P Kadanoff. *Statistical physics: statics, dynamics and renormalization.* World Scientific Publishing Company, 2000.

Masaki Kamakura. Royalactin induces queen differentiation in honeybees. *Nature*, 473(7348):478–483, 2011.

Ioannis Karatzas and Steven E Shreve. Brownian motion. In *Brownian Motion and Stochastic Calculus*, pages 47–127. Springer, 1998.

Peter Karlson and Martin Lüscher. 'pheromones': a new term for a class of biologically active substances. *Nature*, 183(4653):55–56, 1959.

John J Kasianowicz, Eric Brandin, Daniel Branton, and David W Deamer. Characterization of individual polynucleotide molecules using a membrane channel. *Proceedings of the National Academy of Sciences*, 93(24):13770–13773, 1996.

Steven M Kay. *Fundamentals of statistical signal processing.* Prentice Hall PTR, 1993.

E. Kennedy, P. Shakya, M. Ozmen, C. Rose, and J. Rosenstein. Spatiotemporal Information Preservation in Turbulent Vapor Plumes. *Applied Physics Letters*, 112, Jun. 2018.

UF Keyser, J Van der Does, C Dekker, and NH Dekker. Optical tweezers for force measurements on dna in nanopores. *Review of Scientific Instruments*, 77(10): 105105, 2006a.

Ulrich F Keyser, Bernard N Koeleman, Stijn Van Dorp, Diego Krapf, Ralph MM Smeets, Serge G Lemay, Nynke H Dekker, and Cees Dekker. Direct force measurements on dna in a solid-state nanopore. *Nature Physics*, 2(7):473–477, 2006b.

Ladan Khaloopour, Seyed Vahid Rouzegar, Alireza Azizi, Amir Hosseinian, Maryam Farahnak-Ghazani, Nahal Bagheri, Mahtab Mirmohseni, Hamidreza Arjmandi, Reza Mosayebi, and Masoumeh Nasiri-Kenari. An experimental platform for macro-scale fluidic medium molecular communication. *IEEE Transactions on Molecular, Biological and Multi-Scale Communications*, 5(3):163–175, 2019.

Na-Rae Kim and Chan-Byoung Chae. Novel modulation techniques using isomers as messenger molecules for nano communication networks via diffusion. *IEEE Journal on Selected Areas in Communications*, 31(12):847–856, 2013.

AL Kistler and T Vrebalovich. Grid turbulence at large reynolds numbers. *Journal of Fluid Mechanics*, 26(1):37–47, 1966.

Andrey Nikolaevich Kolmogorov. The local structure of turbulence in incompressible viscous fluid for very large Reynolds numbers. *Dokl. Akad. Nauk. SSSR*, 30:9–13, 1941a.

Andrey Nikolaevich Kolmogorov. On degeneration (decay) of isotropic turbulence in an incompressible viscous liquid. *Dokl. Akad. Nauk. SSSR*, 31:538–540, 1941b.

Jinglin Kong, Nicholas AW Bell, and Ulrich F Keyser. Quantifying nanomolar protein concentrations using designed dna carriers and solid-state nanopores. *Nano letters*, 16(6):3557–3562, 2016.

Bon-Hong Koo, Changmin Lee, H Birkan Yilmaz, Nariman Farsad, Andrew Eckford, and Chan-Byoung Chae. Molecular mimo: From theory to prototype. *IEEE Journal on Selected Areas in Communications*, 34(3):600–614, 2016.

Reinhardt Kotzé, Johan Wiklund, Rainer Haldenwang, and Veruscha Fester. Measurement and analysis of flow behaviour in complex geometries using the ultrasonic velocity profiling (uvp) technique. *Flow Measurement and Instrumentation*, 22(2): 110–119, 2011.

Stefan W Kowalczyk, David B Wells, Aleksei Aksimentiev, and Cees Dekker. Slowing down dna translocation through a nanopore in lithium chloride. *Nano letters*, 12 (2):1038–1044, 2012.

Alexander Kraskov, Harald Stögbauer, and Peter Grassberger. Estimating mutual information. *Physical review E*, 69(6):066138, 2004.

Padmini Krishnakumar, Brett Gyarfas, Weisi Song, Suman Sen, Peiming Zhang, Predrag Krstic, and Stuart Lindsay. Slowing dna translocation through a nanopore using a functionalized electrode. *ACS nano*, 7(11):10319–10326, 2013.

Bhuvana Krishnaswamy and Raghupathy Sivakumar. Amplitude-width encoding for error correction in bacterial communication networks. In *Proceedings of the*

5th ACM International Conference on Nanoscale Computing and Communication, pages 1–7, 2018.

Bhuvana Krishnaswamy, Caitlin M Austin, J Patrick Bardill, Daniel Russakow, Gregory L Holst, Brian K Hammer, Craig R Forest, and Raghupathy Sivakumar. Time-elapse communication: Bacterial communication on a microfluidic chip. *IEEE Transactions on Communications*, 61(12):5139–5151, 2013.

Donald E Kroodsma and Edward H Miller. *Ecology and evolution of acoustic communication in birds*. Comstock Pub., 1996.

M. S. Kuran, H. B. Yilmaz, T. Tugcu, and I. F. Akyildiz. Modulation techniques for communication via diffusion in nanonetworks. pages 1–5, June 2011.

Mehmet Şükrü Kuran, H Birkan Yilmaz, Tuna Tugcu, and Ian F Akyildiz. Interference effects on modulation techniques in diffusion based nanonetworks. *Nano Communication Networks*, 3(1):65–73, 2012.

Jong Woo Kwak, H Birkan Yilmaz, Nariman Farsad, Chan-Byoung Chae, and Andrea Goldsmith. Two-way molecular communications. *IEEE Transactions on Communications*, 2020.

Paul Langevin. Sur la théorie du mouvement brownien. *Compt. Rendus*, 146:530–533, 1908.

Marco Lanzagorta. *Underwater communications*. Morgan & Claypool Publishers, 2012.

Joseph Larkin, Robert Henley, David C Bell, Tzahi Cohen-Karni, Jacob K Rosenstein, and Meni Wanunu. Slow dna transport through nanopores in hafnium oxide membranes. *ACS nano*, 7(11):10121–10128, 2013.

Brian Edward Launder and Bahrat I Sharma. Application of the energy-dissipation model of turbulence to the calculation of flow near a spinning disc. *Letters in heat and mass transfer*, 1(2):131–137, 1974.

Brian Edward Launder and Dudley Brian Spalding. The numerical computation of turbulent flows. In *Numerical prediction of flow, heat transfer, turbulence and combustion*, pages 96–116. Elsevier, 1983.

Mark S Leeson and Matthew D Higgins. Error correction coding for molecular communications. In *2012 IEEE International Conference on Communications (ICC)*, pages 6172–6176. IEEE, 2012a.

Mark S Leeson and Matthew D Higgins. Forward error correction for molecular communications. *Nano Communication Networks*, 3(3):161–167, 2012b.

Jiali Li, Derek Stein, Ciaran McMullan, Daniel Branton, Michael J Aziz, and Jene A Golovchenko. Ion-beam sculpting at nanometre length scales. *Nature*, 412(6843): 166–169, 2001.

Jinxing Li, Berta Esteban-Fernández de Ávila, Wei Gao, Liangfang Zhang, and Joseph Wang. Micro/nanorobots for biomedicine: Delivery, surgery, sensing, and detoxification. *Science Robotics*, 2(4), 2017.

T. Lim and T. Nickels. Vortex rings. *Fluid Vortices*, 1995.

Lin Lin, Jiali Zhang, Maode Ma, and Hao Yan. Time synchronization for molecular communication with drift. *IEEE Communications Letters*, 21(3):476–479, 2017.

Lin Lin, Qian Wu, Fuqiang Liu, and Hao Yan. Mutual information and maximum achievable rate for mobile molecular communication systems. *IEEE transactions on nanobioscience*, 17(4):507–517, 2018.

Lin Lin, Qian Wu, Maode Ma, and Hao Yan. Concentration-based demodulation scheme for mobile receiver in molecular communication. *Nano Communication Networks*, 20:11–19, 2019.

Ignacio Llatser, Albert Cabellos-Aparicio, Massimiliano Pierobon, and Eduard Alarcón. Detection techniques for diffusion-based molecular communication. *IEEE J. Sel. Areas Commun.*, 31(12):726–734, Dec. 2013.

Charles G Lomas. *Fundamentals of hot wire anemometry.* Cambridge University Press, 2011.

Pengfei Lu, Yang You, Bo Liu, and ZhenQiang Wu. A vertical channel model of molecular communication based on alcohol molecules. *arXiv preprint arXiv:1603.03530*, 2016.

Yi Lu, Matthew D Higgins, and Mark S Leeson. Comparison of channel coding schemes for molecular communications systems. *IEEE Transactions on Communications*, 63(11):3991–4001, 2015.

Zhenmei Lu, Ye Deng, Joy D Van Nostrand, Zhili He, James Voordeckers, Aifen Zhou, Yong-Jin Lee, Olivia U Mason, Eric A Dubinsky, Krystle L Chavarria, et al. Microbial gene functions enriched in the deepwater horizon deep-sea oil plume. *The ISME Journal*, 6(2):451–460, 2012.

David JC Mac Kay. *Information theory, inference and learning algorithms*. Cambridge university press, 2003.

Mohammad Upal Mahfuz, Dimitrios Makrakis, and Hussein T Mouftah. On the characterization of binary concentration-encoded molecular communication in nanonetworks. *Nano Communication Networks*, 1(4):289–300, 2010.

Lionel Mathelin, M Yousuff Hussaini, and Thomas A Zang. Stochastic approaches to uncertainty quantification in cfd simulations. *Numerical Algorithms*, 38(1-3): 209–236, 2005.

Daniel Tunç McGuiness, Stamatios Giannoukos, Alan Marshall, and Stephen Taylor. Experimental results on the open-air transmission of macro-molecular communication using membrane inlet mass spectrometry. *IEEE Communications Letters*, 22(12):2567–2570, 2018.

Daniel Tunç Mcguiness, Stamatios Giannoukos, Stephen Taylor, and Alan Marshall. Experimental and analytical analysis of macro-scale molecular communications within closed boundaries. *IEEE Transactions on Molecular, Biological and Multi-Scale Communications*, 5(1):44–55, 2019.

Ling-San Meng, Ping-Cheng Yeh, Kwang-Cheng Chen, and Ian F Akyildiz. Mimo communications based on molecular diffusion. In *2012 IEEE Global Communications Conference (GLOBECOM)*, pages 5380–5385. IEEE, 2012.

Ling-San Meng, Ping-Cheng Yeh, Kwang-Cheng Chen, and Ian F Akyildiz. On receiver design for diffusion-based molecular communication. *IEEE Transactions on Signal Processing*, 62(22):6032–6044, 2014.

Christopher A Merchant, Ken Healy, Meni Wanunu, Vishva Ray, Neil Peterman, John Bartel, Michael D Fischbein, Kimberly Venta, Zhengtang Luo, AT Charlie Johnson, et al. Dna translocation through graphene nanopores. *Nano letters*, 10 (8):2915–2921, 2010.

Melissa B Miller and Bonnie L Bassler. Quorum sensing in bacteria. *Annual Reviews in Microbiology*, 55(1):165–199, 2001.

Michael John Moore, Tatsuya Suda, and Kazuhiro Oiwa. Molecular communication: Modeling noise effects on information rate. *IEEE transactions on nanobioscience*, 8(2):169–180, 2009.

COMSOL Multiphysics. Introduction to comsol multiphysics®. *COMSOL Multiphysics, Burlington, MA, accessed Feb*, 9:2018, 1998.

Yonathan Murin, Nariman Farsad, Mainak Chowdhury, and Andrea Goldsmith. Exploiting diversity in one-shot molecular timing channels via order statistics. *IEEE Transactions on Molecular, Biological and Multi-Scale Communications*, 4(1):14–26, 2018.

Saizalmursidi Md Mustam, Sharifah Kamilah Syed Yusof, and Samad Nejatian. Multilayer diffusion-based molecular communication. *Transactions on Emerging Telecommunications Technologies*, 28(1):e2935, 2017.

W Naeem, R Sutton, and J Chudley. Chemical plume tracing and odour source localisation by autonomous vehicles. *The Journal of Navigation*, 60(2):173–190, 2007.

Tadashi Nakano, Andrew W Eckford, and Tokuko Haraguchi. *Molecular Communication*. Cambridge University Press, 1 edition, 2013.

A. Noel, K. C. Cheung, and R. Schober. Optimal receiver design for diffusive molecular communication with flow and additive noise. *IEEE Trans. Nanobiosci.*, 13 (3):350–362, 2014.

Adam Noel, Karen C Cheung, and Robert Schober. A unifying model for external noise sources and isi in diffusive molecular communication. *IEEE Journal on Selected Areas in Communications*, 32(12):2330–2343, 2014.

Nathan Edward Owen. A comparison of polynomial chaos and gaussian process emulation for uncertainty quantification in computer experiments. 2017.

M. Ozmen, E. Kennedy, J. Rose, P. Shakya, J. K. Rosenstein, and C. Rose. High speed chemical vapor communication using photoionization detectors. In *Proc. IEEE Global Commun. Conf. (GLOBECOM)*, pages 1–6, Abu Dhabi, United Arab Emirates, Dec. 2018.

Shuo Pang and Jay A Farrell. Chemical plume source localization. *IEEE Transactions on Systems, Man, and Cybernetics, Part B (Cybernetics)*, 36(5):1068–1080, 2006.

Kyeong-Beom Park, Hyung-Jun Kim, Hyun-Mi Kim, Sang A Han, Kang Hyuck Lee, Sang-Woo Kim, and Ki-Bum Kim. Noise and sensitivity characteristics of solid-state nanopores with a boron nitride 2-d membrane on a pyrex substrate. *Nanoscale*, 8(10):5755–5763, 2016.

Christian Peeters, Thibaud Monnin, and Christian Malosse. Cuticular hydrocarbons correlated with reproductive status in a queenless ant. *Proceedings of the Royal Society of London. Series B: Biological Sciences*, 266(1426):1323–1327, 1999.

Theodore Peters Jr. Serum albumin. In *Advances in protein chemistry*, volume 37, pages 161–245. Elsevier, 1985.

Massimiliano Pierobon and Ian F Akyildiz. A physical end-to-end model for molecular communication in nanonetworks. *IEEE Journal on Selected Areas in Communications*, 28(4):602–611, 2010.

Massimiliano Pierobon and Ian F Akyildiz. Diffusion-based noise analysis for molecular communication in nanonetworks. *IEEE Transactions on Signal Processing*, 59(6):2532–2547, 2011a.

Massimiliano Pierobon and Ian F Akyildiz. Noise analysis in ligand-binding reception for molecular communication in nanonetworks. *IEEE Transactions on Signal Processing*, 59(9):4168–4182, 2011b.

Massimiliano Pierobon and Ian F Akyildiz. Capacity of a diffusion-based molecular communication system with channel memory and molecular noise. *IEEE Transactions on Information Theory*, 59(2):942–954, 2012.

Stephen B Pope. *Turbulent flows.* IOP Publishing, 2001.

Alexander D Poularikas. *Transforms and applications handbook.* CRC press, 2018.

Padarthi Naga Prasanth, Kakani Pruthvi Sumanth, Vijay K Chakka, and Gouriprasanna Roy. Experimental implementation of molecular communication system using sampling based adaptive threshold variation demodulation algorithm. In *2018 IEEE International Conference on Advanced Networks and Telecommunications Systems (ANTS)*, pages 1–5. IEEE, 2018.

Roger W Pryor. *Multiphysics modeling using COMSOL®: a first principles approach.* Jones & Bartlett Publishers, 2009.

Subodh Pudasaini, Seokjoo Shin, and Kyung Sup Kwak. Run-length aware hybrid modulation scheme for diffusion-based molecular communication. In *2014 14th International Symposium on Communications and Information Technologies (ISCIT)*, pages 439–442. IEEE, 2014.

Song Qiu, Weisi Guo, Siyi Wang, Nariman Farsad, and Andrew Eckford. A molecular communication link for monitoring in confined environments. In *2014 IEEE*

International Conference on Communications Workshops (ICC), pages 718–723. IEEE, 2014.

Song Qiu, A Taufiq Asyhari, Weisi Guo, Siyi Wang, Bin Li, Chenglin Zhao, and Mark S Leeson. Molecular channel fading due to diffusivity fluctuations. *IEEE Communications Letters*, 21(3):676–679, 2017.

Markus Raffel, Christian E Willert, Fulvio Scarano, Christian J Kähler, Steve T Wereley, and Jürgen Kompenhans. *Particle image velocimetry: a practical guide.* Springer, 2018.

Gunnar Ritt. Laser safety calculations for imaging sensors. *Sensors*, 19(17):3765, 2019.

Philip JW Roberts and Donald R Webster. *Turbulent diffusion.* ASCE Press, Reston, Virginia, 2002.

M Salehi and J Proakis. Digital communications. *McGraw-Hill Education*, 31:32, 2007.

Partha Sarathi, Roi Gurka, Gregory A Kopp, and Paul J Sullivan. A calibration scheme for quantitative concentration measurements using simultaneous PIV and PLIF. *Experiments in Fluids*, 52(1):247–259, 2012.

Grégory F Schneider and Cees Dekker. Dna sequencing with nanopores. *Nature biotechnology*, 30(4):326–328, 2012.

Grégory F Schneider, Stefan W Kowalczyk, Victor E Calado, Grégory Pandraud, Henny W Zandbergen, Lieven MK Vandersypen, and Cees Dekker. Dna translocation through graphene nanopores. *Nano letters*, 10(8):3163–3167, 2010.

Hoda ShahMohammadian, Geoffrey G Messier, and Sebastian Magierowski. Optimum receiver for molecule shift keying modulation in diffusion-based molecular communication channels. *Nano Communication Networks*, 3(3):183–195, 2012.

Claude E Shannon. A mathematical theory of communication. *The Bell system technical journal*, 27(3):379–423, 1948.

L. Shi and L. L. Yang. Error performance analysis of diffusive molecular communication systems with On-Off keying modulation. *IEEE Trans. Mol. Biol. Multi-Scale Commun.*, 3(4):224–238, Dec. 2017.

Lu Shi and Lie-Liang Yang. Error performance analysis of diffusive molecular communication systems with on-off keying modulation. *IEEE Transactions on Molecular, Biological and Multi-Scale Communications*, 3(4):224–238, 2017.

Po-Jen Shih, Chia-Han Lee, Ping-Cheng Yeh, and Kwang-Cheng Chen. Channel codes for reliability enhancement in molecular communication. *IEEE Journal on Selected Areas in Communications*, 31(12):857–867, 2013.

Amit Singhal, Ranjan K Mallik, and Brejesh Lall. Effect of molecular noise in diffusion-based molecular communication. *IEEE Wireless Communications Letters*, 3(5):489–492, 2014.

Charles G Speziale. Analytical methods for the development of reynolds-stress closures in turbulence. *Annual review of fluid mechanics*, 23(1):107–157, 1991.

Allison H Squires, Joseph S Hersey, Mark W Grinstaff, and Amit Meller. A nanopore–nanofiber mesh biosensor to control dna translocation. *Journal of the American Chemical Society*, 135(44):16304–16307, 2013.

Katepalli R Sreenivasan. On local isotropy of passive scalars in turbulent shear flows. *Proceedings of the Royal Society of London. Series A: Mathematical and Physical Sciences*, 434(1890):165–182, 1991.

Kothapalli V Srinivas, Andrew W Eckford, and Raviraj S Adve. Molecular communication in fluid media: The additive inverse gaussian noise channel. *IEEE transactions on information theory*, 58(7):4678–4692, 2012.

Milica Stojanovic. Acoustic (underwater) communications. *Wiley Encyclopedia of Telecommunications*, 2003.

Milica Stojanovic and James Preisig. Underwater acoustic communication channels: Propagation models and statistical characterization. *IEEE communications magazine*, 47(1):84–89, 2009.

AJ Storm, JH Chen, XS Ling, HW Zandbergen, and C Dekker. Fabrication of solid-state nanopores with single-nanometre precision. *Nature materials*, 2(8):537–540, 2003.

Yasushi Takeda. *Ultrasonic Doppler velocity profiler for fluid flow*, volume 101. Springer Science & Business Media, 2012.

Yuichi Tanaka, Shinichiro Haruyama, and Masao Nakagawa. Wireless optical transmissions with white colored led for wireless home links. In *11th IEEE International*

Symposium on Personal Indoor and Mobile Radio Communications. PIMRC 2000. Proceedings (Cat. No. 00TH8525), volume 2, pages 1325–1329. IEEE, 2000.

William Thielicke and Eize Stamhuis. Pivlab–towards user-friendly, affordable and accurate digital particle image velocimetry in matlab. *Journal of Open Research Software*, 2(1), 2014.

Luis A Torres, Brian A Fleck, David J Wilson, and David S Nobes. Calibration of a planar laser induced fluorescence technique for use in large scale water facilities. *Measurement*, 46(8):2597–2607, 2013.

N. Tuccitto, G. Li-Destri, G. Messinaa, and G. Marlettaa. Fluorescent Quantum Dots Make Feasible Long-Range Transmission of Molecular Bits. *ACS Physical Chemistry Letters*, 2017a.

Nunzio Tuccitto, Giovanni Li-Destri, Grazia ML Messina, and Giovanni Marletta. Fluorescent quantum dots make feasible long-range transmission of molecular bits. *The journal of physical chemistry letters*, 8(16):3861–3866, 2017b.

Nunzio Tuccitto, Giovanni Li-Destri, Grazia Maria Lucia Messina, and Giovanni Marletta. Reactive messengers for digital molecular communication with variable transmitter–receiver distance. *Physical Chemistry Chemical Physics*, 20(48): 30312–30320, 2018.

Meriç Turan, Mehmet Şükrü Kuran, H Birkan Yilmaz, Ilker Demirkol, and Tuna Tugcu. Channel model of molecular communication via diffusion in a vessel-like environment considering a partially covering receiver. In *2018 IEEE International Black Sea Conference on Communications and Networking (BlackSeaCom)*, pages 1–5. IEEE, 2018a.

Meric Turan, Mehmet Sükrü Kuran, Huseyin Birkan Yilmaz, Chan-Byoung Chae, and Tuna Tugcu. Mol-eye: A new metric for the performance evaluation of a molecular signal. In *accepted to IEEE Wireless Communications and Networking Conference (WCNC)*, April 2018b.

PL Tyack. Acoustic communication under the sea. In *Animal acoustic communication*, pages 163–220. Springer, 1998.

B. D. Unluturk and I. F. Akyildiz. An End-to-End Model of Plant Pheromone Channel for Long Range Molecular Communication. *IEEE Transactions on Nanobioscience*, 2017a.

Bige D Unluturk and Ian F Akyildiz. An end-to-end model of plant pheromone channel for long range molecular communication. *IEEE Transactions on Nanobioscience*, 16(1):11–20, 2017b.

Harald Unterweger, Jens Kirchner, Wayan Wicke, Arman Ahmadzadeh, Doaa Ahmed, Vahid Jamali, Christoph Alexiou, Georg Fischer, and Robert Schober. Experimental molecular communication testbed based on magnetic nanoparticles in duct flow. In *2018 IEEE 19th International Workshop on Signal Processing Advances in Wireless Communications (SPAWC)*, pages 1–5. IEEE, 2018.

Bala Murali Venkatesan and Rashid Bashir. Nanopore sensors for nucleic acid analysis. *Nature nanotechnology*, 6(10):615–624, 2011.

Sergio Verdú et al. A general formula for channel capacity. *IEEE Transactions on Information Theory*, 40(4):1147–1157, 1994.

Donald Voet, Judith G Voet, and Charlotte W Pratt. *Fundamentals of biochemistry: life at the molecular level*. Number 577.1 VOE. 2013.

Robert Walters. Towards stochastic fluid mechanics via polynomial chaos. In *41 st AIAA Aerospace Sciences Meeting & Exhibit, Reno, NV*, 2003.

Siyi Wang, Weisi Guo, Song Qiu, and Mark D McDonnell. Performance of macro-scale molecular communications with sensor cleanse time. In *2014 21st International Conference on Telecommunications (ICT)*, pages 363–368. IEEE, 2014.

Meni Wanunu. Nanopores: A journey towards dna sequencing. *Physics of life reviews*, 9(2):125–158, 2012.

Christopher M Waters and Bonnie L Bassler. Quorum sensing: cell-to-cell communication in bacteria. *Annu. Rev. Cell Dev. Biol.*, 21:319–346, 2005.

Marc J Weissburg. Waterborne chemical communication: stimulus dispersal dynamics and orientation strategies in crustaceans. In *Chemical communication in crustaceans*, pages 63–83. Springer, 2010.

MJ Weissburg, DB Dusenbery, H Ishida, J Janata, T Keller, PJW Roberts, and DR Webster. A multidisciplinary study of spatial and temporal scales containing information in turbulent chemical plume tracking. *Environmental Fluid Mechanics*, 2(1-2):65–94, 2002.

Frank M White. *Fluid mechanics*. McGraw-hill, 1999.

www.turnerdesigns.com. Cyclops-7 submersible sensors, 2010.

Tristram D Wyatt. *Pheromones and animal behavior: chemical signals and signatures.* Cambridge University Press, 2014.

Dongbin Xiu and George Em Karniadakis. Modeling uncertainty in flow simulations via generalized polynomial chaos. *Journal of Computational Physics*, 187(1):137–167, 2003.

Zhengji Zhang. *LDA application methods: laser Doppler anemometry for fluid dynamics.* Springer Science & Business Media, 2010.

Robert M Ziff, Satya N Majumdar, and Alain Comtet. Capture of particles undergoing discrete random walks. *The Journal of chemical physics*, 130(20):204104, 2009.

Dennis Zill, Warren S Wright, and Michael R Cullen. *Advanced engineering mathematics.* Jones & Bartlett Learning, 2011.

William BJ Zimmerman. Introduction to comsol multiphysics. *Multiphysics Modeling with Finite Element Methods. Citation Key: Zimmerman2006. World Scientific Publishing Company*, pages 1–26, 2006.

Mohammad Zoofaghari and Hamidreza Arjmandi. Diffusive molecular communication in biological cylindrical environment. *IEEE transactions on nanobioscience*, 18(1):74–83, 2018.